UNIVERSITY OF
BIRMINGHAM

Studying Novel Electrolytes for Zinc Electrochemical Technologies using NMR and MRI

Thesis submitted for the degree of
Doctor of Philosophy
at the University of Birmingham

By
Yasmeen Moeid Abdullah AlZahrani
Department of Chemistry
University of Birmingham

July 2021

Abstract

Studying Novel Electrolytes for Zinc Electrochemical Technologies using NMR and MRI

Yasmeen Moeid Abdullah AlZahrani

University of Birmingham 2021

This thesis investigates novel electrolytes for zinc electroplating using NMR and MRI. Three systems have been investigated, two ChCl-based deep eutectic solvents, ethaline and reline, and the ionic liquid [$C_2C_1Im(TfO)$]. Previously, these three electrolytes have been investigated as alternative electrolytes for electroplating Zn. They have also shown promise as electrolytes for different Zn electrochemical technologies such as zinc-based batteries. A range of ethaline and reline DESs and [$C_2C_1Im(TfO)$] IL have been investigated, in the presence and absence of Zn and water. Molecular interactions and dynamics in these systems have been investigated using 1D NMR measurements such as spectroscopy, relaxation, and diffusion. These NMR relaxation studies have been used as a foundation to visualize the electroplating of zinc from $Zn(TfO)_2$-[$C_2C_1Im(TfO)$] systems (*in operando*) and $ZnCl_2$-ethaline (*in situ*), using MR relaxation maps.

^{19}F MRI of the TfO anion, in the 0.15 M $Zn(TfO)_2$-[$C_2C_1Im(TfO)$] systems, has revealed changes in both T_1 and T_2 during the electroplating of zinc. To understand the causes of these changes in relaxation times, we need to consider the influence of Zn and water on the relaxation time of the TfO anion. It has been observed that ^{19}F T_1 and T_2 MR relaxation times are affected by the concentrations of zinc and water. The electroplating of zinc from $ZnCl_2$-ethaline systems was imaged using ^{1}H MR T_2 relaxation time, *in situ*, before and after electroplating, which was performed outside the magnet. The influence of water and zinc on ^{1}H NMR relaxation times has been used as a key for interpreting MRI results.

Publications

Poster:

1. Yasmeen M. AlZahrani, Joshua M. Bray, Melanie M. Britton, Developing magnetic resonance imaging (MRI) for studying batteries, *14th International Conference on Magnetic Resonance Microscopy (ICMRM)*, 13 -17 August 2017, Dalhousie University, Halifax, Canada.

2. Yasmeen M. AlZahrani, Joshua M. Bray, Melanie M. Britton, Developing magnetic resonance imaging (MRI) for studying batteries, *Electrochem 2017*, 10 -12 September 2017, University of Birmingham, Birmingham, UK.

3. Yasmeen M. AlZahrani, Melanie M. Britton, Studying Novel Electrolytes for Zn-Electrochemical Technologies using NMR,*14th International conference on materials chemistry (MC14)*, 8 -11 July 2019, Aston University, Birmingham, UK.

Paper:

1. Yasmeen M. AlZahrani, Melanie M. Britton; Probing the influence of Zn and water on solvation and dynamics in ethaline and reline deep eutectic solvents by ^{1}H nuclear magnetic resonance. *Phys Chem Chem Phys*. 2021;**23**:21913-21922.

Acknowledgments

First and foremost, I would like to thank Allah for giving me the chance, patience, and health to carry out this research. Second, I would like to thanks my supervisor Dr. Melanie Britton for her support and engorgements. I appreciate all the help you have given me, especially how to have faith in myself and my ability. You have made me more optimistic, positive, and successful not only in my study but in general life. Thank you for being patient and supportive. I appreciate the time you've spent mentoring me during my first few months on NMR and MRI techniques. I don't know what to say no words can express how grateful I am.

A big thanks to all Britton's group members (Emma Thompson, Joshua Bray, Gabriele Cimmarusti, Claire Doswell, Helen Abbott, and Pooja Kumari) for their help and support during my Ph.D. journey. I really appreciate our tea time when we just set and talk about silly subjects! Thank you for making my Ph.D. journey enjoyable even when we have bad days in the lab. A special thanks to Claire Doswell, I really appreciate the time you've spent mentoring and training me on different lab equipments.

Finally, I would like to thank the Saudi Arabia Ministry of Higher Education and the chemistry department in Imam Abdulrahman Bin Faisal University for the financial support to achieve my Ph.D. A warmest thanks to my dad (Moeid AlZahrani), mom (Fawziah AlZahrani), sisters (Asmahan and Eman), and brothers (Abdullah, Ahmed, Omar, Khalid and Faisal) for being so supportive and believing in me. A special thanks to my old brother Ahmed, I really appreciate your consideration, guidance, help, and time.

A quote changed my life

Optimism is the faith that leads to achievement. Nothing can be done without hope and confidence.

List of content

List of Figures

List of Tables

Chapter 1 Introduction

Zinc-based electrochemical technologies are important across many areas of industry and society. One key area is zinc electroplating, which is a critical manufacturing process, used in many industries applications for functional and decorative purposes.[1-3] In addition, Zinc electrochemical processes (electroplating/electrodissolution) are important in zinc-based batteries.[4] In general, any battery consists of three main components: the anode, the cathode and the electrolyte.[4] It is known that batteries operated through two types of electrochemical reactions (oxidation and reduction), these reactions convert the chemical energy to electrical energy.[4-5] For zinc-based batteries, upon the discharge of the battery, typically, zinc metal is oxidized to zinc ions, this process known as electrodissolution, **Equation 1.1**.[4-5] While upon charging, zinc ions are reduced to the zinc metallic state, this process known as electroplating, **Equation 1.2**.[4-5] The electrolyte is the medium where redox reactions occur, and it is typically liquid.[4]

$$Zn \rightarrow Zn^{2+} + 2e^{-} \qquad \textbf{Equation 1.1}$$

$$Zn^{2+} + 2e^{-} \rightarrow Zn \qquad \textbf{Equation 1.2}$$

Batteries have been classified into two types, primary batteries (non-rechargeable), and secondary batteries (rechargeable).[4] Zinc-based primary batteries are commonly used worldwide in many electronic devices.[6-8] However, there is increasing interest in zinc-based secondary batteries, which are not commercialized yet.[9-12] There is a lot of interest in improving these technologies to optimize their performance, environmental impact, reduce their cost, and make them more sustainable.[10, 13]

Zinc electroplating is a very important process across a range of different industries, including vehicles, aerospace, constructions, and oil and gas.[14] A range of metals, which can be oxidized when exposed to oxygen from air or moisture, such as steel and iron, have been coated with zinc metal as anticorrosion resistance.[2, 15] The coated zinc layer is applied to protect the metal object and form a corrosion-resistant layer.[2] For economic reasons, zinc is a good choice of coating for corrosion protection, because it is abundant and hence, less expensive than other metals.[3] In addition, it can be easily deposited on various metals.[3] Currently, zinc electroplating relies on toxic and corrosive electrolytes such as cyanide acid solution, non-cyanide alkaline solution, and acid chloride solution.[3, 16] The electroplating process affected by some factors, such as mass transport, speciation, and nucleation mechanism.[17] Mass transport depends on the physical properties of the electrolytes such as viscosity.[17] The low viscous electrolyte has a high mass transport, and that increases the nucleation growth rate.[17] Speciation difference affects the deposited film morphology.[17] Nucleation occurs on the electrode surface, and it can be instantaneous or progressive.[17] The instantaneous nucleation occurs when the rate of growth is slow in comparison to the rate of nucleation, where the nuclei continue to form in all surface sites within a short time.[17] Whereas in the progressive nucleation mechanism, the nucleation rate is slow, here, nucleation is continued to occur at the surface, whilst previous nucleation centers continue to grow.[17]

Zinc-based primary batteries, such as zinc-carbon (Leclanche´) and alkaline-zinc batteries are commonly used worldwide.[4] This is due to their low-cost and higher capacity, good low-temperature performance.[4] Primary batteries are an important power source for many daily electronic devices, and they can be used only once.[4] Consequently, there will be an increase in the consumption of these batteries which requires facilities to dispose of properly, which will be costly and time-consuming. Therefore, there is an increased interest in developing rechargeable, safe, and environmentally friendly batteries. Zinc-based rechargeable batteries have been considered as a good candidate that can meet the energy storage demands. Different studies[10, 12-13, 18-20] have been carried out to improve rechargeable zinc-batteries, however, these batteries are not commercialized yet.

Significant research efforts have been exerted to develop and improve zinc electrochemical technologies. For zinc electroplating, researchers have been focusing on developing new electrolytes as alternative solutions of current toxic and corrosive aqueous electrolytes.[14, 21-22] Their aim to find new electrolytes which meet economic and environmental demands. For zinc-batteries, different aspects have been investigated to improve battery performance, including electrodes[23], cell design[24], and electrolytes[18, 25-26]. This thesis focuses on the development of novel electrolytes for zinc electrochemical technologies by developing new analytical techniques to study the processes involved in zinc batteries and electroplating. Novel electrolytes based on ionic liquids[27-34] (ILs) and deep eutectic solvents[35-38] (DESs) are promising alternative electrolytes, in such electrochemical technologies, due to their performance and environmental impacts.[26]

1.1 Zinc electrochemical technologies

1.1.1 Zinc electroplating

Zinc has become widely used as anti-corrosion layer, in several industrial applications, over cadmium which have some safety concerns.[14] Zinc metal is safe, abundant, easy to deposit, and it has the ability to protect metals from oxidation.[39] From the cathodic potential series[40] it can be seen that zinc (– 0.76 V vs SHE) is less noble or more active than iron and steel (–0.44 V vs SHE).[40-41] Therefore, when iron and steel metals coated with zinc, they will be corrosion-resistance. Zinc electroplating is as a galvanization process.[42] This process is performed by applying an electrical current through a zinc aqueous solution, which contains zinc anode and steel cathode.[42] Zinc ions are reduced to zinc metal on the surface of the steel cathode.[39] Currently, zinc coating is performed commercially by immersing cleaned metal objects into an aqueous solution of zinc sulfates or zinc chloride, **Figure 1.1** [39]

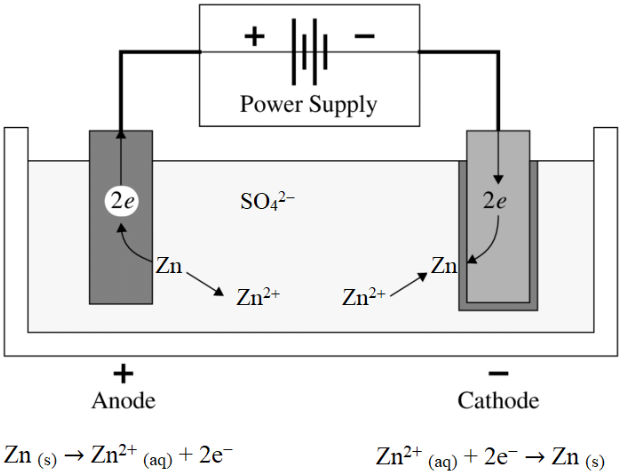

Figure 1.1: Schematic diagram of the zinc electroplating process, showing zinc oxidation reaction at the anode (zinc electrodissolution), and zinc reduction reaction at the cathode (zinc electroplating). Adapted from reference [43].

Zinc cyanide electrolyte is the most widely used for zinc electroplating.[44] This electrolyte typically consists of zinc cyanide, sodium cyanide, and sodium hydroxide.[44] However, these cyanide solutions are not popular anymore due to their toxicity, and hence, their costly disposal.[44] Therefore, alternative cyanide-free solutions are used commercially in zinc electroplating.[44] The first alternative solutions are mild acid solutions, which typically consist of zinc chloride and ammonium chloride.[44] These types of solutions are cyanide-free, so they can eliminate cyanide pollution and its expensive cost.[44] The second are alkaline-zincate solution, which is composed of zinc oxide and sodium hydroxide.[44] These types of non-cyanide electrolytes are cheap, easy to prepare, environmentally friendly, and have a high conductivity.[44] However, in spite of all these advantages, there are some problems associated with aqueous electrolytes, such as their narrow electrochemical window, low thermal stability, and their ability to evaporate.[14] In addition, aqueous electrolytes can lead to the hydrogen evolution reaction on the cathode, which competes with the desired zinc plating process, and influence the deposited zinc morphology.[14] Advanced non-aqueous electrolytes, such as ILs and DESs, are promising to be used in the electroplating process due to their capability to overcome aqueous electrolytes drawbacks.[14]

1.1.2 Zinc batteries

The development of energy storage has gained much interest in order to reach energy market demands, which based on safety, cost, and environment. Rechargeable lithium-ion batteries (LIBs) are the current worldwide used batteries due to their superior advantages including their higher energy density, their ability to have a large number of charge/discharge cycles, their ability to be operated over a wide temperature range, and their lightweight.[4, 45] This type of battery is used as an energy source in many applications, including mobile phones, cameras, and vehicles.[4] In spite of all LIBs advantages, these batteries suffer from some safety concerns, as a consequence of dendrite formation, which leads to a short circuit and a risk of fire.[4, 45] Dendrite can be defined as a metallic microstructure (whiskers) formed on the negative electrode while charging the battery, **Figure 1.2**.[46] In addition, materials used in LIBs such as lithium, nickel, and cadmium are less abundant in the earth's crust, and that makes them expensive which lead to some economic concerns.[4, 45] Therefore, it is important to find alternative inexpensive, high efficiency, and environmental-friendly energy storage.

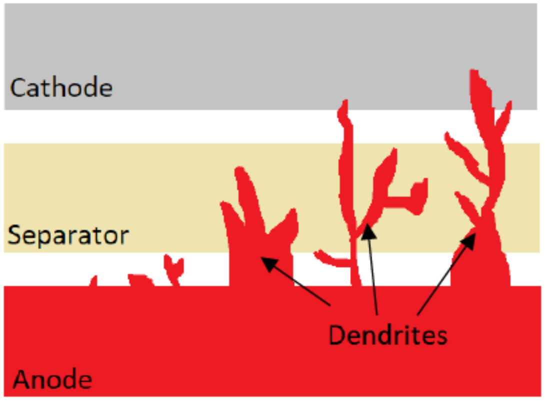

Figure 1.2: A schematic diagram illustrates the formation of the metallic microstructure (dendrites) on the anode during the charge.

Zinc-based batteries have been proposed as a promising alternative to LIBs, due to zinc metal advantages.[47] Zinc metal is safe, environmentally friendly and highly abundant, therefore, it is inexpensive.[48-49] Moreover, zinc has a high energy density owing to its ability to transfer two-electrons during the redox reaction.[48-49] It has been reported that zinc-air, zinc-silver oxide, and zinc-mercuric batteries have the potential to match the capability of lithium batteries at 20 °C.[4] Presently, primary zinc-based batteries, such as zinc-air[50] and zinc-ion[48] batteries, have been successfully commercialized. Zinc-carbon battery has been developed by Georges-Lionel Leclanche´ in 1866, and that why it is known as Leclanche´cell.[4] This zinc electrochemical cell was safe, cheap, easily maintained, and it has an excellent shelf-life.[4] In this zinc battery, a zinc bar was used as an anode (the negative electrode), while a carbon rod used as a cathode (the positive electrode).[4] These two electrodes were immersed in a mixture of ammonium chloride and zinc chloride.[4] Leclanche´cell materials considered as the base for today's zinc-carbon batteries.[4]

For rechargeable zinc-ion battery, different zinc salts have been studied as aqueous zinc-ion electrolytes including, $ZnSO_4$, $Zn(ClO_4)_2$, $ZnCl_2$, ZnF_2, $Zn(NO_3)_2$, and $Zn(CH_3COO)_2$.[48] The solubility of ZnF_2 in water is low, therefore, it does not seems to be the ideal electrolyte for zinc-ion batteries.[48] Zinc chloride has a narrow potential window, whereas, $Zn(ClO_4)_2$ showed a higher overpotential, thus, both of them are not suitable to use as electrolytes.[51] $ZnSO_4$ is commonly used in zinc-ion batteries as an electrolyte due to its low-cost, high solubility and stability in water. However, $ZnSO_4$ electrolyte also does not seems to be perfect, due to the formation of $Zn_4(OH)_6SO_4.nH_2O$ precipitate during the charge/discharge process, resulting in a reduction in the battery capacity.[52]

In general, aqueous electrolytes seem to be ideal for such metal-ion batteries owing to their excellent properties. These kinds of electrolytes are cheap, non-flammable, easy to prepare, environmentally friendly, in addition to their high conductivity and their ability to dissolve a range of metal salts.[48] However, aqueous electrolytes also have some drawbacks including their ability to evaporate, their narrow potential window, and their low thermal stability.[26, 48] Moreover, in such electrolytes, hydrogen evolution occurs as a competitive side reaction, and this leads to battery performance degradation, and hence a reduction in the life-time of battery.[13] The formation of zinc dendrites and zinc passivation layer has been considered as a critical drawback of alkaline aqueous electrolytes, such as KOH and NaOH.[13, 26] The passivation layer is formed when zinc ions interact with oxygen forming a ZnO film on the anode surface during the discharge.[5] This ZnO layer blocks certain areas of zinc anode, and that affects the re-chargeability of the battery.[5] It has been reported that the battery is easily charged in the absence of ZnO by reducing zinc ions to their metallic state.[5] Huge efforts have been made to develop new electrolytes, for electrochemical application, to overcome aqueous solutions drawbacks.[26] Non-aqueous solutions including ILs and DESs are promising electrolyte candidates for different secondary batteries.[27-28, 33, 53]

1.2 Novel electrolytes

1.2.1 Ionic liquids (ILs)

Ionic liquids were discovered in the 20th century.[54] Paul Walden discovered one of the earliest ionic liquid, which is $[EtNH_3][NO_3]$ with a melting point of 12 °C, in 1914 while he was searching for a molten salt that is liquid at room temperature.[54] The interest in ionic liquids, and their properties, has been increasing since the 1980s.[54] ILs are composed solely of anions and cations, as a salt, which is a liquid below 100 °C.[55] The transition from solid to liquid is a consequence of the structure of constituent cations and anions.[55] The large size asymmetric cations form weak hydrogen bonds with anions, besides their steric factor, which lower their capability to crystallize.[55] A great advantage with ionic liquids is that can be designed, through a selection of anion and cation, enabling optimization of their physical properties specific to a diverse range of applications.[34] Different salts have been used to design ionic liquids, with a range of desired properties, including pyrroldinium, imidazolium and quaternary ammonium salts as cations, and bis(fluorosulphonyl)imide and trifluoromethanesulfonate as anions.[55] **Figure 1.3** shows the chemical structures of common anions and cations used to prepare ILs. It has been reported that the type of cation primarily controls the physical properties of ILs, while anions control their chemical properties.[56]

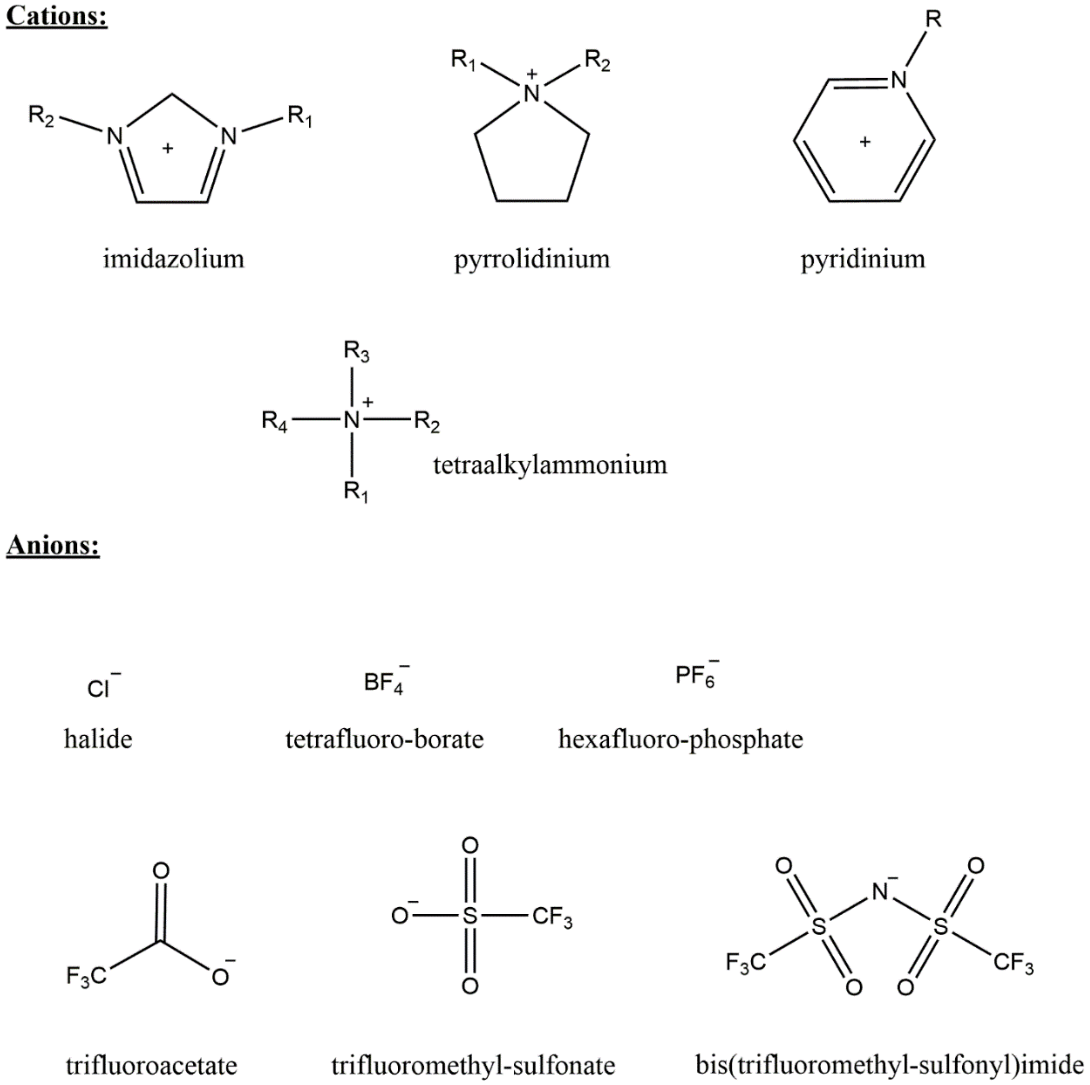

Figure 1.3: Chemical structures of common cations and anions of ionic liquids.

Ionic liquids have excellent properties, which make them key materials for various electrochemical application developments including batteries[33], supercapacitors[57], and fuel cells[58]. ILs are non-flammable, non-volatile, with wide potential window and high chemical stability.[32] The main drawbacks of these liquids are their high cost, thus they cannot be used in large scale applications.[34] In addition, they are typically highly hygroscopic, making these liquids harder to handle under the atmosphere.[34] Moreover, these kinds of liquids are highly viscous which affects their conductivity.[34] It has been found that the addition of co-solvents, such as water or organic solvents, enhanced the physical properties of ionic liquids.[59-62] For example, the dissolution rate of cellulose in 1-butyl-3-methylimidazolium acetate, [C_4C_1Im][OAc], has been increased with the addition of dimethyl sulfoxide.[61] Different carbonate solvents have been added to 1-ethyl-3-methylimidazolium bis(trifluoromethanesulfonyl), [C_2C_1Im][TFSI], to enhance the electrolyte physical properties for sodium-ion batteries application.[59] It was found that the viscosity of [C_2C_1Im][TFSI], is greatly decreased, by the carbonate solvents addition, while the electrochemical properties and thermal stability remain similar to those of pure ILs.[59] However, it was found that the presence of chloride impurities in ionic liquids increases the ionic liquid viscosity.[62] Therefore, when purchase or synthesis ILs, careful consideration should be given to the purification steps and purity measurements, especially when physical parameters of IL are critical for the desired application. The high cost and poor performance of current ILs have led researchers to investigate alternative non-aqueous electrolytes. One promising family of electrolytes are deep eutectic solvent, which attracted researchers' attention due to their comparable properties to ionic liquids, besides their lower-cost.[26, 38]

1.2.2 Deep eutectic solvents (DESs)

DESs have been considered as a new generation of ionic liquids.[63] In 2001, Abbott *et. al.* published the first paper on DESs,[64] which introduced a range of molten salts, based on quaternary ammonium salts and metal chloride. DESs are typically prepared by mixing a quaternary ammonium salt, as hydrogen bond acceptor (HBA), and molecular hydrogen bond donor (HBD).[63] Strong interaction occurs between HBD and HBA results in a supermolecular complex, which forms a eutectic solvent.[63] This eutectic solvent has a melting point lower than their initial constitutes, i.e. HBA and HBD. **Figure 1.4** shows the typical phase diagram of deep eutectic solvent that consists of two components.[63]

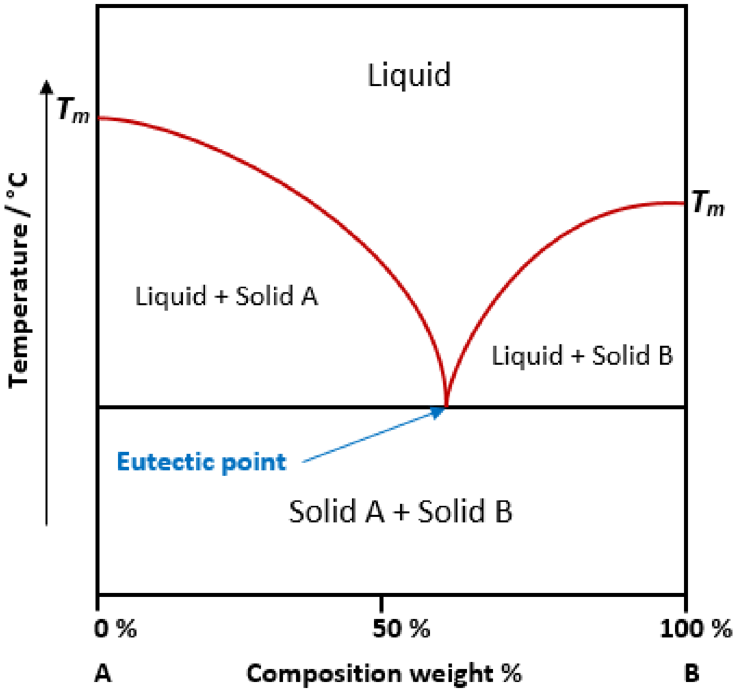

Figure 1.4: A schematic diagram of two-components, (A and B), phase diagram, showing the eutectic point which is lower than the melting point, T_m, of both A and B components.

DESs have been classified into four types, depending on their initial components, as shown in **Table 1.1**.[63] Type I are mixtures of metal halide salts and chloroaluminate salts, but are limited due to the limited number of anhydrous metal salts.[63] Type II DESs, are formed with hydrated metal salts, instead of anhydrous salts, which overcomes the limitation of type I DESs.[63] Type III DESs are formed using quaternary ammonium salts, as HBA, and an HBD, such as alcohols, amides, and weak acids.[63] Type III DESs constituents are cheap, low toxic, and biodegradable, thus they are the most widely studied DESs.[63] Finally, type IV of DESs which has been studied mostly to be an electrolyte for metal electroplating process.[63] It has been reported, that the eutectic point depends on the melting point of metal halide salt.[63] Since the melting point of hydrated metal salt is much lower than their corresponding non-hydrated salt, type II of DESs has a lower eutectic point compared to type I.[63]

Table 1.1: Deep eutectic solvent classification.[63]

Type	Formed between	General formula	Terms
type I	metal halide & quaternary ammonium salts	$Cat^+X^-zMCl_x$	M = Zn, Sn, Fe, Al
type II	hydrated metal halides & quaternary ammonium salts	$Cat^+X^-zMCl_x \cdot yH_2O$	M = Cr, Co, Cu, Ni, Fe
type III	quaternary ammonium salts & hydrogen bond donor	Cat^+X^-zRZ	Z = $CONH_2$, COOH, OH
type IV	metal halide & hydrogen bond donor	$MCl_x + RZ = MCl_{x-1}^+ \cdot RZ + MCl_{x+1}^-$	M = Al, Zn and Z = $CONH_2$, OH

DESs have similar properties as those observed in ionic liquids, including non-flammability, non-volatility, and their wide potential window.[38] However, DESs have some advantages that make them promising candidates to replace ionic liquids in many applications.[63] DESs are inexpensive, owing to their low-cost constituents.[38] Moreover, DESs are easy to prepare, by simply mixing two or three components with moderate heating, without the need of purification.[38] Therefore, such liquids can be easily prepared for large scale applications. Additionally, DESs are capable of dissolving different metal salts, which is very critical for their electrochemical applications, such as electroplating[35, 65] and batteries.[18, 53] DESs based on choline chloride (ChCl) are the most widely investigated, owing to ChCl low-cost and low toxicity.[66] Moreover, the ChCl-based DESs shown the lowest melting points.[66] **Table 1.2** shows common ChCl-based DESs, type III, and their initial components, as well as, their melting points. **Figure 1.5** shows the chemical structure of ethaline, reline and glyceline DESs constituents.[67]

Table 1.2: Common type III DESs and their initial components. The melting point of DESs and their combination are shown between brackets.

Hydrogen bond acceptor, HBA	Hydrogen bond donor, HBD	Molar ratio of HBA:HBD	DES name	Ref.
Choline chloride, (302 °C)	Urea, (133 °C)	1:2	Reline, (12 °C)	68
	Ethylene glycol, (–12.9 °C)	1:2	Ethaline, (–40 °C)	63
	Glycerol, (17.8 °C)	1:2	Glyceline, (–66 °C)	69

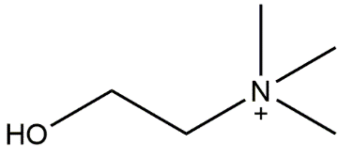

choline chloride, ChCl

ethylene glycol, EG

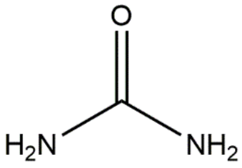

urea, U

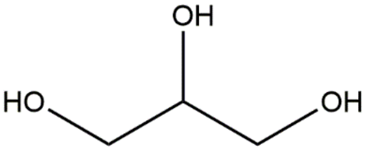

glycerol, Gly

Figure 1.5: Chemical structures of common type III DESs components.

1.3 Structure and inter/intra molecular interactions of ILs

In order to be able to tailor the properties of ILs and DESs, it is important to understand the structure of ILs and DESs species, which is the key to understand their chemical, physical and dynamic properties. Prior research suggests that bulk ILs structure is similar to that of homogenous molecular liquids.[70] Then, another study suggested, that the bulk ILs structure analogous to the highly concentrated salts solutions structure.[71] There is extensive literature indicating ILs are structured solvents,[71] where cations and anions form ion pairs, ions clusters, and hydrogen bond networks, as shown in **Figure 1.6**.[71] Some studies have referred to ions clusters as an aggregation or nanostructure.[71] Ion pairs, formed as a consequence of cation-anion interactions, are the basic unit of ion liquids structure, whereas, ions cluster is formed when three or more ions are interacting together.[71]

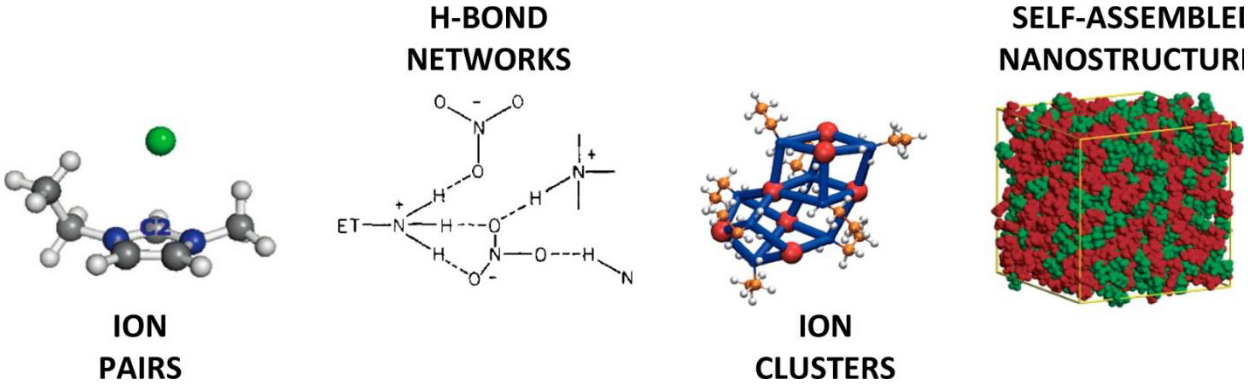

Figure 1.6: Models of Bulk structure of ionic liquids. Reproduced with permission from ref [71].

Ion pairs form when cations and anions interact with each other directly, via a hydrogen bond or electrostatic interaction or van der Waals.[72] The formation of cation-anion pairs lowers the fluidity of ionic liquids.[72] Different characterisation techniques have been used to study cation-anion interactions in ILs including infrared (IR) and Raman spectrocopies[73], nuclear magnetic resonance (NMR) spectroscopy[74], and computational simulation methods such molecular dynamics (MD).[75] It is found that hydrogen bonds (H-bonds) formed between the cation and anion, in ILs, are not linear and it is longer than that of "ideal" H-bond.[72] The physical properties of any ionic liquid rely on the ionic liquid structure and their intra/ intermolecular interactions.[72] Therefore, it is essential to study inter/intra molecular interactions of imidazolium-based ILs, which is the most widely investigated system. It was reported that imidazolium-based ionic liquids stability rely on their H-bond network.[72] Imidazolium cations form H-bonds, via the relatively acidic protons on the imidazolium ring, C(2)–H and N–H.[76] When these hydrogen bond sites alkylated by substitute the hydrogen on C(2) or N by alkyl, there will be a disruption in the ILs H-bond network.[76] It was found that the methylation of C(2) of imidazolium ring increase the melting point and viscosity of ILs, as a consequence of ILs entropy reduction.[76] The viscosity of ionic liquids is also affected by the structure of cations, the ionic liquid that consist of large asymmetric cations has a high viscosity.[77]

1.4 Structure and inter/intra molecular interactions of DESs

Deep eutectic solvents consist of hydrogen bond donor (HBD) and hydrogen bond acceptor (HBA) which forms together a hydrogen bond network.[63] As a consequence, a supermolecular complex is formed and that establish the melting point depression of DESs. The DES formation results in an increase in H-bonds number, formed between DES constituents, and a simultaneous reduction in the original H-bonds existing among each constituent.[63] To illustrate this, ethaline, (1ChCl:2EG), will be taken as an example. When ethaline is formed, the hydrogen bond number of ChCl-EG is increased, while the hydrogen bond number of ChCl-ChCl and EG-EG are decreased. This reduction in the original H-bonds leads to the eutectic point.[67]

Physical properties of DESs are affected by the strength and the nature of the HBD.[78] In the case of ethaline and reline, in ethaline, the HBD is ethylene glycol, which is a weak HBD, whereas in reline the HBD is urea, a strong HBD.[78] Therefore, the H-bond formed between ChCl-urea is much stronger than that formed between ChCl-EG, and hence reline has a higher viscosity (790 cP) than ethaline (40 cP), these values measured at 22 °C. Previous research shows that ethaline has three important interactions: nitrogen atom of choline cation, Ch^+, and chloride anion ($N^+ \cdots Cl^-$), the hydroxyl groups in choline cation and ethylene glycol ($HO_{Ch+} \cdots HO_{EG}$), and the hydroxyl group of ethylene glycol and chloride anion ($OH_{EG} \cdots Cl^-$).[78] It was reported that the

HBD⋯Cl^- interaction is the key in these DESs (Type III) formation.[78] Prior research suggests that DESs form a three-dimensional hydrogen bond network, using neutron diffraction and atomistic modelling.[79] In the case of reline, a 3D H-bond network is formed includes two urea molecules, one chloride, and one choline cation.[79]

1.5 Applications of ILs and DESs novel electrolytes

Ionic liquids and deep eutectic solvents have many potential applications, due to their excellent properties. Ionic liquids have been investigated for organic synthesis, carbon capture, and electrochemical applications.[34] However, the high-cost of ionic liquids as well as their need for purification, limits their potential to be commercialized or used in large scale applications. The only commercialized application of ILs is when ILs were used as catalyst in organic synthesis.[56] As mentioned earlier, these types of liquids are designable, which gave them an advantage over other liquids. It is possible to design a novel non-aqueous liquid, IL or DES, with specific properties to match the desired properties of a particular application. For example, electrochemical applications, such as electroplating[29] and energy storages[80], it is important to have an electrolyte that is inexpensive, non-flammable, non-volatile, highly conductive.

1.5.1 Electroplating using ILs and DESs novel electrolytes

Ionic liquids have been used to electroplate a variety of metals including Zn, Cu, Al, Ni and Cr.[29, 81] However, metal electroplating using ILs has not been commercialized yet.[29] ILs are used as non-aqueous electrolytes for metal electroplating to overcome the limitations of aqueous electrolyte. In addition, using ILs as electrolyte can enable a direct electroplating of water-sensitive metals, such as Al and Mg.[55] Aluminium metal has been deposited on a carbon steel substrate as an anti-corrosion layer using 1-butyl-3-methyl-imidazolium heptachloroaluminate, $[C_4C_1Im][Al_2Cl_7]$, as an electrolyte.[82] The efficiency of this aluminium corrosion-layer is increased with the layer thickness.[82]

Developing a new electrolyte for zinc electroplating has been a focus of researchers for the past decade. Ionic liquids and deep eutectic solvents are good candidates for the zinc electroplating process, because of their ability to dissolve different zinc salts.[21] Different imidazolium-based ILs have been investigated for Zn and Zn-alloy electroplating.[14] This is owing to their lower melting points and viscosities compared to other ILs.[14] Zinc has been deposited using 1-ethyl-3-methylimidazoliumchloride, $[C_2C_1Im]Cl$, with $ZnCl_2$.[83] It was found that zinc speciation, ($ZnCl_3^-$, $Zn_2Cl_5^-$ and $Zn_3Cl_7^-$), depends on the concentration of $ZnCl_2$ in the IL and, as the concentration of $ZnCl_2$ increases, a larger cluster of zinc species, $Zn_3Cl_7^-$, is formed.[83] The effect of cation has been investigated by using TfO^-, as an anion, and varying imidazolium-based cations.[84] The effect of anion has been investigated by using $[C_2C_1Im]^+$, as cation, and use different anions.[85] It was reported in the literature that, the strength of cation-anion interaction influences zinc speciation and hence, the deposited zinc morphologies.[84-85] It should be noted that, the electroplating process was performed at 120 °C to lower ionic liquids' viscosities and enhance their conductivities.[84]

DESs offer improvements over the, typically, greater viscosity ionic liquids for zinc electroplating. ChCl-based DESs are the most widely investigated system for zinc electroplating and they are considered closest to commercialization in the metal finishing industry.[14] Zinc has been plated using a DES formulation composed of ChCl and $ZnCl_2$, in 1:2 molar ratio.[86] A smooth thick grey/white deposit on mild steel and act as a corrosion-resistance layer.[86] Type III DESs have also been used to deposit zinc, including ethaline (1Chcl:2EG) and reline (1ChCl:2U), with $ZnCl_2$.[21] The deposited zinc film morphology plated from the reline has a rice-grain morphology, with a homogeneous crystal size. In the case of ethaline, very thin platelets were deposited on the surface.[17, 21] It has been found that the deposited zinc morphology affects both the nucleation and growth rates of zinc.[21] The nucleation rate in ethaline is slow, but the bulk growth rate is fast. Yet, the opposite was observed for reline system. This was attributed to the viscosity difference of these two liquids.[21] Another study[17] challenges these observation , and suggests that zinc electroplating is not mass transport limited.[17] Extended X-ray absorption fine structure (EXAFS) spectroscopy has shown that in both ethaline and reline, zinc species are the same, $[ZnCl_4]^{2-}$, thus, the difference in deposited zinc morphologies is not attributed to the zinc speciation.[17] The difference in morphologies was proposed to be a consequence of chloride species adsorption on the electrode surface. In the case of ethaline, the weak interaction between Cl and EG (week HBD), permits chloride ions to be adsorbed on the surface. This adsorption blocked certain crystal faces of the surface, which led to a small platelets shaped deposition.[17]

1.5.2 IL or DES electrolytes for batteries

Ionic liquids and deep eutectic solvents have been investigated to be used as an electrolyte in energy storage applications, such as batteries.[26, 80] A variety of metal-ion batteries have been studied using these novel electrolytes, including Li-ion[87], Al-ion[88], Mg-ion[33], and Zn-ion[89] batteries. The main drawbacks of rechargeable zinc-based batteries are their short lifetime and low power density, which have been attributed to the battery components including the electrolytes.[33] IL and DES electrolytes overcome current aqueous zinc-based electrolyte problems, such as H_2 evolution, dying-out, and zinc dendrite formation.[33]

A dense deposited zinc film without dendrite formation was obtained using $[C_2C_1Im]TfO$ ionic liquid containing 0.2 M $Zn(TfO)_2$ for rechargeable Zn-batteries.[89] This liquid has a high conductivity (7.3 ms cm^{-1}) and exhibits a wide potential window (2.8 V Vs Zn^{2+}/Zn), which is ideal for battery applications.[89] It was found that adding 0.015 M $Ni(TfO)_{2,}$ as an additive, to the $[C_2C_1Im]TfO$ IL containing 0.1 M $Zn(TfO)_{2,}$ led to the formation of a thin layer of Zn-Ni alloy, in the initial stages of electroplating, which affected the nucleation and growth of zinc, and that suppressed the formation of dendrites.[90] It was promising to have nano-crystalline zinc deposited with high stability, even after 50 plating/stripping cycles.[90] Previous research has shown it is possible to have reversible ZnO_2/O_2 chemistry in rechargeable zinc-air batteries by using non-alkaline aqueous fluorinated electrolytes, $Zn(TfO)_2$.[91] Zinc peroxide forms during the discharge process, while in the charging process a decomposition of ZnO_2 is occurred through a $2e^-/O_2$ process. The formation of zinc peroxide is favourable in the $Zn(TfO)_2$ electrolyte due to the weak affinity between TfO^- anion and Zn^{2+} cation.[91]

A mixture of acetamide and zinc perchlorate, molten salt, was investigated to be used as electrolytes for zinc-based rechargeable batteries.[18] This mixture forms a highly conductive liquid and shows excellent reversibility over several cycles, which is essential for rechargeable Zn-batteries.[18] A reline DES was investigated as a safe, low-cost, and environmentally friendly electrolyte for zinc-ion batteries.[53] it was found that reline showed reversible plating/stripping of zinc with no sign of dendrite formation or the formation of a passivation layer on zinc anode electrode, and that promising for a rechargeable zinc-ion battery development.[53]

Unfortunately, the high viscosity of ionic liquids and deep eutectic solvents limits their electrochemical applications, despite their other excellent properties.[62, 92] Therefore, there is increasing interest in improving the viscosity through the use of additives/co-solvents to reduce their higher viscosities, and hence, increase their conductivities.[62] Water is the most studied co-solvent, particularly due to the hygroscopic nature of many ILs and DESs, which leads to water being present, frequently, as an impurity, when handling in the atmosphere.[93] Their studies were focused on understanding the structure of water-IL mixture and water-DES mixture, and how that affects the ILs and DESs properties, using different characterization techniques.

1.6 The role of water in IL/DES systems

Different studies have used the molecular dynamics (MD) simulation method to analyse water effects on ILs and DESs.[67, 94] These studies show that the addition of water affects the ionic structure of ILs and DESs, as well as their dynamic properties.[62, 94] These dynamic properties include viscosity, conductivity, density, melting temperature, ionic self-aggregation.[86] Previous studies report that the addition of water weakens the cation-anion interactions of ionic liquids and HBD-HBA interaction in deep eutectic solvents.[75, 95] It has been reported that the amount of added water is critical to the water-ILs and water-DES mixtures.[96] Molecular dynamics studies show that when a small amount of water is added to ILs, water molecules isolate from each other forming small water clusters embedded in the ILs structure.[96] As the amount of water increases, water molecules aggregate and form a continuous "chain like" H-bonded network.[97] It has been observed that at high concentrations of water, free water molecules almost disappear, and water forms a separate phase.[97] It is known that when water is added to an organic liquid three types of solution can be formed: homogenous solution, heterogeneous solution, and nano-structured or micro-structured mixture.[98] Different studies have been considered the ILs-water mixture structure as nano-structured or micro-structured.[75, 78, 99] **Figure 1.7** shows a schematic representation of the ILs-water mixture nano-structured or micro-structured.[98]

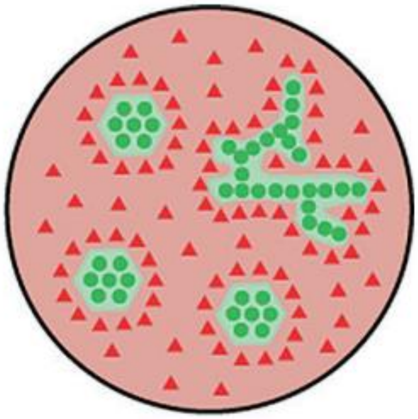

Figure 1.7: A schematic representation of nano-structured or micro-structured mixture. (▲) represents organic molecule, (●) represents water molecule. Reproduced with permission from reference [98].

The type of anions and cations in the ionic liquids influence the formation of water cluster as well as the miscibility of IL/water mixture.[95, 100-102] It was observed that water preferred to form clusters when anion-water interaction is less favourable.[95] The radial distribution function (RDF) simulation method indicate that water prefers to interact with $[BF_4]^-$ anions more than $[Tf_2N]^-$.[95] Therefore, water clusters were more formed in the $[C_4C_1Im][Tf_2N]$ than $[C_4C_1Im][BF_4]$.[95] The nature of the cation is found to affect the miscibility of IL/water mixtures.[100-101] It has been reported that as the length of the cation chain increases, the miscibility of IL and water mixtures decrease.[100-101] In addition, it has been founded that protic ionic liquids have an acidic proton (N–H) therefore protic ILs can form a strong H-bond with water.[102] Whereas aprotic ionic liquids form weak H-bonds with water, through C–H of the cation. The strength of cation-water interactions directly increase the IL/water miscibility.[102]

DESs-water mixtures have also been studied, to investigate the effect of water on DESs structure and their physical properties.[67] ChCl-based deep eutectic solvents are the most widely investigated, therefore researchers focused on study their water mixture. Reline-water mixtures have been explored in prior studies, with a series of (1:1 to 1:30) reline:water molar ratio.[75] It was observed that the melting point of reline influenced by the amount of added water.[75] When the amount of added water increases, the melting point of reline is decreased indicating water forms a strong H-bond with reline constitutes, i.e. choline chloride and urea.[67, 75] Molecular dynamic simulation studies have shown that the number of H-bonds formed in the DES is decreased with the addition of water, due to the formation of water-DES H-bonds.[67] For example, in reline, the number of hydrogen bonds that formed between, urea-water, choline cation-water, and chloride anion-water is increased with the amount of water in the system.[67] Whereas the opposite is observed for choline cation-urea, chloride anion-urea, urea-urea interactions.[67] DESs properties are affected by the addition of water, as a consequence of changing intermolecular interactions of DESs.[67, 103] However, it has been reported that reline retains its nanostructure even when the hydration level reaches approximately 42 wt.%.[75] Above this level, reline-water mixtures can be considered as aqueous solutions of the reline components.[75]

Pulsed field gradient (PFG) NMR has been used to elucidate the effect of water on the intermolecular interactions and ionic species mobility of different ChCl-based DESs.[103] This study suggests that water-DESs are not homogenous, and they form a microscopic water-rich phase when a high amount of water (20 wt.%) is added, using the self-diffusion data of water molecules.[103] In addition, it was observed that ionic species diffuse much faster with the addition of water, indicating that water has influenced these DESs, (i.e. ethaline, reline, and glyceline) intermolecular interactions.[103] As a consequence, the viscosity of DESs decrease, with the addition of water, leading to conductivity increases.[103]

The wide potential window is one of the most important features of DESs and ILs, for their electrochemical applications. Previous studies have shown that the electrochemical potential window of ILs is very sensitive to the amount of water.[104] The wide potential window of ILs or DESs depends on their H-bond network structured.[104] Adding a large amount of water to reline, makes reline system lose its H-bond network, and hence, narrowed its potential window.[104] The water was added to reline, containing 0.2 M of $NiCl_2$ for nickel electroplating, to reduce reline viscosity and hence, enhance their conductivity.[104] It was observed that adding a small amount of water, less than 6 wt.%, reduces reline viscosity, and enhances its conductivity, without narrowing its wide electrochemical potential window.[104] These properties are excellent for nickel electroplating, where a compact-dense nickel deposit was obtained at moderate temperature.[104] The effect of the concentration of water on ethaline DES, containing 0.1 M of $CuCl_2.2H_2O$ for copper electroplating, was investigated using UV-vis spectroscopy.[105] It was observed that the morphologies of deposited copper affected by several factors including speciation, mass transport, nucleation mechanism and reduction kinetics.[105] The speciation of copper was affected by the water content, and changed from $[CuCl_4]^{2-}$ to $[Cu(H_2O)_6]^{2+}$ complex.[105] Another study was investigated the water effect on $[C_2C_1Im][dca]$ IL containing 10 mol% of $Zn(dca)_2$ for zinc electroplating.[106] Uniform, dendrite free deposit zinc was obtained when 3 wt%. of water is added to the IL.[106] This IL-water mixture was considered as a promising electrolyte for zinc-air batteries development.[106] Water effect on zinc speciation of three ILs have been investigated using Far-Infrared and Raman spectroscopies.[84] In the dry ionic liquids, $[C_1Im][TfO]$, $[C_2C_1Im][TfO]$ and $[C_2C_1C_1Im][TfO]$,different zinc species form in each IL depending on the strength of anion-cation interaction.[84] From Far-IR spectroscopy, the band of cation-anion interaction shifts from 116 cm^{-1} to 75 cm^{-1}, indicating that the strength of cation-anion interaction is getting lower in the order of $[C_1Im]^+ > [C_2C_1Im]^+ > [C_2C_1C_1Im]^+$.[84] As the strength of cation-anion interaction become low, the anion prefers to coordinate with zinc ions and form zinc ions complex.[84] Zinc species are $[Zn(TfO)_3]^-$, $[Zn(TfO)_4]^{2-}$ and $[Zn(TfO)_5]^{3-}$ in $[C_1Im][TfO]$, $[C_2C_1Im][TfO]$ and $[C_2C_1C_1Im][TfO]$, respectively.[84] Raman spectroscopy has been used to determine the zinc speciation, when 0.2 M of $Zn(TfO)_2$ added to the three ionic liquids, $[C_1Im(TfO)]$, $[C_2C_1Im(TfO]$ and $[C_2C_1C_1Im(TfO)]$.[73, 84] The Raman spectrum of all ionic liquids shows two peaks, the highest intensity one is attributed to the free TfO anion, while the lowest intensity peak is associated with the coordinated TfO anion.[73, 84] This indicates that in all ionic liquid, zinc ion prefers to associates with TfO anion and form zinc-TfO complex.[73, 84] However, it was found that in the presence of 10 wt% of water, Raman spectroscopy shows that in all ionic liquids, only one peak appeared in the Raman spectrum, which is attributed to the free TfO anion.[70] This indicated that zinc ions do not coordinate with TfO anion in the presence of water, it is preferred to form zinc aqueous species.[70]

Although numerous studies have been shown that ionic liquids and deep eutectic solvents are promising for zinc electrochemical processes, they are not commercialized yet. Most of ILs and DESs studies were focused on studying their structure and their intra/intermolecular interactions in order to understand their unique properties. In addition to studying ILs and DESs ability to dissolve different metal salts and deposit a variety of metals. However, in order to improve ILs or DESs based electrochemical applications, such as batteries or electroplating, a full understanding of the distribution of chemical species, ion transport, side reactions, and structural changes of the electrodes, *in operando*, is required, that's mean while the current is running in the electrochemical cell.

1.7 Characterization techniques used for ILs and DES electrochemical applications development

Numerous techniques have been used to explore battery chemistries, both *in situ* and *ex situ*. *Ex situ* analysis can be performed on batteries after the electrochemical measurements have been taken which give information on the processes that occur during battery operation. Examples of these *ex situ* techniques, scanning electron microscopy (SEM)[107], anodic stripping voltammetry (ASV)[108], and X-ray diffraction (XRD)[109]. The main disadvantage of *ex situ* measurements is that the electrochemical cell must be disassembled in order to perform these characterization techniques. In addition, the electrode often rinses and that might cause structural changes on the electrode to be examined.

Alternatively, *in situ*, techniques such as nuclear magnetic resonance (NMR) are a very important technique for indicating intra/inter-molecular interactions of individual atoms in the system as well as molecular structures.[110] In addition, the self-diffusion coefficient of a desired species in the sample can be measured by using NMR techniques and that count as a huge advantage of this technique.[103] ^{1}H NMR pulsed field gradient has been used to study the effect of water on ions diffusion in different choline chloride based DESs.[103] By using this PFG NMR technique, the diffusion co-efficient of each proton in DESs species can be determined.[103] Ions diffusivity in ethaline and reline increases with the addition of water, as a result of viscosity reduction.[103] In both, ethaline and reline, the proton of the hydroxyl group of choline cation (Ch^+) diffuses much faster than Ch^+ aliphatic protons.[103] This has been explained, that the hydroxyl proton of Ch^+, undergo a proton exchange with water protons.[103]

NMR relaxation measurements have been used to determine the concentration of metal ions, such as copper ions.[108] ^1H NMR relaxation times are sensitive to the metal ions concentration.[108] In the case of copper ions, relaxation times are increased as the concentration of copper ions decreases.[108] This relation between the concentration of copper ions and relaxation times has been used as a key to visualize the dissolution of a copper electrode, *in operando*, by using magnetic resonance imaging.[108] The distribution of copper ions has been imaged indirectly using ^1H MRI.[108] The ^1H T_1 relaxation maps have been converted to concentration maps, using the relation between T_1 relaxation time and the concentration of Cu^{2+}.[108] It has been found that the dissolution of Cu anode is not uniform across the Cu surface.[108] The main drawback of using NMR to study the battery chemistry is that it does not provide any spatial information and we can overcome this by using MRI.[111-112]

Different MRI studies have been carried out on lithium batteries in order to visualize the growth of Li dendrites, *in operando*, while the battery is in operation.[113-116] In these studies, they used ^7Li MRI to directly image lithium dendrites and spatially quantify lithium electro species concentration, during the charging and discharging processes of lithium-ion batteries.[114-116] In another study, three-dimensional images of lithium microstructure growth were visualized, *in operando*, using ^{1}H MRI indirect imaging of the surrounding electrolyte.[117] This indirect ^{1}H MRI experiment is fast compering to the direct ^{7}Li MRI experiment, as well as providing an image with a high resolution.[117] Imaging dendrite growth, *in operando*, gives us information on the rate of dendrite's growth. Other studies were focused on improving alternative batteries including zinc-air[118] and sodium-ion[119] batteries. A recent study by Bray *et. al.*[119] has shown the electrochemistry of sodium battery, *in operando*, using ^{1}H and ^{23}Na nuclear magnetic resonance spectroscopy and imaging techniques. They observed the formation of sodium metallic on a carbon electrode surface upon the first charge, as well as visualizing the distribution of sodium electro species during sodium-battery charging and discharging processes.[119]

The electrochemistry of zinc-battery or zinc corrosion cannot be imaged directly through ^{67}Zn MRI due to the lower sensitivity of ^{67}Zn and their large width, which makes direct ^{67}Zn MRI a challenge.[112] Therefore, most of the zinc electrochemistry MRI studies used indirect ^{1}H MRI.[118, 120] Ions transportation were visualized in the zinc-air battery, *in operando*, using T_1 relaxation images, a long T_1 relaxation time was observed in the vicinity of the zinc anode indicating the transport of zincate ions away from zinc anode.[118] Whereas, the T_1 relaxation reduction was attributed to OH^{-} formation.[118] Interestingly, it has been observed that at some point the anodic and cathodic reactions occur on the zinc anode, as a consequence of potential differences which imposed in the zinc metal.[118] Zinc corrosion process were investigated using magnetic resonance relaxation images, where T_1 and T_2 relaxation times were changed as a result of zinc speciation difference during zinc corrosion.[120] An initial reduction in ^{1}H T_1 relaxation time, due to the formation of Zn structure-making ions, where water molecules coordinate to Zn, and that increases the rotational correlation time of water which led to T_1 reduction.[120] A T_1 increase is observed when Zn structure-breaking ions are formed, which led to a reduction in the rotational correlation time of water.[120]

1.8 Aims of project

Ethaline and reline DESs and 1-ethyl-3-methylimidazolium trifluoromethanesulfonate, [C_2C_1Im(TfO)], ionic liquid have been used as electrolytes for zinc electrochemical applications. It has been observed that zinc metal deposit successfully with different morphologies depends on the formed zinc speciation. The role of water on zinc speciation, the physical or chemical properties has also been investigated of [C_2C_1Im(TfO)] electrolytes, using Far-Infrared and Raman spectroscopies. Whereas, the effect of water on the zinc species in ethaline and reline has not been studied yet. Moreover, none of the previous characterization techniques have provided spatial information of electroactive zinc species in the electrochemical cell. Therefore, there is a demand for non-invasive, *in situ* techniques, which are able to provide information on the distribution and dynamics of zinc species in ILs or DES electrolytes.

This project aims to develop analytical techniques to investigate zinc electrochemical processes. The main goal is to visualize the electrodissolution and electrodeposition processes of Zn in DES and IL systems, *in operando*, in real-time. Promising DESs and ILs electrolytes for zinc electrochemical applications are used and further investigated, in this thesis, using NMR and MRI techniques. In this thesis, the role of water and zinc on the intra/intermolecular interactions as well as the physical and the chemical properties of ethaline, reline, and [C_2C_1Im(TfO)] will be further investigated.

One-dimensional (1D) NMR measurements such as diffusion and relaxation times are the key for MRI. In this project, a range of ethaline and reline DESs, and [C_2C_1Im(TfO)] ionic liquids have been investigated in the presence and absence of zinc and water. Molecular interaction and dynamics, in [C_2C_1Im(TfO)], have been investigated using one-dimensional (1D) ^{1}H and ^{19}F NMR techniques including spectroscopy, and diffusion and relaxation measurements. Molecular interactions and dynamics, in ethaline and reline systems, have been investigated using one-dimensional (1D) ^{1}H NMR and two-dimensional (2D) ^{1}H-^{1}H nuclear Overhauser exchange (NOESY) and exchange (EXSY) NMR spectroscopy. Finally, zinc electroplating chemistry was visualized using MRI, from [C_2C_1Im][TfO] IL containing Zn(TfO)$_2$ electrolyte, with and without water. Zinc electroplating is an important process in zinc batteries, therefore this work will be useful for zinc batteries development research. The following chapter explains the theory of NMR and MRI techniques.

1.9 References

1. Geduld, H., Zinc Plating. Finishing Publications Ltd.: England, 1998.
2. Martyak, N. M.; McCaskie, J. E.; Harrison, L., Corrosion behavior of zinc chromate coatings. Met. Finish. **1996,** 94, 65-67.
3. Sekar, R.; Jayakrishnan, S., Characteristics of zinc electrodeposits from acetate solutions. J. Appl. Electrocem. **2006,** 36, 591-597.
4. Kirby, W. B., Linden's Handbook of Batteries, Fifth Edition. McGraw-Hill Education: New York, 2019.
5. Shin, J.; Lee, J.; Park, Y.; Choi, J. W., Aqueous zinc ion batteries: focus on zinc metal anodes. Chem. Sci. J. **2020,** 11, 2028-2044.
6. Chakkaravarthy, C.; Waheed, A. K. A.; Udupa, H. V. K., Zinc—air alkaline batteries — A review. J. Power Sources **1981,** 6, 203-228.
7. Yadav, G. G.; Wei, X.; Meeus, M., Chapter 3 - Primary zinc-air batteries. In Electrochemical Power Sources: Fundamentals, Systems, and Applications, Arai, H.; Garche, J.; Colmenares, L., Eds. Elsevier: 2021; pp 23-45.
8. Kunz, U.; Linke, K.; Turek, T., Zinc-air batteries: prospects and challenges for future improvement. Z. Phys. Chem. **2012,** 226, 151-166.
9. Zhu, A. L.; Wilkinson, D. P.; Zhang, X.; Xing, Y.; Rozhin, A. G.; Kulinich, S. A., Zinc regeneration in rechargeable zinc-air fuel cells—A review. J. Energy Storage **2016,** 8, 35-50.
10. Mainar, A. R.; Colmenares, L. C.; Blázquez, J. A.; Urdampilleta, I., A brief overview of secondary zinc anode development: The key of improving zinc-based energy storage systems. Int. J. Energy Res. **2018,** 42, 903-918.
11. Liu, S.; Han, W.; Cui, B.; Liu, X.; Zhao, F.; Stuart, J.; Licht, S., A novel rechargeable zinc-air battery with molten salt electrolyte. J. Power Sources **2017,** 342, 435-441.
12. Mainar, A. R.; Leonet, O.; Bengoechea, M.; Boyano, I.; Meatza, I.; Kvasha, A.; Guerfi, A.; Blázquez, J. A., Alkaline aqueous electrolytes for secondary zinc–air batteries: an overview. Int. J. Energy Res. **2016,** 40, 1032-1049.
13. Li, H.; Ma, L.; Han, C.; Wang, Z.; Liu, Z.; Tang, Z.; Zhi, C., Advanced rechargeable zinc-based batteries: Recent progress and future perspectives. Nano Energy **2019,** 62, 550-587.
14. Paul, S.; Maniam, K., Progress in Electrodeposition of Zinc and Zinc Nickel Alloys Using Ionic Liquids. Appl. Sci. **2020,** 10, 5321.
15. Wilcox, G. D.; Gabe, D. R., Electrodeposited zinc alloy coatings. Corrs. Sci. **1993,** 35, 1251-1258.
16. Alesary, H. F.; Cihangir, S.; Ballantyne, A. D.; Harris, R. C.; Weston, D. P.; Abbott, A. P.; Ryder, K. S., Influence of additives on the electrodeposition of zinc from a deep eutectic solvent. Electrochim. Acta **2019,** 304, 118-130.
17. Abbott, A. P.; Barron, J. C.; Frisch, G.; Gurman, S.; Ryder, K. S.; Fernando Silva, A., Double layer effects on metal nucleation in deep eutectic solvents. Phys. Chem. Chem. Phys. **2011,** 13, 10224-31.

18. Venkata Narayanan, N. S.; Ashokraj, B. V.; Sampath, S., Ambient temperature, zinc ion-conducting, binary molten electrolyte based on acetamide and zinc perchlorate: Application in rechargeable zinc batteries. J. Colloid Interface Sci. **2010,** 342, 505-512.

19. Liu, Z.; Zein El Abedin, S.; Endres, F., Electrodeposition and stripping of zinc from an ionic liquid polymer gel electrolyte for rechargeable zinc-based batteries. J. Solid State Electrochem. **2014,** 18, 2683-2691.

20. Xu, C.; Li, B.; Du, H.; Kang, F., Energetic zinc ion chemistry: the rechargeable zinc ion battery. Angew. Chem. Int. Ed. Engl. **2012,** 51, 933-5.

21. Abbott, A. P.; Barron, J. C.; Ryder, K. S., Electrolytic deposition of Zn coatings from ionic liquids based on choline chloride. Trans. Inst. Met. Finish. **2009,** 87, 201-207.

22. Xu, M.; Ivey, D. G.; Qu, W.; Xie, Z., Study of the mechanism for electrodeposition of dendrite-free zinc in an alkaline electrolyte modified with 1-ethyl-3-methylimidazolium dicyanamide. J. Power Sources **2015,** 274, 1249-1253.

23. Tomboc, G. M.; Yu, P.; Kwon, T.; Lee, K.; Li, J., Ideal design of air electrode—A step closer toward robust rechargeable Zn–air battery. APL Mater. **2020,** 8, 050905.

24. Bonnick, P.; Dahn, J. R., A Simple Coin Cell Design for Testing Rechargeable Zinc-Air or Alkaline Battery Systems. J. Electrocem. Soc. **2012,** 159, A981-A989.

25. Gelman, D.; Shvartsev, B.; Ein-Eli, Y., Challenges and Prospect of Non-aqueous Non-alkali (NANA) Metal–Air Batteries. Top. Curr. Chem. **2016,** 374, 82.

26. Mainar, A. R.; Iruin, E.; Colmenares, L. C.; Kvasha, A.; de Meatza, I.; Bengoechea, M.; Leonet, O.; Boyano, I.; Zhang, Z.; Blazquez, J. A., An overview of progress in electrolytes for secondary zinc-air batteries and other storage systems based on zinc. J. Energy Storage **2018,** 15, 304-328.

27. Gelman, D.; Shvartsev, B.; Ein-Eli, Y., Aluminum-air battery based on an ionic liquid electrolyte. J. Mater. Chem. A **2014,** 2, 20237-20242.

28. Sakaebe, H.; Matsumoto, H.; Tatsumi, K., Application of room temperature ionic liquids to Li batteries. Electrochim. Acta **2007,** 53, 1048-1054.

29. Abbott, A. P.; McKenzie, K. J., Application of ionic liquids to the electrodeposition of metals. Phys. Chem. Chem. Phys. **2006,** 8, 4265-79.

30. Endres, F.; MacFarlane, D. R.; Abbott, A., Electrodeposition from Ionic Liquids. John Wiley & Sons: 2008.

31. Abbott, A. P.; Frisch, G.; Ryder, K. S., Electroplating Using Ionic Liquids. Annu. Rev. of Mater. Res. **2013,** 43, 335-358.

32. Galiński, M.; Lewandowski, A.; Stępniak, I., Ionic liquids as electrolytes. Electrochim. Acta **2006,** 51, 5567-5580.

33. Giffin, G. A., Ionic liquid-based electrolytes for "beyond lithium" battery technologies. J. Mater. Chem. A **2016,** 4, 13378-13389.

34. Ghandi, K., A Review of Ionic Liquids, Their Limits and Applications. Green Sustain. Chem. **2014,** 4, 10.

35. Whitehead, A. H.; Pölzler, M.; Gollas, B., Zinc Electrodeposition from a Deep Eutectic System Containing Choline Chloride and Ethylene Glycol. J. Electrochem. Soc. **2010,** 157, D328-D334.

36. Chakrabarti, M. H.; Mjalli, F. S.; AlNashef, I. M.; Hashim, M. A.; Hussain, M. A.; Bahadori, L.; Low, C. T. J., Prospects of applying ionic liquids and deep eutectic solvents for renewable energy storage by means of redox flow batteries. Renew. Sustain. Energy Rev. **2014,** 30, 254-270.

37. Ge, X.; Gu, C.; Wang, X.; Tu, J., Deep eutectic solvents (DESs)-derived advanced functional materials for energy and environmental applications: challenges, opportunities, and future vision. J. Mater. Chem. A **2017,** 5, 8209-8229.

38. Zhang, Q.; De Oliveira Vigier, K.; Royer, S.; Jerome, F., Deep eutectic solvents: syntheses, properties and applications. Chem. Soc. Rev. **2012,** 41, 7108-7146.

39. Peng, W.-j.; Wang, Y.-y., Mechanism of zinc electroplating in alkaline zincate solution. J. Cent. South Univ. **2007,** 14, 37-41.

40. P. W. Atkins, J. D. P., J. Keeler Atkins' Physical Chemistry. Oxford University Press: Oxford, 2018.

41. Winand, R., Electrodeposition of Zinc and Zinc Alloys. In Modern Electroplating, 2010; pp 285-307.

42. Kanani, N., Electroplating: Basic Principles, Processes and Practice. 2nd ed.; Elsevier Science: 2005.

43. Judy, J. W. Magnetic Microactuators with Polysilicon Flexures. 1994.

44. Loto, C. A., Electrodeposition of Zinc from Acid Based Solutions: A Review and Experimental Study. Asian J. Appl. Sci. **2012,** 5, 314-326.

45. Dutta Pramanik, P.; Sinhababu, N.; Mukherjee, B.; Sanjeevikumar, P.; Maity, A.; Upadhyaya, B.; Holm-Nielsen, J.; Choudhury, P., Power Consumption Analysis, Measurement, Management, and Issues: A State-of-the-Art Review of Smartphone Battery and Energy Usage. IEEE Access **2019,** 7, 182113-182172.

46. Shen, X.; Li, Y.; Qian, T.; Liu, J.; Zhou, J.; Yan, C.; Goodenough, J. B., Lithium anode stable in air for low-cost fabrication of a dendrite-free lithium battery. Nat. Commun. **2019,** 10, 900.

47. Gu, P.; Zheng, M.; Zhao, Q.; Xiao, X.; Xue, H.; Pang, H., Rechargeable zinc–air batteries: a promising way to green energy. J. Mater. Chem. A **2017,** 5, 7651-7666.

48. Song, M.; Tan, H.; Chao, D.; Fan, H. J., Recent Advances in Zn-Ion Batteries. Adv. Funct. Mater. **2018,** 28, 1802564.

49. Xie, C.; Zhang, H.; Xu, W.; Wang, W.; Li, X., A Long Cycle Life, Self-Healing Zinc–Iodine Flow Battery with High Power Density. Angew. Chem. Int. Ed. **2018,** 57, 11171-11176.

50. Li, Y.; Dai, H., Recent advances in zinc-air batteries. Chem. Soc. Rev. **2014,** 43, 5257-75.

51. Kasiri, G.; Trócoli, R.; Bani Hashemi, A.; La Mantia, F., An electrochemical investigation of the aging of copper hexacyanoferrate during the operation in zinc-ion batteries. Electrochim. Acta **2016,** 222, 74-83.

52. Lee, B.; Seo, H. R.; Lee, H. R.; Yoon, C. S.; Kim, J. H.; Chung, K. Y.; Cho, B. W.; Oh, S. H., Critical Role of pH Evolution of Electrolyte in the Reaction Mechanism for Rechargeable Zinc Batteries. Chem. Sus. Chem. **2016,** 9, 2948-2956.

53. Kao-ian, W.; Pornprasertsuk, R.; Thamyongkit, P.; Maiyalagan, T.; Kheawhom, S., Rechargeable Zinc-Ion Battery Based on Choline Chloride-Urea Deep Eutectic Solvent. J. Electrochem. Soc. **2019,** 166, A1063-A1069.

54. Welton, T., Ionic liquids: a brief history. Biophys. rev. **2018,** 10, 691-706.

55. Armand, M.; Endres, F.; MacFarlane, D. R.; Ohno, H.; Scrosati, B., Ionic-liquid materials for the electrochemical challenges of the future. Nat. Mater. **2009,** 8, 621-629.
56. Plechkova, N. V.; Seddon, K. R., Applications of ionic liquids in the chemical industry. Chem. Soc. Rev. **2008,** 37, 123-150.
57. Yu, L.; Chen, G. Z., Ionic Liquid-Based Electrolytes for Supercapacitor and Supercapattery. Front. Chem. **2019,** 7.
58. Liu, S.; Zhou, L.; Wang, P.; Zhang, F.; Yu, S.; Shao, Z.; Yi, B., Ionic-Liquid-Based Proton Conducting Membranes for Anhydrous H2/Cl2 Fuel-Cell Applications. ACS Appl. Mater. Interfaces **2014,** 6, 3195-3200.
59. Vo, T. D.; Nguyen, H. V.; Nguyen, Q. D.; Phung, Q.; Tran, V. M.; Le, P. L. M., Carbonate Solvents and Ionic Liquid Mixtures as an Electrolyte to Improve Cell Safety in Sodium-Ion Batteries. J. Chem. **2019,** 2019, 7980204.
60. Chaban, V. V., Acetone as a polar cosolvent for pyridinium-based ionic liquids. RSC Adv. **2016,** 6, 8906-8912.
61. Andanson, J.-m.; Bordes, E.; Devémy, J.; Leroux, F.; Pádua, A.; Gomes, M., Understanding the Role of Co-solvents in the Dissolution of Cellulose in Ionic Liquids. Green Chem. **2014,** 16.
62. McAuley, B.; Seddon, K.; Stark, A.; Torres, M., Influence of chloride, water, and organic solvents on the physical properties of ionic liquids. Abstr. Pap. - Am. Chem. Soc. **2001,** 221, IEC-277.
63. Smith, E. L.; Abbott, A. P.; Ryder, K. S., Deep Eutectic Solvents (DESs) and Their Applications. Chem. Rev. **2014,** 114, 11060-11082.
64. Abbott, A. P.; Capper, G.; Davies, D. L.; Munro, H. L.; Rasheed, R. K.; Tambyrajah, V., Preparation of novel, moisture-stable, Lewis-acidic ionic liquids containing quaternary ammonium salts with functional side chains. Chem. Commun. **2001**, 2010-2011.
65. Abbott, A. P.; El Ttaib, K.; Frisch, G.; McKenzie, K. J.; Ryder, K. S., Electrodeposition of copper composites from deep eutectic solvents based on choline chloride. Phys. Chem. Chem. Phys. **2009,** 11, 4269-4277.
66. Florindo, C.; Oliveira, F. S.; Rebelo, L. P. N.; Fernandes, A. M.; Marrucho, I. M., Insights into the Synthesis and Properties of Deep Eutectic Solvents Based on Cholinium Chloride and Carboxylic Acids. ACS Sustain. Chem. Eng. **2014,** 2, 2416-2425.
67. Zhekenov, T.; Toksanbayev, N.; Kazakbayeva, Z.; Shah, D.; Mjalli, F. S., Formation of type III Deep Eutectic Solvents and effect of water on their intermolecular interactions. Fluid Phase Equilib. **2017,** 441 (Supplement C), 43-48.
68. Abbott, A. P.; Capper, G.; Davies, D. L.; Rasheed, R. K.; Tambyrajah, V., Novel solvent properties of choline chloride/urea mixtures. Chem. Commun. **2003**, 70-71.
69. Hayyan, M.; Mjalli, F. S.; Hashim, M. A.; AlNashef, I. M., A novel technique for separating glycerine from palm oil-based biodiesel using ionic liquids. Fuel Process.Technol. **2010,** 91, 116-120.
70. Bernal, J. D., The Bakerian Lecture, 1962. The Structure of Liquids. Proc. Math. Phys. Eng. Sci. P ROY SOC A **1964,** 280, 299-322.
71. Hayes, R.; Warr, G. G.; Atkin, R., Structure and Nanostructure in Ionic Liquids. Chem. Rev. **2015,** 115, 6357-6426.

72. Fumino, K.; Peppel, T.; Geppert-Rybczyńska, M.; Zaitsau, D. H.; Lehmann, J. K.; Verevkin, S. P.; Köckerling, M.; Ludwig, R., The influence of hydrogen bonding on the physical properties of ionic liquids. Phys. Chem. Chem. Phys. **2011,** 13, 14064-14075.

73. Liu, Z.; El Abedin, S. Z.; Endres, F., Raman and FTIR spectroscopic studies of 1-ethyl-3-methylimidazolium trifluoromethylsulfonate, its mixtures with water and the solvation of zinc ions. Chem. phys. chem. **2015,** 16, 970-7.

74. D'Agostino, C.; Harris, R. C.; Abbott, A. P.; Gladden, L. F.; Mantle, M. D., Molecular motion and ion diffusion in choline chloride based deep eutectic solvents studied by 1H pulsed field gradient NMR spectroscopy. Phys. Chem. Chem. Phys. **2011,** 13, 21383-21391.

75. Hammond, O. S.; Bowron, D. T.; Edler, K. J., The Effect of Water upon Deep Eutectic Solvent Nanostructure: An Unusual Transition from Ionic Mixture to Aqueous Solution. Angew. Chem. Int. Ed. **2017,** 56, 9782-9785.

76. Hunt, P. A., Why Does a Reduction in Hydrogen Bonding Lead to an Increase in Viscosity for the 1-Butyl-2,3-dimethyl-imidazolium-Based Ionic Liquids. J. Phys. Chem. B **2007,** 111, 4844-4853.

77. Sanmamed, Y. A.; González-Salgado, D.; Troncoso, J.; Romani, L.; Baylaucq, A.; Boned, C., Experimental methodology for precise determination of density of RTILs as a function of temperature and pressure using vibrating tube densimeters. J. Chem. Thermodyn. **2010,** 42, 553-563.

78. Stefanovic, R.; Ludwig, M.; Webber, G. B.; Atkin, R.; Page, A. J., Nanostructure, hydrogen bonding and rheology in choline chloride deep eutectic solvents as a function of the hydrogen bond donor. Phys. Chem. Chem. Phys. **2017,** 19, 3297-3306.

79. Hammond, O. S.; Bowron, D. T.; Edler, K. J., Liquid structure of the choline chloride-urea deep eutectic solvent (reline) from neutron diffraction and atomistic modelling. Green Chem. **2016,** 18, 2736-2744.

80. MacFarlane, D. R.; Tachikawa, N.; Forsyth, M.; Pringle, J. M.; Howlett, P. C.; Elliott, G. D.; Davis, J. H.; Watanabe, M.; Simon, P.; Angell, C. A., Energy applications of ionic liquids. Energy Environ. Sci. **2014,** 7, 232-250.

81. Abbott, A. P.; McKenzie, K. J.; Ryder, K. S., Electropolishing and Electroplating of Metals Using Ionic Liquids Based on Choline Chloride. In Ionic Liquids IV, American Chemical Society: 2007; Vol. 975, pp 186-197.

82. Caporali, S.; Fossati, A.; Lavacchi, A.; Perissi, I.; Tolstogouzov, A.; Bardi, U., Aluminium electroplated from ionic liquids as protective coating against steel corrosion. Corros. Sci. **2008,** 50, 534-539.

83. Hsiu, S.-I.; Huang, J.-F.; Sun, I. W.; Yuan, C.-H.; Shiea, J., Lewis acidity dependency of the electrochemical window of zinc chloride–1-ethyl-3-methylimidazolium chloride ionic liquids. Electrochim. Acta **2002,** 47, 4367-4372.

84. Liu, Z.; El Abedin, S. Z.; Endres, F., Electrochemical and spectroscopic study of Zn(ii) coordination and Zn electrodeposition in three ionic liquids with the trifluoromethylsulfonate anion, different imidazolium ions and their mixtures with water. Phys. Chem. Chem. Phys. **2015,** 17, 15945-15952.

85. Liu, Z.; Cui, T.; Lu, T.; Shapouri Ghazvini, M.; Endres, F., Anion Effects on the Solid/Ionic Liquid Interface and the Electrodeposition of Zinc. J. Phys. Chem. C **2016,** 120, 20224-20231.
86. Capper, G.; Davies, D. L.; Rasheed, R. K.; Tambyrajah, V., Novel Ambient Temperature Ionic Liquids for Zinc and Zinc Alloy Electrodeposition Trans. Inst. Met. Finish. **2001,** 79, 204-206.
87. Sugimoto, T.; Atsumi, Y.; Kikuta, M.; Ishiko, E.; Kono, M.; Ishikawa, M., Ionic liquid electrolyte systems based on bis(fluorosulfonyl)imide for lithium-ion batteries. J. Power Sources **2009,** 189, 802-805.
88. Ferrara, C.; Dall'Asta, V.; Berbenni, V.; Quartarone, E.; Mustarelli, P., Physico-Chemical Characterization of AlCl3-[EMIm]Cl Ionic Liquid Electrolytes for Aluminum Rechargeable Batteries. J. Phys. Chem. C **2017**.
89. Fan, J.; Xiao, Q.; Fang, Y.; Li, L.; Yuan, W., A rechargeable Zn/graphite dual-ion battery with an ionic liquid-based electrolyte. Ionics **2019,** 25, 1303-1313.
90. Liu, Z.; Cui, T.; Pulletikurthi, G.; Lahiri, A.; Carstens, T.; Olschewski, M.; Endres, F., Dendrite-Free Nanocrystalline Zinc Electrodeposition from an Ionic Liquid Containing Nickel Triflate for Rechargeable Zn-Based Batteries. Angew. Chem. Int. Ed. **2016,** 55, 2889-2893.
91. Sun, W.; Wang, F.; Zhang, B.; Zhang, M.; Küpers, V.; Ji, X.; Theile, C.; Bieker, P.; Xu, K.; Wang, C.; Winter, M., A rechargeable zinc-air battery based on zinc peroxide chemistry. Science **2021,** 371, 46.
92. Bezerra-Neto, J. R.; Sousa, N. G.; dos Santos, L. P. M.; Correia, A. N.; de Lima-Neto, P., The effect of water on the physicochemical properties of an ethylene glycol and choline chloride mixture containing Cu2+ ions: electrochemical results and dynamic molecular simulation approach. Phys. Chem. Chem. Phys. **2018,** 20, 9321-9327.
93. Widegren, J. A.; Saurer, E. M.; Marsh, K. N.; Magee, J. W., Electrolytic conductivity of four imidazolium-based room-temperature ionic liquids and the effect of a water impurity. J. Chem. Thermodyn. **2005,** 37, 569-575.
94. Celebi, A. T.; Vlugt, T. J. H.; Moultos, O. A., Structural, Thermodynamic, and Transport Properties of Aqueous Reline and Ethaline Solutions from Molecular Dynamics Simulations. J. Phys. Chem. B **2019,** 123, 11014-11025.
95. Zhou, J.; Liu, X.; Zhang, S.; Zhang, X.; Yu, G., Effect of small amount of water on the dynamics properties and microstructures of ionic liquids. AIChE J. **2017,** 63, 2248-2256.
96. Sharma, A.; Ghorai, P. K., Effect of water on structure and dynamics of [BMIM][PF6] ionic liquid: An all-atom molecular dynamics simulation investigation. J. Chem. Phys. **2016,** 144, 114505.
97. Moreno, M.; Castiglione, F.; Mele, A.; Pasqui, C.; Raos, G., Interaction of Water with the Model Ionic Liquid [bmim][BF4]: Molecular Dynamics Simulations and Comparison with NMR Data. J. Phys. Chem. B **2008,** 112, 7826-7836.
98. Kashin, A. S.; Galkin, K. I.; Khokhlova, E. A.; Ananikov, V. P., Direct Observation of Self-Organized Water-Containing Structures in the Liquid Phase and Their Influence on 5-(Hydroxymethyl)furfural Formation in Ionic Liquids. Angew. Chem. Int. Ed. **2016,** 55, 2161-2166.
99. Sapir, L.; Harries, D., Restructuring a Deep Eutectic Solvent by Water: The Nanostructure of Hydrated Choline Chloride/Urea. J. Chem. Theory Comput. **2020,** 16, 3335-3342.

100. Kohno, Y.; Ohno, H., Ionic liquid/water mixtures: from hostility to conciliation. Chem. Commun. (Camb) **2012,** 48, 7119-7130.

101. D. Holbrey, J.; R. Seddon, K., The phase behaviour of 1-alkyl-3-methylimidazolium tetrafluoroborates; ionic liquids and ionic liquid crystals. J. Chem. Soc. Dalton Trans. **1999**, 2133-2140.

102. Reid, J. E. S. J.; Gammons, R. J.; Slattery, J. M.; Walker, A. J.; Shimizu, S., Interactions in Water–Ionic Liquid Mixtures: Comparing Protic and Aprotic Systems. J. Phys. Chem. B **2017,** 121, 599-609.

103. D'Agostino, C.; Gladden, L. F.; Mantle, M. D.; Abbott, A. P.; Ahmed, E. I.; Al-Murshedi, A. Y. M.; Harris, R. C., Molecular and ionic diffusion in aqueous - deep eutectic solvent mixtures: probing inter-molecular interactions using PFG NMR. Phys. Chem. Chem. Phys. **2015,** 17, 15297-15304.

104. Du, C.; Zhao, B.; Chen, X.-B.; Birbilis, N.; Yang, H., Effect of water presence on choline chloride-2urea ionic liquid and coating platings from the hydrated ionic liquid. Sci. Rep. **2016,** 6, 29225.

105. Al-Murshedi, A. Y. M.; Hartley, J. M.; Abbott, A. P.; Ryder, K. S., Effect of water on the electrodeposition of copper on nickel in deep eutectic solvents. Trans. Inst. Met. Finish. **2019,** 97, 321-329.

106. Simons, T. J.; Torriero, A. A. J.; Howlett, P. C.; MacFarlane, D. R.; Forsyth, M., High current density, efficient cycling of Zn2+ in 1-ethyl-3-methylimidazolium dicyanamide ionic liquid: The effect of Zn2+ salt and water concentration. Electrochem. Commun. **2012,** 18, 119-122.

107. Chen, D.; Indris, S.; Schulz, M.; Gamer, B.; Mönig, R., In situ scanning electron microscopy on lithium-ion battery electrodes using an ionic liquid. J. Power Sources **2011,** 196, 6382-6387.

108. Bray, J. M.; Davenport, A. J.; Ryder, K. S.; Britton, M. M., Quantitative, In Situ Visualization of Metal-Ion Dissolution and Transport Using H-1 Magnetic Resonance Imaging. Angew. Chem. Int. Ed. **2016,** 55, 9394-9397.

109. Balasubramanian, M.; Sun, X.; Yang, X. Q.; McBreen, J., In situ X-ray diffraction and X-ray absorption studies of high-rate lithium-ion batteries. J. Power Sources **2001,** 92, 1-8.

110. Claridge, T. D. W., High-Resolution NMR Techniques in Organic Chemistry. Second ed.; Elsevier: Oxford, UK, 2009.

111. Britton, M. M., Magnetic resonance imaging of chemistry. Chem. Soc. Rev. **2010,** 39, 4036-4043.

112. Britton, M. M., Magnetic Resonance Imaging of Electrochemical Cells Containing Bulk Metal. Chem. Phys. Chem. **2014,** 15, 1731-1736.

113. Klamor, S.; Zick, K.; Oerther, T.; Schappacher, F. M.; Winter, M.; Brunklaus, G., (7)Li in situ 1D NMR imaging of a lithium ion battery. Phys. Chem. Chem. Phys. **2015,** 17, 4458-65.

114. Chandrashekar, S.; Trease, N. M.; Chang, H. J.; Du, L.-S.; Grey, C. P.; Jerschow, A., 7Li MRI of Li batteries reveals location of microstructural lithium. Nat. Mater. **2011,** 11, 311–315

115. Chandrashekar, S.; Oparaji, O.; Yang, G.; Hallinan, D., Communication—7Li MRI Unveils Concentration Dependent Diffusion in Polymer Electrolyte Batteries. J. Electrocem. Soc. **2016,** 163, A2988-A2990.

116. Chang, H. J.; Ilott, A. J.; Trease, N. M.; Mohammadi, M.; Jerschow, A.; Grey, C. P., Correlating Microstructural Lithium Metal Growth with Electrolyte Salt Depletion in Lithium Batteries Using 7Li MRI. J. Am. Chem. Soc. **2015,** 137, 15209-15216.
117. Ilott, A. J.; Mohammadi, M.; Chang, H. J.; Grey, C. P.; Jerschow, A., Real-time 3D imaging of microstructure growth in battery cells using indirect MRI. Proc. Natl. Acad. Sci. U.S.A. **2016,** 113, 10779-10784.
118. Britton, M. M.; Bayley, P. M.; Howlett, P. C.; Davenport, A. J.; Forsyth, M., In Situ, Real-Time Visualization of Electrochemistry Using Magnetic Resonance Imaging. J. Phys. Chem. Lett. **2013,** 4, 3019-3023.
119. Bray, J. M.; Doswell, C. L.; Pavlovskaya, G. E.; Chen, L.; Kishore, B.; Au, H.; Alptekin, H.; Kendrick, E.; Titirici, M.-M.; Meersmann, T.; Britton, M. M., Operando visualisation of battery chemistry in a sodium-ion battery by 23Na magnetic resonance imaging. Nat. Commun. **2020,** 11, 2083.
120. Davenport, A. J.; Forsyth, M.; Britton, M. M., Visualisation of chemical processes during corrosion of zinc using magnetic resonance imaging. Electrochem. Commun. **2010,** 12, 44-47.

Chapter 2 Theory of Nuclear Magnetic Resonance

2.1 The principle of nuclear magnetic resonance (NMR)

A nucleus is considered to be NMR active when the spin angular momentum number, I, is non-zero. The spin angular momentum number, I, is the sum of spins of unpaired protons or neutrons, each unpaired protons or neutrons have a spin of ½.[1-2] Spinning nuclei possess a spin angular momentum, I. The spinning motion of the nucleus generates a magnetic moment, $\boldsymbol{\mu}$. The magnetic moment and spin angular momentum are directly proportional to each other according to the **Equation 2.1**, where γ is the constant of proportionality, known as the magnetogyric ratio of the nucleus, which measures the magnetic strength of the nucleus.[1-2]

$$\boldsymbol{\mu} = \gamma I \qquad \textbf{Equation 2.1}$$

Thus, NMR active nuclei behave like a magnet, and when an external magnetic field, $\boldsymbol{B}_{0,}$ is applied, the magnetic moment of nuclei align with respect to $\boldsymbol{B}_{0.}$[1-2] Moreover, in the presence of external magnetic field, spins precess, as shown in **Figure 2.1**.[3] The rate of this motion is dependent on the strength of the external magnetic field, and magnetogyric ratio of the nucleus, γ. This rate known as Larmor frequency, ω_0, which can be determined by **Equation 2.2**.[3]

$$\omega_0 = -\gamma \boldsymbol{B}_0 \qquad \textbf{Equation 2.2}$$

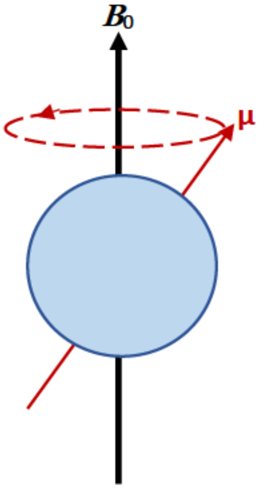

Figure 2.1: A schematic diagram of precession motion of nucleus in the presence of external magnetic field $\boldsymbol{B}_0$.

For a nucleus of spin quantum number, I, there are $2I + 1$ spin states or, in other words, energy levels. In the absence of an external magnetic field, all spins have the same energy. When the external magnetic field is applied, the energy levels are separated by ΔE, **Equation 2.3**, where h is Plank's constant.[3] The energy of each energy level is determined by $E_m = \left(\frac{h}{2\pi}\right) \gamma m \boldsymbol{B}_0$, where m is the magnetic quantum number, and it can be determined by $m = -I, \ldots, 0, \ldots, +I$.[3]

$$\Delta E = \left(\frac{h}{2\pi}\right) \gamma \boldsymbol{B}_0 \quad \text{Equation 2.3}$$

Both ^1H and ^{19}F nuclei have a spin quantum number of ½, therefore, there are two possible energy levels, with m = ½ and −½. The population of the energy levels depends on Boltzmann distribution, as shown in **Figure 2.2**, **Equation 2.4**. Spins align either parallel to the external field, known as α spins, or anti-parallel, known as β spins.[1, 3]

$$\frac{N_\alpha}{N_\beta} = exp\frac{-\Delta E}{k_B\,T}$$ **Equation 2.4**

N_α and N_β correspond to the number of spins in the α, spin up, state and the number of spins in β, spin down, state, respectively, while k_B is the Boltzmann constant and T is the temperature.[3-4] At thermal equilibrium, $N_\alpha > N_\beta$ and there is a slight excess of α spins. By summing all spins, an overall magnetisation vector, $\boldsymbol{M}_0$, results, as shown in **Figure 2.3.**[3-4]

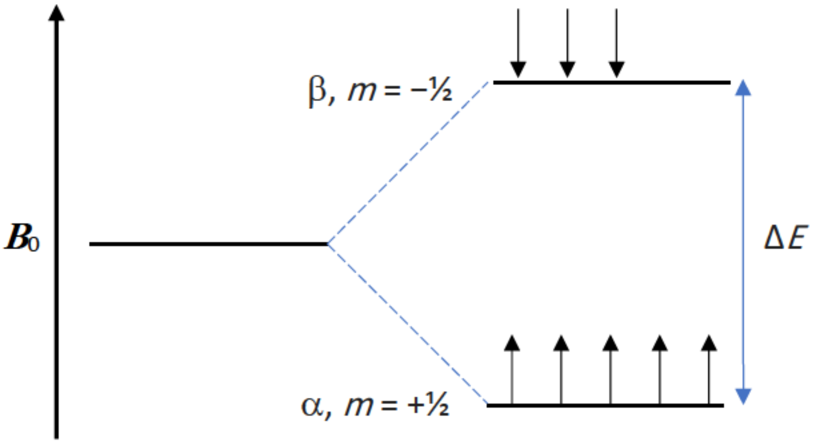

Figure 2.2: The energy levels for a nucleus with I = ½, when applied external field, at thermal equilibrium when Boltzmann distribution is applied, with an excess of α spins.

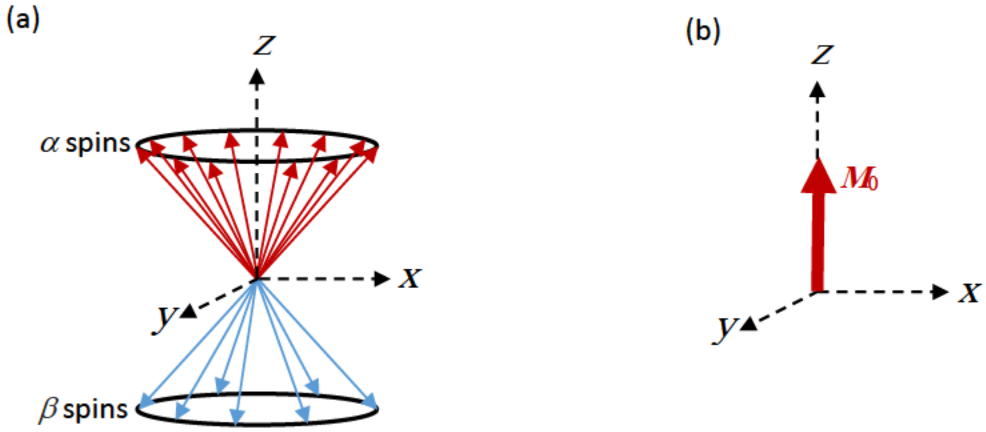

Figure 2.3: A schematic diagram of (a) spins orientations at thermal equilibrium and (b) the net magnetisation vector, $\boldsymbol{M}_0$.

2.2 The effect of radio frequency

Applying radiofrequency (rf) radiation can affect the net magnetisation vector, $\boldsymbol{M}_0$, by inducing a transition between spin states.[4] This rf radiation is produced by the rf coil, and is applied over a period of time, and it has specific angle, known as tip angle, θ.[2] The tip angle is proportional directly to the strength and the duration of radiofrequency pulse.[2] Applying a pulse with 90° tip angle transfers the net magnetisation, from *z*-axis into transverse plane (*x*-*y* plane), in this case α and β states have an equal population.[2] A 180° rf pulse will place $\boldsymbol{M}_0$ onto the −*z*-axis, as a result of inverting the population between α and β states, which means the β state will have a slight excess.[2] In NMR theory, it is common to use a rotating frame to show the movement of the $\boldsymbol{M}_0$ as a function of the applied rf pulse.[5] This allows the rf field to be viewed as stationary and the time dependence of the rf pulse is removed[5], see **Figure 2.4**.

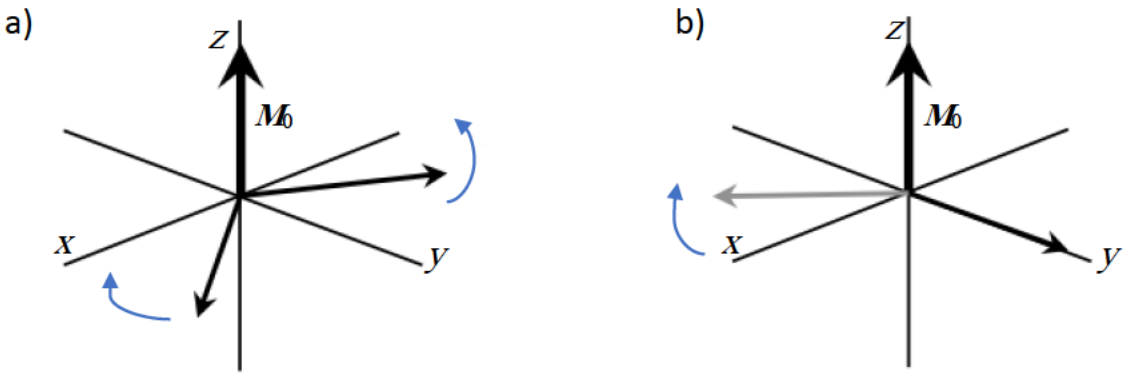

Figure 2.4: A schematic representation of (a) the laboratory frame, where the net magnetisation appears to be moving and (b) the rotating frame, where it appears stationary.

2.3 NMR signal and the free induction decay (FID)

The maximum NMR signal is acquired immediately after a 90° pulse, when spins are in phase and the net magnetisation vector is fully in the transverse plane.[3, 6] This rotating magnetisation vector generates an oscillating electric field resulting in an oscillating electric current, which produces the NMR signal.[3] The net magnetisation, $\boldsymbol{M}_0$, will not remain in the transverse plane, but will return over time to the thermal equilibrium position along the *z*-axis. This decay of NMR signal is known as the free induction decay (FID).[3] The FID signal can be acquired using pulse-acquire sequence, as shown in **Figure 2.5**.[2] Fourier transformation of the FID, will transfer the NMR signal from time domain to frequency domain, which gives NMR spectrum.[2, 4]

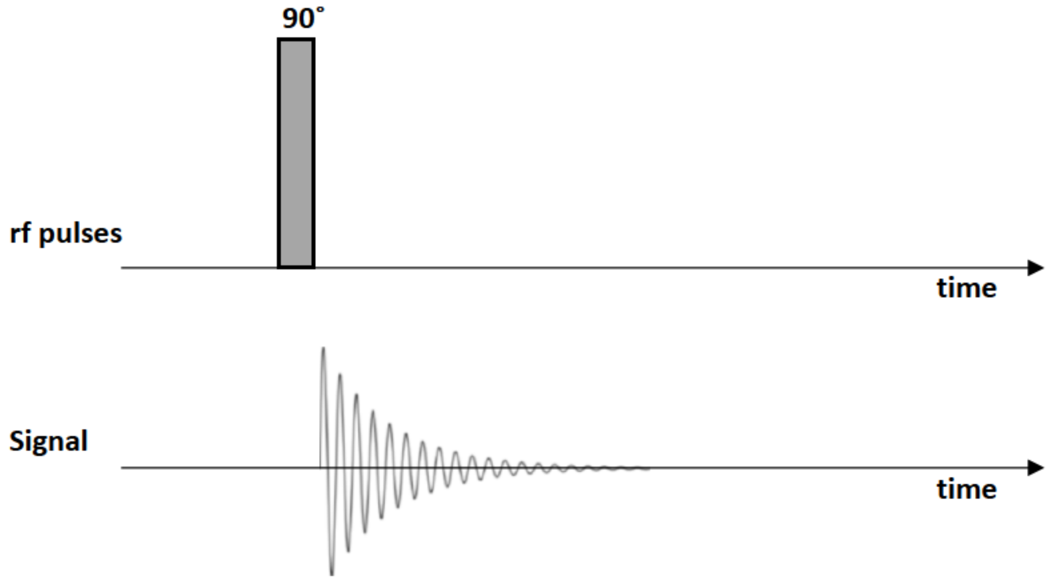

Figure 2.5: A schematic diagram of pulse-acquire pulse sequence. The FID is acquired after applying 90° pulse.

2.4 Chemical shift

Larmor frequency, as indicated in **Equation 2.2**, is dependent on the gyromagnetic ratio and the strength of the magnetic field, but it also sensitive to the chemical environment of nuclei, which influence $\boldsymbol{B}_0$.[1] The chemical shift is a measure of the difference in frequency for nuclei with respect to a reference frequency, which is typically TMS (tetramethylsilane) in ^{1}H NMR.[1] Accordingly, different peaks appear in an NMR spectrum at different frequencies, associated with their local environment, **Figure 2.6**, therefore, chemical shift is useful for the determination of molecular structure, as well as the characterisation of the chemical and physical environment of nuclei.[1, 4]

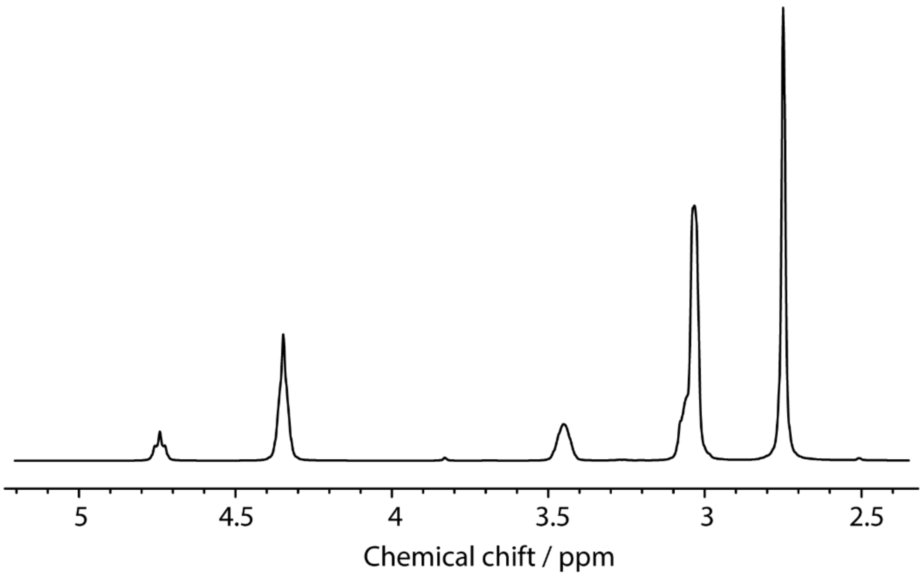

Figure 2.6: ^{1}H NMR spectrum for organic molecules which have several protons at different chemical environments, resulting in different resonance frequencies.

2.5 Relaxation

NMR spectroscopy is a revolution in elucidating the structure of molecules, using the information of an NMR spectrum, such as the position of peaks and their multiplicity.[2] Relaxation is another characterization technique calculated using NMR.[2] Relaxation can be also used to characterise the chemical environment of spins and give some information about molecular mobility, as well as proximity to other spins, particularly paramagnetic ions.[2, 4] As mentioned earlier, at thermal equilibrium, spins distribute themselves between α and β states with respect to the Boltzmann distribution, with an excess of α spins. Applying a 90° pulse will flip the magnetisation vector from *z*-axis to the transverse plane, and that enables spins to be detectable by NMR. After a period of time, the magnetisation vector will return to equilibrium, this process is known as relaxation.[2] There are two types of relaxation: T_1 relaxation, which is known as spin-lattice or longitudinal relaxation, and T_2 relaxation, which is known as spin-spin or transverse relaxation.[2] Relaxation can be caused by different mechanisms such as dipolar coupling, molecular motions.[1-2] Dipolar coupling is an interaction between spins through space.[1-2]

2.5.1 Spin-lattice relaxation

T_1 relaxation is the process where net magnetisation recovers to equilibrium along the z-axis, when spins return to the Boltzmann distribution.[2] In order to recover the net magnetisation to equilibrium, a spin transition between α and β states must occur. This transition is caused by the motion of spins, which gives rise to fluctuations in the local magnetic field through dipolar coupling.[1-2] When spins move from β state to α states this transfers energy to the lattice[2], which is why this relaxation is known as spin-lattice relaxation. T_1 relaxation time is measured using either inversion recovery or saturation recovery sequences.[2, 5] **Figure 2.7** shows the inversion recovery sequence, which applies a 180˚ pulse, to deflect $\boldsymbol{M}_0$ from the z-axis to $-z$-axis. Here the β spins have the highest population. During the period τ, spin-lattice relaxation occurs, returning the net magnetisation to thermal equilibrium (and an excess of α spins). Then, a 90˚ pulse is applied to flip these spins to the transverse plane, where the NMR signal can be detected and collected. This process is carried out repeatedly for different τ values. At short τ values, the β spins still are in excess compared to α spins, which result in an NMR signal which gives a negative peak after Fourier transformation. This is a consequence of the little relaxation which keeps $\boldsymbol{M}_0$ in the $-z$-axis. As τ increases, the net magnetisation has time to return gradually to the z-axis, and the associated peaks become positive. As the process is repeated for increasing τ values, the systems approaches equilibrium, which is shown in **Figure 2.8**. The average T_1 relaxation time can be determined[2, 5] by fitting the normalised signal intensity ($S_{(\tau)}$ / $S_{(0)}$), as a function of time, to **Equation 2.5**, where $S_{(\tau)}$ is the signal intensity at time τ, and $S_{(0)}$ is the initial signal intensity at τ = 0.

$$\frac{S_{(\tau)}}{S_{(0)}} = 1 - 2\, exp^{\frac{-\tau}{T_1}} \qquad \textbf{Equation 2.5}$$

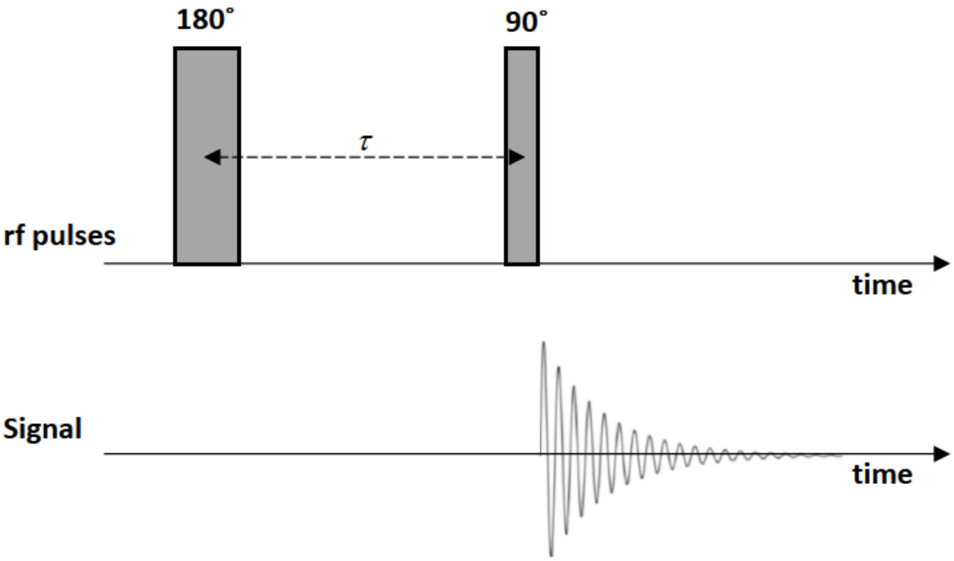

Figure 2.7: A schematic diagram of Inversion recovery pulse sequence. Here, a 90° and 180° rf pulses are separated by a time τ, and the FID signal forms after the 90° pulse.

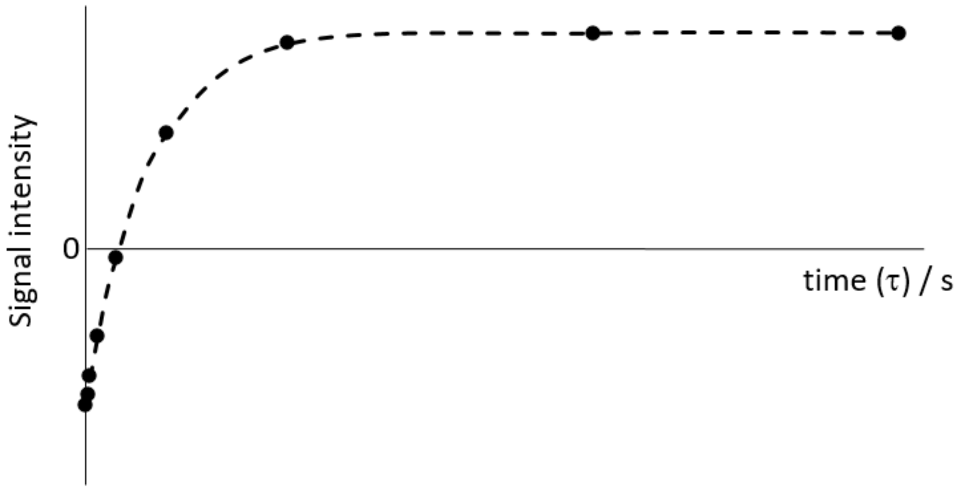

Figure 2.8: T_1 relaxation curve, which is a plot of the collected NMR signal, using inversion recovery sequence, as a function time, τ. The dashed line is the fit of Equation 2.5.

2.5.2 Spin-Spin relaxation

T_2 relaxation time is the time taken by spins to lose phase coherence in the transverse plane, following an rf pulse.[2, 5] This relaxation time can be measured using the spin-echo sequence, **Figure 2.9**.[2, 5] Applying a 90˚ pulse will flip $\boldsymbol{M}_0$ onto the transverse plane. Initially, spins have phase coherence. During a period of time, τ, spins lose phase coherence, because each spin will precess at different frequencies depending on their local magnetic field.[5] The local magnetic field of each spin differs as a result of their chemical environment, intra- and inter-molecular interactions and molecular motion.[5] Inhomogeneity of the external magnetic field, $\boldsymbol{B}_0$, also affects the local magnetic field of spins[2]. However, this inhomogeneity, $\Delta\boldsymbol{B}_0$, can be reduced by shimming the magnet. Therefore, the effective T_2, which is known as T_2*, is determined in **Equation 2.6**.[2, 5]

$$\frac{1}{T_2^*} = \frac{1}{T_2} + \frac{1}{T_{2(\Delta B_0)}}$$ **Equation 2.6**

The effective T_2* can also be determined by the linewidth of a half-height of the peak, $\Delta\nu$ ½, **Equation 2.7**, where ν is the Larmor frequency in Hz (i.e. $\omega/2\pi$).[2] Thus, a broad peak corresponds to a short T_2*, while a longer T_2* will give a narrower peak.

$$\Delta\nu_{1/2} = \frac{1}{\pi T_2^*}$$ **Equation 2.7**

Spins refocused by applying a 180° pulse for a period of time, τ. At this time spins will continue to de-phase but in the opposite direction, so at the end of second τ, all spins will be completely refocused and form a spin echo, **Figure 2.10**.[2] However, spins which de-phase, during the first τ delay, as a result of molecular motion or molecular interactions will not be totally refocused, after the second τ delay, and that causes a signal decay.[2, 5, 7]

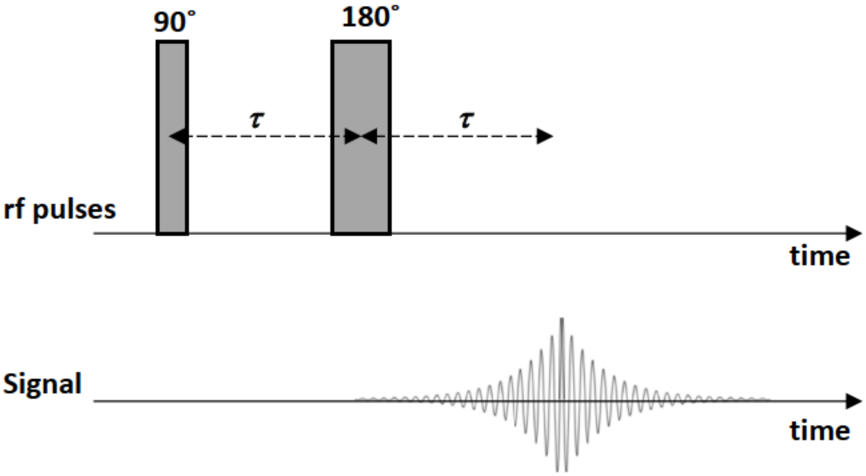

Figure 2.9: A schematic diagram of spin-echo pulse sequence. Here, there is a 90° and 180° rf pulse separated by a time τ, and the echo forms in a two τ after the 90°.

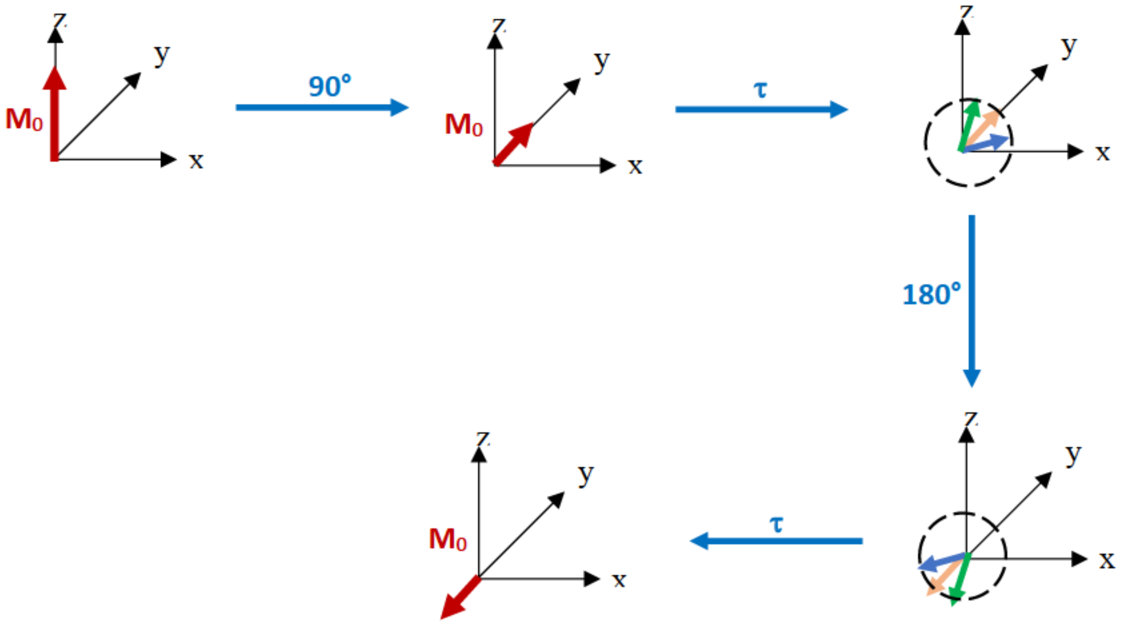

Figure 2.10: A schematic representation of dephasing and refocusing spins during the spin-echo experiment. The green, yellow and blue vectors are used to show the magnetisation vector, ***M***$_0$, evolution over time during the experiment.

However, during the τ period, spins diffuse to another region and experience slightly different magnetic field, thus, spins will not be fully refocused after the τ period.[2] In order to minimise the effect of diffusion, multiple 180° pulse should be applied to refocus spins constantly, where the diffusion has negligible effect.[2, 5] This pulse sequence known as Carr-Purcell-Meiboom-Gill[8] (CPMG) pulse sequence and it forms multiple echoes, shown in **Figure 2.11** T_2 relaxation time can be determined by acquiring a series of CPMG experiments, as a function of *n* values, which is an even positive integer and plot the echo decay against the time, **Figure 2.12.**[2] The average T_2 relaxation time can be measured[2, 5] by fitting the normalised signal intensity ($S_{(\tau)}$ / $S_{(0)}$), as a function of time, to **Equation 2.8**, where $S_{(2\tau)}$ is the signal intensity at two τ time, and $S_{(0)}$ is the initial signal intensity at $\tau = 0$.

$$\frac{S_{(2\tau)}}{S_{(0)}} = exp^{\frac{-2\tau}{T_2}}$$ **Equation 2.8**

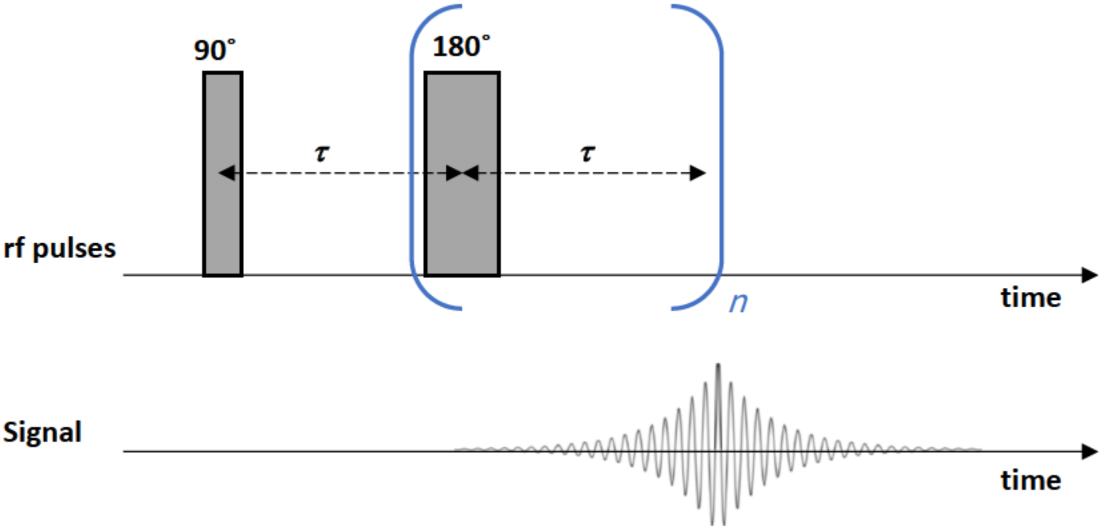

Figure 2.11: A schematic diagram of the Carr-Purcell-Meiboom-Gill (CPMG) pulse sequence. There is a 90° and 180° rf pulse separated by a time τ, and the echo forms in a two τ after the 90°. A series of 180° pulses are applied n times, where n is a positive even integral. This sequence produces a series of n echoes.

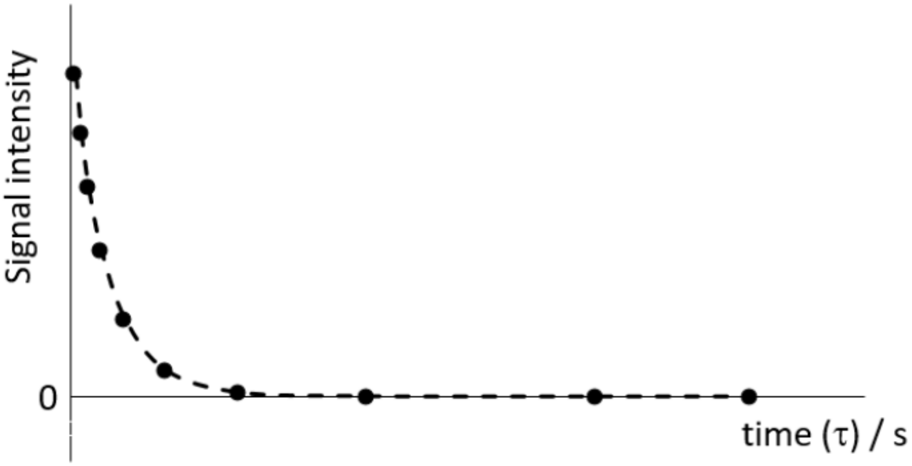

Figure 2.12: T_2 relaxation curve, which is a plot of the collected NMR signal using CPMG sequence as a function time, τ. The dashed line is the fit of Equation 2.8.

2.5.3 Rotational time effect on relaxation

T_1 and T_2 relaxation times are sensitive to molecular tumbling.[1] Molecular mobility and molecular tumbling depend on sample conditions, such as temperature, viscosity and molecular size.[1] As the temperature of a sample increases, the viscosity is typically decreased and resulting in shorter rotational correlation time.[1] The rotational correlation time, τ_c, can be defined as the time taken by a molecule to completely change its orientation, thus smaller molecules will have shorter τ_c.[1] The relation between T_1 and T_2 relaxation times and the rotational correlation time, τ_c, can be shown in **Figure 2.13**.

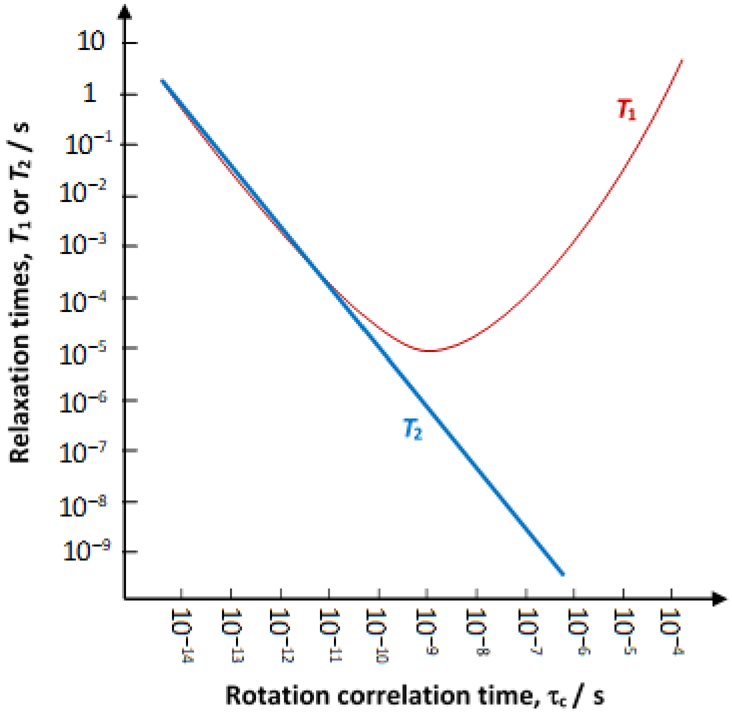

Figure 2.13: The relationship between relaxation times and the rotational correlation time, τ_c.

T_2 relaxation time has an inverse relationship with the rotational correlation time.[1] When the rate of molecular tumbling is increased, i.e. it has a shorter τ_c, the T_2 relaxation time become longer and vice versa. Whereas, T_1 relaxation time has a different trend. A long T_1 relaxation time obtained when the molecule has a short τ_c, due to the faster magnetic field fluctuations frequencies compared to the Larmor frequency, ω_0.[1] Furthermore, a long T_1 relaxation time observed when the molecule has a long τ_c, due to slower magnetic field fluctuations frequencies compared to ω_0.[1] However, when the magnetic field fluctuations frequency matches the ω_0, the shortest T_1 relaxation time will be observed.[1]

2.5.4 Relaxation pathways and nuclear Overhauser effect (nOe)

Relaxation pathways and nuclear Overhauser effect can be explained by considering a two inequivalent spins I and S, which are interacting by dipolar coupling. These two inequivalent spins, I and S, have four energy levels, $\alpha_I\alpha_S$, $\beta_I\beta_S$, $\alpha_I\beta_S$ and $\alpha_S\beta_I$, as shown in **Figure 2.14**.[1] $\alpha_I\alpha_S$ is the energy level has an energy of $-\omega_0$, and it is where I and S are both α spins, whereas the $\beta_I\beta_S$ energy level has an energy of $+\omega_0$, and I and S are both β spins.[1] In between are $\alpha_I\beta_S$ and $\alpha_S\beta_I$ energy levels with zero energy, where one of I or S pins is α spin and the other is β spin.[1] Six relaxation pathways are available for I and S spins. Four of these pathways are single flip pathways, W_1^I and W_1^S, and the others are double spin flips, W_0^{IS} and W_2^{IS}.[1] The single flip pathways relaxations are spin-lattice relaxation, T_1, which caused by the rf pulse. Whereas the double spin flip pathways are known as cross-relaxation, which caused by dipolar coupling.[1] The nuclear Overhauser (nOe) effect is a consequence of cross-relaxation, where the magnetisation is transferred e.g. from S spin to I spin.[1, 4] The rate of this cross-relaxation has an inverse relationship with the distance between the two coupling spins.[4] As the distance is increases between the coupling spins, the rate of cross-relaxation is decreased. The occurrence of cross-relaxation, nOe, is dependent on the distance between the coupled spins, which must be 5 Å or less.[4] Therefore, it can be consider the nOe as a very important tool for structural elucidation, by enabling the determination of the spins which are in close proximity in the space.[4] This can be obtained through the two dimensional nuclear Overhauser effect spectroscopy (NOESY).[2, 4]

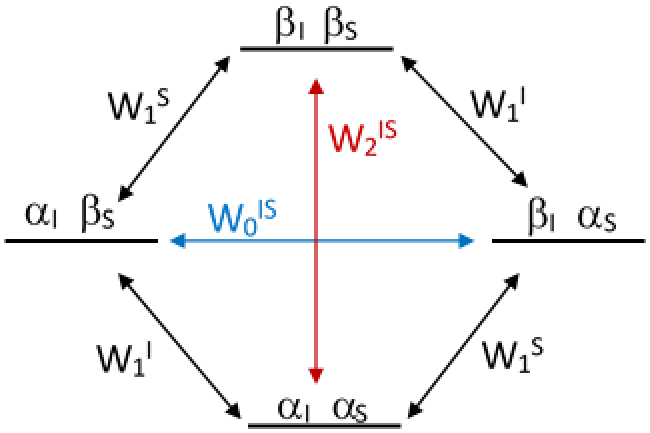

Figure 2.14: A representation diagram of two inequivalent spins, I and S, energy levels, and their six relaxation pathways.

2.6 Diffusion

Self-diffusion can be defined as random molecular motions at thermal equilibrium, which measured by the self-diffusion coefficient, *D*.[2, 9] It can be seen from the Stokes-Einstein[10] **Equation 2.9**, that the self-diffusion coefficient, *D*, depends on several factors such as temperature, *T*, viscosity, η, and molecular size, *r*.

$$D = \frac{k_B T}{6\pi\eta r} \qquad \textbf{Equation 2.9}$$

According to the Stokes-Einstein relation[10], increases in viscosity, or molecular size, will make a molecule move slower and that results in a reduction of its self-diffusion coefficient. However, this relation does not appear to be fit some ionic liquids, which thus do not behave as classical hydrodynamic fluids.[11] For instance, in the [C_2C_1Im(TfO)] ionic liquid, the TfO anion has lower diffusivity than the bulky C_2C_1Im cation.[11] Self-diffusion is measured by diffusion NMR techniques[2, 9], which uses pulsed magnetic field gradients to encode for a molecule's position and displacement. By applying a magnetic field gradient, ***G***, spins will experience different magnetic field depending on their position, along the gradient axis.[9] The Larmor frequency of each spin depends on their position and the strength of the applied gradient pulse[9, 12], as shown in **Equation 2.10**. The main NMR diffusion techniques are pulsed gradient spin echo (PGSE) and pulsed gradient stimulated echo (PGSTE).[2]

$$\omega(r) = \gamma \boldsymbol{B}_{\mathbf{0}} + \gamma \boldsymbol{G}\boldsymbol{r} \qquad \text{Equation 2.10}$$

The pulsed gradient spin echo[2] (PGSE) sequence is shown in **Figure 2.15**. Where ***G*** is the gradient strength, δ is the gradient pulse duration and Δ is the observation time, which is the allowed time for the molecule to diffuse.[2]

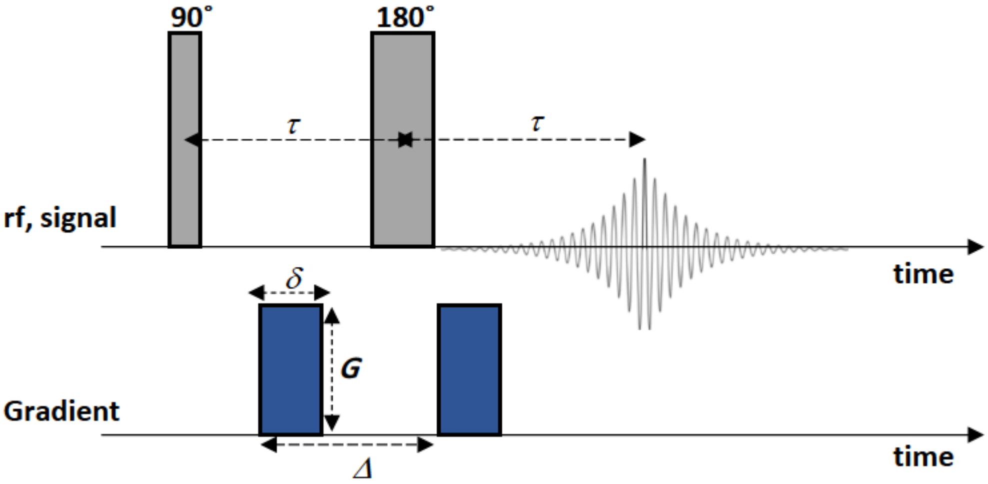

Figure 2.15: A schematic diagram of the pulsed gradient spin echo (PGSE) sequence. There is 90° and 180° rf pulse separated by a time, τ. The echo forms in a two τ after the 90°. Two gradient pulses are applied with a duration of δ and strength of ***G***, separated by the observation time, Δ.

After applying a 90° pulse, the magnetisation vector will be flipped onto the transverse plane, where spins have phase coherence.[9, 12] After a period of time, by applying a gradient pulse spins start to de-phase, each spin will de-phase and precess at different frequencies depending on their position, and that produce a helix of phase.[9, 12] Applying a 180° pulse will flip the magnetisation, in order to be refocused. After applying a 180° pulse and a second gradient, which has the same duration and strength as the first one, spins will be refocused and have the phase coherence again, if they did not move during the observation time, Δ.[9, 12] However, if any molecules diffuse during, Δ, they experience a different magnetic field for the second gradient, compared to the first one, and hence their magnetisation will not be fully refocussed. [9, 12] This difference in gradient strength will cause a phase shift, which is proportional to Δr, the amount of displacement after the diffusion.[9, 12]

During the observation time, in the PGSE sequence, the magnetisation remains in the transverse plane and hence is susceptible to T_2 relaxation.[12] Consequently, It is better to use PGSE pulsed sequence when the T_2 relaxation time of spins is longer than the (Δ) because if it is shorter, that will cause a loss of signal, and that is a problem.[12] In order to overcome this limitation, the pulsed gradient stimulated echo (PGSTE) is used.[2, 9, 12] The pulsed gradient stimulated echo[13] (PGSTE) sequence is shown in **Figure 2.16**. In PGSTE sequence, during the observation time, the magnetisation vector is flipped back on the *z*-axis, by the second 90° pulse, and hence it is susceptible to T_1 relaxation.[12-13] This is the significance of this sequence, where the magnetization vector is sensitive to T_1 relaxation time, which is typically longer than T_2, and that enables employing a longer Δ.[12-13]

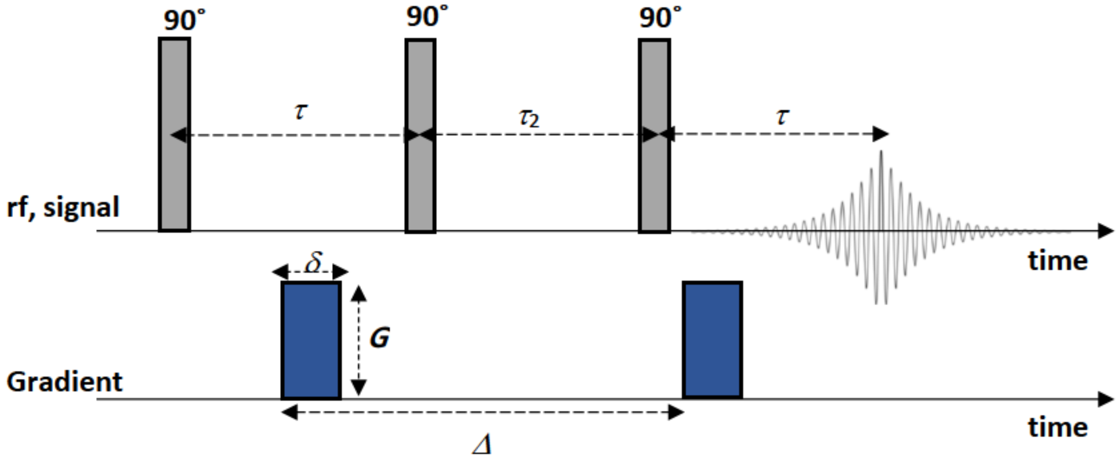

Figure 2.16: A schematic diagram of the pulsed gradient stimulated echo (PGSTE) sequence. Here, there are three 90° rf pulse separated by a time, τ. Two gradient pulses are applied with a duration of δ and strength of $\boldsymbol{G}$, separated by the observation time, Δ.

The self-diffusion coefficient, D, can be determined by repeating the experiment, either the PGSE or the PGSTE sequence, as a function of gradient strength, $\boldsymbol{G}$, or gradient duration, δ, or the observation time, Δ. These experiments are typically performed by running the sequence multiple times with changing the $\boldsymbol{G}$, while keeping δ and Δ constant. This increment leads to a signal decay which is associated with the self-diffusion coefficient. The self-diffusion coefficient, D, can be determined by fitting the normalised signal intensity as a function of gradient strength, ($S_{(\mathbf{G})}$ / $S_{(0)}$), to the Stejskal-Tanner relation[14], **Equation 2.11**. $S_{(\mathbf{G})}$ is the signal intensity at gradient strength $\boldsymbol{G}$, $S_{(0)}$ is the initial signal intensity at zero gradient.

$$\frac{S_{(\boldsymbol{G})}}{S_{(0)}} = exp^{-(\gamma^2\delta^2\boldsymbol{G}^2D(\Delta-\frac{\delta}{3}))} \qquad \textbf{Equation 2.11}$$

The advantage of the NMR diffusion experiment is that, it is possible to determine the self-diffusion coefficient for each resonance in the NMR spectrum.[12] However, where species are in different environments, it is possible for more than one diffusion coefficient to be observed. As a result , the signal attenuation curve requires fitting more than one diffusion co-efficient, such as **Equation 2.12**, which results in the determination of two diffusion co-efficients.[14]

$$\frac{S_{(\boldsymbol{G})}}{S_{(0)}} = x\ (exp^{-(\gamma^2\delta^2\boldsymbol{G}^2D(\Delta-\frac{\delta}{3}))})\ + (1-x)\ exp^{-(\gamma^2\delta^2\boldsymbol{G}^2D(\Delta-\frac{\delta}{3}))} \qquad \textbf{Equation 2.12}$$

2.7 Two-dimensional nuclear magnetic resonance spectroscopy

The two-dimensional nuclear magnetic resonance (2D NMR) is an extremely important technique, which revolutionized structure elucidation. The 2D NMR spectroscopy gives information of nuclei that are in close proximity to each other, either chemically bonded or not. These 2D NMR experiments consist of multi 90° pulses separated by a period of time, t_1, and then followed by the acquisition as a function of different time, t_2.[2] 2D NMR spectroscopy produces a plot with two frequencies axis, F_1 and F_2, after applying a Fourier transformation into both time dimensions (t_1 and t_2).[2] In general, the 2D NMR experiments can be homonuclear or heteronuclear.[2] During the t_1, the magnetisation is transferred due to different mechanism, such as scalar coupling, dipolar coupling and chemical exchange, each mechanism gives different 2D NMR experiment.[2] A 2D COSY experiment, which is correlation spectroscopy, provides information of scalar coupling, and that arises from spin-spin interactions via bonds.[2] Whereas a 2D NOESY experiment, which referred to nuclear Overhauser effect spectroscopy, provides information of dipolar coupling, that arises when spins are in close proximity to each other but they are not bondend.[2] Chemical exchange information can be also provided using EXSY experiment, which is chemical exchange spectroscopy.[2, 15] In 2D NMR spectrum, two types of peaks can be observed, diagonal-peaks, and off-diagonal peaks which also known as cross-peaks.[2] The diagonal peaks appeared when the magnetisation transferred between identical spins, i.e. F_1 and F_2 frequencies are identical.[2] When magnetisation transferred from one spin to another different spin, during the mixing time, the F_1 and F_2 frequencies are different, and that gives rise to cross-peaks.[2]

NOESY and EXSY experiments are based on the same pulse sequence, shown in **Figure 2.17**.[2, 15] This sequence consists of three 90° pulses with time delays, evolution time (τ_1), mixing time (τ_{mix}), and acquisition time (τ_2). In the NOESY experiment, the first 90° pulse rotates the magnetisation vector to the transverse *x*-*y* plane, and get away from the thermal equilibrium. During the evolution time, τ_1, spins precess freely at transverse plane. During the mixing time, a 90° pulse is applied to rotate the magnetization vector back a long *z*-axis, however only one component is back. During the mixing time in NOESY experiment, some of the magnetization vector transfer from one nucleus to another nucleus, which are in close proximity. This transfer magnetization result a cross-peak, as a consequence of nOe effect. The final 90° pulse, is applied to flip the magnetisation, which remains in the *z*-axis, to the transverse plane to enable the detection of the NMR signal. A NOESY 2D spectrum can provide information of nuclei that are in close proximity to each other from their cross-peaks. The diagonal-peaks in the NOESY spectrum have a positive phase, whereas the phase sign of cross-peaks can be positive or negative depends on the molecular size and the solvent viscosity.[6] In the case of the lower viscosity system, where the tumbling rates are faster, the nOe cross-peaks are expected to be negative.[6] However, for the higher viscosity systems, where molecular tumbling is slow, the nOe cross-peaks are expected to be positive and have the same phase as the diagonal peaks.[6]

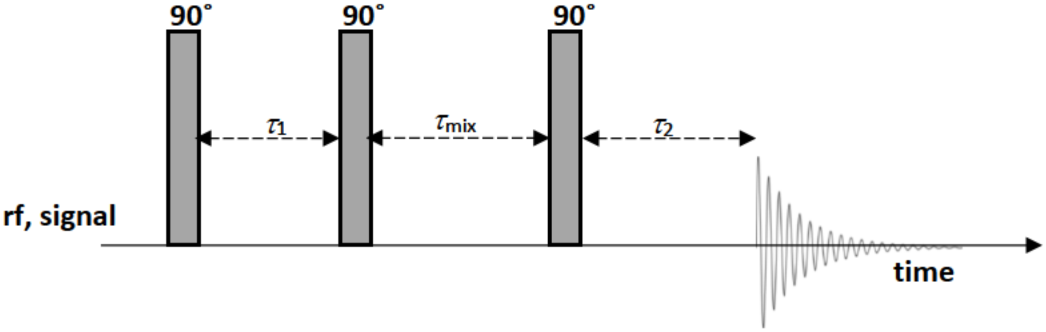

Figure 2.17: A schematic diagram of three pulses two-dimensional spectroscopy sequence. Here, there are three 90° rf pulses separated by different time values. τ_1 is the evolution time, τ_{mix} is the mixing time and τ_2 is the acquisition time.

EXSY experiment have the same sequence of NOESY experiment the only difference is during the mixing time a chemical exchange occur between two spins in different conformers. The EXSY experiment produces a 2D spectrum with diagonal-peaks, and cross-peaks that are arising from a chemical exchange.[6] In the EXSY experiments, the phase sign of diagonal peaks and cross-peaks are the same, which is positive.[6] Since NOESY and EXSY experiments are based on the same pulse sequence, it is possible to have cross-peaks associated with nOe and others associated with the chemical exchange at the same 2D spectrum. For the small size molecular, in the low viscous liquids, it is possible to distinguish between nOe cross-peaks and exchange cross-peaks by their opposite phase sign, as shown in **Figure 2.18**. Whereas for high viscous liquids, it is hard to distinguish between them because both have a positive phase.

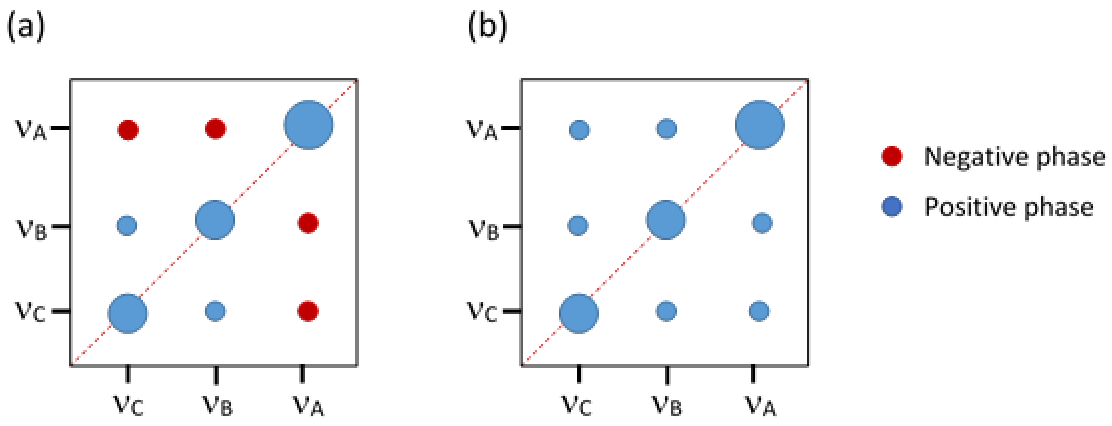

Figure 2.18: A schematic representation of 2D spectrum for (A) low and (B) high viscous liquids. For low viscos liquids, the nOe cross-peaks are distinguishable, which appears with opposite phase sign (negative), than the diagonal peaks and exchange cross-peaks (positive).

By increasing the mixing time, τ_{mix}, the nOe or chemical exchange effects increases and that result in an increment in the cross-peak intensity until reaches the T_1 limited maximum, it start to decay, **Figure 2.19**.[16-17] A series of EXSY experiments can be acquired as a function of τ_{mix} to calculate the exchange rate (k_{ex}) by fitting the signal intensity of exchange peaks (I_{AB} and I_{BA}), as a function of τ_{mix}, to **Equation 2.13**.[17]

$$I_{\text{AB}} = I_{\text{BA}} = P_{\text{A}}P_{\text{B}}\left(1 - \exp(-k_{\text{ex}}\tau_{\text{mix}})\right)\exp(-R_1\tau_{\text{mix}}) \qquad \textbf{Equation 2.13}$$

Where $P_{\text{A}} = \frac{I_{\text{A}}}{I_{\text{A}} + I_{\text{B}}}$, $P_{\text{B}} = \frac{I_{\text{B}}}{I_{\text{A}} + I_{\text{B}}}$ and $R_1 = (R_{1\text{A}} + R_{1\text{B}})$, I_{A} and I_{B} are the intensities at τ_{mix} = 0 ms, and $R_{1\text{A}}$, $R_{1\text{B}}$ are the relaxation rates of species A and B.[17]

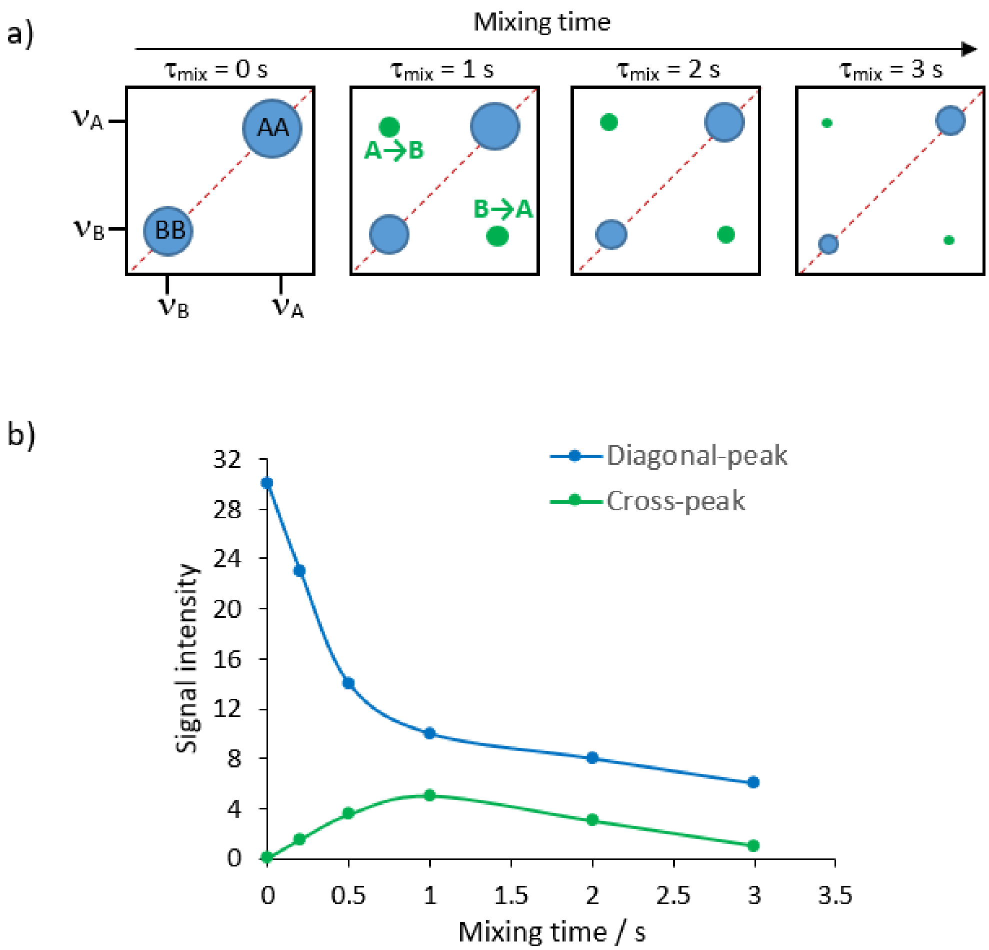

Figure 2.19: a) A schematic representation of cross-peak and diagonal-peaks signals over mixing time, and b) The build-up curve of cross-peak intensity as a function of τ_{mix} which can be fit to equation [2.13] to determine the exchange rate.

2.8 Magnetic resonance imaging (MRI)

Magnetic resonance imaging (MRI) is based on nuclear magnetic resonance (NMR). In MRI, spins experience different magnetic field strengths depends on their positions, and it is spatially located by applying magnetic field gradients.[5, 18] This magnetic field gradients makes spins precess at different Larmor frequencies and the phase of spins become spatially dependent[5], as shown in **Equation 2.10**. Magnetic field gradient can be applied in three directions (*x*, *y* and *z*), spins are located along the direction of the gradient.[5, 18] The centre of the magnetic where (x,y,z) = (0,0,0).[5, 18] Therefore, the Larmor frequency of each spin can be spatially encoded with respect to their *x*, *y* and *z* directions. In general, acquiring a 2D image requires applying two magnetic field gradients in two direction, with a third gradient in the third for slice selection.[5, 18] The spatial information within the NMR signal can be encoded using two ways, frequency encoding, and phase encoding.[5]

2.8.1 Frequency encoding

In the frequency encoding, the spatial information within the NMR signal is frequency encoded by applying a gradient with a constant strength during data acquisition.[5] The applied constant gradient is also known as read gradient, $\boldsymbol{G_R}$.[5] By applying the constant gradient during the data acquisition, all spins experience the same gradient strength but they will have different Larmor frequency depending to their position.[5] The number of spins at each position is directly proportional to the signal intensity.[5]

2.8.2 Phase encoding

Phase encoding is obtained by applying a gradient of varying strength during a fixed time, this gradient is called a phase gradient, $\boldsymbol{G}_{\mathrm{PE}}$.[5] In this encoding method, the gradient is switched off during the acquisition, at this point all spins precess at the same Larmor frequency, however, they have a phase shift.[5] The phase shift increases as the gradient strength is ramped up, and hence the signal is phase encoded.[5] The phase of each spin is dependent on spins position, this enable the spatial information to be encoded in phase direction.[5]

2.8.3 *k*-space

The *k*-space is a reciprocal space where the raw data is stored once a slice had been selectively excited.[19-20] Then the real space data (the image) is obtained by applying the Fourier transformation. In order to obtain the spatial information within the NMR signal, *k*-space needs to be traversed through time (using frequency encoding) or gradient strength (using phase encoding).[5, 19-20] The direction through which *k*-space is traversed is defined by the direction of the gradient. In MRI the construction of a *k*-space raster is essential.[5] **Figure 2.20** shows a typical *k*-space raster for a two-dimensional 8 × 8 matrix using cartesian coordinates.[5] Position in the raster is defined by the strength of the gradient in the phase direction and the time delay in the read (frequency) direction.[5] The initial phase before either the read or the phase gradients are applied is the origin of *k*-space and corresponds to $k_x = k_y = 0$.[5] The *k*-space raster can be traversed by applying a particular phase encoding gradient, then applying a read encoding gradient, acquiring data over time.[5]

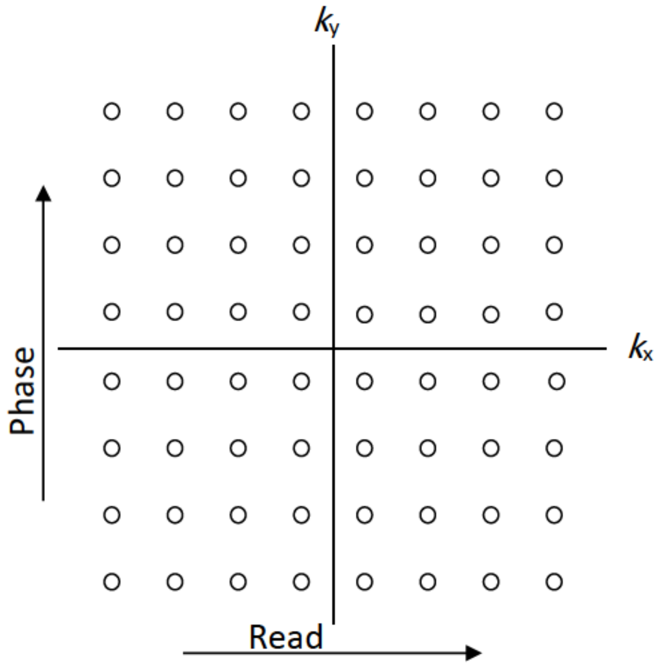

Figure 2.20: A schematic diagram of a typical *k*-space raster for a 8 x 8 matrix selected about the *z*-axis. The *x* and *y*-gradients are responsible for the frequency and phase encoding respectively.

2.8.4 Imaging sequence

Two dimensional images can be produced using spin echo-sequence.[19-20] A selective excitation pulse is applied to excite a specific layer within the sample.[19] The selective pulse excites only a narrow range of frequencies and it has a low power, this known also as a soft pulse.[19] The width of the exited layer depends on the duration of the rf pulse, since they are inversely proportional. [19] Then, a magnetic gradient applied in the first dimension to spatially encode spins using phase encoding.[19] After that, a non-selective 180° pulse is applied to produces a spin echo. The non-selective pulse excites a wide range of frequencies and it has a high power, this known also as a hard pulse.[19] Then, the spins will be frequency encoded by applying a magnetic gradient along the second dimension. In this sequence, a full line of *k*-space along *x*-direction is collected at a fixed gradient strength.[19-20] This spin-echo sequence can be adjusted by applying a multiple 180° pulses which results in multiples echoes[21], as shown in **Figure 2.21**. This sequence known as a RARE[21] sequence which is an abbreviation for rapid acquisition with relaxation enhancement. In this sequence, multiple lines of *k*-space can be collected by a single excitation and that causes a beneficial reduction in the experiment time.[21] The number of simultaneous collected *k*-space line is equal to the echoes number, at it is known as a RARE factor.[21]

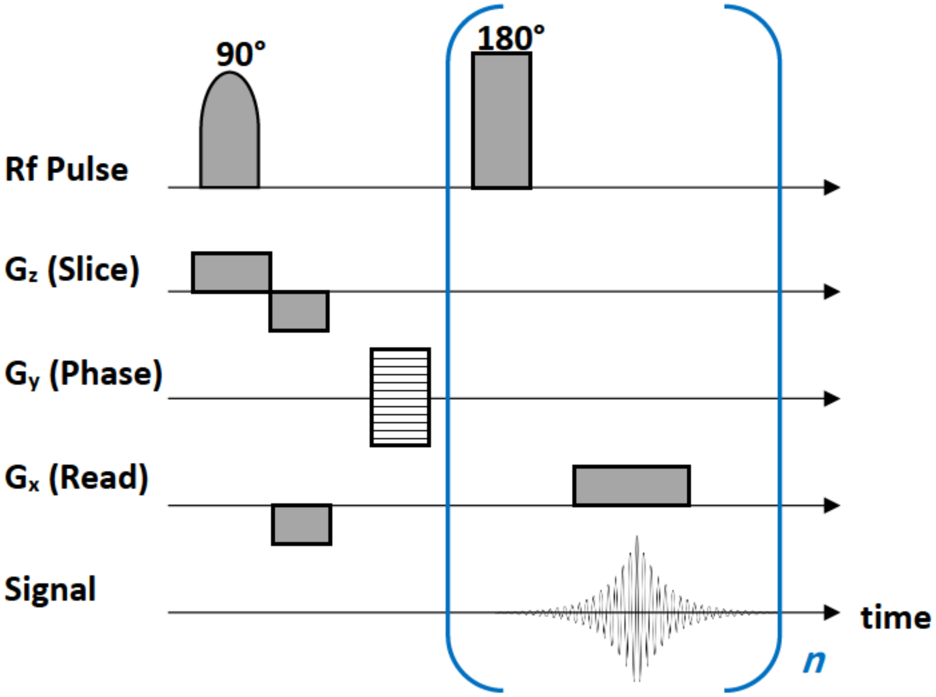

Figure 2.21: A schematic diagram of rapid acquisition with relaxation enhancement (RARE) pulse sequence. Here, there is a selective 90° pulse and non-selective 180° rf pulse. A series of 180° pulses are applied *n* times, where *n* is a positive even integral. This sequence produces a series of *n* echoes.

2.8.5 Image contrast

Image contrast is used to identify different compositions in the image.[19-20] It is known that the digital image is consists of a number of pixels, and when the signal intensity varies between pixels, image contrast can be produced.[20] There are different ways to obtain contrast within an image, such as spin density, relaxation times, chemical shift and diffusion.[20] Each image contrast is depends on the imaging sequence and values of key parameters, such as echo time (T_E) and repetition time (T_R).[20] Echo time is the time between 90° excitation pulse and the centre of the echo, whereas repetition time is the time between excitation pulses.[20] A pure spin density image can be acquired using a spin-echo pulse sequence and optimize T_E and T_R to eliminate any relaxation contrast.[20] This can be obtained by keeping T_E much lower than T_2 relaxation time while T_R must be longer than 5 $*T_1$ relaxation time.[20] On other hand, T_1 or T_2-weighted images can be obtained when image contrast depends on the signal intensity as well as the relaxation time.[20] For the T_2 weighted image, it is necessary to have a longer echo time compared to the T_2 relaxation time, and the repetition time should be kept sufficiently long to eliminate the T_1 relaxation effect.[19-20] Conversely, the T_1-weighted image acquired by keeping the echo time sufficiently short, to eliminate the T_2 relaxation effect, and reduce the repetition time to be lower than the T_1 of the system. [19-20] T_1 or T_2 maps are a 2D-images which provide an information about T_1 and T_2 values in a specific region. These maps can be acquired by collecting a series of T_1 or T_2 weighted images with a variation in the signal intensities.[19-20]

2.9 References

1. Hore, P. J., Nuclear Magnetic Resonance. Second ed.; Oxford University Press: USA, 2015.
2. Claridge, T. D. W., High-Resolution NMR Techniques in Organic Chemistry. Third ed.; Elsevier Science: 2016.
3. Levitt, M. H., Spin Dynamics: Basics of Nuclear Magnetic Resonance. Second ed.; John Wiley & Sons Ltd: 2008.
4. Keeler, J., Understanding NMR Spectroscopy. Second ed.; John Wiley & Sons Ltd: 2010.
5. Blümich, B., Essential NMR for Scientists and Engineers. Springer-Verlag Berlin Heidelberg: 2005.
6. Claridge, T. D. W., High-Resolution NMR Techniques in Organic Chemistry. Second ed.; Elsevier: Oxford, UK, 2009.
7. Hahn, E. L., Spin Echoes. Phys. Rev. **1950,** 80, 580-594.
8. Meiboom, S.; Gill, D., Modified Spin-Echo Method for Measuring Nuclear Relaxation Times. Rev. Sci. Instrum. **1958,** 29, 688-691.
9. Price, W. S., NMR Studies of Translational Motion Principles and Applications. Cambridge University Press: 2009.
10. P. W. Atkins, J. D. P., J. Keeler Atkins' Physical Chemistry. Oxford University Press: Oxford, 2018.
11. Yaghini, N.; Nordstierna, L.; Martinelli, A., Effect of water on the transport properties of protic and aprotic imidazolium ionic liquids - an analysis of self-diffusivity, conductivity, and proton exchange mechanism. Phys. Chem. Chem. Phys. **2014,** 16, 9266-9275.
12. Callaghan, P. T., Translational Dynamics and Magnetic Resonance: Principles of Pulsed Gradient Spin Echo NMR. Oxford University Press: 2011.
13. Tanner, J. E., Use of the Stimulated Echo in NMR Diffusion Studies. J. Chem. Phys. **1970,** 52, 2523-2526.
14. Stejskal, E. O.; Tanner, J. E., Spin Diffusion Measurements: Spin Echoes in the Presence of a Time-Dependent Field Gradient. J. Chem. Phys. **1965,** 42, 288.
15. William R. Croasmun, R. M. K. C., Two-Dimensional NMR Spectroscopy Applications for Chemists and Biochemists Second ed.; Wiley-VCH: 1994.
16. Perrin, C. L.; Dwyer, T. J., Application of two-dimensional NMR to kinetics of chemical exchange. Chem. Rev. **1990,** 90, 935-967.
17. Kleckner, I. R.; Foster, M. P., An introduction to NMR-based approaches for measuring protein dynamics. Biochim. Biophys. Acta **2011,** 1814, 942-968.
18. Bernhard, B., NMR imaging of materials. First ed.; Oxford: Clarendon Press.: 2004.
19. Callaghan, P. T., Principles of nuclear magnetic resonance microscopy. Oxford University Press: Oxford, 1993.
20. Britton, M. M., Magnetic resonance imaging of chemistry. Chem. Soc. Rev. **2010,** 39, 4036-4043.
21. Hennig J, N. A., Friedburg H. , RARE imaging: a fast imaging method for clinical MR. Magn. Reson. Med. **1986,** 3, 823-833.

Chapter 3 Probing the influence of Zn and water on solvation and dynamics in [C_2C_1Im(TfO)] Ionic Liquid by ^{1}H and ^{19}F nuclear magnetic resonance

3.1 Introduction

Using aqueous electrolytes in electrochemical applications face challenges due to their narrow potential window, which can give rise to H_2 evolution, as well as their ability to dry-out and form a passivation layer on the anode.[1] While organic electrolytes have serious safety concerns owing to their flammability, volatility, and toxicity.[2] Therefore, it is essential to discover new electrolytes to overcome aqueous and organic electrolytes limitations. Ionic liquids (ILs) are non-flammable solvents with high chemical stability, wide potential window, and negligible vapor pressure; such properties make them promising alternative electrolytes for the conventional aqueous and organic electrolytes for many electrochemical applications.[3-4]

Different studies have been recently focused on employing ionic liquids, as novel electrolytes, for zinc electrochemical applications, such as zinc electroplating[5-11] and rechargeable zinc-based batteries[12-14]. Various kind of ILs have been used to deposit Zn, including 1-ethyl-3-methylimidazolium dicyanamide[11] ([C_2C_1Im]DCA), 1-ethyl-3-methylimidazolium chloride ([C_2C_1Im]Cl), 1-butyl-1-methylpyrrolidinium trifluoromethylsulfonate[5] ([$Py_{1,4}$]TfO), and 1-ethyl-3-methylimidazolium trifluoromethylsulfonate[5] ([C_2C_1Im]TfO). Studies of Zn electroplating in ILs have shown that the morphology of deposited zinc is dependent on zinc speciation.[6] These zinc species vary according to the cations and anions of ionic liquids.[6] The following anions have been combined with [C_2C_1Im] cation to form four different ILs for zinc deposition:

bis(trifluoroemthylsulfonyl)imide ($TFSI^-$), trifluoromethylsulfonate (TfO^-), methylsulfonate (OMs^-) and acetate (OAc^-).[6] This study has shown that anion strongly affects the solid/liquid interface, zinc speciation, and deposited zinc morphology. In these four ILs, the strength of cation-anion interaction is in the order $OAc^- > OMS^- > TfO^- > TFSI^-$.[6] It was observed that anions that form weaker cation-anion interactions, such as TfO^- and $TFSI^-$, formed multilayer structures at solid/liquid interface.[6] Owing to the weak cation-anion interaction of TfO and TFSI anions, their ability to coordinate to zinc ions is high. That results in a larger zinc species, and hence dense zinc deposit.[6] Another study[15] investigated the effect of cations on the deposited zinc morphologies and zinc speciation. The following cations have been combined with TfO^- anion to form three different ILs for the deposition of zinc: 1-methylimidazolium $[C_1Im]^+$, 1-ethyl-3-methylimidazolium $[C_2C_1Im]^+$, and 1-ethyl-2,3-dimethyl-imidazolium $[C_2C_1C_1Im]^+$.[15] In all these three ILs, the zinc species that form is $[Zn(TfO)_n]^{2-n}$, where (n) is the coordination number, and it depends on cation-anion interaction strength.[15] The cation-anion interaction strength is in the order $[C_2C_1C_1Im]^+ < [C_2C_1Im]^+ < [C_1Im]^+$.[15] Therefore, when cation-anion interaction is weak, the anion is more likely associated with zinc.[15] Thus, the TfO^- coordination number (n) was 5, 4 and 3 in $[C_2C_1C_1Im(TfO)]$, $[C_2C_1Im(TfO)]$ and $[C_1Im(TfO)]$, respectively.[15]

It is expected for a solution consist of ions to be highly conductive. However, this is not the case for ILs, because they are composed of bulky ions, which increases their viscosity and hence lowers the mobility of ions.[16] It has been found that the physical properties of ILs can be altered and optimized by mixing them with less viscous solvents, such as water. A trace amount of water, as impurities, reduces the viscosity of ILs, which leads to enhance their conductivity.[17]

This chapter is focusing on understanding the effect of water and Zn on the physical and chemical properties of [C_2C_1Im(TfO)] ionic liquid. It was reported in the literature[18] that [C_2C_1Im] cation and TfO^- anion, in the neat dry [C_2C_1Im(TfO)], interact with each other via electrostatic interaction, as well as hydrogen bonding. This interaction results in an ion-pair which is the basic unit of the ionic liquid. Previous studies[18-19] suggest that H-bonds which formed in the [C_2C_1Im(TfO)] are formed between oxygen atoms in -SO_3 of TfO anion and H atom in the C2 site of imidazolium ring, as shown in **Figure 3.1.** Previous studies[19] have reported that TfO anion prefers to form H-bond through the oxygen atoms rather than the fluorine atoms. This is because oxygen atoms are more negatively charged compared to fluorine atoms.[19] It was reported[18] in the literature that the distance between the H atom that attached to (C2) in the cation and the O atom in -SO_3 of the anion is 2.23 Å. This is almost identical to what was found in the solid phase of [C_2C_1Im(TfO)].[18]

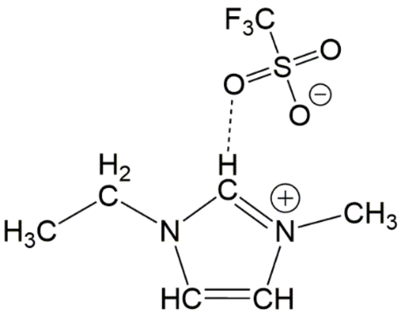

Figure 3.1: A scheme of proposed cation-anion interactions forming an ion-pair in the neat dry [C_2C_1Im(TfO)] ionic liquid. The dashed line represents the hydrogen bond. Adapted from reference 19.

The addition of water induces new interactions in the ILs-water mixture formed between water-cation and water-anion.[8] As a consequence, cation-anion interactions get interrupted due to their association with water molecules.[8] When water is added, the viscosity of [C_2C_1Im(TfO)] decreases because the interaction of cation-anion gets weaker, and the size of voids between cations and anions gets larger.[8] Reducing ionic liquid viscosity enhances the mobility of ILs ions. A previous study[20] has shown that the diffusivity of both [C_2C_1Im] cation and TfO anion increases as water content increases. It is known from Stokes-Einstein relation that the smaller molecules diffuse faster than the larger molecular, and vice versa. A previous study[20] reported the Van der Waals radii of [C_2C_1Im]$^+$ and TfO$^-$, which are 0.30 nm and 0.26 nm, respectively. By considering the ions radii, it is expected to see TfO anion diffuses faster than the bulky [C_2C_1Im]$^+$ cation. However, an anomalous behaviour were observed in the neat dry [C_2C_1Im(TfO)] ionic liquid, where the larger cation diffuses faster than the TfO anion.[20] This anomalous behaviour was also noted in [C_2C_1Im(TfO)]-water mixtures, indicating that ILs do not act as classical hydrodynamic fluids.[20] The molecular dynamics of [C_2C_1Im(TfO)] have been studied using the pulsed field gradient (PFG) NMR method, over a range of temperatures, as a function of water.[21] It was found that as water content increases, the diffusivity of all ions (cation, anion, and water) increases.[21] They found that water diffusivity, even at the highest amount of water (14 wt. %), is lower than the diffusivity of pure water.[21]

Adding water to ILs enhances their ions' mobility and hence, increases their conductivities. However, the amount of added water is critical, because adding a large amount of water can affect the IL structure, and that affects IL's potential window.[22] It has been reported[23] that, in the presence of low water mole fraction ($\chi_{\text{water}} < 0.1$) in IL system, water molecules are isolated from each other, and interrupting the formation of cation-anion interaction. As water content increases, $\chi_{\text{water}} > 0.1$, water molecules start to aggregates and form water clusters which percolate through the system.[23] However, when $\chi_{\text{water}} > 0.8$, the ILs-water mixture became an aqueous solution of ILs species.[23] According to Abbott et al.[24], ILs lose their wide potential windows, when water clusters are formed, leading to H_2 evolution. This is not ideal for ILs electrochemical applications.

The effect of water on zinc speciation formed in [C_2C_1Im(TfO)] has also been investigated. It was reported[8, 15] that, in the presence of water, zinc ion prefers to associate with water molecules rather than TfO anions. This means that, the addition of water changes the speciation of zinc from $[Zn(TfO)_4]^{2-}$ to $[Zn(H_2O)_n]^{2+}$, where $n = 1 - 6$.[8, 15] Previous research[25] has been studied the molecular dynamic of 1-ethyl-3-methylimidazolium bis(trifluoromethanesulfonyl)-amide, [C_2C_1Im(TFSA)], in the presence and absence of Li(TFSA), as a function of water, using ^{1}H and ^{7}Li NMR techniques. It is known from an NMR theory that, re-orientational and translational motions of a molecule affect the T_1 relaxation time.[26] It was found that, in the presence of a trace amount of water (water molality, $m_{\text{water}} < 0.1$ mol Kg^{-1}), the ^{7}Li T_1 NMR relaxation time is decreased.[25] This T_1 reduction was attributed to the change in the solvation structure of Li.[25] At this point, all TFSA$^-$ anions that solvate to Li$^+$ are replaced by water molecules.[25] Then, when $m_{\text{water}} > 0.1$ mol Kg^{-1}, ^{7}Li T_1 NMR relaxation time has a direct relationship with water content. This is because at this hydration level, lithium species,$[Li(water)_6]^+$, were affected mostly by changing the viscosity of the system.[25]

In this chapter, a range of [C_2C_1Im(TfO)] ionic liquid solutions have been investigated, in the absence and presence of Zn (0 - 0.15 M) and water (0 – 0.25 mole fraction). Molecular interactions and dynamics have been investigated using one-dimensional (1D) ^{1}H and ^{19}F NMR spectroscopy, relaxation and diffusion measurements. These measurements help us to understand the effect of Zn salt concentration and the hydration level on [C_2C_1Im(TfO)] ionic liquid inter and intra-molecular interactions and speciation. This study is useful and crucial not only for understanding the effect of water and zinc on the physical and chemical properties of the IL mixtures but also for mixtures' practical use.

3.2 Experimental

3.2.1 Materials and Samples Preparation

Zinc trifluoromethanesulfonate ($Zn(TfO)_2$, 99 %) was purchased from Sigma-Aldrich, 1-ethyl-3-methylimidazolium trifluoromethylsulfonate ([C_2C_1Im(TfO)], 99 %) was obtained from IO-LI-TEC, Germany. $Zn(TfO)_2$ was dried in a vacuum oven, at 120 °C, under reduced pressure (100 mbar). [C_2C_1Im(TfO)] was dried using a high vacuum pump, at 50 °C, under reduced pressure (10^{-7} mbar). Both were dried for a minimum of 24 hours and stored in a glove-box under argon atmosphere. Zinc in IL solutions were prepared, in a glove box, by dissolving $Zn(TfO)_2$ in [C_2C_1Im(TfO)] to form a range of $Zn(TfO)_2$ concentrations (0.02 – 0.15 M) before sonication and heating to 60 °C until homogenous clear yellowish liquids were formed. The heating process enhances the solubility of $Zn(TfO)_2$ in the [C_2C_1Im(TfO)] IL. Water in [C_2C_1Im(TfO)] solutions were prepared by adding water to a range of [C_2C_1Im(TfO)] IL samples containing 0, 0.02, 0.08 and 0.15 M of $Zn(TfO)_2$. The moles (n) and mole fraction (χ) of each component in the ILs mixtures are listed in **Table 3.1**.

Table 3.1: The concentration of $[C_2C_1Im(TfO)]$ IL, $Zn(TfO)_2$ and water in all IL mixtures described by moles and mole fraction, for 4 different $Zn(TfO)_2$ concentrations (0. 0.02, 0.08 and 0.15 M), and 7 mole fractions of water (0, 0.015, 0.5, 0.1, 0.15, 0.2 and 0.25).

a) 0.00 M $Zn(TfO)_2$ in $[C_2C_1Im(TfO)]$-water mixtures							
n_{IL} [10^{-3} mol]	5	5	5	5	5	5	5
n_{water} [10^{-3} mol]	0	0.07	0.24	0.5	0.8	1.1	1.5
χ_{IL} [%]	100	98	95	90	85	80	75
χ_{water} [%]	0	1.5	5	10	15	20	25
b) 0.02 M $Zn(TfO)_2$ in $[C_2C_1Im(TfO)]$-water mixtures							
n_{IL} [10^{-3} mol]	5	5	5	5	5	5	5
n_{water} [10^{-3} mol]	0	0.07	0.24	0.5	0.8	1.1	1.5
n_{Zn} [10^{-3} mol]	0.02	0.02	0.02	0.02	0.02	0.02	0.02
χ_{IL} [%]	99.62	98.13	94.64	89.66	84.78	79.7	74.72
χ_{water} [%]	0	1.5	5	10	15	20	25
χ_{Zn} [%]	0.38	0.37	0.36	0.34	0.32	0.30	0.28
c) 0.08 M $Zn(TfO)_2$ in $[C_2C_1Im(TfO)]$-water mixtures							
n_{IL} [10^{-3} mol]	5	5	5	5	5	5	5
n_{water} [10^{-3} mol]	0	0.07	0.24	0.5	0.8	1.1	1.5
n_{Zn} [10^{-3} mol]	0.07	0.07	0.07	0.07	0.07	0.07	0.07
χ_{IL} [%]	98.5	97	93.6	88.7	83.7	78.8	73.9
χ_{water} [%]	0	1.5	5	10	15	20	25
χ_{Zn} [%]	1.5	1.5	1.4	1.3	1.3	1.2	1.1
d) 0.15 M $Zn(TfO)_2$ in $[C_2C_1Im(TfO)]$-water mixtures							
n_{IL} [10^{-3} mol]	5	5	5	5	5	5	5
n_{water} [10^{-3} mol]	0	0.07	0.24	0.5	0.8	1.1	1.5
n_{Zn} [10^{-3} mol]	0.13	0.13	0.13	0.13	0.13	0.13	0.13
χ_{IL} [%]	97.3	95.8	92.4	87.5	82.7	77.8	72.9
χ_{water} [%]	0	1.5	5	10	15	20	25
χ_{Zn} [%]	2.7	2.7	2.6	2.5	2.3	2.2	2.1

Samples were put, immediately after preparation, into 5 mm Wilmad® NMR tubes fitted with J Young valves, to prevent the absorption of additional water. NMR measurements were performed < 12 h after sample preparation. The amount of water in each sample was determined using ^{1}H NMR spectroscopy.

3.2.2 NMR Measurements

NMR data were collected on a Bruker AVANCE III HD 300 spectrometer equipped with a 7 T vertical wide-bore superconducting magnet, operating at a proton resonance frequency of 300.13 MHz and a fluorine resonance frequency of 282.4 MHz. By employing the fact that ^{1}H is the NMR-active nucleus on the $C_2C_1Im^+$, whereas ^{19}F is the NMR-active nucleus on the TfO^-. The behaviour of cations and anions, in $[C_2C_1Im(TfO)]$ systems, were studied separately using ^{1}H and ^{19}F 10 mm diff30 radiofrequency coils, respectively. NMR experiments were performed at 293 ± 0.3 K, controlled by the temperature of the water-cooled gradient coils. The 90° radiofrequency pulse was calibrated for each sample, and found to be 21 ± 2 µs for ^{1}H coil and 43 ± 2 µs for ^{19}F coil. ^{1}H and ^{19}F NMR spectra were acquired using a pulse-acquire sequence, with a repetition time of 15 s. The chemical shift of peaks was calibrated using CF_3COOH and TMS as an external reference for ^{19}F and ^{1}H, respectively. The external reference was assembled by placing the 5 mm sample tube inside a 10 mm containing the external reference to avoid any interactions between the sample and the reference.

^{1}H and ^{19}F spin-lattice (T_1) magnetic resonance relaxation times were measured using an inversion recovery sequence[26], $[180° - \tau - 90° - \text{acq}]_n$, with a repetition time of 10 s and 8 signal averages. A series of experiments ($n = 10$) were collected, with logarithmically spaced time delays,

τ, ranging from 5×10^{-6} s to 9 s. The average T_1 relaxation times were determined by fitting the normalised signal intensity ($I_{(\tau)}/I_{(0)}$), as a function of time, to (**Equation 2.5)** using *Kaleidagraph*[27] software. ^{1}H and ^{19}F spin-spin (T_2) magnetic resonance relaxation times were measured using Carr Purcell Meiboom Gill (CPMG)[28] sequence, $[90° - (\tau - 180° - \tau)_m - \text{acq}]_n$. A series of experiments ($n = 12$) were collected with a repetition time of 10 s, a delay (τ) of 0.001 s, and m value varied from 0 to 2048. The average T_2 relaxation times were determined by fitting the normalised signal intensity ($I_{(2\tau)}/I_{(0)}$), as a function of time, to (**Equation 2.8)** using *Kaleidagraph*[27] software. Self-diffusion co-efficients (D) were measured using a pulsed gradient stimulated echo (PGSTE) sequence[26] with 16 gradient steps. ^{1}H and ^{19}F diffusion measurements were collected using a maximum gradient ($\boldsymbol{G}_{\max}$) of 300 G cm^{-1}, pulse duration (δ) of 2 ms, observation time (Δ) of 60 ms, and a repetition time of 2 s. The average self-diffusion co-efficients (D) were determined by fitting the normalised signal intensity as a function of gradient strength, ($I_{(G)}/I_{(0)}$), to the Stejskal−Tanner[29] (**Equation 2.11)** using *Kaleidagraph*[27] software.

3.3 Results

Figure 3.2 shows the ^{1}H NMR spectrum for dry [C_2C_1Im(TfO)] ionic liquid, along with the molecular structures of IL ions, with a labelling scheme for each proton environment. The chemical shift values for [C_2C_1Im(TfO)] peaks are listed in **Table 3.2**.

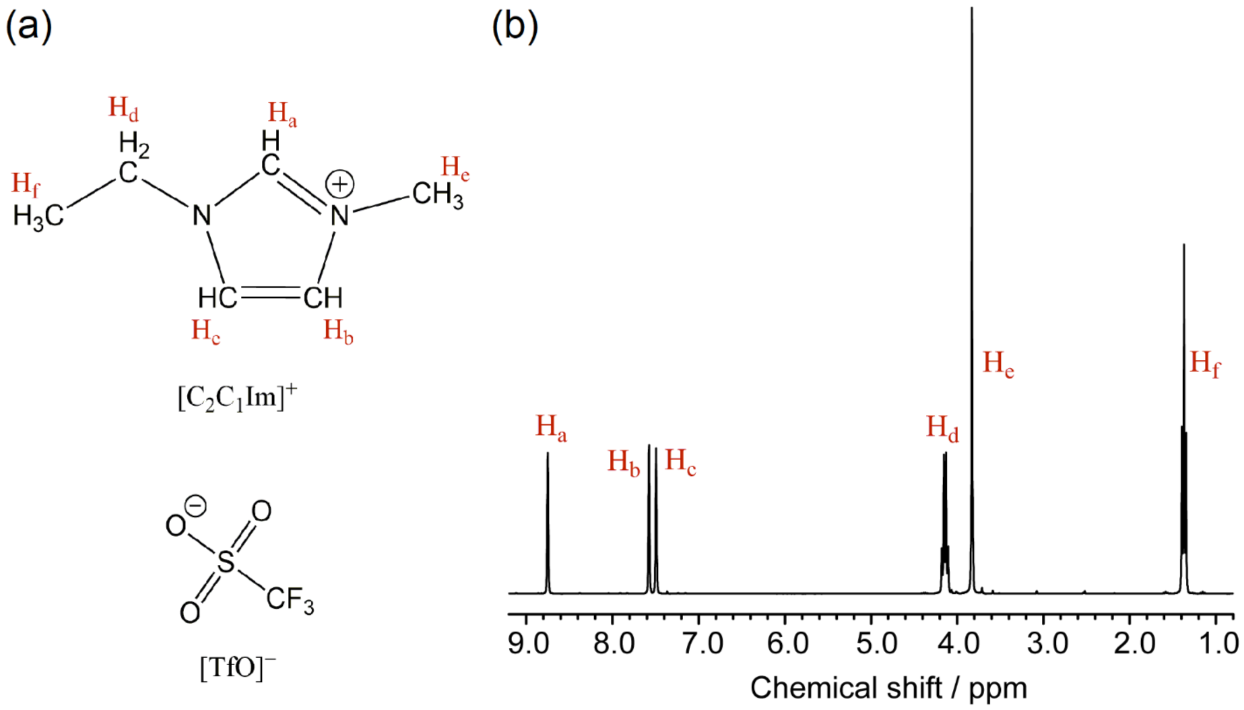

Figure 3.2: (a) Molecular structures of $[C_2C_1Im(TfO)]$ IL ions with proton numbering scheme. (b) ^1H NMR spectrum for neat dry $[C_2C_1Im(TfO)]$, at 293 K.

Table 3.2: ^1H and ^{19}F NMR chemical shifts of neat dry $[C_2C_1Im(TfO)]$ ionic liquid. The chemical shift of ^1H peaks were calibrated TMS at 0 ppm, while the chemical shift of ^{19}F peak was calibrated to (CF_3COOH) at 0 ppm. Both references were used as external reference.

Species	Proton **OR** Fluorine atoms		^1H NMR / ppm	^{19}F NMR / ppm
$C_2C_1Im^+$	N-C**H**-N	H_a	8.75 (s)	-
	N-C**H**-CH-N	H_b	7.57 (s)	-
	N-CH-C**H**-N	H_c	7.50 (s)	-
	N-C**H₂**-CH₃	H_d	4.14 (q)	-
	N-C**H₃**	H_e	3.83 (s)	-
	N-CH₂-C**H₃**	H_f	1.37 (t)	-
TfO^-	S-C**F₃**	-	-	4.035 (s)

^1H and ^{19}F NMR spectra for dry [$C_2C_1Im(TfO)$] IL, with increasing $Zn(TfO)_2$ concentration, are shown in **Figure 3.3**. As the zinc concentration increases in the [$C_2C_1Im(TfO)$] ionic liquid, a slight upfield shift is observed for (H_a, H_b and H_c) protons peaks, and the peak of TfO anion. The chemical shift of H_c, H_d and H_f protons peaks, in $C_2C_1Im^+$, were observed to not be affected by the presence of $Zn(TfO)_2$ and, therefore, are not shown. Chemical shifts values of all protons in the [C_2C_1Im] cation, as a function of Zn, are listed in **Table A.1**, in **Appendix 1**.

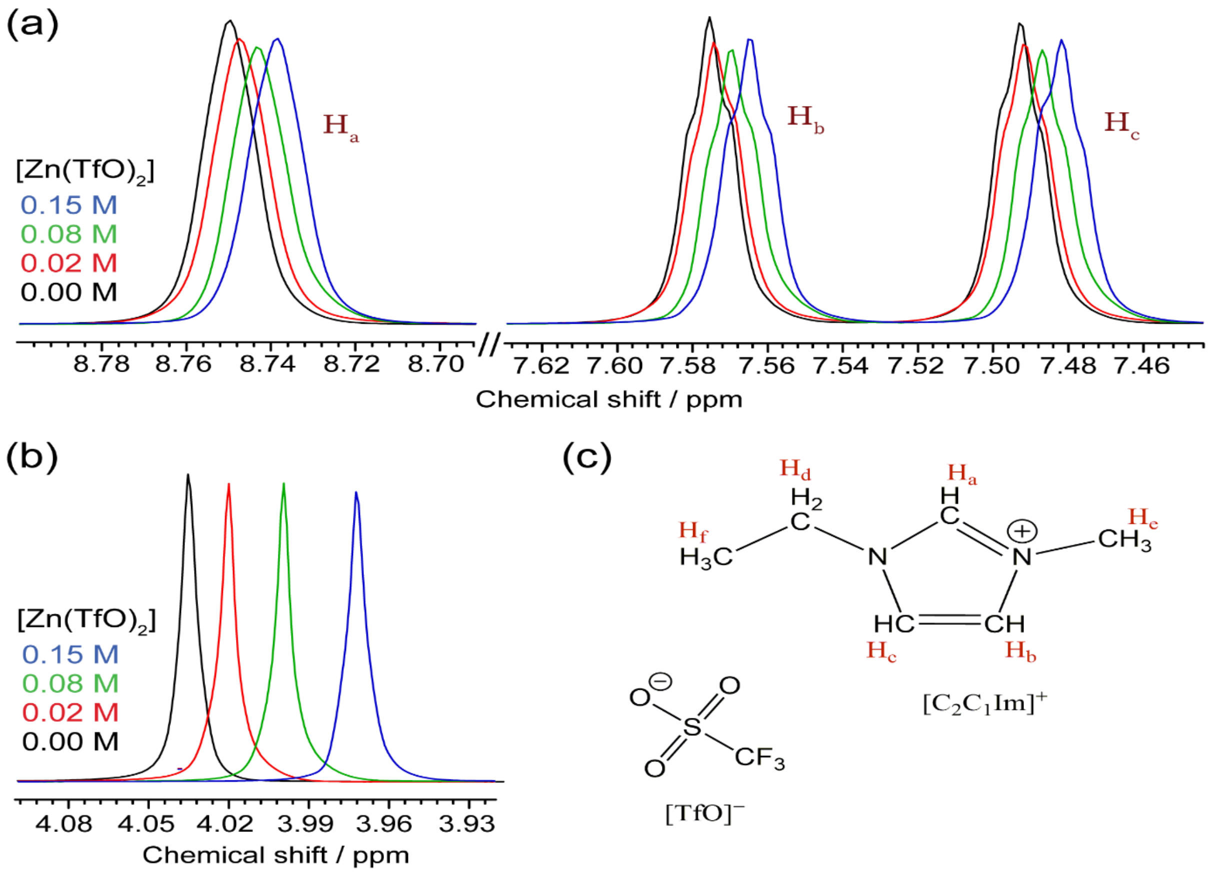

Figure 3.3: (a) ^1H NMR spectra of H_a, H_b, and H_c protons in $C_2C_1Im^+$ and (b) ^{19}F NMR spectra of TfO^-, as a function of $Zn(TfO)_2$ concentration. ^1H peaks were calibrated to TMS, while the ^{19}F peak was calibrated to (CF_3COOH) at 0 ppm. Both references were used as external reference.

Figure 3.4 shows the ^{1}H NMR spectra of [C_2C_1Im(TfO)], as a function of water, for different Zn(TfO)$_2$ concentrations. The chemical shift of the water peak is the most peak affected by the concentration of zinc. At a higher concentration of zinc (0.15 M), a strong downfield shift is observed for water peak indicating that they are more de-shielded in the presence of zinc, as shown in (**Figure 3.4, c**). Furthermore, a gradual upfield shift is observed for water peak, as water content increases in [C_2C_1Im(TfO)], in the presence of Zn. However, an anomalous behaviour is noted for the chemical shift of water peak, in the absence of zinc, as water content increases, as shown in (**Figure 3.4, a**). It should be noted that, water peak in the lowest water content in (**Figure 3.4, a**) could not be observed. Chemical shift values of all protons in the [C_2C_1Im] cation, as a function of water for different zinc concentrations, are listed in **Tables A. 2-5**, in **Appendix 1**.

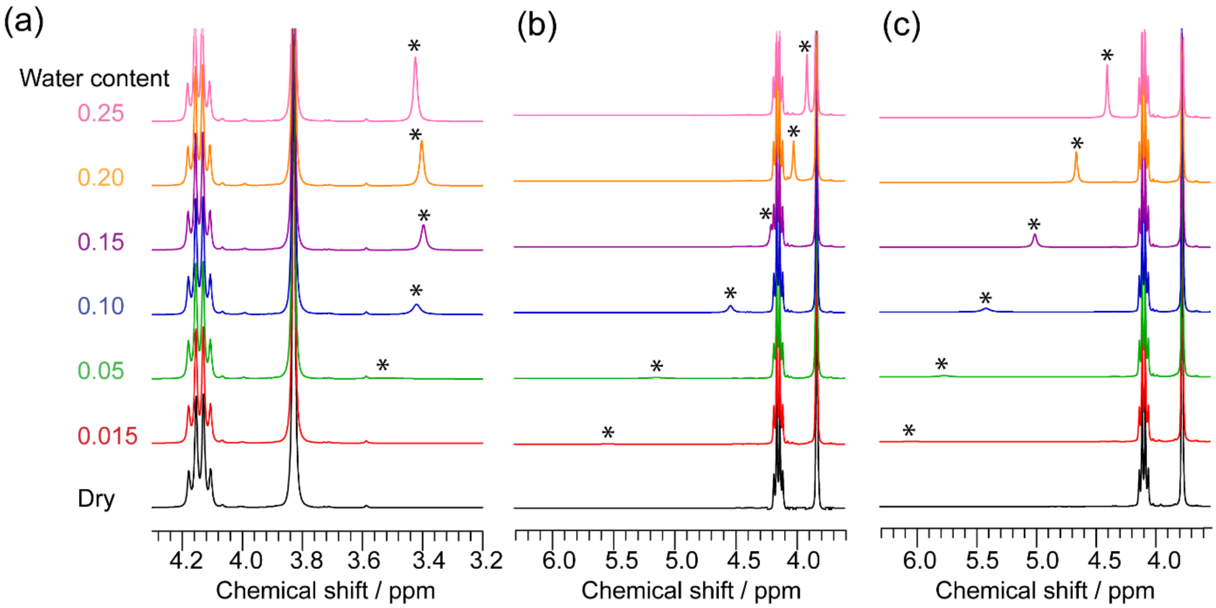

Figure 3.4: A series of ^{1}H NMR spectra of [C_2C_1Im(TFO)] IL, as a function of water mole fraction in the (a) absence of Zn, and presence of (b) 0.08 M and (c) 0.15 M Zn(TfO)$_2$. Water peak is indicated by (*).

The addition of water also affects the chemical shift of the (H_a) peak, in $C_2C_1Im^+$, as well as the fluorine peak in the TfO^-, as shown in **Figure 3.5**. A slight upfield shift is observed for the H_a peak, as water content increases, both in the presence and absence of Zn. The TfO^- peak slightly shifts to a lower chemical shift and then remains constant, in the absence of Zn, as water content increases. However, in the presence of Zn, the chemical shift of the TfO^- peak increases with the initial addition of water and then remains constant at the higher water concentrations.

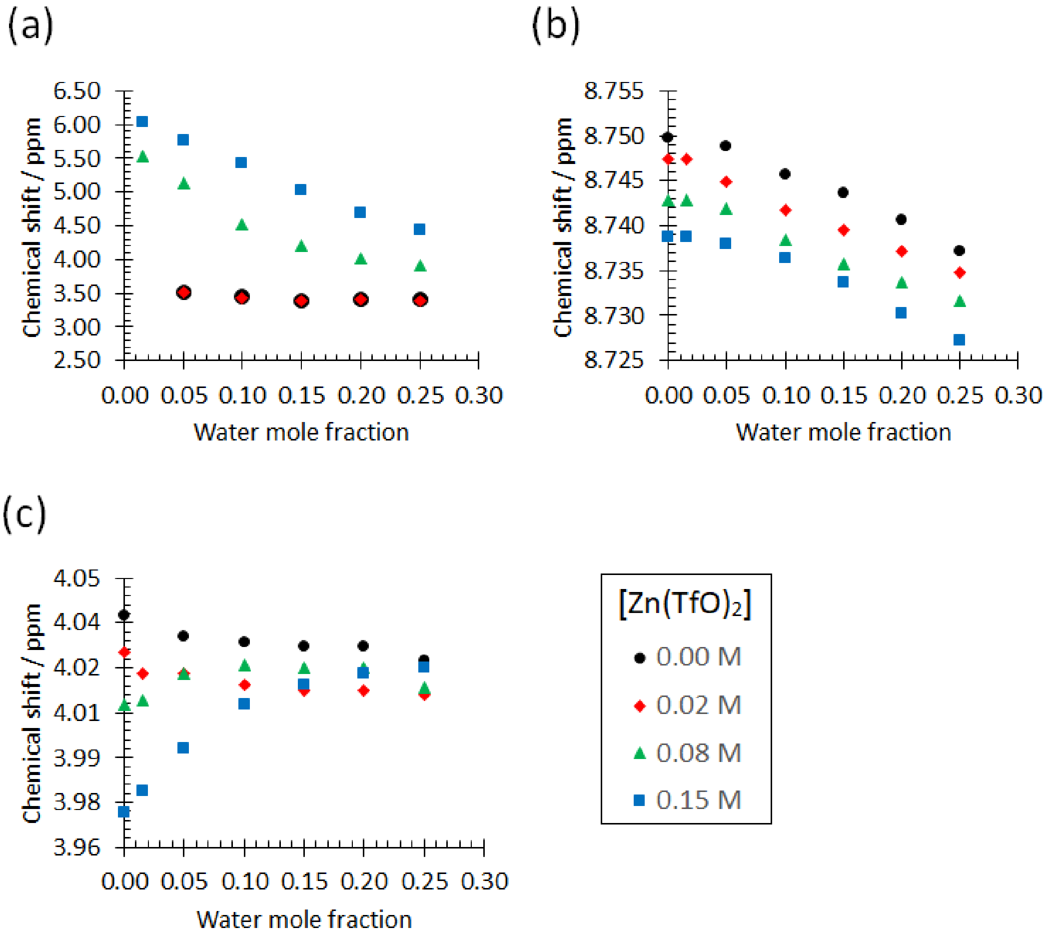

Figure 3.5: ^1H NMR chemical shifts of (a) water and (b) H_a proton in the $C_2C_1Im^+$ and (c) ^{19}F NMR chemical shift of CF_3 in the TfO^-, as a function of water mole fraction, in the presence of different $Zn(TfO)_2$ concentrations, 0 M, 0.02 M, 0.08 M and 0.15 M.

The effect of zinc on the self-diffusion co-efficients of $C_2C_1Im^+$ (D^+) and TfO^- (D^-) are investigated as a function of water. **Figure 3.6** shows D^+ and D^-, and the diffusion co-efficient of water (D_{water}), in the presence and absence of Zn, as a function of water. Since the $C_2C_1Im^+$ protons are not exchangeable, all protons are expected to have identical diffusion co-efficients. The diffusion data of $C_2C_1Im^+$, in **Figure 3.6**, are that related to the (H_a) proton. Diffusion co-efficients of all protons in the $C_2C_1Im^+$ cation are presented in **Figure A. 1**, in **Appendix 1**. The data in **Figure 3.6** shows that the TfO^- anion diffuses slower than the bulkier $C_2C_1Im^+$ cation.

In the absence of Zn, a direct relationship is observed between water concentration and the diffusivity of $C_2C_1Im^+$, TfO^-, and water species. In the presence of zinc, a minimum in the D^+ and D^-, is observed at 0.05 mole fraction of water. As water content increases ($\chi_{water} > 0.05$), the diffusion co-efficients (D^+ and D^-) are changed toward the direct relationship between the viscosity of the system and molecular diffusivity. The D_{water} is much lower than the diffusivity of pure water[21] (2.3×10^{-9} m^2 s^{-1} at 20 °C), even at high water concentration, in the presence and absence of Zn. It should be noted that, D_{water} at ($\chi_{water} = 0.05$) in the absence of Zn, could not be measured because of the weak signal of water.

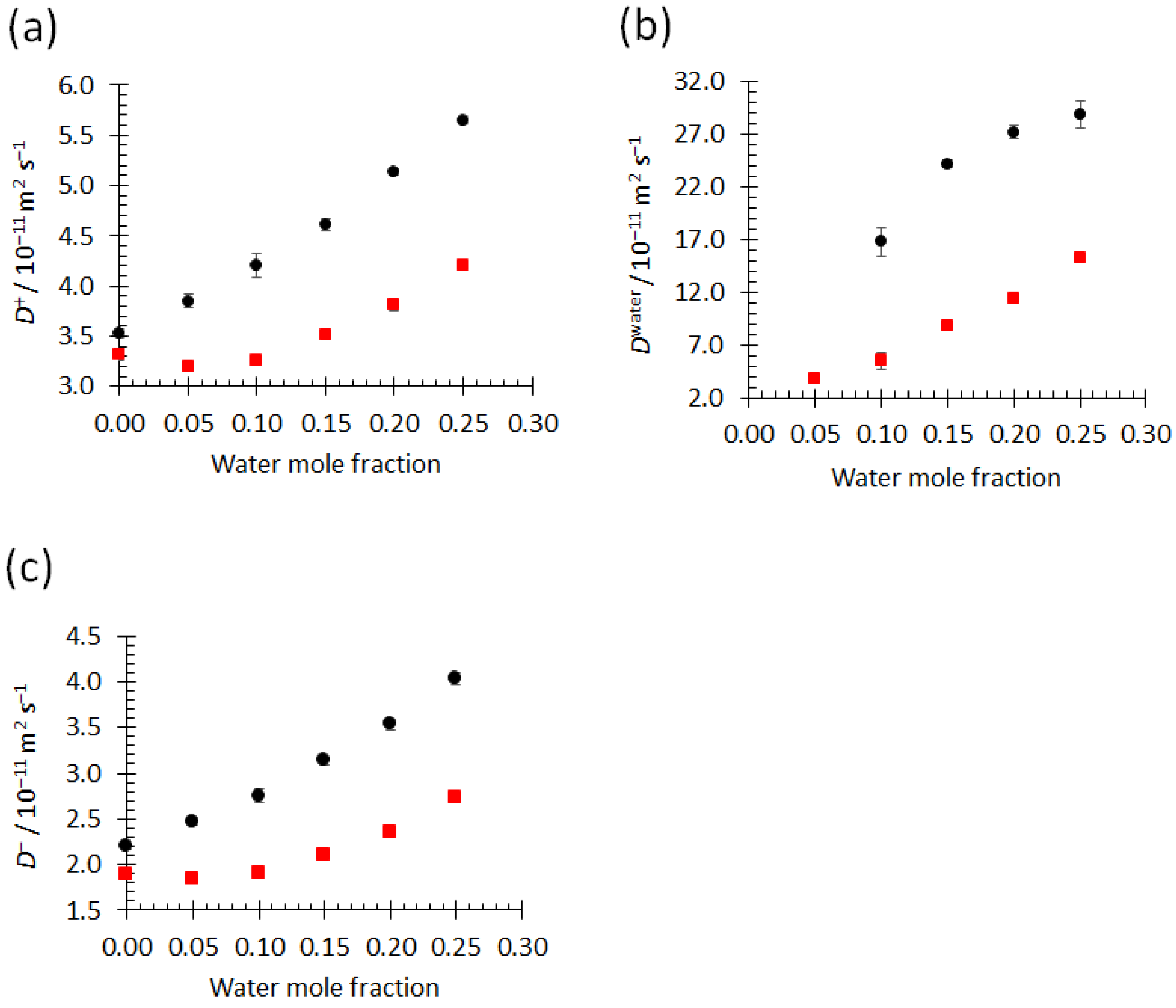

Figure 3.6: ^1H NMR diffusion co-efficients of (a) water and (b) $C_2C_1Im^+$cation, and (c) ^{19}F NMR diffusion co-efficient of TfO^- anion, as a function of water mole fraction, in the presence (■) and absence (●) of 0.15 M $Zn(TfO)_2$. ^1H and ^{19}F diffusion measurements were collected using a maximum gradient ($\boldsymbol{G}_{max}$) of 300 G cm^{-1}, pulse duration (δ) of 2 ms and observation time (Δ) of 60 ms.

^{1}H T_1 NMR relaxation times, for water proton and $C_2C_1Im^+$ protons (H_a, H_b and H_c) as a function of water, in the presence and absence of Zn, are shown in **Figure 3.7**. ^{1}H T_1 NMR relaxation of cation protons (H_a, H_b and H_c), in the dry sample, were not affected by the addition of Zn. However, by the addition of water, an immediate reduction in ^{1}H T_1 NMR relaxation times of cation is observed at ($\chi_{water} < 0.05$) hydration level. **Figure 3.7** shows that, upon addition of more water ($\chi_{water} > 0.05$), the T_1 NMR relaxation times of $C_2C_1Im^+$ protons (H_a, H_b and H_c) rise steadily as water content increases. However, it can be noticed that the presence of zinc slows down the T_1 NMR relaxation times increment. It should be noted that, the T_1 NMR relaxation time value of water, in the ($\chi_{water} < 0.05$) and absence of Zn, could not be measured, because of the weak signal of water.

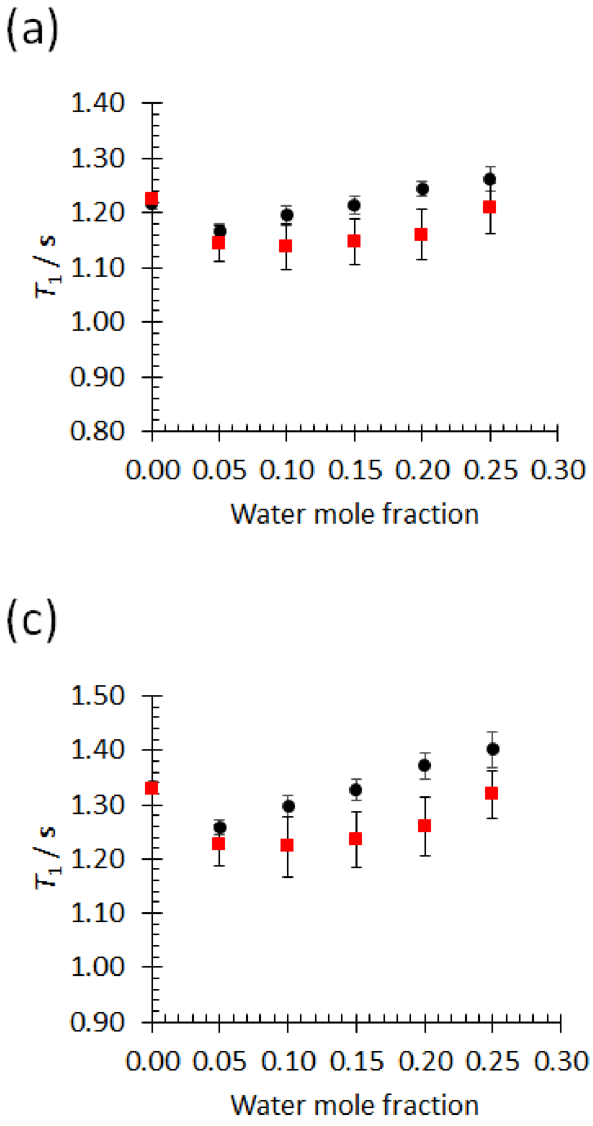

Figure 3.7: ^1H T_1 NMR relaxation times for (a) H_a, (b) H_b, (c) H_c protons in $C_2C_1Im^+$ cation and (d) water proton as a function of water mole fraction, in the presence (■) and absence (●) of 0.15 M $Zn(TfO)_2$.

^{19}F T_1 NMR relaxation times for the TfO^- anion, as a function of Zn and water, are presented in **Figure 3.8**. ^{19}F T_1 NMR relaxation times for TfO^- also follow the same trend as ^1H T_1 NMR relaxation time of the cation, with respect to the addition of water. **Figure 3.8** shows that the ^{19}F T_1 NMR relaxation values are affected by the zinc concentration. In the dry solutions, ^{19}F T_1 NMR relaxation time decreases as Zn concentration increases.

By the addition of water, two regimes are observed for ^{19}F T_1 NMR relaxation time, in the absence of Zn. First regime is observed with the initial addition of water ($\chi_{water} < 0.05$), and show a reduction in the ^{19}F T_1 NMR relaxation time. As water content increases, ($\chi_{water} > 0.05$), a second regime is observed, where ^{19}F T_1 NMR relaxation times increase with water content. T_1 relaxation time, in the absence of Zn, and presence of 0.015 mole fraction of water, could not be measured, because of the weak signal of water. However, it can be estimated from the ^{19}F T_1 relaxation time at ($\chi_{water} = 0.015$) and presence of 0.02 M $Zn(TfO)_2$. Owing to the fact that such low zinc concentration, does not have a big effect on the ^{19}F T_1 relaxation times. However, at the highest amount of Zn (0.15 M), the ^{19}F T_1 NMR relaxation times seem to have three regimes, as water content increases. With the initial addition of water ($\chi_{water} < 0.015$) an immediate reduction in T_1 is observed. Then at ($0.015 < \chi_{water} < 0.1$), a modest change is observed in the ^{19}F T_1 relaxation time. Finally, at ($\chi_{water} > 0.1$), the T_1 relaxation times increase gradually with water content.

^{19}F T_2 NMR relaxation times for the TfO^- anion, as a function of water, in the presence and absence of Zn, are presented in **Figure 3.9**. ^{19}F T_2 NMR relaxation times for TfO^- also follow the same trend as ^{19}F T_1 NMR relaxation time, with respect to the addition of water. The presence of Zn lowers the T_2 relaxation time of TfO^- anion. An immediate reduction in the ^{19}F T_2 relaxation time by the addition of 0.05 mole fraction of water. When the water content becomes (χ_{water} > 0.05), the T_2 relaxation increases with water content, in the presence and absence of Zn.

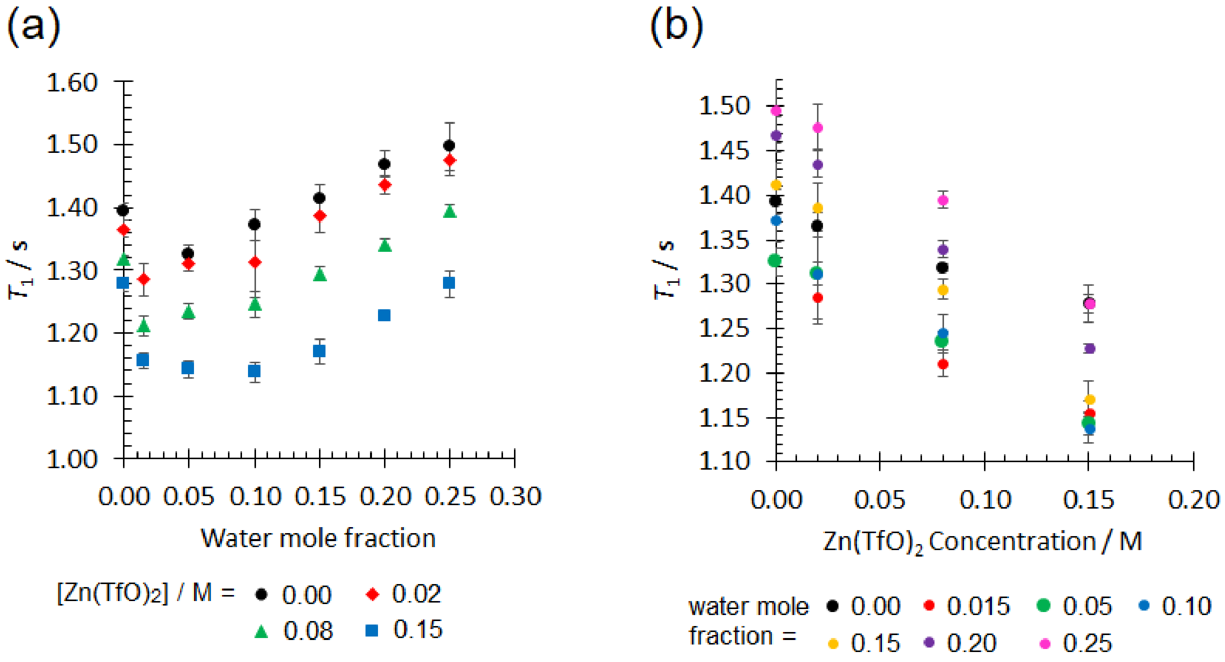

Figure 3.8: (a) ^{19}F T_1 NMR relaxation times of TfO anion as a function of water mole fraction in the presence of different $Zn(TfO)_2$ concentrations. (b) ^{19}F T_1 NMR relaxation times of TfO anion as a function of $Zn(TfO)_2$ in presence of different amounts of water.

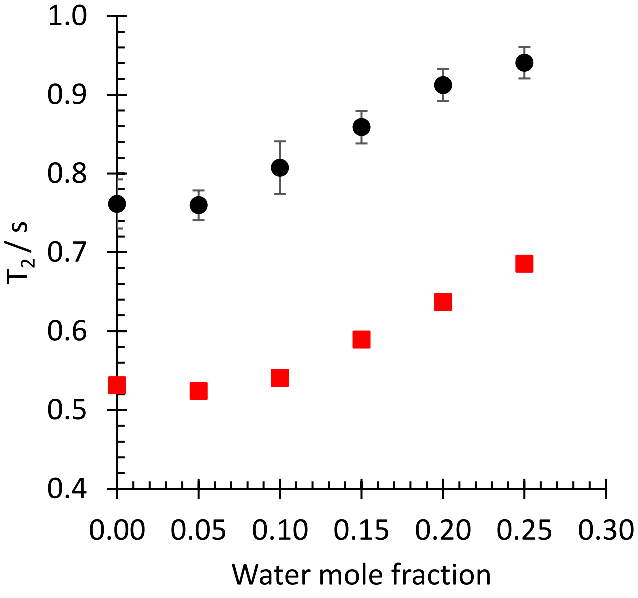

Figure 3.9: ^{19}F T_2 NMR relaxation times for TfO^{-} anion as a function of water mole fraction, in the presence (🟥) and absence (●) of 0.15 M $Zn(TfO)_2$.

3.4 Discussion

From previous studies[8] of neat [$C_2C_1Im(TfO)$], it's known that the C_2C_1Im cation and TfO anion interact, with each other, by strong electrostatic interaction and H-bonds forming (cation-anion) ions pairs. All hydrogen atoms in the C_2C_1Im cation are capable of forming H-bonds. However, it was reported[8] that the protons that attached to imidazolium ring's carbons, (H_a,H_b and H_c), are more active to form H-bonds. Some authors[30] have also suggested that, C_2C_1Im cation form a strong H-bond with the TfO anion, via (H_a) proton, which is the most acidic H atom of the imidazole ring. They also suggest that methyl and ethyl protons interact with SO_3 in the TfO anion and form weak H-bonds.[30] The large negative charge of oxygen atoms in TfO anion makes them more favorable to form H-bond than fluorine atoms.[19] **Figure 3.10** shows the possible conformers of cation-anion pair in the dry neat [$C_2C_1Im(TfO)$] IL, including their suggested H-bonds.

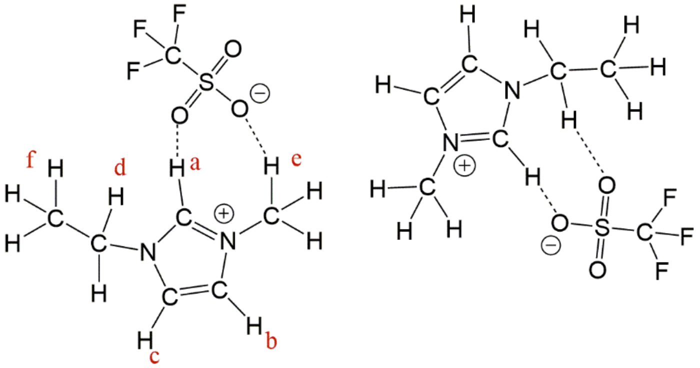

Figure 3.10: A proposed scheme of the possible conformers of cation-anion pair in the dry neat [C_2C_1Im(TfO)] IL, including their suggested H-bonds. The dashed line represents the hydrogen bond.

When Zn$(TfO)_2$ is added, cation-anion interactions get disrupted because TfO anions prefer to associate with Zn ions rather than C_2C_1Im cations. This change in the IL's interactions is observed in this study by the ^{1}H and ^{19}F NMR spectroscopies, (**Figure 3.3**). These spectra show a slight upfield shift for the peaks of (H_a, H_b and H_c) protons in C_2C_1Im cation and fluorine peak in TfO anion as zinc concentration increases. This indicates that these protons and fluorine atoms form fewer H-bonds, in the presence of Zn, as a consequence of cation-anion interaction reduction. Upon the addition of Zn, TfO anions prefer to associate with Zn rather than C_2C_1Im cations. Previous studies[8, 15] suggested that $[Zn(TfO)_4]^{2-}$, are the expected zinc complexes. The reduction of ^{19}F T_1 NMR relaxation time support that, because TfO anions associate with Zn and form $[Zn(TfO)_4]^{2-}$. Forming such large zinc species, increase the rotational correlation time of fluorine atom, and hence decrease the ^{19}F T_1 relaxation time. On the other hand, the ^{1}H T_1 NMR relaxation time of C_2C_1Im protons do not affected by the addition of Zn. This indicates that Zn ions do not interact with C_2C_1Im cations. **Figure 3.11** shows the possible interactions between Zn species and [C_2C_1Im(TfO)] ions.

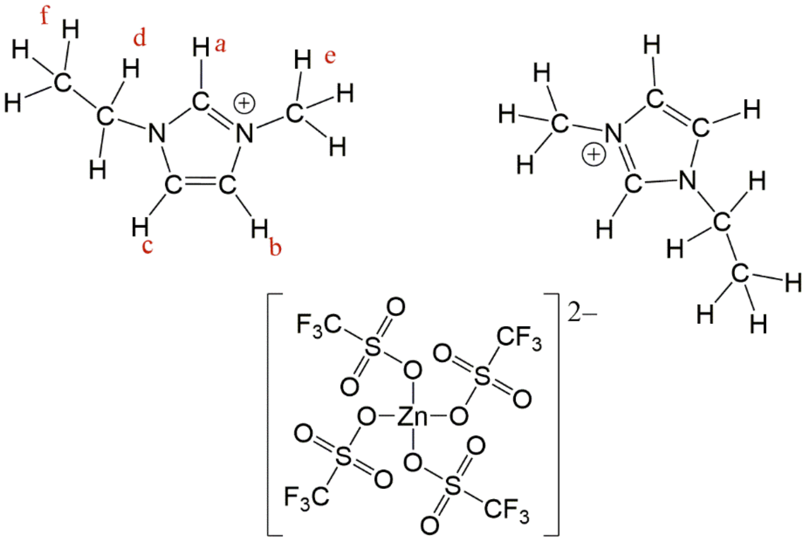

Figure 3.11: A proposed zinc species and interactions formed in the dry [C_2C_1Im(TfO)] ionic liquid, in presence of Zn(TfO)$_2$. The dashed line represents the hydrogen bond.

When water is added to dry [C_2C_1Im(TfO)], it is known[31] that water molecules screen the H-bond sites of cation-anion pair. This lowers the formation of cation-anion pair because TfO anions prefer to associate with water rather than C_2C_1Im cations. As a consequence, the viscosity, of the [C_2C_1Im(TfO)] system, decreases leading to an increase in ions mobility. This can be observed from diffusion measurements, (**Figure 3.6**), where the self-diffusion co-efficients of the cation (D^+), anion (D^-), and water (D^{water}) increases with water content increment. The amount of added water is very crucial to IL-water mixtures interactions. When a small amount of water is added ($\chi_{water} < 0.05$), water molecules are embedded in cavities between neighbouring cation-anion pairs. As a consequence, cation-water-anion triple complexes are formed. This can explain the immediate reduction in ^{1}H T_1 NMR relaxation time of the cations, (**Figure 3.7**), and ^{19}F T_1 NMR relaxation time of anions, (**Figure 3.8**), with the initial addition of water ($\chi_{water} < 0.05$) to the dry ionic liquid. Forming such a large triple complex (cation-water-anion) increases the availability of hydrogen bonding. These H-bonds slow down the mobility of ions, and hence, lower T_1 NMR relaxation time. **Figure 3.12** shows the proposed speciation and interactions when a small amount of water ($\chi_{water} < 0.05$) is added to the [C_2C_1Im(TfO)] ionic liquid.

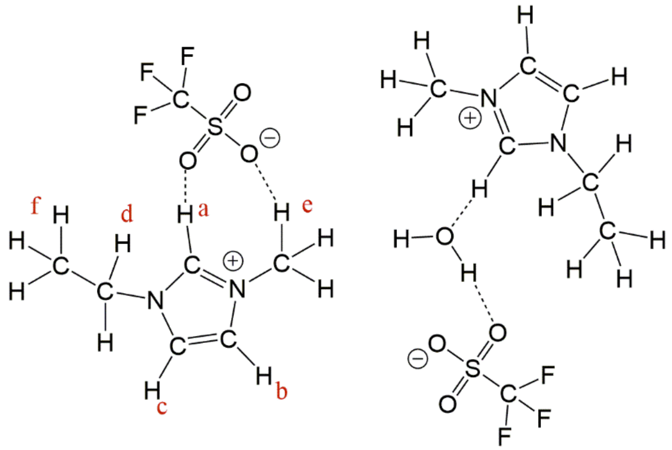

Figure 3.12: A proposed scheme of embedded water molecules in [C_2C_1Im(TfO)] ionic liquid structure, and the formation of cation-water-anion triple complex, in the presence of small amount of water ($\chi_{water} < 0.05$). The dashed line represents the hydrogen bond.

Increasing water content ($\chi_{water} > 0.05$), initiates the aggregation of water molecules, and the formation of water clusters. The anomalous behaviour of the chemical shift of water, as water content increases, (**Figure 3.4, a)**, shows an evidence of water cluster formation. When water molecules aggregates, more H-bonds are formed, that results in a downfield shift of water peak. At ($\chi_{water} > 0.05$) hydration level, a steadily increase in ^{1}H T_1 NMR relaxation time of the cations, (**Figure 3.7**), and ^{19}F T_1 NMR relaxation time of the anions, **Figure 3.8**, are observed, which consistent with the reduction of water-IL mixtures viscosity. These two competing effects, increasing H-bonds availability and lowering viscosity, result in a minimum at a certain amount of water, which is $\chi_{\text{water}} = 0.05$ in our system. This minimum in T_1 NMR relaxation has been observed before in the NMR relaxometry measurements of [C_2C_1Im(acetate)]-water mixture.[31] **Figure 3.13** shows the proposed speciation and interactions when a ($\chi_{\text{water}} > 0.05$) is added to the [$C_2C_1$Im(TfO)] ionic liquid.

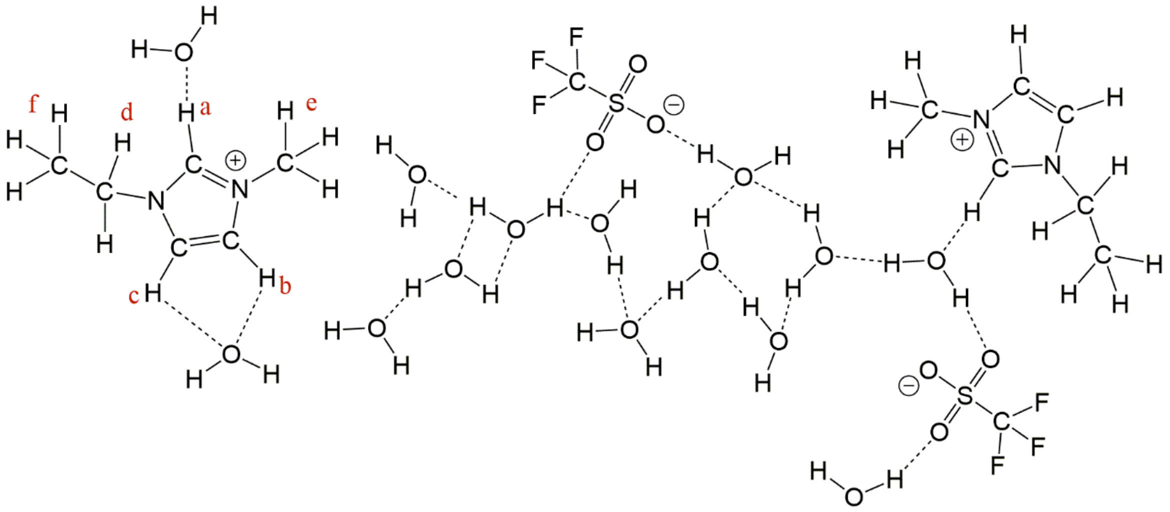

Figure 3.13: A proposed scheme of water molecules aggregation in [C_2C_1Im(TfO)] ionic liquid structure, and the formation of water cluster, in the presence of ($\chi_{\text{water}} > 0.05$). The dashed line represents the hydrogen bond.

However, in the presence of zinc and water, different speciation and interactions are formed. Previous studies[8, 15] reported that zinc ions prefer to associate with water, rather than the TfO anion. This results in changes in zinc speciation from $[Zn(TfO)_4]^{2-}$ to an aqueous zinc species $[Zn(H_2O)_n]^{2+}$, n = 1-6. The chemical shift of water, at different zinc concentrations, gives evidence of Zn-water interactions, as shown in **Figure 3.4**. At the same hydration level, e.g. (χ_{water} = 0.1), the water peak shifts downfield as the concentration of zinc increases. This result ties well with previous studies[25] wherein a downfield shift of the water peak has been observed when the concentration of Li^+ increased. This increment in the chemical shift of water peak was attributed to Li-water interactions.[25] Then, as water content increases, in the presence of zinc, the water peak shifts upfield (more shielded), due to water-anion interactions through the oxygen atom of the anion. ^{19}F NMR spectroscopy, (**Figure 3.5**), gives an evidence of water-anion interactions. The chemical shift of TfO anion increase with increasing water content, as a result of forming more H-bond between water and TfO anions. Then at ($\chi_{water} > 0.15$), in presence of 0.15 M Zn, the chemical shift of TfO anion remains constant as water content increases. This indicates that at this hydration level all TfO anions are solvated by water molecules. **Figure 3.14** shows the proposed speciation and interactions of $[C_2C_1Im(TfO)]$ ions, in the presence of zinc and water.

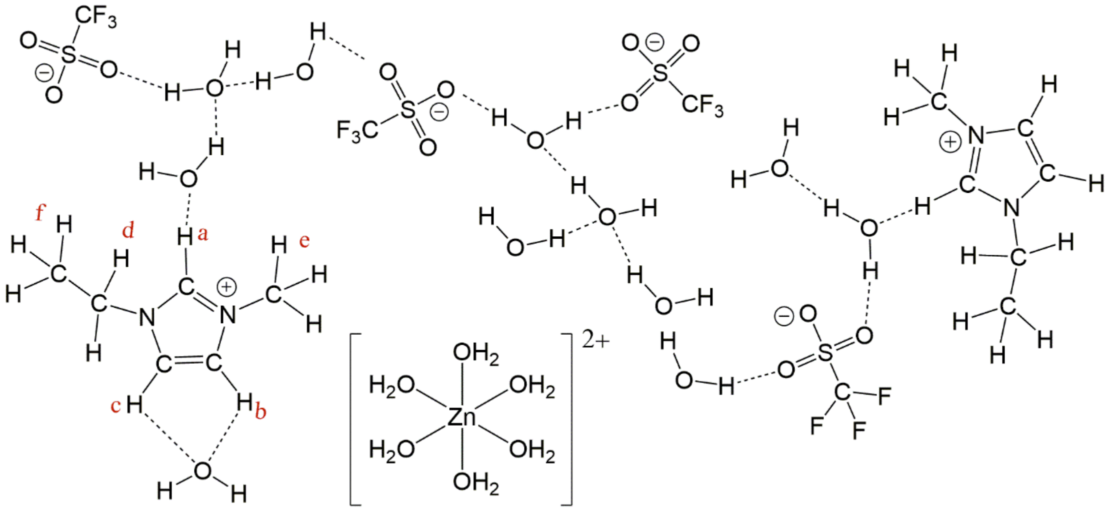

Figure 3.14: A proposed scheme of zinc speciation and interactions in $[C_2C_1Im(TfO)]$ ionic liquid, in the presence of zinc and water. The dashed line represents the hydrogen bond.

Diffusion data, (**Figure 3.6**), reflect the effect of zinc and water on speciation. An overall reduction is observed for both D^- and D^+, in the presence of Zn, compared to those obtained in the absence of Zn at the same hydration level. This is due to the presence of zinc ion complexes, $[Zn(TfO)_4]^{2-}$, which changed to $[Zn(H_2O)_n]^{2+}$ with increasing water content.[8, 15] Where, the presence of these zinc complexes decreases the size of voids in the IL system, and that slows down the diffusivity of anions and cations. Moreover, **Figure 3.6** shows that the diffusivity of TfO anion is lower than that of larger C_2C_1Im cation. By considering Stokes–Einstein relation, this is the opposite of what was expected, since the C_2C_1Im cation has a larger Van der Waals radii. This has been observed before[20] in ILs, indicating that ILs do not act as classical hydrodynamic fluids. Another study[31] explained this anomalous behaviour of diffusion co-efficient of anion, in ILs, by the cooperative diffusion of ion pairs.

In order to understand how zinc and water affect the diffusional properties on a molecular level, a normalized diffusion co-efficient ($D_{\text{ion}}/D_{\text{neat}}$) is used to analyze the excess ionic diffusivity.[20] Where D_{neat} is the diffusion co-efficient of D_{ion} in the dry ionic liquid. **Figure 3.15** shows that in the absence of Zn, an overall increase of D^-/D_{neat}^- and D^+/D_{neat}^+ is observed as a result of lower viscosity. At all water concentrations, D^- exceeds D^+, this supports our argument that TfO anions interact more with water than the C_2C_1Im cation. In the presence of Zn, when a small amount of water is added ($\chi_{\text{water}} < 0.1$), D^- is almost constant and lower than D^+. This indicates that, at this hydration level, water molecules interact more with Zn rather than TfO anion. As water content increases ($\chi_{\text{water}} > 0.1$), D^- start to increase and exceeds D^+, indicating that TfO anion has interacted with water. This means that TfO anions would not associate with water until all zinc ions are solvated by water molecules.

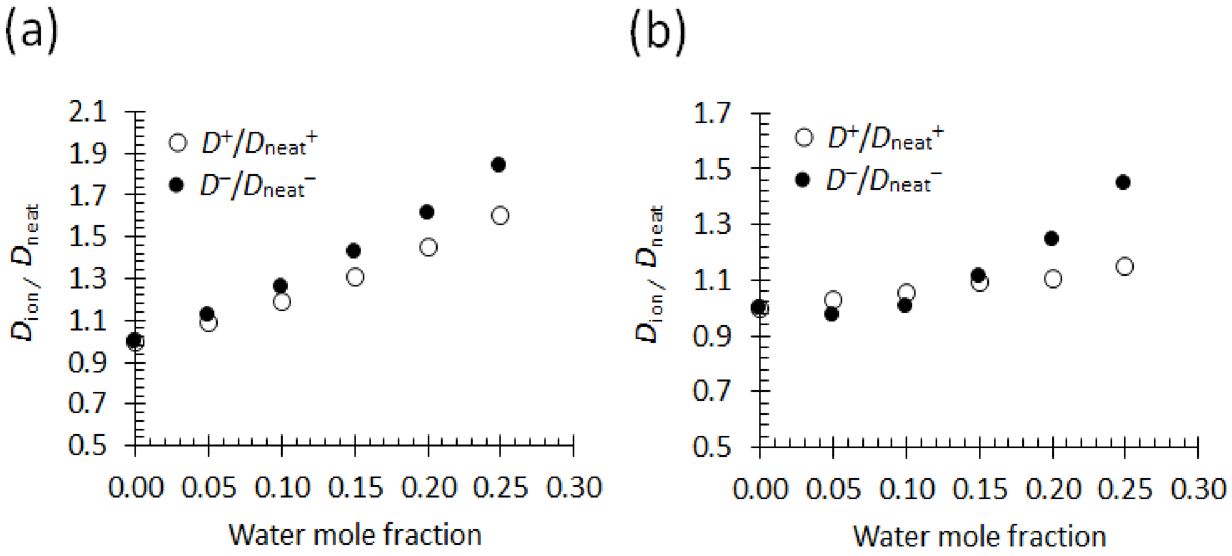

Figure 3.15: Normalized self-diffusion co-efficients with respect to the bulk values for C_2C_1Im cation (D^+/D_{neat}^+) and TfO anion (D^-/D_{neat}^-), as a function of water mole fraction, (a) in the absence and (b) presence of 0.15 M $Zn(TfO)_2$.

Figure 3.8 shows the ^{19}F T_1 NMR relaxation time of TfO anion, as a function of water, in the presence of different Zn concentrations. It has been mention before that the addition of water, results in a minimum in the T_1 NMR relaxation, as a consequence of two competing effects. This means that the trend line of T_1 NMR relaxation, (**Figure 3.8**), is the sum of two lines (in the absence of Zn). The rate of T_1 NMR relaxation change can be indicated from the slopes of these lines. However, in the presence of zinc, the trend line of T_1 NMR relaxation, as a function of water, seems to be a sum of three lines. These three lines (or regimes) are clearer in the highest concentration of zinc, see **Figure 3.16** for clarity.

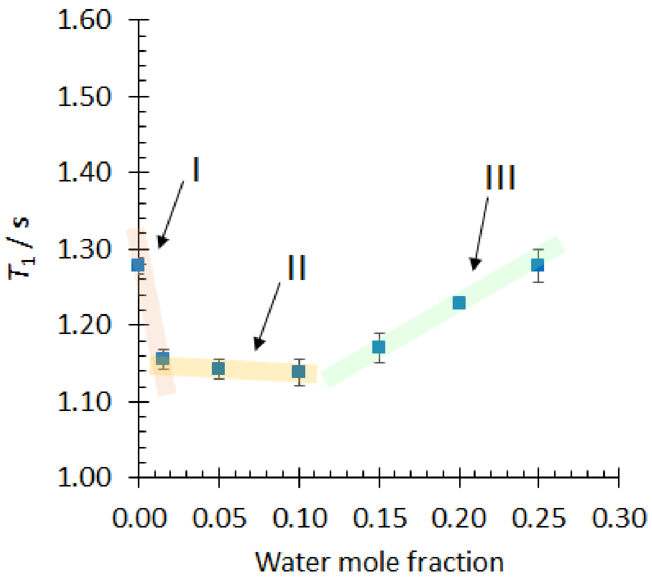

Figure 3.16: ^{19}F T_1 NMR Relaxation time for TfO anion in presence of 0.15 M $Zn(TfO)_2$, as a function of water, with a clarity of the three regimes.

At 0.15 M of zinc, in the first regime (I), an immediate reduction in ^{19}F T_1 NMR relaxation time of the anion is observed, when a small amount of water (χ_{water} < 0.015) is added. Water molecules in such low water content are embedded in the IL structure. Thus, T_1 reduction is attributed to an increase in the availability of H-bonds between water and [C_2C_1Im(TfO)] ions. In the second regime (II), by increasing water content, (0.015 < χ_{water} < 0.1), water molecules are associated with Zn, replacing the coordinated TfO anions. Thus, the T_1 relaxation of TfO anions slightly affected by the addition of water. The slope of the second line (II) suggests that the rate of zinc speciation changes is slow. Finally, in the third regime (III), when water content reaches (χ_{water} > 0.1), at this hydration level, all zinc ions are completely solvated by water molecules. T_1 of TfO anion increases as a result of lower viscosity. This give a good agreement with diffusion data, (**Figure 3.15**), which suggests from $D^{-}/D_{\text{neat}}^{-}$, that the addition of water do not affects D^{-} until all zinc ions are solvated by water molecules, which is around 0.1 mole fraction of water.

3.5 Conclusions

NMR measurements of relaxation and diffusion have been used to investigate the effect of water and Zn on the physical and chemical properties of $[C_2C_1Im(TfO)]$ ionic liquid. The addition of $Zn(TfO)_2$, initiates the formation of a large zinc complex, $[Zn(TfO)_4]^{2-}$. However, when water is added, Zn ions prefer to associates with water molecules rather than the TfO anions. ^{19}F T_1 NMR relaxation data have shown that this speciation change occurs gradually until all four coordinated TfO ions replaced with water. The addition of water results in a minimum in T_1 relaxation time of anion and cation, as a result of two effects, increasing the availability of H-bonds and lowers viscosity.

Normalized diffusion co-efficient ($D_{\text{ion}}/D_{\text{neat}}$) is used to analyze the excess ionic diffusivity, to understand how zinc and water affect the diffusional properties on a molecular level. At all water concentrations, D^{-} exceeds D^{+}, indicating that TfO anions interact more with water than the C_2C_1Im cation. In the presence of Zn, when a small amount of water is added ($\chi_{\text{water}} < 0.1$), D^{-} is almost constant and lower than D^{+}. This indicates that, at this hydration level, water molecules interact more with Zn rather than TfO anion. As water content increases ($\chi_{\text{water}} > 0.1$), D^{-} start to increase and exceeds D^{+}, indicating that TfO anion has interacted with water. This means that TfO anions would not associate with water until all zinc ions are solvated by water molecules.

Different speciation and interactions have been proposed of the [C_2C_1Im(TfO)] ionic liquid, in presence and absence of Zn at different hydration levels. However, molecular modelling work needs to be undertaken to have a better understanding of the speciation and their interactions. To the best of our knowledge, the effect of such a small amount of water, (χ_{water} = 0.015 - 0.25), on the properties of [C_2C_1Im(TfO)] ionic liquid, in presence of Zn, have not been studied before.

Altogether, these NMR bulk measurements including spectroscopy, relaxation and diffusion provide information to have a better understanding of the ionic liquid structure in presence and absence of water and/or zinc. In addition, these NMR bulk measurement considers as a foundation for MRI, which benefit researchers who are interested in using such ionic liquid as an electrolyte for different zinc electrochemical technology. In chapter 5, MRI techniques have been used to visualize, *in operando*, zinc electroplating process using [C_2C_1Im(TfO)] ionic liquid, in the presence and absence of water.

3.6 References

1. Gelman, D.; Shvartsev, B.; Ein-Eli, Y., Challenges and Prospect of Non-aqueous Non-alkali (NANA) Metal–Air Batteries. Top. Curr. Chem. **2016,** 374, 82.
2. Zhong, C.; Deng, Y.; Hu, W.; Qiao, J.; Zhang, L.; Zhang, J., A review of electrolyte materials and compositions for electrochemical supercapacitors. Chem. Soc. Rev. **2015,** 44, 7484-7539.
3. Armand, M.; Endres, F.; MacFarlane, D. R.; Ohno, H.; Scrosati, B., Ionic-liquid materials for the electrochemical challenges of the future. Nat. Mater. **2009,** 8, 621-629.
4. Galiński, M.; Lewandowski, A.; Stępniak, I., Ionic liquids as electrolytes. Electrochim. Acta **2006,** 51, 5567-5580.
5. Liu, Z.; Abedin, S. Z. E.; Endres, F., Electrodeposition of zinc films from ionic liquids and ionic liquid/water mixtures. Electrochim. Acta **2013,** 89, 635-643.
6. Liu, Z.; Cui, T.; Lu, T.; Shapouri Ghazvini, M.; Endres, F., Anion Effects on the Solid/Ionic Liquid Interface and the Electrodeposition of Zinc. J. Phys. Chem. C **2016,** 120, 20224-20231.
7. Liu, Z.; Elbasiony, A. M.; Zein El Abedin, S.; Endres, F., Electrodeposition of Zinc–Copper and Zinc–Tin Films and Free-Standing Nanowire Arrays from Ionic Liquids. Chem. Electro. Chem. **2015,** 2, 389-395.
8. Liu, Z.; El Abedin, S. Z.; Endres, F., Raman and FTIR spectroscopic studies of 1-ethyl-3-methylimidazolium trifluoromethylsulfonate, its mixtures with water and the solvation of zinc ions. Chem. phys. chem. **2015,** 16, 970-7.
9. Liu, Z.; Pulletikurthi, G.; Lahiri, A.; Cui, T.; Endres, F., Suppressing the dendritic growth of zinc in an ionic liquid containing cationic and anionic zinc complexes for battery applications. Dalton Trans. **2016,** 45, 8089-8098.
10. He, W.; Shen, L.; Shi, Z.; Gao, B.; Hu, X.; Xu, J.; Wang, Z., Zinc Electrodeposition from Zinc Oxide in the Urea/1-ethyl-3-methylimidazolium Chloride at 353 K. Electrochemistry **2016,** 84, 872-877.
11. Simons, T. J.; Torriero, A. A. J.; Howlett, P. C.; MacFarlane, D. R.; Forsyth, M., High current density, efficient cycling of Zn2+ in 1-ethyl-3-methylimidazolium dicyanamide ionic liquid: The effect of Zn2+ salt and water concentration. Electrochem. Commun. **2012,** 18, 119-122.
12. Liu, Z.; Cui, T.; Pulletikurthi, G.; Lahiri, A.; Carstens, T.; Olschewski, M.; Endres, F., Dendrite-Free Nanocrystalline Zinc Electrodeposition from an Ionic Liquid Containing Nickel Triflate for Rechargeable Zn-Based Batteries. Angew. Chem. Int. Ed. **2016,** 55, 2889-2893.
13. Giffin, G. A., Ionic liquid-based electrolytes for "beyond lithium" battery technologies. J. Mater. Chem. A **2016,** 4, 13378-13389.
14. Mainar, A. R.; Iruin, E.; Colmenares, L. C.; Kvasha, A.; de Meatza, I.; Bengoechea, M.; Leonet, O.; Boyano, I.; Zhang, Z.; Blazquez, J. A., An overview of progress in electrolytes for secondary zinc-air batteries and other storage systems based on zinc. J. Energy Storage **2018,** 15, 304-328.
15. Liu, Z.; El Abedin, S. Z.; Endres, F., Electrochemical and spectroscopic study of Zn(ii) coordination and Zn electrodeposition in three ionic liquids with the trifluoromethylsulfonate

anion, different imidazolium ions and their mixtures with water. Phys. Chem. Chem. Phys. **2015,** 17, 15945-15952.

16. Singh, V. V.; Nigam, A. K.; Batra, A.; Boopathi, M.; Singh, B.; Vijayaraghavan, R., Applications of Ionic Liquids in Electrochemical Sensors and Biosensors. Int. j. electrochem. **2012,** 2012, 165683.

17. Ma, C.; Laaksonen, A.; Liu, C.; Lu, X.; Ji, X., The peculiar effect of water on ionic liquids and deep eutectic solvents. Chem. Soc. Rev. **2018,** 47, 8685-8720.

18. Trequattrini, F.; Celeste, A.; Capitani, F.; Palumbo, O.; Cimini, A.; Paolone, A., Temperature and Pressure Dependence of the Infrared Spectrum of 1-Ethyl-3-Methylimidazolium Trifluoromethanesulfonate Ionic Liquid. Appl. Sci. **2020,** 10, 4404-4415.

19. Tsuzuki, S.; Tokuda, H.; Hayamizu, K.; Watanabe, M., Magnitude and Directionality of Interaction in Ion Pairs of Ionic Liquids: Relationship with Ionic Conductivity. J. Phys. Chem. B **2005,** 109, 16474-16481.

20. Yaghini, N.; Nordstierna, L.; Martinelli, A., Effect of water on the transport properties of protic and aprotic imidazolium ionic liquids - an analysis of self-diffusivity, conductivity, and proton exchange mechanism. Phys. Chem. Chem. Phys. **2014,** 16, 9266-9275.

21. Menjoge, A.; Dixon, J.; Brennecke, J. F.; Maginn, E. J.; Vasenkov, S., Influence of Water on Diffusion in Imidazolium-Based Ionic Liquids: A Pulsed Field Gradient NMR study. J. Phys. Chem. B **2009,** 113, 6353-6359.

22. Abbott, A. P.; McKenzie, K. J., Application of ionic liquids to the electrodeposition of metals. Phys. Chem. Chem. Phys. **2006,** 8, 4265-4279.

23. Chang, T. M.; Dang, L. X.; Devanathan, R.; Dupuis, M., Structure and Dynamics of N,N-Diethyl-N-methylammonium Triflate Ionic Liquid, Neat and with Water, from Molecular Dynamics Simulations. J. Phys. Chem. A **2010,** 114, 12764-12774.

24. Abbott, A. P.; McKenzie, K. J., Application of ionic liquids to the electrodeposition of metals. Phys. Chem. Chem. Phys. **2006,** 8, 4265-79.

25. Umecky, T.; Takamuku, T.; Matsumoto, T.; Kawai, E.; Takagi, M.; Funazukuri, T., Effects of dissolved water on Li+ solvation in 1-ethyl-3-methylimidazolium bis(trifluoromethanesulfonyl)amide ionic liquid studied by NMR. J. Phys. Chem. B **2013,** 117, 16219-16226.

26. Claridge, T. D. W., High-Resolution NMR Techniques in Organic Chemistry. Second ed.; Elsevier: Oxford, UK, 2009.

27. KaleidaGraph Synergy Software: United States.

28. Meiboom, S.; Gill, D., Modified Spin-Echo Method for Measuring Nuclear Relaxation Times. Rev. Sci. Instrum. **1958,** 29, 688-691.

29. Stejskal, E. O.; Tanner, J. E., Spin Diffusion Measurements: Spin Echoes in the Presence of a Time-Dependent Field Gradient. J. Chem. Phys. **1965,** 42, 288.

30. Singh, D. K.; Rathke, B.; Kiefer, J.; Materny, A., Molecular Structure and Interactions in the Ionic Liquid 1-Ethyl-3-methylimidazolium Trifluoromethanesulfonate. J. Phys. Chem. A **2016,** 120, 6274-6286.

31. Allen, J. J.; Bowser, S. R.; Damodaran, K., Molecular interactions in the ionic liquid emim acetate and water binary mixtures probed via NMR spin relaxation and exchange spectroscopy. Phys. Chem. Chem. Phys. **2014,** 16, 8078-8085.

Chapter 4 Probing the influence of Zn and water on solvation and dynamics in ethaline and reline deep eutectic solvents by ^{1}H nuclear magnetic resonance.

4.1 Introduction

In recent years, there has been increasing interest in the use of deep eutectic solvents (DESs) as a replacement for aqueous and organic electrolytes in many electrochemical applications, including metal electrodeposition[1-3], metal electropolishing[4-5] and batteries[6]. This increasing interest largely arises from their high chemical stability, wide potential window, low flammability and volatility. Another important benefit of DESs is that they can be formed by mixing, typically, inexpensive, low-toxicity, biodegradable components, and, hence, also offer economic and environmental benefits.[7-9]

A widely investigated class of DES is based on the quaternary ammonium salt choline chloride (ChCl).[6, 10-11] This class includes ethaline, which is a mixture of 1:2 molar ratio of ChCl and ethylene glycol (EG), and reline, a 1:2 molar ratio mixture of ChCl and urea (U).[12] While multiple interactions contribute to the intermolecular network within DESs, including van der Waals interactions, hydrogen bonding and/or ionic bonding,[13] it is hydrogen bonding that is considered to be the primary cause of their melting point depression and physicochemical properties, such as viscosity and conductivity.[8] Ethaline and reline have been investigated as more sustainable electrolytes in the electrodeposition of Zn, as an anti-corrosion layer.[3, 11, 14-15] However, the deposited zinc have been found to have different morphologies, depending on the DES used, which has been attributed to differences in the hydrogen bond network between ethaline and reline systems[15] and zinc ion species, which play an important role in the mechanisms of deposition.[3] Abbott et al. proposed that zinc species in both ethaline and reline systems is the $[ZnCl_4]^{2-}$.[15] Reline has also been investigated as a novel electrolyte for rechargeable zinc-batteries.[6] Reversible plating/stripping of zinc species has been observed, without hydrogen evolution or the formation of a passivation layer on the zinc electrode.[6] However, despite this initial interest in these DES systems for these Zn-electrochemical applications, there are several challenges currently preventing their commercialisation. Primarily, these are associated with poor physical properties, such as their typically high viscosity, and, hence, lower their conductivity.[12] Also, a lack of understanding of the species formed has limited the optimisation of DES formulations.[16]

In order to overcome these limitations in physical properties, the addition of water has been investigated.[12, 17-20] Computer simulations have revealed that the addition of water to ethaline or reline DESs decrease the number of hydrogen bonds formed and consequently lowers the viscosity of both DES systems.[20] However, as more water is added, it has been observed[12] that ChCl-based DESs start to lose their DES structure and form aqueous solutions, above a 1:1 mole equivalent of water:chloride. This transition is also reported to change the electrochemical properties of ChCl-based DESs, in particular, by narrowing their potential window.[21-22] Cyclic voltammetry (CV) experiments have shown that reline retains a wide potential window until the amount of added water reaches 9 wt.% .[21] The effects of adding water to reline[21] and ethaline[22], for electroplating Cu[22] and Ni[21] have been investigated. It has been observed that the addition of 15 wt.% water in ethaline, for Cu electroplating, results in a reduction in the ethaline viscosity without reducing the wide potential of the electolyte.[22] Adding 6 wt.% of water to reline, for nickel electroplating, lowers the reline viscosity, and this suppresses the nickel dendritic growth, resulting in a smooth dense nickel deposit.[21]

The study of speciation and solvation and the effect of additives, such as water, on the chemical and physical properties of DES have been investigated computationally, using quantum mechanics (QM) simulation[18, 23], and experimentally using nuclear magnetic resonance (NMR)[24], Fourier-transform infra-red (FTIR) and Raman spectroscopies[25]. In these studies, it has been proposed that the addition of water affects the hydrogen bond network of DESs, by forming new hydrogen bonds between water and DESs components, which affects the properties of the DESs, such as viscosity.[18, 23] Moreover, it has been observed that the number of hydrogen bonds formed between water and EG ,in ethaline, are comparatively higher than those formed between water and U in the reline system.[25] In the case of reline, while water can hydrogen bond with ChCl and U[19, 23], it has been found that water molecules also occupy the interstices within the hydrogen bond network, reducing the number of hydrogen bonds between water and ChCl or U.[25] Following investigation by diffusion NMR, D'Agostino *et al.*[12] proposed that, in the presence of 20 wt.% of water, ethaline forms a homogenous ethaline-water mixture, while reline forms a non-homogeneous reline-water mixture with a rich-water region. Zinc speciation in ethaline and reline has been studied using mass spectrometry.[26] However, as this is typically an *ex situ* technique, it is not able to provide information on speciation during electrochemical processes. Non-invasive, *in situ* techniques have been explored, which are able to provide information on speciation and dynamics of metal ions in DES electrolytes.[26] Furthermore, there is growing interest in developing *operando* techniques for observing speciation and dynamics, *in situ* and in real time, under working conditions. Such techniques have been demonstrated using ^{1}H NMR T_1 relaxation times to determine Zn speciation in aqueous electrolytes during Zn corrosion and discharging of a Zn-battery.[27-28]

In this chapter, a range of ethaline and reline DESs have been investigated, in the absence and presence of Zn (0 - 0.3 M) and water (0 - 29 wt.%). Molecular interactions and dynamics have been investigated using one-dimensional (1D) ^{1}H NMR and two-dimensional (2D) ^{1}H-^{1}H nuclear Overhauser exchange (NOESY) and exchange (EXSY) NMR spectroscopy. The influence of zinc and water, on the mobility and microstructure with each DES system, has been investigated using ^{1}H NMR T_1 relaxation time and diffusion measurements. We demonstrate that the zinc species are different in ethaline and reline, and the interaction between zinc and water is also different in ethaline and reline.

4.2 Experimental Details

4.2.1 Materials and Samples Preparation

Choline chloride (ChCl, 99 %), ethylene glycol (EG, 99.8 %), urea (U, 99.9%) and zinc chloride ($ZnCl_2$, 99.99 %) were supplied by Sigma-Aldrich. All components were used without further purification, but dried in a vacuum oven under reduced pressure (100 mbar), at 80 °C (ChCl, EG and U) or at 120 °C ($ZnCl_2$), for a minimum of 24 hours and were stored in a glove-box under argon atmosphere. In a glove-box, ethaline was prepared by mixing ChCl and EG in a 1:2 molar ratio and reline was prepared by mixing ChCl and U in a 1:2 molar ratio before sonication and heating to 60 °C until homogenous clear colourless liquids were formed. Solutions of zinc in ethaline or reline were prepared in a glove-box by dissolving dry $ZnCl_2$ in either ethaline or reline, over a range of $ZnCl_2$ concentrations (0.1, 0.2 and 0.3 M in ethaline and 0.3 M in reline) at 25 °C. A range of concentrations of water were prepared by adding water (Nanopure filtered, resistivity 18 MΩ cm), to ethaline and reline, in the presence and absence of 0.3 M $ZnCl_2$. Solutions of water in ethaline, at concentrations of 2.7, 5.5, 8.3, 16 and 29.2 wt.%, were prepared by adding 26, 52, 79, 151 and 277 µl of water, respectively, to 850 µl of ethaline. Solutions of water in reline, at concentrations of 5.5, 8.3 and 26.2 wt.%, were prepared by adding 58.5, 88 and 279 µl of water, respectively, to 850 µl of reline. Samples were put, immediately after preparation, into 5 mm Wilmad® NMR tubes fitted with J Young valves, to prevent the absorption of additional water. NMR measurements were performed < 12 h after sample preparation. The amount of water in each sample was determined using ^1H NMR spectroscopy.

4.2.2 NMR Measurements

NMR data were collected on a Bruker AVANCE III HD 300 spectrometer equipped with a 7 T vertical wide-bore superconducting magnet, operating at a proton resonance frequency of 300.13 MHz, with a 10 mm ^1H diff30 radiofrequency (rf) coil. NMR experiments were performed at 293 ± 0.3 K, controlled by the temperature of the water-cooled gradient coils. The 90° rf pulse was calibrated for each sample and found to be 20 ± 1 µs.

^1H NMR spectra were acquired using a pulse-acquire sequence, with a repetition time of 6 s. The chemical shift of peaks were calibrated to an external reference of TMS in deuterated chloroform which was put in a 10 mm NMR tube with 5 mm NMR tube inside. 2D ^1H-^1H NOESY experiments were acquired using the sequence, [$90^\circ - \tau_1 - 90^\circ - \tau_{\mathrm{mix}} - 90^\circ$ – acq], with 256 point in the F_1 direction and 2048 in the F_2 direction, with a repetition time of 2 s, 16 signal averages and 16 dummy scans. The mixing time, τ_{mix}, was increased from 0 to 300 ms, over a series of six experiments. Proton exchange rates (k_{ex}) were calculated[29], by fitting, in *Kaleidagraph*[30], the signal intensity of exchange peaks (I_{AB} and I_{BA}), as a function of mixing time (τ_{mix}), to (**Equation 2.13**). In the fitting, an average value of I_{AB} and I_{BA} was used. Exchange peaks were identified as having the same phase as the diagonal peaks, which, in this study, are plotted positively. Cross-peaks arising from the nOe have a phase depending on the molecular size of species and viscosity of the solvent.[31] In the case of small molecules in low viscosity DES, where tumbling rates are faster, the nOe cross-peaks are expected to have the opposite sign to diagonal peaks and are negative where diagonal peaks are positive. For molecules in high viscosity solvents, where molecular tumbling is slow, the nOe cross-peaks are expected to be positive, where diagonal peaks are also positive.

Spin-lattice (T_1) NMR relaxation times were measured using an inversion recovery experiment[31], [$180^\circ - \tau - 90^\circ$– acq]$_n$, with a repetition time of 6 s and 8 signal averages. A series of spectra (n = 12) were collected with logarithmically spaced time delays, τ, ranging from 5×10^{-6} s to 6 s. The average T_1 relaxation times were determined by fitting the normalised signal intensity ($I_{(\tau)}/I_{(0)}$), as a function of time, to (**Equation 2.5)** using *Kaleidagraph*[30] software. Spin-spin (T_2) NMR relaxation times were measured using Carr Purcell Meiboom Gill (CPMG)[32] sequence, [$90^\circ - (\tau - 180^\circ - \tau)_m$ – acq]$_n$. A series of spectra (n = 12) were collected with a repetition time of 6 s, a delay (τ) of 0.001 s, and m value varied from 0 to 1024. The average T_2 relaxation times were determined by fitting the normalised signal intensity ($I_{(2\tau)}/I_{(0)}$), as a function of time, to (**Equation 2.8**) using *Kaleidagraph*[30] software.

Self-diffusion co-efficients (D) were measured using a pulsed gradient stimulated echo (PGSTE) sequence[31] with 16 gradient steps. Diffusion measurements of dry ethaline samples were collected with a maximum gradient ($\boldsymbol{G}_{\text{max}}$) of 300 G cm^{-1}, pulse duration (δ) of 2 ms, observation time (Δ) of 60 ms, and repetition time of 2 s. Diffusion measurements of dry reline samples were collected using $\boldsymbol{G}_{\text{max}}$ = 600 G cm^{-1}, δ = 2 ms, Δ = 100 ms, with a repetition time of 2 s. Diffusion measurements for ethaline and reline systems containing water were collected using $\boldsymbol{G}_{\text{max}}$ = 300 G cm^{-1}, δ = 2 ms, Δ = 30 ms, and a repetition time of 4 s. The average self-diffusion co-efficients (D) were determined by fitting the normalised signal intensity as a function of gradient strength, ($I_{(\mathbf{G})}/I_{(0)}$), to the Stejskal–Tanner[33] (**Equation 2.11)** using *Kaleidagraph*[30] software. Where a single diffusion co-efficient was not sufficient to fit the data, fitting to a bi-exponential function was performed.

4.3 Results

Figure 4.1 shows the ^{1}H NMR spectra for dry ethaline and reline DESs, along with the molecular structures and proton labelling scheme of constituent species in each DES. The broad line widths observed for peaks in the ^{1}H NMR spectrum of reline are indicative of the higher viscosity for reline compared to ethaline. The chemical shift values for dry ethaline and reline peaks are listed in **Table 4.1**.

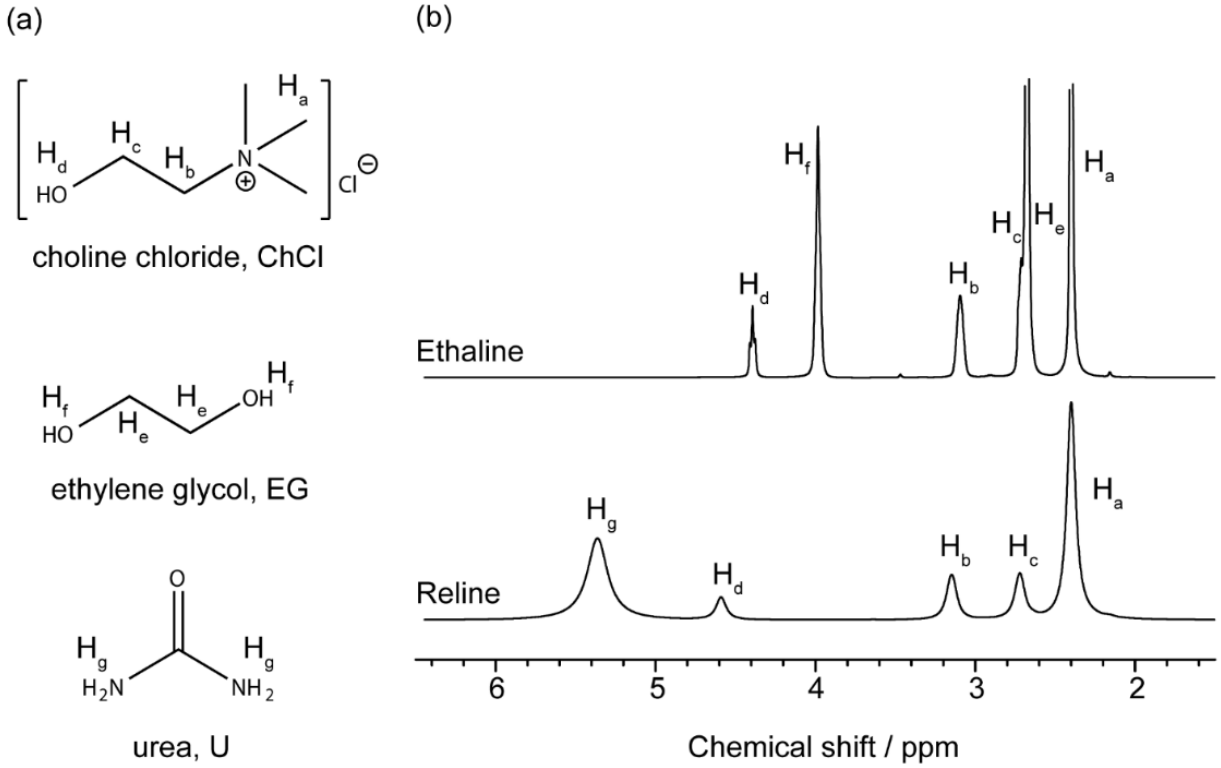

Figure 4.1: a) Molecular structures for the constituent species of ethaline (1ChCl:2EG) and reline (1ChCl:2U) with proton numbering scheme, and b) ^{1}H NMR spectra for pure dry ethaline and reline systems, at 293 K.

Table 4.1: ^{1}H NMR chemical shifts of neat dry ethaline and reline DESs. The chemical shift was calibrated to an external reference of TMS in deuterated chloroform which was put in a 10 mm NMR tube with 5 mm NMR tube inside.[12, 34]

Species	**Proton atoms**		**^{1}H NMR chemical shift / ppm**	
			Ethaline	**Reline**
Choline chloride	N-(C**H**$_3$)$_3$	H$_a$	2.4	2.4
	N-C**H**$_2$	H$_b$	3.1	3.15
	C**H**$_2$-OH	H$_c$	2.7	2.7
	CH$_2$-O**H**	H$_d$	4	4.6
Ethylene glycol	C**H**$_2$-OH	H$_e$	2.67	-
	CH$_2$-O**H**	H$_f$	4.4	-
Urea	-N**H**$_2$	H$_g$	-	5.36

^{1}H NMR spectra for dry ethaline and reline, with increasing ZnCl$_2$ concentration, are shown in **Figure 4.2**. For both reline and ethaline, no visible change in viscosity was observed upon the addition of zinc. This observation is consistent with the ^{1}H NMR spectra in **Figure 4.2**, which do not show a change in linewidth for the peaks of the non-exchanging protons (H$_a$, H$_b$, H$_c$ and H$_e$). In the ethaline system, the line widths for hydroxyl protons in choline cation (Ch$^+$) and EG (H$_d$ and H$_f$ respectively) are observed to increase gradually, as the concentration of Zn increases. This is matched by a slight upfield shift of the peak for the hydroxyl proton in Ch$^+$ (H$_d$). However, in the reline system, the line width and chemical shift for the H$_d$ peak do not appear to be affected by the addition of zinc.

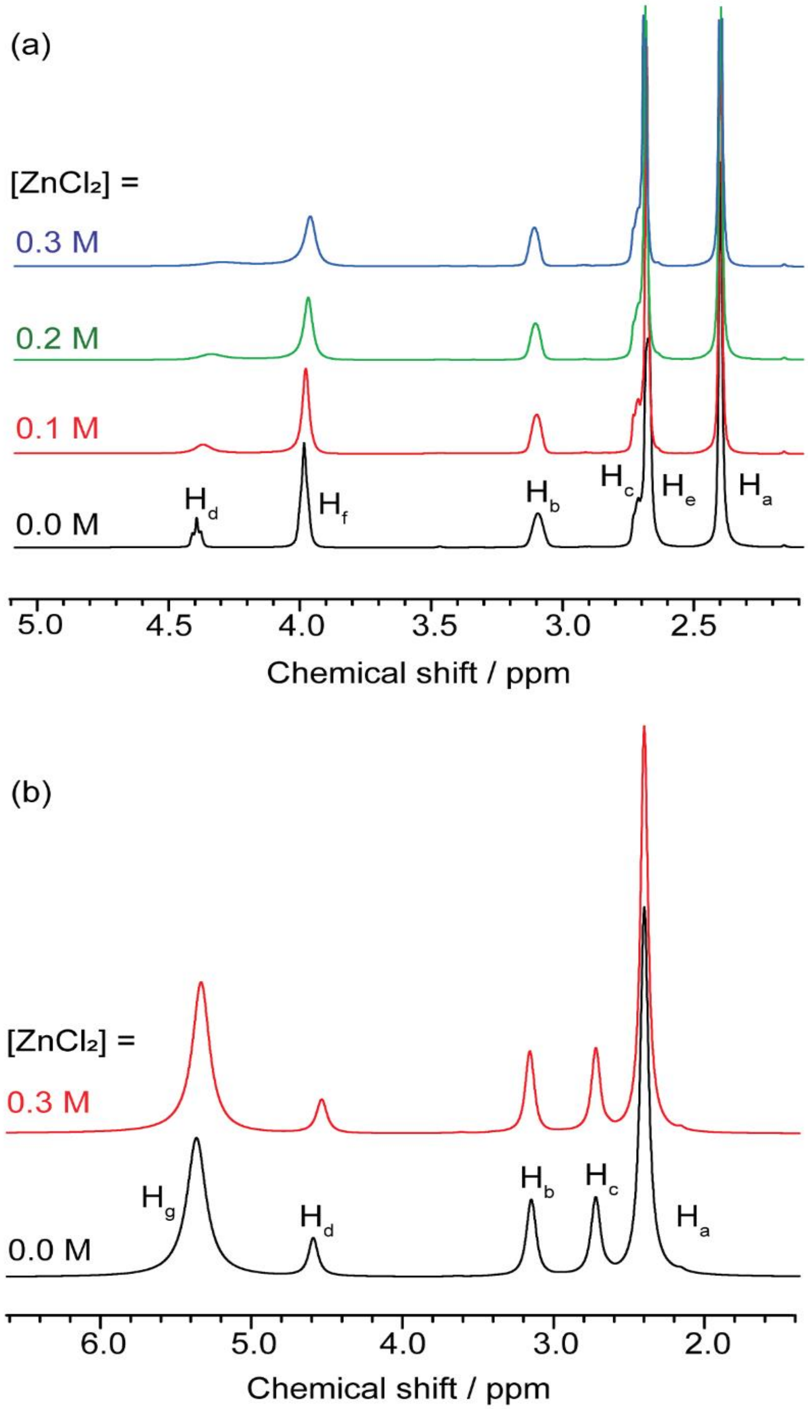

Figure 4.2: A series of ^{1}H NMR spectra for dry a) ethaline and b) reline as a function of $ZnCl_2$ concentration, at 293 K. Molecular structures and numbering scheme of peak assignments were presented in Figure 4.1.

Figure 4.3 shows ^{1}H NMR spectra for ethaline, in the presence and absence of Zn and water. There is a gradual shift for all hydroxyl proton peaks (H_d, H_f and H_w) downfield, as the water content increases. Also, the addition of water narrows the line width for (H_a, H_b, H_c and H_e) peaks, irrespective of whether Zn is present or not. However, the presence of zinc broadens the H_d, H_f and H_w peaks. **Figure 4.4** shows ^{1}H NMR spectra for reline, in the presence and absence of Zn and water. The presence of Zn does not appear to have a significant effect on the spectra. However, the presence of water leads to a significant reduction in line width of the urea peak (H_g), which also shifts upfield as the water content increases. The water peak (H_w) shifts gradually to higher chemical shift, as water content increases. As the water content increases, both in the presence and absence of Zn, there is a slight reduction in the line width of the H_a, H_b, H_c and H_g peaks. The addition of water broadens, and slightly shifts down field, the hydroxyl proton in Ch^+ (H_d). At the highest water content, the H_d peak overlaps completely with H_w peak, in the absence of Zn (**Figure 4.4, a**), whereas in the presence of Zn (**Figure 4.4, b**), the H_d peak remains at 4.6 ppm. However, the presence of zinc affects the line width of H_d and H_w peaks, which become narrower in the presence of Zn.

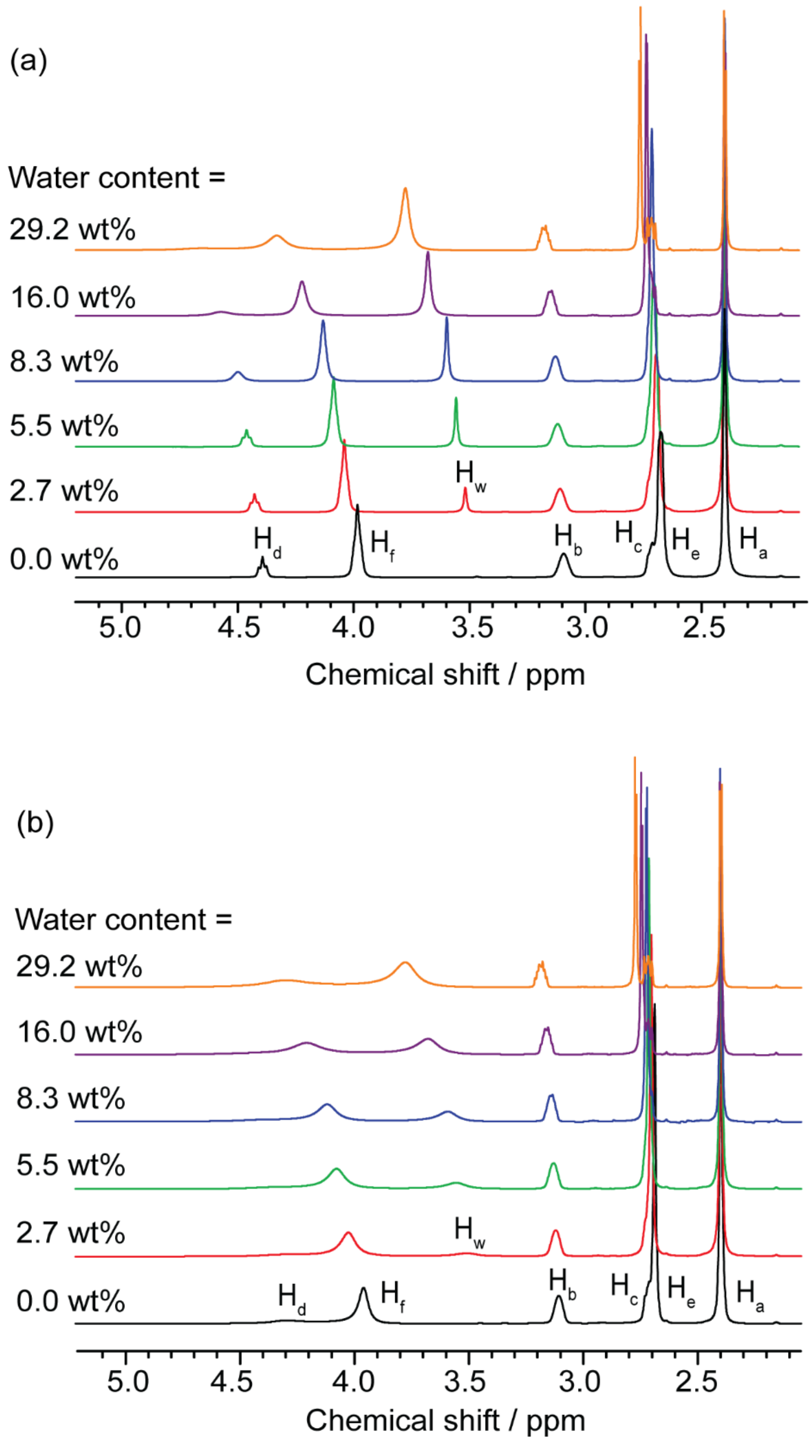

Figure 4.3: A series of ^{1}H NMR spectra for ethaline system (a) in the absence and (b) presence of 0.3 M $ZnCl_2$ as a function of water content (H_w), at 293 K. Molecular structures and numbering scheme of peak assignments were presented in Figure 4.1.

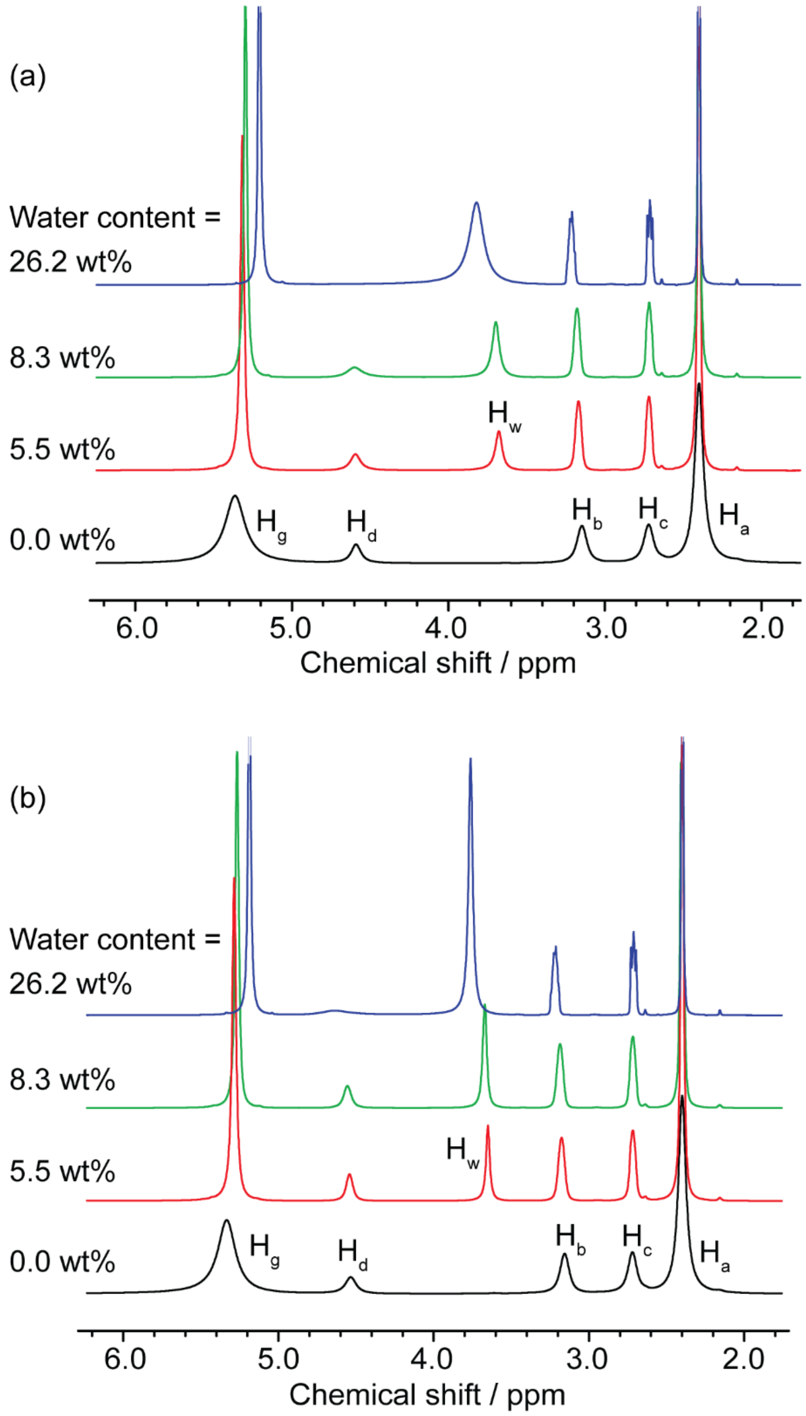

Figure 4.4: A series of ^1H NMR spectra for reline system (a) in the absence and (b) presence of 0.3 M $ZnCl_2$ as a function of water content (H_w), at 293 K. Molecular structures and numbering scheme of peak assignments were presented in Figure 4.1.

Figure 4.5 shows 2D NOESY spectra for dry ethaline, in the presence and absence of $ZnCl_2$. In the absence of Zn, intense exchange (positive) peaks are observed between the hydroxyl protons of Ch^+ and EG (H_d and H_f) (**Figure 4.5, a**). The hydroxyl proton peaks, and exchange peaks, broaden in the presence of Zn (**Figure 4.5, b**), indicating increased exchange. 2D NOESY spectra for ethaline with 8.3 wt.% water, in the presence and absence Zn, are shown in **Figure 4.6**. Exchange peaks are observed between water (H_w) and the hydroxyl protons in Ch^+ and EG (H_d and H_f). In the presence of Zn, however, these exchange peaks are broader. In addition to the exchange peaks, nOe (negative) cross-peaks are also observed between the other protons in EG and Ch^+, which appear to become less intense in the presence of Zn.

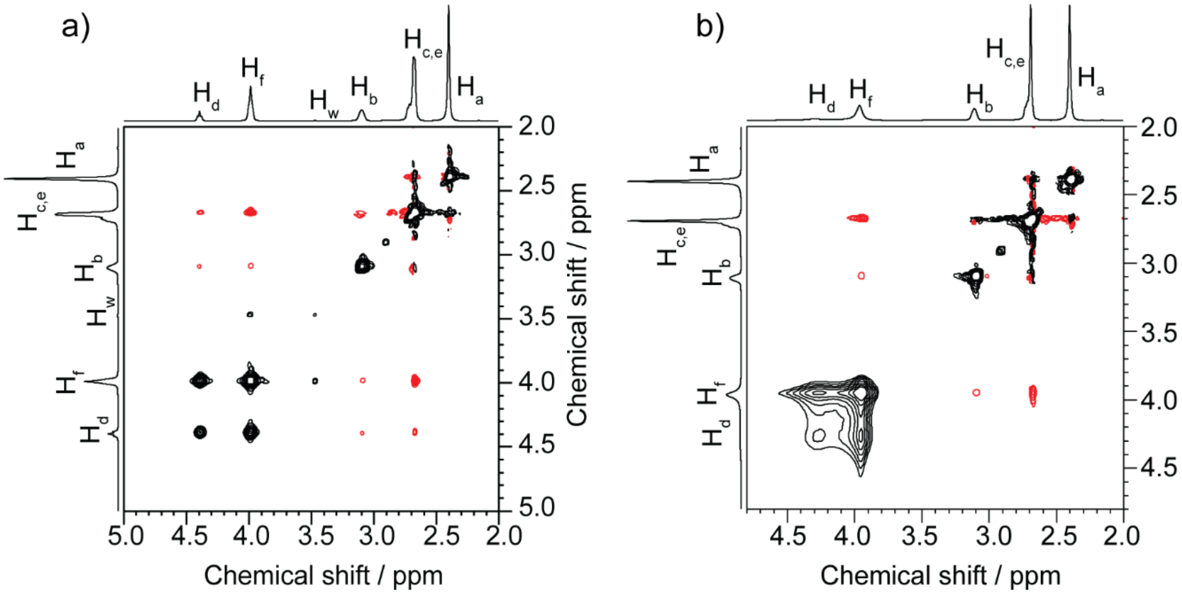

Figure 4.5: ^1H-^1H NOESY NMR spectra for dry ethaline samples a) in the absence and b) presence of 0.3 M $ZnCl_2$, for a mixing time τ_m 300 ms. Positive peaks are black, negative peaks are red.

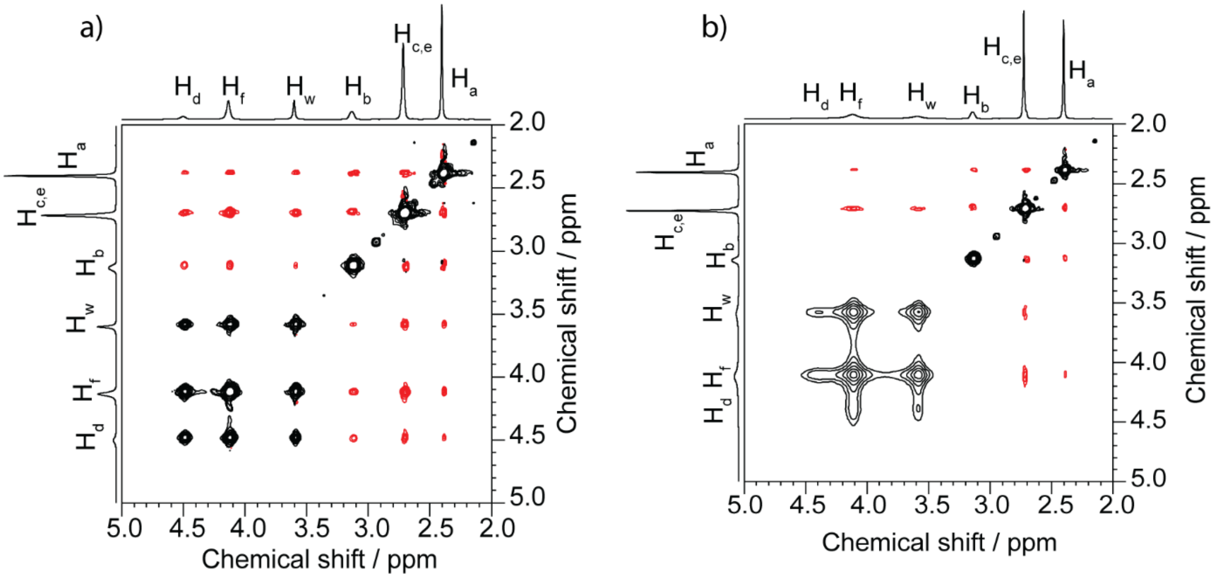

Figure 4.6: ^1H-^1H NOESY NMR spectra for ethaline samples with addition of 8.3 wt.% water a) in the absence and b) presence of 0.3 M $ZnCl_2$, for a mixing time τ_m 300 ms. Positive peaks are black, negative peaks are red.

Figure 4.7, Figure 4.8, and **Figure 4.9** show 2D NOESY spectra for reline with 0, 8.3 and 26 wt.% water, respectively, in the presence and absence of $ZnCl_2$. The higher viscosity of reline at 0 and 8.3 wt.% water has led to all cross-peaks being positive .[35] In the dry reline system (**Figure 4.7**), cross-peaks peaks are observed between the hydroxyl protons in Ch^+ (H_d) and the amide protons in U (H_g). However, as the viscosity of this system is high, it is not possible to identify whether these cross-peaks arise from exchange or nOe interactions. In the presence of water (**Figure 4.8**), no cross-peaks are observed between these protons, indicating no exchange nor spatial proximity. The spectra in **Figure 4.8** show cross-peaks between H_g protons and the aliphatic protons in Ch^+ (H_a, H_b and H_c). These are negative and hence arise from the nOe, indicating their close spatial-proximity. **Table 4.2** shows the proton exchange rates (k_{ex}), for both reline and ethaline, determined from the 2D ^{1}H-^{1}H NOESY spectra. Proton exchange is observed between the hydroxyl protons in Ch^+ (H_d) and water protons (H_w) in **Figure 4.8** and **Figure 4.9** This exchange appears to increase with increasing water concentration, resulting in a coalesced peak in the NOESY spectrum (**Figure 4.9**) and a cross peak between $H_{d,w}$ and the amide protons H_g.

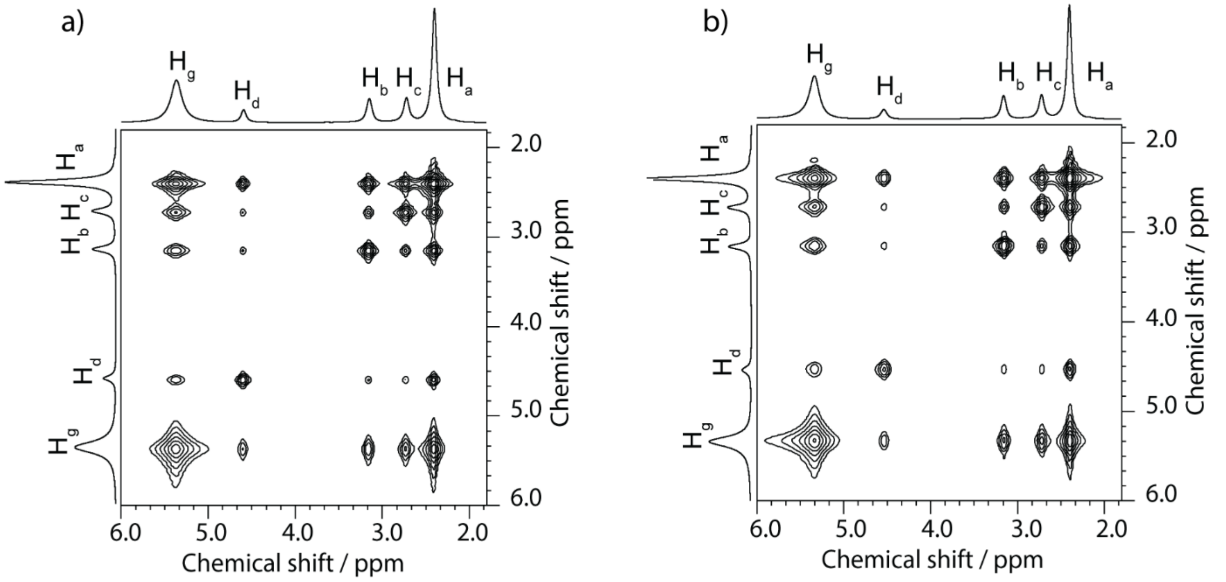

Figure 4.7: ^{1}H-^{1}H NOESY NMR spectra for dry reline samples a) in the absence and b) presence of 0.3 M $ZnCl_2$, for a mixing time τ_m 100 ms. All peaks are positive (black) and no negative peaks (red) are observed.

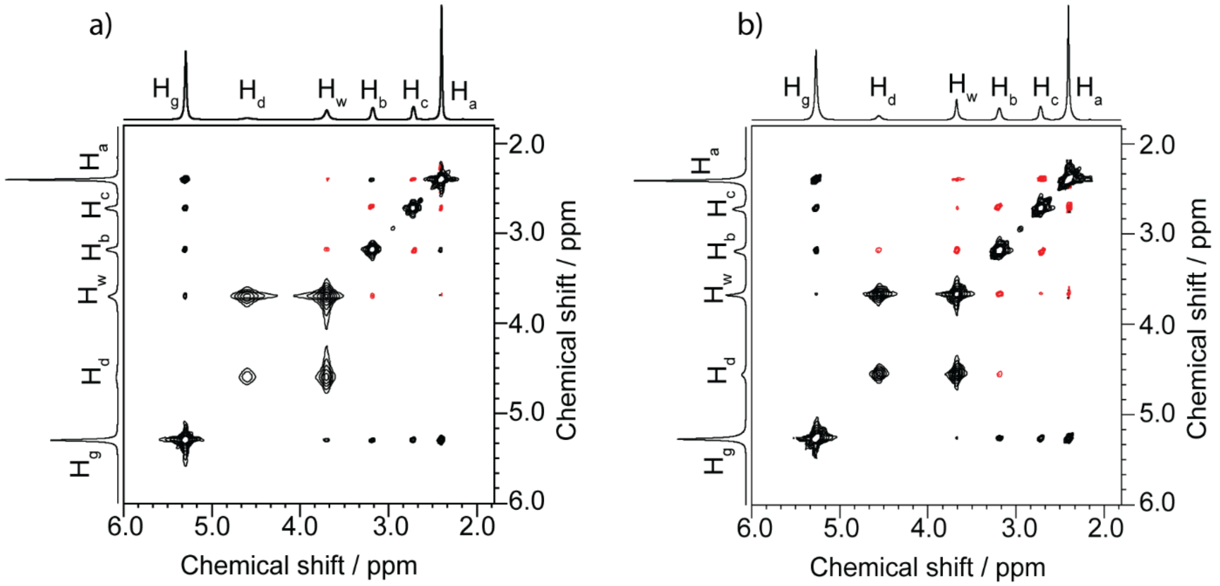

Figure 4.8: ^{1}H-^{1}H NOESY NMR spectra for reline samples with addition of 8.3 wt.% water a) in the absence and b) presence of 0.3 M $ZnCl_2$, for a mixing time τ_m 300 ms. Positive peaks are black, negative peaks are red.

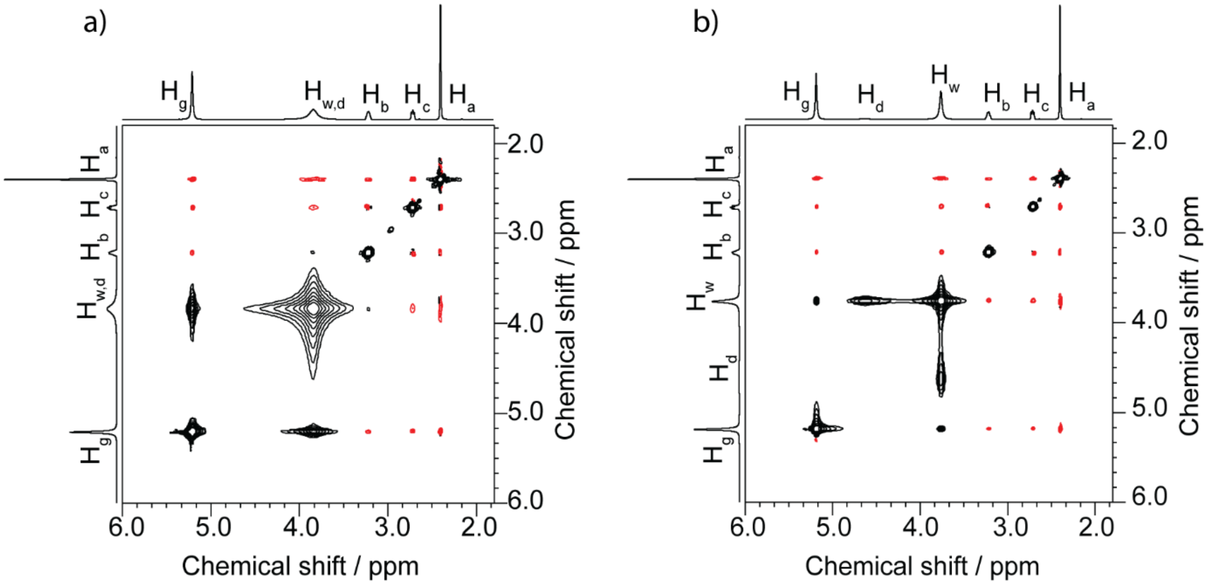

Figure 4.9: ^{1}H-^{1}H NOESY NMR spectra for reline samples with addition of 26 wt.% water a) in the absence and b) presence of 0.3 M $ZnCl_2$, for a mixing time τ_m 100 ms. Positive peaks are black, negative peaks are red.

Table 4.2: Proton exchange rates (k_{ex}) for ethaline and reline systems, at [Zn^{2+}] = 0 and 0.3 M, at different water concentrations, calculated using (**Equation 2.13**). Some of exchange rates could not determine due to overlap of peaks such as H_f-H_d of dry ethaline in presence of Zn, H_g-H_w does not shown here because its need higher mixing time range to get enough data to calculate their exchange rate.

Water wt. %	**[Zn^{2+}] = 0 M**	**[Zn^{2+}] = 0.3 M**
	Ethaline	
0	k_{ex} (H_f-H_d) = 11.36 s^{-1}	-
8.3	k_{ex} (H_f-H_d) = 8.66 s^{-1} k_{ex} (H_w-H_f) = 5.71 s^{-1} k_{ex} (H_w-H_d) = 1.03 s^{-1}	k_{ex} ($H_{d,f}$-H_w) = 77.8 s^{-1}
29	k_{ex} (H_f-H_d) = 7.96 s^{-1} k_{ex} (H_w-H_f) = 29.3 s^{-1} k_{ex} (H_w-H_d) = 10.8 s^{-1}	k_{ex} ($H_{d,f}$-H_w) = 124.8 s^{-1}
	Reline	
8.3	k_{ex} (H_d-H_w) = 77 s^{-1}	k_{ex} (H_d-H_w) = 24 s^{-1}

Diffusion co-efficients for choline cation, Ch^+, in dry ethaline and reline, are shown in **Table 4.3**. It can be seen that, Ch^+ has a lower mobility in reline than ethaline, as expected because of the higher viscosity of reline system. The diffusion coefficient for Ch^+ is be largely unaffected by the presence of zinc. However, in ethaline, the diffusion co-efficient for the hydroxyl (H_d) and methyl protons (H_a), in Ch^+, are the same in the absence of Zn, but are different in the presence of Zn.

Table 4.3: Diffusion co-efficients of Ch^+ alkyl protons (H_a) and Ch^+ hydroxyl protons (H_d) in dry ethaline and reline species in the absence and presence of $ZnCl_2$.

System	**Diffusion co-efficient / 10^{-11} m^2 s^{-1}**	
	H_a	**H_d**
Ethaline	1.92 ± 0.06	1.90 ± 0.07
Ethaline + 0.3 M $ZnCl_2$	1.76 ± 0.01	2.23 ± 0.07
Reline	0.056 ± 0.005	0.060 ± 0.001
Reline + 0.3 M $ZnCl_2$	0.059 ± 0.004	0.059 ± 0.002

Diffusion co-efficients for ethaline species, with increasing water content, in the absence and presence of $ZnCl_2$, are presented in **Table 4.4** and **Table 4.5**, respectively. These data show that diffusion co-efficients, for all species, increase with increasing water content. At lower concentration of water (≤ 8.3 wt %), two diffusion co-efficients are observed for water. However, at high concentration of water (29 wt %), only a single diffusion co-efficient is observed.

Table 4.4: Diffusion co-efficients of ethaline species, Ch^+ (H_a) and EG (H_e), as a function of water (H_w) in the absence of zinc.

Water wt.%	**Diffusion co-efficient / 10^{-11} m^2 s^{-1}, (contribution %)**		
	H_a	**H_e**	**H_w**
5.5	3.12 ± 0.01	5.46 ± 0.03	3.40 ± 0.08 (5 ± 0.02 %) 15.46 ± 0.38 (95 ± 0.08 %)
8.3	3.66 ± 0.01	6.33 ± 0.14	4.24 ± 0.02 (14 ± 1.1 %) 16.26 ± 0.31 (86 ± 0.3 %)
29.2	8.91 ± 0.07	14.61 ± 1.0	30.75 ± 0.46

Table 4.5: Diffusion co-efficients of ethaline species, Ch^+ (H_a) and EG (H_e), as a function of water (H_w) in the presence of 0.3 M $ZnCl_2$.

Water wt.%	**Diffusion co-efficient / 10^{-11} m^2 s^{-1}, (contribution %)**		
	H_a	**H_e**	**H_w**
5.5	2.91 ± 0.03	5.19 ± 0.01	1.52 ± 0.51 (13 ± 3.4 %) 14.22 ± 0.24 (87 ± 1.3 %)
8.3	3.54 ± 0.06	6.34 ± 0.2	3.47 ± 0.48 (56 ± 23.7 %) 14.22 ± 2.50 (44 ± 11.5%)
29.2	8.90 ± 0.45	16.24 ± 2.00	9.62 ± 0.54 (10.7 ± 2.6 %) 31.81 ± 0.56 (89.3 ± 1.7 %)

Diffusion co-efficients for Ch^+, U and water in reline with increasing water content, in the absence and presence of $ZnCl_2$, are presented in **Table 4.6** and **Table 4.7**, respectively. It can be seen that the diffusion co-efficient of both Ch^+ and U increases with the addition of water, as expected. Two diffusion co-efficients are observed for water for all water concentrations.

Table 4.6: Diffusion co-efficients of reline species, Ch^+ (H_a) and U (H_g) as a function of water (H_w) in the absence of zinc.

Water wt.%	**Diffusion co-efficient / 10^{-11} m^2 s^{-1}, (contribution %)**		
	H_a	**H_g**	**H_w**
5.5	0.60 ± 0.04	1.02 ± 0.07	0.94 ± 0.06 (20 ± 1.2 %) 4.57 ± 0.2 (80 ± 0.3 %)
8.3	1.18 ± 0.15	1.98 ± 0.23	1.77 ± 0.13 (13 ± 1.1 %) 7.84 ± 0.5 (87 ± 0.07 %)
26.2	9.26 ± 0.45	14.33 ± 0.61	12.41 ± 0.9 (3 ± 0.5 %) 37.55 ± 1.0 (97 ± 0.2 %)

Table 4.7: Diffusion co-efficients of reline species, Ch^+ (H_a) and U (H_g) as a function of water (H_w) in the presence of 0.3 M $ZnCl_2$.

Water wt.%	**Diffusion co-efficient / 10^{-11} m^2 s^{-1}, (contribution %)**		
	H_a	**H_g**	**H_w**
5.5	0.64 ± 0.03	1.12 ± 0.05	1.08 ± 0.12 (17 ± 0.4 %) 6.00 ± 0.15 (83 ± 0.4 %)
8.3	1.28 ± 0.09	2.19 ± 0.15	2.22 ± 0.09 (11.7 ± 0.4 %) 9.64 ± 0.42 (88.3 ± 0.6 %)
26.2	10.01 ± 0.25	15.67 ± 0.7	10.11 ± 0.06 (23.7 ± 1.6 %) 32.8 ± 0.3 (75.3 ± 2 %)

Figure 4.10 shows the T_1 relaxation times for Ch^+, in ethaline and reline, in the presence and absence of zinc and water. It can be seen that for ethaline, the T_1 NMR relaxation time for the H_a proton in Ch^+ increases, monotonically, with water content, but with a slight discontinuity around 8 wt.% of water. However, for reline, the T_1 relaxation time for the H_a protons in Ch^+ decreases on addition of water, but then increases with increasing water content.

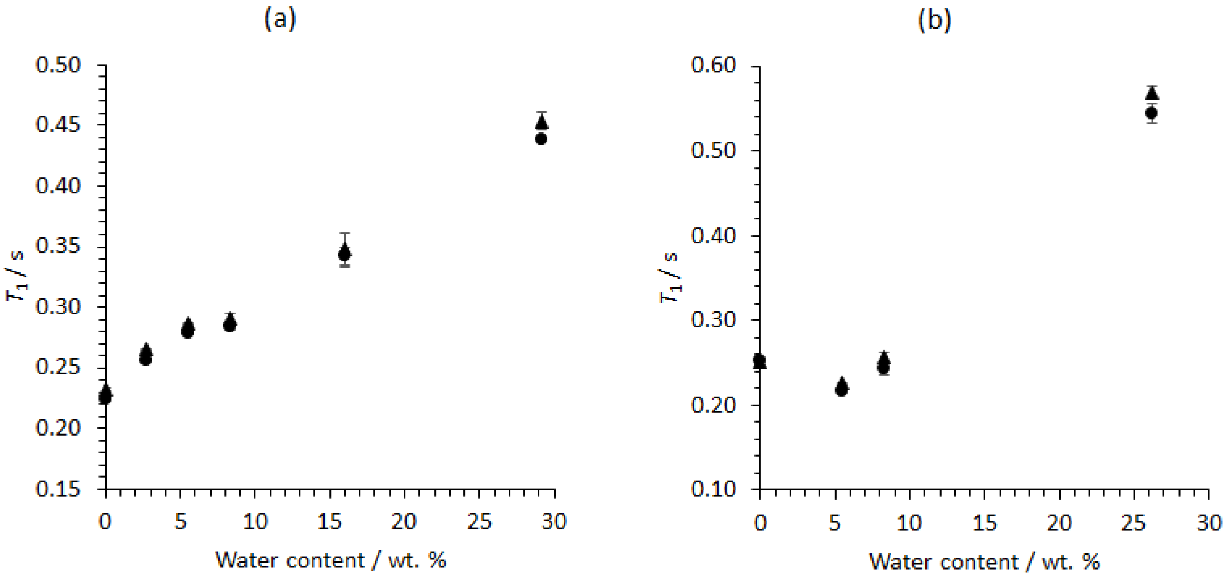

Figure 4.10: T_1 relaxation times for Ch^+ protons (H_a), in (a) ethaline and (b) reline, as a function of water content, (●) in the absence and (▲) presence of 0.3 M $ZnCl_2$.

Figure 4.11 shows the average ^{1}H T_2 relaxation times in the pure dry ethaline as a function of Zn, and 0.3 M $ZnCl_2$-ethaline as a function of water. It can be seen that for pure dry ethaline, the T_2 NMR relaxation time decreases with increasing the concentration of Zn. For 0.3 M $ZnCl_2$-ethaline, the ^{1}H T_2 relaxation time decreases on addition of water, but then increases with increasing water content. These T_2 data have been included in this chapter to be used in interpreting ^{1}H MR T_2 relaxation data in chapter 5.

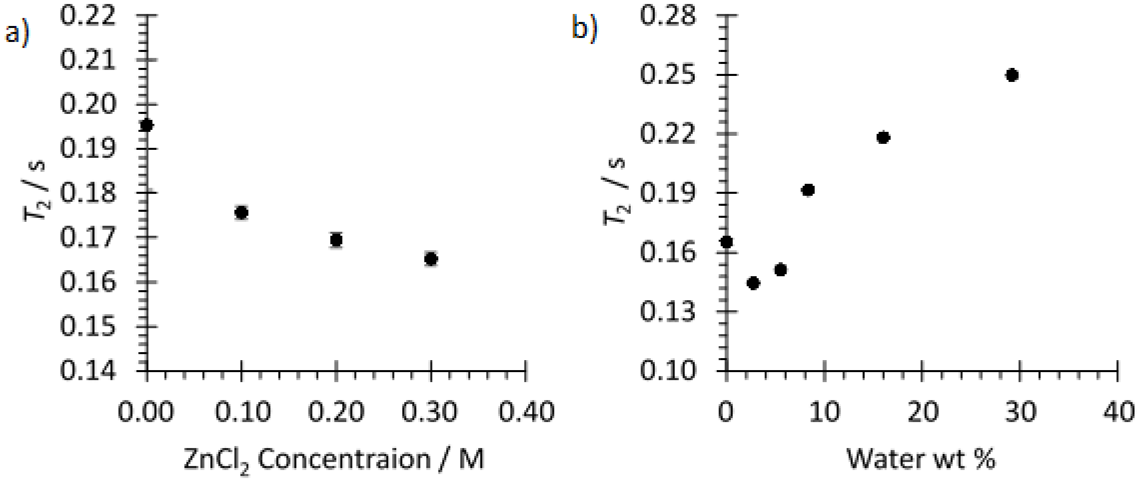

Figure 4.11: Average ^{1}H T_2 relaxation times for (a) pure dry ethaline as a function of $ZnCl_2$ and (b) 0.3 M $ZnCl_2$-ethaline as a function of water.

4.4 Discussion

The viscosity or ethaline is lower than the viscosity of reline, because U is much stronger HBD than EG, therefore reline is 10 times viscous than ethaline.[15] The effect of zinc on the viscosity in reline and ethaline has been studied.[15] It has been shown that the viscosity of ethaline is largely unaffected by the addition of Zn, but in reline, a significant decrease in viscosity is observed with increasing Zn.[15] This is because ethaline has a much lower viscosity (~ 22 cP for [$ZnCl_2$] = 0 to 0.3 mol.dm^{-3}), than reline (~ 800 cP to 280 cP for [$ZnCl_2$] = 0 to 0.3 mol.dm^{-3}).[15] However, the significant change in viscosity for reline, when Zn was added, was not observed in this study. This could be explained by our use of dried $ZnCl_2$, compared to previous study[15], which used $ZnCl_2$ as obtained. As $ZnCl_2$ is hygroscopic, it is possible the previously observed changed in viscosity could be due to the introduction of water.

From previous studies of ethaline[36], it is known that the hydroxyl groups of Ch^+ and EG coordinate around the Cl^-, bringing the H_d and H_f protons into close proximity. It is expected that this close proximity will facilitate proton exchange, which is observed in this study, by the presence of positive cross-peaks between H_d and H_f protons in the NOESY spectrum of pure ethaline (**Figure 4.5, a**). When water is added, it is known[17] that water also coordinates with Cl^-, Ch^+ and EG. Again, this proximity is expected to facilitate exchange between H_d, H_f and H_w protons. This has been observed previously by diffusion NMR[12] and is also observed in this study by the positive cross-peaks between H_d, H_f and H_w protons in the NOESY spectrum (**Figure 4.6, a**). However, this study has shown, for the first time, that the addition of zinc, to both pure ethaline and ethaline-water systems, increases the rate of exchange between these protons (**Table 4.2**).

This increase in proton exchange explains the increase in diffusion co-efficient for the H_d proton in the presence of Zn (**Table 4.3**). These observations indicate that EG, Ch^+ and water are predominantly co-ordinated around Zn^{2+}, rather than $Cl^–$.

From previous studies of reline[37], it has been suggested that the hydroxyl group in Ch^+ and carbonyl group in U co-ordinate around the $Cl^–$ ion. It is expected that this orientation reduces the opportunity for proton exchange between H_g (U) and H_d (Ch^+) protons. This is supported by the diffusion data (**Table 4.3**), which show that alkyl and hydroxyl protons in Ch^+ diffuse at the same rate. However, the 2D ^1H-^1H NOESY spectrum shows a cross peak between H_d and H_g protons (**Figure 4.7, a**). If proton exchange is not the origin of this cross peak, it can arise from the nOe, indicating these protons are in close ($\lesssim$ 3Å) proximity. The addition of Zn does not appear to change the interactions between U and Ch^+ species, where 1D ^1H (**Figure 4.4**) and 2D ^1H-^1H NOESY (**Figure 4.7**) spectra and ^1H diffusion data (**Table 4.3**) are observed to remain largely unchanged.

When water is added to reline, it has been previously observed[23] that water coordinates with $Cl^–$ and Ch^+. This co-ordination brings the H_w and H_d protons into close proximity, facilitating proton exchange between these protons. This is observed in this study in the 2D ^1H-^1H NOESY spectra (**Figure 4.8 and Figure 4.9**). In the NOESY spectrum with 8.3 % wt water (**Figure 4.8, a**), not only is a cross peak observed between H_d and H_w protons, but there is now an absence of an nOe interaction between H_g and H_d protons, indicating a change in co-ordination between U and Ch^+ species. The addition of water to reline, in the presence of Zn, does not appear to change the interactions between U or Ch^+ species. However, the presence of zinc appears to slow the exchange rate between H_d and H_w protons (**Table 4.2**). This is also supported by the 1D ^1H NMR spectra (**Figure 4.4, b**), where, in the presence of Zn, there is a narrowing of the line width of H_d and H_w peaks, which suggests that the presence of Zn slows down proton exchange. It is not clear why this is, but it could be because Zn^{2+} may compete with Cl^- to co-ordinate with either the water or Ch^+, or both, and thus reduces the number H_d and H_w protons able to exchange.

For both ethaline and reline, the addition of water reduces the viscosity.[12] This can be seen in the narrowing of peaks for non-exchangeable protons (**Figure 4.3** and **Figure 4.4**) and increase in T_1 relaxation times (**Figure 4.10**) and diffusion co-efficient with increasing water (**Tables 4.4 – 4.7**). However, the T_1 relaxation time and diffusion co-efficient data also indicate a phase transition for both reline and ethaline with increasing water concentration. This can be seen in **Figure 4.12**, where these data are combined into a single plot for each DES. In ethaline, a discontinuity is observed in T_1 data around 8.3 wt.% of water. A more marked discontinuity in the T_1 relaxation time is observed for reline, where there is an initial decrease, before it increases. It should be noted, that a similar discontinuity can also be observed in the diffusion co-efficient data reported by D'Agostino *et al.*[12] where a wider range of water concentrations were investigated. The origins of this behaviour in reline is most likely to come from a change in the distribution of water within the system. At low concentrations, water molecules embed in the reline network, forming a supermolecular complex. In such structures, there is an associated increase in size, leading to a higher rotational correlation time, for Ch^+, and, hence, lower T_1 relaxation time.[38] However, when the water content increases (> 6 wt.%), there is an increase in the T_1 relaxation time for ChCl, which suggests a reduction in the tumbling rate for ChCl, indicating a change in the structures (solvation) formed within reline. This observation could be indicative of a transition to the heterogeneous distribution of water from discrete microscopic 'pockets' of water, within the reline network, proposed by D'Agostino *et al.*[12] at high water concentrations. Ethaline shows more of a monotonic increase in T_1 relaxation time, with increasing water content. However, a slight discontinuity can also be observed around 8 wt.% of water, which is at a concentration equivalent to 1:1 (water:ChCl) mole ratio, a concentration that has previously[12] been observed to correspond to a transition in behaviour of other deep eutectic solvents.

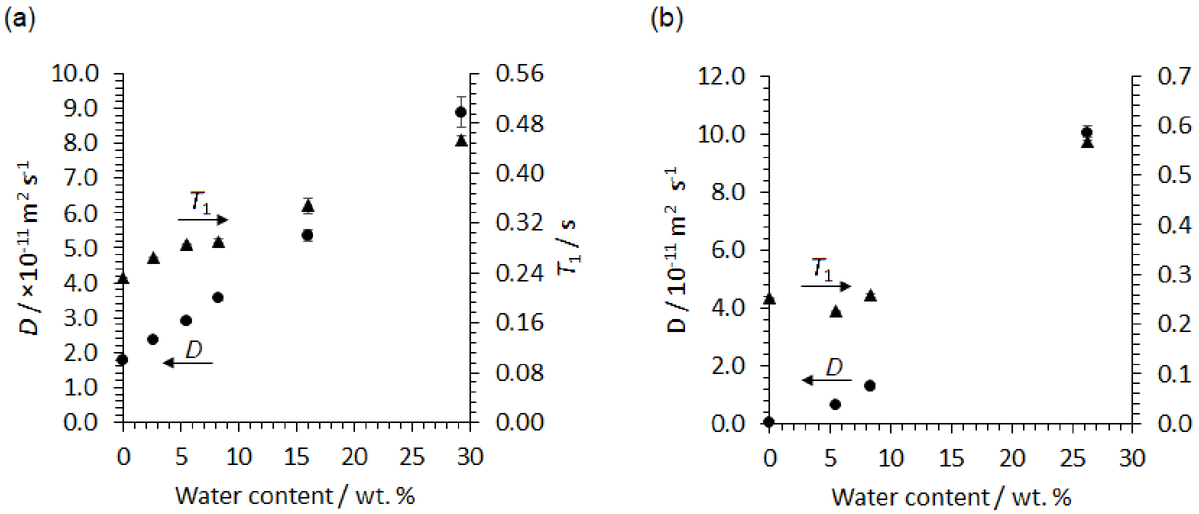

Figure 4.12: Plot of T_1 relaxation times (▲) and diffusion co-efficient (●) for Ch^+ protons (H_a), in (a) ethaline and (b) reline, as a function of water content.

Lastly, diffusion measurements for both reline and ethaline have shown that water has two diffusion co-efficients, over all water concentrations, in the presence and absence of Zn. This suggest that water exist in two different environments, with no or slow exchange between these environments. As we see this bi-exponential diffusion co-efficient for water, over all water concentrations, it is unlikely that these environments are associated with the water within the DES network and interstitial water, which has been observed at > 6% wt. water (reline) and > 8% wt. (ethaline). It is unclear what the origins are for the bi-exponential diffusion co-efficient of water, and further studies are required.

4.5 Conclusions

This chapter has investigated the role of Zn and water on solvation, and dynamics, in reline and ethaline DES systems, using ^{1}H NMR spectroscopy T_1 NMR relaxation times, NMR diffusion and 2D NOESY/EXSY spectroscopy. In ethaline, it is found that Zn promotes proton exchange between hydroxyl protons (H_d and H_f) in ChCl and EG, in the presence and absence of water. However, in reline, the presence of Zn was found to have little effect on the interactions between ChCl and U species, but did reduce the proton exchange between hydroxyl (H_d) and water (H_w) protons, in systems containing water. The presence of water was also found to change the interaction between ChCl and U species, removing the nOe cross-peak between amide and hydroxyl protons. These findings reveal key changes in solvation and dynamics, in both reline and ethaline, as a function of water and Zn concentration, proving insight into the role of solvation and dynamics in these electrolytes for a range of Zn electrochemical applications. These data support previous observations of changes in microstructure for both reline and ethaline, with increasing water content. To the best of our knowledge, this is the first study that investigates the effect of zinc or both (water and zinc) on the ^{1}H NMR spectra of ethaline and reline systems. In addition, the effect of Zn and water on relaxation times have been investigated using the ^{1}H NMR techniques. This would be useful for the relaxation MRI studies of these two systems. *In situ* ^{1}H MRI study of zinc electroplating from $ZnCl_2$-ethaline system is presented in this thesis in chapter 5.

4.6 References

1. Danilov, F. I.; Protsenko, V. S.; Kityk, A. A.; Shaiderov, D. A.; Vasil'eva, E. A.; Kumar, U. P.; Kennady, C. J., Electrodeposition of Nanocrystalline Nickel Coatings from a Deep Eutectic Solvent with Water Addition. Prot. Met. Phys. Chem. **2017,** 53, 1131-1138.
2. Protsenko, V. S.; Bobrova, L. S.; Golubtsov, D. E.; Korniy, S. A.; Danilov, F. I., Electrolytic Deposition of Hard Chromium Coatings from Electrolyte Based on Deep Eutectic Solvent. Russ. J. Appl. Chem. **2018,** 91, 1106-1111.
3. Abbott, A. P.; Barron, J. C.; Ryder, K. S., Electrolytic deposition of Zn coatings from ionic liquids based on choline chloride. Trans. Inst. Met. Finish. **2009,** 87, 201-207.
4. Abbott, A. P.; McKenzie, K. J.; Ryder, K. S., Electropolishing and Electroplating of Metals Using Ionic Liquids Based on Choline Chloride. In Ionic Liquids IV, American Chemical Society: 2007; Vol. 975, pp 186-197.
5. Abbott, A. P.; Capper, G.; McKenzie, K. J.; Glidle, A.; Ryder, K. S., Electropolishing of stainless steels in a choline chloride based ionic liquid: an electrochemical study with surface characterisation using SEM and atomic force microscopy. Phys. Chem. Chem. Phys. **2006,** 8, 4214-4221.
6. Kao-ian, W.; Pornprasertsuk, R.; Thamyongkit, P.; Maiyalagan, T.; Kheawhom, S., Rechargeable Zinc-Ion Battery Based on Choline Chloride-Urea Deep Eutectic Solvent. J. Electrochem. Soc. **2019,** 166, A1063-A1069.
7. Smith, E. L.; Abbott, A. P.; Ryder, K. S., Deep Eutectic Solvents (DESs) and Their Applications. Chem. Rev. **2014,** 114, 11060-11082.
8. Zhang, Q.; De Oliveira Vigier, K.; Royer, S.; Jerome, F., Deep eutectic solvents: syntheses, properties and applications. Chem. Soc. Rev. **2012,** 41, 7108-7146.
9. Smith*, E. L., Deep eutectic solvents (DESs) and the metal finishing industry: where are they now? Trans. Inst. Met. Finish. **2014,** 91 (5), 241-248.
10. Abbott, A. P.; El Ttaib, K.; Frisch, G.; McKenzie, K. J.; Ryder, K. S., Electrodeposition of copper composites from deep eutectic solvents based on choline chloride. Phys. Chem. Chem. Phys. **2009,** 11, 4269-4277.
11. Whitehead, A. H.; Pölzler, M.; Gollas, B., Zinc Electrodeposition from a Deep Eutectic System Containing Choline Chloride and Ethylene Glycol. J. Electrochem. Soc. **2010,** 157, D328-D334.
12. D'Agostino, C.; Gladden, L. F.; Mantle, M. D.; Abbott, A. P.; Ahmed, E. I.; Al-Murshedi, A. Y. M.; Harris, R. C., Molecular and ionic diffusion in aqueous - deep eutectic solvent mixtures: probing inter-molecular interactions using PFG NMR. Phys. Chem. Chem. Phys. **2015,** 17, 15297-15304.
13. Hansen, B. B.; Spittle, S.; Chen, B.; Poe, D.; Zhang, Y.; Klein, J. M.; Horton, A.; Adhikari, L.; Zelovich, T.; Doherty, B. W.; Gurkan, B.; Maginn, E. J.; Ragauskas, A.; Dadmun, M.; Zawodzinski, T. A.; Baker, G. A.; Tuckerman, M. E.; Savinell, R. F.; Sangoro, J. R., Deep Eutectic Solvents: A Review of Fundamentals and Applications. Chem. Rev. **2021,** 121, 1232-1285.

14. Abbott, A. P.; Barron, J. C.; Frisch, G.; Ryder, K. S.; Silva, A. F., The effect of additives on zinc electrodeposition from deep eutectic solvents. Electrochim. Acta **2011,** 56, 5272-5279.

15. Abbott, A. P.; Barron, J. C.; Frisch, G.; Gurman, S.; Ryder, K. S.; Fernando Silva, A., Double layer effects on metal nucleation in deep eutectic solvents. Phys. Chem. Chem. Phys. **2011,** 13, 10224-31.

16. Ge, X.; Gu, C.; Wang, X.; Tu, J., Deep eutectic solvents (DESs)-derived advanced functional materials for energy and environmental applications: challenges, opportunities, and future vision. J. Mater. Chem. A **2017,** 5, 8209-8229.

17. Celebi, A. T.; Vlugt, T. J. H.; Moultos, O. A., Structural, Thermodynamic, and Transport Properties of Aqueous Reline and Ethaline Solutions from Molecular Dynamics Simulations. J. Phys. Chem. B **2019,** 123, 11014-11025.

18. Zhekenov, T.; Toksanbayev, N.; Kazakbayeva, Z.; Shah, D.; Mjalli, F. S., Formation of type III Deep Eutectic Solvents and effect of water on their intermolecular interactions. Fluid Phase Equilib. **2017,** 441 (Supplement C), 43-48.

19. Ma, C.; Laaksonen, A.; Liu, C.; Lu, X.; Ji, X., The peculiar effect of water on ionic liquids and deep eutectic solvents. Chem. Soc. Rev. **2018,** 47, 8685-8720.

20. Bezerra-Neto, J. R.; Sousa, N. G.; dos Santos, L. P. M.; Correia, A. N.; de Lima-Neto, P., The effect of water on the physicochemical properties of an ethylene glycol and choline chloride mixture containing Cu2+ ions: electrochemical results and dynamic molecular simulation approach. Phys. Chem. Chem. Phys. **2018,** 20, 9321-9327.

21. Du, C.; Zhao, B.; Chen, X.-B.; Birbilis, N.; Yang, H., Effect of water presence on choline chloride-2urea ionic liquid and coating platings from the hydrated ionic liquid. Sci. Rep. **2016,** 6, 1–14

22. Valverde, P. E.; Green, T. A.; Roy, S., Effect of water on the electrodeposition of copper from a deep eutectic solvent. J. Appl. Electrochem. **2020,** 50, 699-712.

23. Hammond, O. S.; Bowron, D. T.; Edler, K. J., The Effect of Water upon Deep Eutectic Solvent Nanostructure: An Unusual Transition from Ionic Mixture to Aqueous Solution. Angew. Chem. Int. Ed. **2017,** 56, 9782-9785.

24. Posada, E.; López-Salas, N.; Jiménez Riobóo, R. J.; Ferrer, M. L.; Gutiérrez, M. C.; del Monte, F., Reline aqueous solutions behaving as liquid mixtures of H-bonded co-solvents: microphase segregation and formation of co-continuous structures as indicated by Brillouin and 1H NMR spectroscopies. Phys. Chem. Chem. Phys. **2017,** 19, 17103-17110.

25. Pandey, A.; Pandey, S., Solvatochromic Probe Behavior within Choline Chloride-Based Deep Eutectic Solvents: Effect of Temperature and Water. J. Phys. Chem. B **2014,** 118, 14652-14661.

26. Barron, J. C. The Electrochemistry of Zn in Deep Eutectic Solvents University of Leicester, Leicester, 2009.

27. Davenport, A. J.; Forsyth, M.; Britton, M. M., Visualisation of chemical processes during corrosion of zinc using magnetic resonance imaging. Electrochem. Commun. **2010,** 12, 44-47.

28. Britton, M. M.; Bayley, P. M.; Howlett, P. C.; Davenport, A. J.; Forsyth, M., In Situ, Real-Time Visualization of Electrochemistry Using Magnetic Resonance Imaging. J. Phys. Chem. Lett. **2013,** 4, 3019-3023.

29. Kleckner, I. R.; Foster, M. P., An introduction to NMR-based approaches for measuring protein dynamics. Biochim. Biophys. Acta **2011,** 1814, 942-968.
30. KaleidaGraph Synergy Software: United States.
31. Claridge, T. D. W., High-Resolution NMR Techniques in Organic Chemistry. Second ed.; Elsevier: Oxford, UK, 2009.
32. Meiboom, S.; Gill, D., Modified Spin-Echo Method for Measuring Nuclear Relaxation Times. Rev. Sci. Instrum. **1958,** 29, 688-691.
33. Stejskal, E. O.; Tanner, J. E., Spin Diffusion Measurements: Spin Echoes in the Presence of a Time-Dependent Field Gradient. J. Chem. Phys. **1965,** 42, 288.
34. D'Agostino, C.; Harris, R. C.; Abbott, A. P.; Gladden, L. F.; Mantle, M. D., Molecular motion and ion diffusion in choline chloride based deep eutectic solvents studied by 1H pulsed field gradient NMR spectroscopy. Phys. Chem. Chem. Phys. **2011,** 13, 21383-21391.
35. Gil, R. R.; Navarro-Vázquez, A., Chapter 1 Application of the Nuclear Overhauser Effect to the Structural Elucidation of Natural Products. In Modern NMR Approaches to the Structure Elucidation of Natural Products: Volume 2: Data Acquisition and Applications to Compound Classes, The Royal Society of Chemistry: 2017; Vol. 2, pp 1-38.
36. Stefanovic, R.; Ludwig, M.; Webber, G. B.; Atkin, R.; Page, A. J., Nanostructure, hydrogen bonding and rheology in choline chloride deep eutectic solvents as a function of the hydrogen bond donor. Phys. Chem. Chem. Phys. **2017,** 19, 3297-3306.
37. Ashworth, C. R.; Matthews, R. P.; Welton, T.; Hunt, P. A., Doubly ionic hydrogen bond interactions within the choline chloride-urea deep eutectic solvent. Phys. Chem. Chem. Phys. **2016,** 18, 18145-18160.
38. Bloembergen, N.; Purcell, E. M.; Pound, R. V., Relaxation Effects in Nuclear Magnetic Resonance Absorption. Physical Review **1948,** 73, 679-712.

Chapter 5 Visualize the Electroplating of Zinc from $Zn(TfO)_2$-[$C_2C_1Im(TfO)$] and $ZnCl_2$-ethaline Systems using MRI

5.1 Introduction

Zinc has been electroplated successfully from ILs and DES.[1-5] Therefore, these liquids might be promising to be used as electrolytes for zinc electrochemical applications, such as zinc electroplating and zinc-based batteries. Zinc has been electroplated from $Zn(TfO)_2$-[$C_2C_1Im(TfO)$] which is an IL system[4-5] and $ZnCl_2$-ethaline[1-2] which is a DES system. NMR techniques have been used to investigate the effect of zinc on the physical and chemical properties of these two systems, as shown in chapters 3 and 4. These NMR techniques such as spectroscopy, relaxation, and diffusion measurements give information on intermolecular interactions, zinc speciation, and the mobility of ions. However, NMR techniques cannot spatially locate ions. Therefore, MRI techniques can be used to spatially locate ion transports, chemical reactions, non-invasively while the metal is being plated.[6-7] MRI techniques have the power to spatially locate metal ions in electrolytes directly or indirectly.[6-7] A direct MRI is used to image the distribution of NMR active metal ions, such as ^{7}Li and ^{23}Na.[8-11] An indirect MRI used to spatially locate metal ions using the ^{1}H signal from the surrounding species, which is sensitive to the presence and speciation of metal ions.[12]

A direct ^{67}Zn MRI has been considered a challenge due to the lower sensitivity of ^{67}Zn and their short T_2 relaxation time.[6] Therefore, previous MRI studies of zinc electrochemistry inside a zinc-based battery[13] and zinc corrosion[14] have been used indirect ^{1}H MRI. Transportation of zinc ions was visualized in the zinc-air battery, *in operando*, using T_1 relaxation images.[13] A long T_1

relaxation time was observed in the vicinity of the zinc anode indicating the formation and transport of zincate ions away from zinc anode.[13] Whereas, a reduction of T_1 relaxation reduction time was attributed to the O_2 reduction reaction.[13] Zinc corrosion processes have also been investigated using magnetic resonance relaxation.[14] In these experiments, T_1 and T_2 relaxation times of water in saturated LiCl solution were observed to change as a result of zinc speciation difference during zinc corrosion.[14] At the start of zinc corrosion process, an initial reduction in ^1H T_1 relaxation time was observed, due to the formation of Zn structure-making ions.[14] Where water molecules coordinate to Zn, and that increases the rotational correlation time of water, and hence lower the T_1 relaxation time.[14] Then after approximately 17 hours of corrosion, a T_1 increase is observed, this change in T_1 relaxation was attributed to changes in the structure of zinc species.[14] When Zn structure-breaking ions were formed, the mobility of water molecules is increased, and that lowered their rotational correlation time and hence increases the T_1 relaxation time.[14]

In this chapter, the electroplating of zinc from $Zn(TfO)_2$-[$C_2C_1Im(TfO)$] IL and $ZnCl_2$-ethaline DES systems, in the presence and absence of water, has been imaged using MR relaxation techniques. The electroplating of Zn from [$C_2C_1Im(TfO)$] systems, is imaged, *in operando*, using indirect ^{19}F MR relaxation techniques. Whereas the electroplating of Zn from $ZnCl_2$-ethaline is imaged, *in situ*, before and after the electroplating, using indirect ^1H MR relaxation techniques. These MRI studies build on the previous results of ^{19}F and ^1H NMR spectroscopy studies of [$C_2C_1Im(TfO)$] and ethaline systems, presented in this thesis in chapters 3 and 4, respectively. The effect of zinc and water on ^{19}F NMR T_1 and T_2 relaxation times has been used as a key to interpreting the ^{19}F and ^1H MR relaxation maps in this chapter. Where ^{19}F MRI of the TfO anion, in the $Zn(TfO)_2$-$[C_2C_1Im(TfO)]$ systems, have revealed changes in both T_1 and T_2 during the electroplating of zinc. Whereas ^1H MRI of ethaline species (ChCl & EG), in the $ZnCl_2$-ethaline systems show changes in T_2 relaxation time after the electroplating of Zn.

5.2 Experimental

5.2.1 Material and sample preparation

Choline chloride (ChCl, 99 %), ethylene glycol (EG, 99.8 %) and zinc chloride ($ZnCl_2$, 99.99 %) and Zinc trifluoromethanesulfonate ($Zn(TfO)_2$, 99 %) were purchased from Sigma-Aldrich. 1-ethyl-3-methylimidazolium trifluoromethylsulfonate ($[C_2C_1Im(TfO)]$, 99 %) was obtained from IO-LI-TEC, Germany. All components were used without further purification, but dried in a vacuum oven under reduced pressure (100 mbar), at 120 °C ($ZnCl_2$ and $Zn(TfO)_2$) and at 80 °C (ChCl and EG), for a minimum of 24 hours. The $[C_2C_1Im(TfO)]$ ionic liquid was dried under high vacuum pump (10^{-7} mbar), at 50 °C, for a minimum of 24 hours. Once dried, all samples were stored in a glove-box under argon atmosphere.

In a glove-box, ethaline liquid was prepared by mixing ChCl and EG in a 1:2 molar ratio before sonication and heating to 60 °C until homogenous clear colourless liquids were formed. Zinc in ethaline solutions were prepared by dissolving dry $ZnCl_2$ in ethaline, over a range of $ZnCl_2$ concentrations (0.01 - 0.3 M) at 25 °C. Zinc in IL solutions were prepared, in the glove-box, by dissolving $Zn(TfO)_2$ in $[C_2C_1Im(TfO)]$ to form a range of (0.02 – 0.15 M) concentration of $Zn(TfO)_2$ before sonication and heating to 60 °C until homogenous clear yellowish liquids were formed. Heating was used to enhance the solubility of $Zn(TfO)_2$ in the $[C_2C_1Im(TfO)]$ IL. In the glove-box, a range of dry zinc-$[C_2C_1Im(TfO)]$ solutions and dry zinc-ethaline solutions were transferred to 5 mm airtight NMR tubes for phantom imaging. A phantom sample comprising multiple 5 mm airtight NMR tubes containing different zinc concentrations, **Figure 5.1**.

Water in ethaline and water in [C_2C_1Im(TfO)] samples were prepared, outside the glove-box. 4.02 µl and 5.02 µl of Milli-Q® water, (resistivity of 18 MΩ.cm at 25°C and a TOC < 5 ppb), to 1 ml of 0.3 M $ZnCl_2$-ethaline and 1 ml of 0.15 M $Zn(TfO)_2$-[C_2C_1Im(TfO)], respectively. This amount of added water is equivalent to a 0.05 mole fraction of water.

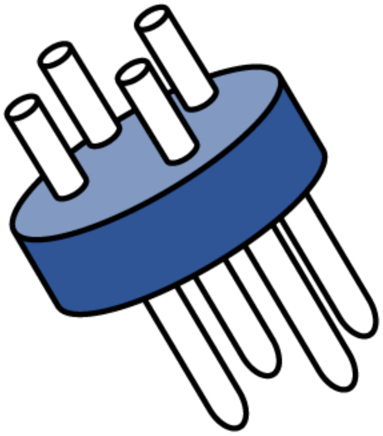

Figure 5.1: Schematic diagram of a phantom containing four 5 mm NMR tubes.

5.2.2 Electrochemical cell setup

An electrochemical cell was constructed using a Swagelok cell made of polytetrafluoroethylene (PTFE), Swagelok®. The inner diameter of the Swagelok cell was 3/8" = 9.5 mm. A copper metal disk (0.25 mm thickness, 10 mm diameter, copper foil, 99.8% metal basis, Sigma Aldrich) was used as the working electrode (WE) and a zinc metal disk (0.25 mm thickness, 10 mm diameter, copper foil, 99.8% metal basis, Sigma Aldrich) was used as the counter electrode (CE). These two electrodes were separated by three PTFE washers (OD = 9.5 mm, ID = 5.5 mm and thickness of 1.5 mm, Modus Gauges Limited). Both electrodes were cleaned by immersing them in 10 % (v/v) nitric acid for 1 minute, and then rinsed with Milli-Q® water, before left to dry on a paper towel. A schematic diagram of the Swagelok cell is shown in **Figure 5.2**. The Swagelok cell setup depend on the electrolyte type. Where a dry electrolyte was used, the cell was assembled in a glove-box. Where the electrolyte contained water was used, the cell was assembled outside a glove box. A volume of approximately 140 µl of electrolyte was required to fill the cavity, sandwiched between the two electrodes, which were separated by three PTFE washers. This Swagelok electrochemical cell was used in the electroplating of zinc from either 0.3 M $ZnCl_2$-ethaline or 0.15 M $Zn(TfO)_2$-[$C_2C_1Im(TfO)$], in the presence or absence of 0.05 mole fraction of water.

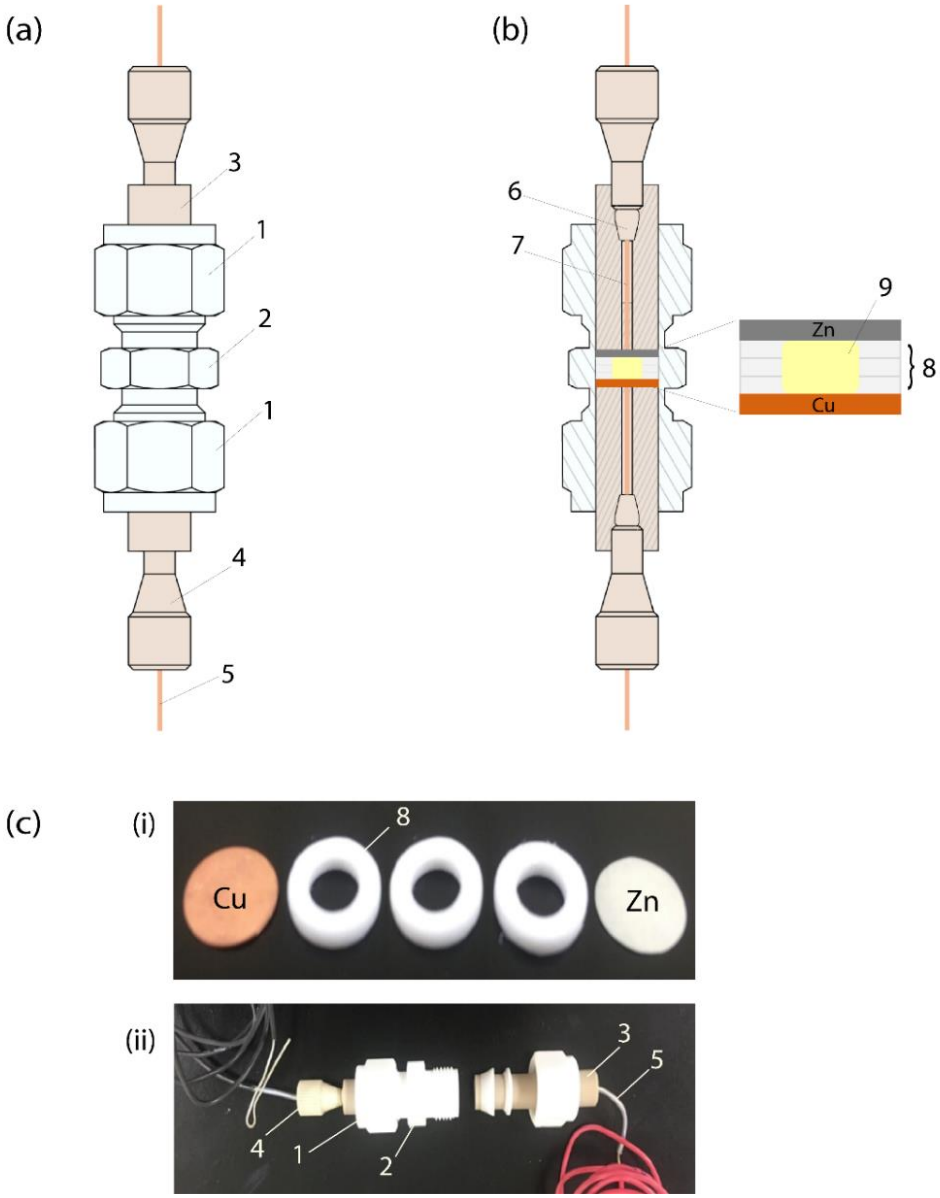

Figure 5.2: Schematic diagram of Swagelok cell design. (a) Outside view of the Swagelok cell shows 1. Swagelok net, 2. PTFE Swagelok union, 3. Custom-made PEEK plug, 4. PEEK HPLC nut and 5. Insulated Cu wire. (b) Interior view of Swagelok cell shows 6. PEEK HPLC ferrule, 7. Cu wire with PTFE sheath, 8. Three PTFE washers (OD=9.5 mm, ID=5.5 mm and thickness = 1.5 mm) sandwiched between Zn and Cu discs (OD= 10 mm, thickness = 0.25 mm) and 9. Electrolyte placed in the cavity of PTEF washers. (c) A photograph of (i) Cu, Zn discs and three PTFE washers (ii) Swagelok cell with all labelled components.

5.2.3 Electrochemical measurements

Electrochemical measurements were performed using an Ivium Octostat 5000 potentiostat connected to the cell in a 2-electrode configuration, where a zinc electrode was used as the CE and a copper electrode used as the WE. Cyclic voltammetry (CV) measurements were performed for $Zn(TfO)_2$-$[C_2C_1Im(TfO)]$ samples, with a potential scan from – 0.1 V to – 1.3 V (for dry sample) and from – 0.2 V to – 1.3 V (for the sample containing 0.05 mole fraction of water), with a scan rate of 10 mV / s. The CV of $ZnCl_2$-ethaline samples, either dry or contains 0.05 mole fraction of water, were performed with a potential scan from – 0.1 V to – 0.6 V and a scan rate of 50 mV / s. These CV measurements were performed on the bench, outside the magnet, to identify the target potential for the electroplating of Zn.

The deposition of zinc has been performed using a chronoamperometry experiment. In this experiment, the electrode current is measured as a function of time by applying a constant potential to the working electrode. The electroplating of zinc from $[C_2C_1Im(TfO)]$ containing 0.15 M $Zn(TfO)_2$, in the presence and absence of water, was performed by applying – 0.1 V to the copper electrode for 14400 s (4 hours). Whereas the electroplating of zinc from ethaline containing 0.3 M $ZnCl_2$ was performed by applying – 0.43 V (for dry sample) and – 0.35 V (for the sample containing 0.05 mole fraction of water) to the copper electrode for 7500 s (2 hours).

5.2.4 Magnetic Resonance Experiments

MRI data were collected on a Bruker AVANCE III HD 300 spectrometer equipped with a 7 T vertical wide-bore superconducting magnet, and a 25 mm micro 2.5 radiofrequency (rf) resonator, at ambient temperature of 19 ± 0.2 °C. [C_2C_1Im(TfO)] samples were imaged using ^{19}F coil and signal were collected from fluorine nuclei of TfO anion. Ethaline samples were imaged using 10 mm QRT ^{1}H coil and collect signal from proton nuclei of ethaline species (ChCl and EG). A series of 2D images were acquired using the fast spin-echo imaging sequence RARE[15] (Rapid Acquisition with Relaxation Enhancement) to produce T_1 and T_2 maps for the phantom and the electrochemical cell.

Horizontal ^{19}F MR $T_{1,2}$ relaxation maps of the phantom sample, comprising four 5 mm airtight NMR tubes containing a range of [C_2C_1Im(TfO)] samples with Zn(TfO)$_2$ (0 - 0.2 M), were acquired with a FOV of 20 ×20 mm and 64 × 64 pixels. The slice thickness of [C_2C_1Im(TfO)] samples was 10 mm, to increase the signal-to-noise. Vertical ^{19}F MR $T_{1,2}$ relaxation maps of the Swagelok cell, containing 0.15 M Zn(TfO)$_2$ in [C_2C_1Im(TfO)], with and without 0.05 mole fraction of water, were acquired with a 6 mm slice thickness, 15 × 10 mm field of view (FOV) and a pixel size of 64 × 64. T_1 and T_2 maps of phantoms and electrochemical cell were acquired using the same T_R and T_E parameters. T_1 maps were produced for [C_2C_1Im(TfO)] from seven 2D images, using a saturation recovery method, where the recovery time (T_R) was increased from 55 ms to 7500 ms. All images were collected with 3 ms echo time (T_E) and 16 echo images to increase the signal-to-noise ratio without increasing the experiment time. T_2 maps were produced, for [C_2C_1Im(TfO)] system, from eight echo images with an echo time of 100 ms and a RARE factor of 8, and a repetition time (T_R) of 15 s.

Horizontal ^1H MR $T_{1,2}$ relaxation maps of the phantom sample of dry ethaline with a range of $ZnCl_2$ concentrations (0 – 0.3 M) were acquired with a FOV of 20 ×20 mm, 64 × 64 pixels and a slice thickness of 1 mm. Vertical ^1H MR T_2 relaxation maps of Swagelok cell, contains 0.3 M $ZnCl_2$ in ethaline, with and without water, were acquired with a 6 mm slice thickness, 15 × 10 mm field of view (FOV) and a pixel size of 64 × 64. T_1 maps were produced from seven 2D images using saturation recovery with recovery time (T_R) running from 55 ms to 3000 ms, all images were collected with 3 ms echo time (T_E) and 16 echo images. T_2 maps were produced from 8 echo images with an echo time of 60 ms and a RARE factor of 64, and T_R = 15 s. T_2 maps of phantoms and electrochemical cell were acquired using the same T_R and T_E parameters.

5.3 Results

Figure 5.3 shows the ^{19}F magnetic resonance T_1 and T_2 relaxation maps of NMR tubes containing dry [$C_2C_1Im(TfO)$], as a function of $Zn(TfO)_2$. It can be seen that, T_1 relaxation time increases gradually from 1.23 s to 1.34 s, whereas T_2 relaxation time goes from 0.66 s to 0.77 s as the concentration of Zn^{2+} decreases in the ionic liquid. However, it is clear that T_1 relaxation time shows the greatest variation with zinc concentration and that enables the mapping of Zn concentration in the IL, across the electrochemical cell, than the T_2 relaxation time.

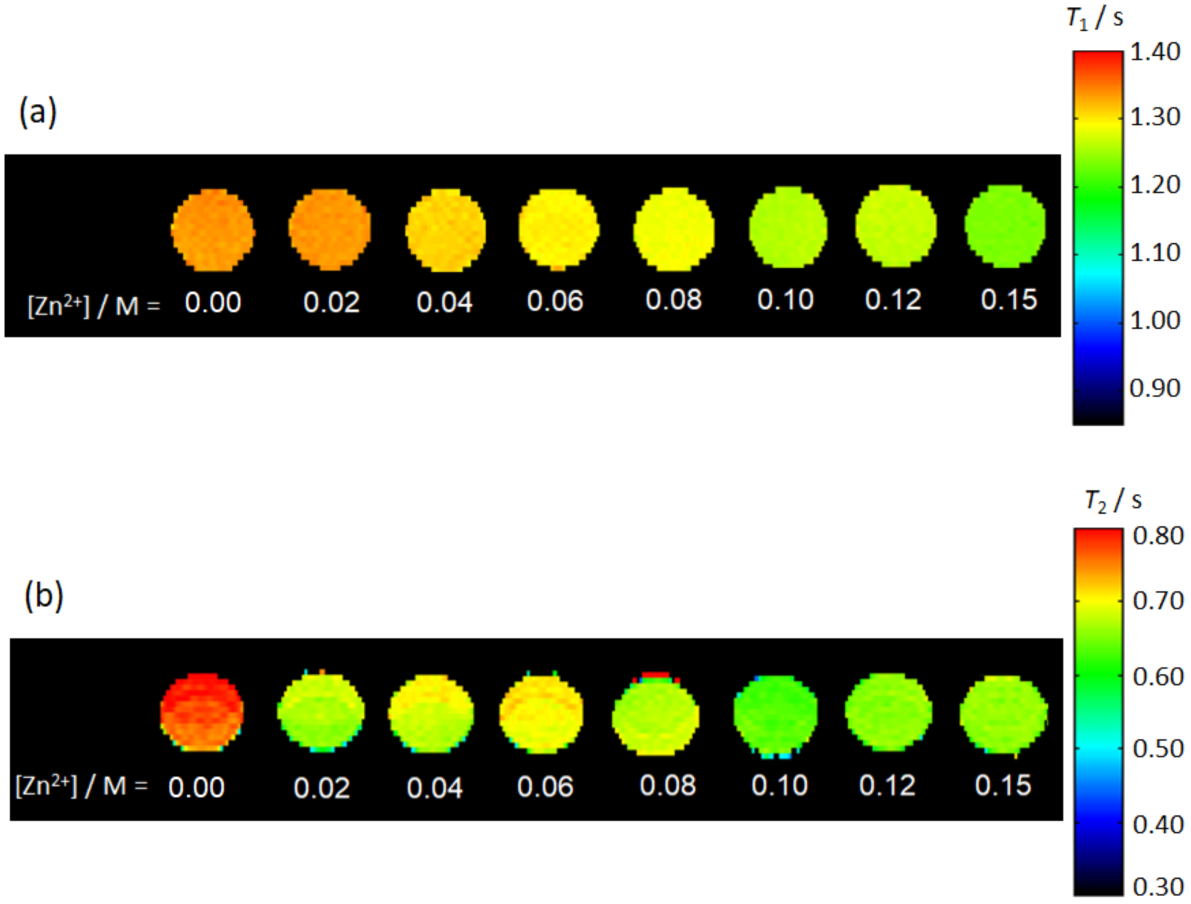

Figure 5.3: Horizontal 2D ^{19}F MR a) T_1 and b) T_2 relaxation maps of NMR tubes containing dry [C_2C_1Im(TfO)] as a function of Zn(TfO)$_2$ concentration, the signal is from the TfO$^-$ anion. These were extracted from the phantom ^{19}F MR T_1 and T_2 relaxation maps and then lined up in the order of Zn(TfO)$_2$ concentration.

Figure 5.4 shows the ^{1}H MR T_1 and T_2 relaxation maps of NMR tubes contain dry ethaline as a function of $ZnCl_2$. It can be seen that, T_2 relaxation times of ethaline increases gradually as the concentration of Zn^{2+} decreases in the ethaline solution. Whereas, T_1 relaxation time of ethaline is not affected by the addition of Zn, and remains constant around 0.32 s. This indicates that T_1 relaxation maps are not appropriate to visualize the distribution of zinc ions during electroplating in $ZnCl_2$-ethaline. Therefore, T_2 relaxation time maps were acquired to visualize the electrochemistry inside the electrochemical cell, *in situ* before and after zinc deposition, in the presence and absence of water.

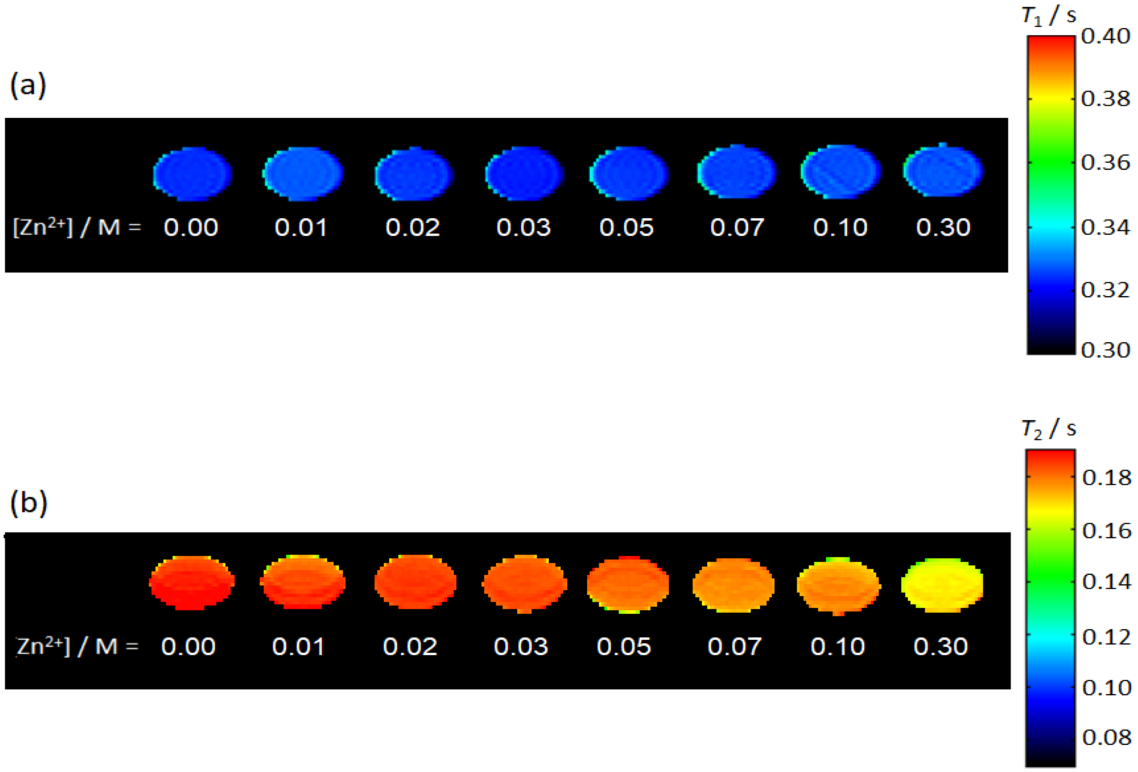

Figure 5.4: Horizontal 2D ^{1}H MR a) T_1 and b) T_2 relaxation maps of NMR tubes containing dry ethaline as a function of $ZnCl_2$ concentration, the signal is from ethaline species (ChCl and EG). These were extracted from the phantom ^{1}H MR T_1 and T_2 relaxation maps and then lined up in the order of $ZnCl_2$ concentration.

Cyclic voltammograms of 0.15 M $Zn(TfO)_2$ in $[C_2C_1Im(TfO)]$, in the presence and absence of water, are presented in **Figure 5.5**. The cathodic peak, which is ascribed to Zn^{2+} reduction to zinc metal, is observed around – 1 V, in both the dry sample and sample containing 0.05 mole fraction of water. Therefore, the electroplating of zinc from 0.15 M $Zn(TfO)_2$-$[C_2C_1Im(TfO)]$, in the presence and absence of water, was performed by applying a fixed potential of – 1 V, using a chronoamperometry experiment. **Figure 5.6** shows the cyclic voltammograms of 0.3 M $ZnCl_2$ in ethaline, in the presence and absence of water. The cathodic peak observed about – 0.43 V for the dry sample, and about – 0.35 V for $ZnCl_2$-ethaline sample containing 0.05 mole fraction of water. Therefore, the electroplating of zinc from 0.3 M $ZnCl_2$-ethaline, in the presence and absence of water, was performed by applying a fixed potential of – 0.43 V (for dry sample) and – 0.35 V (for the sample containing water), using a chronoamperometry experiment. The current of the electrode measured as a function of time during the chronoamperometry experiment of zinc electroplating, as shown in **Figure 5.7**.

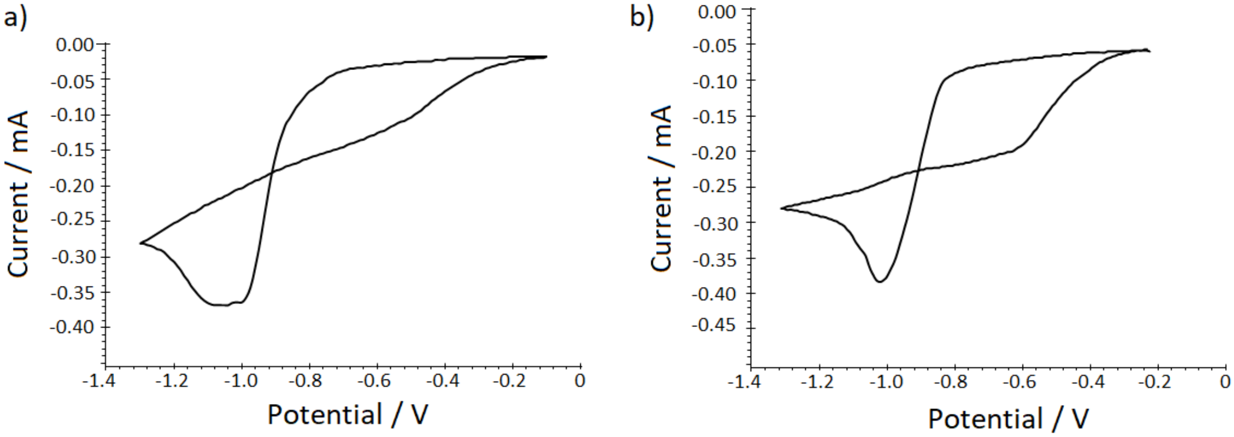

Figure 5.5: Cyclic voltammograms (CVs) for 0.15 M $Zn(TfO)_2$ in $[C_2C_1Im(TfO)]$ (a) In the absence and (b) presence of 0.05 mole fraction of water, with a scan rate of 10 mV / s.

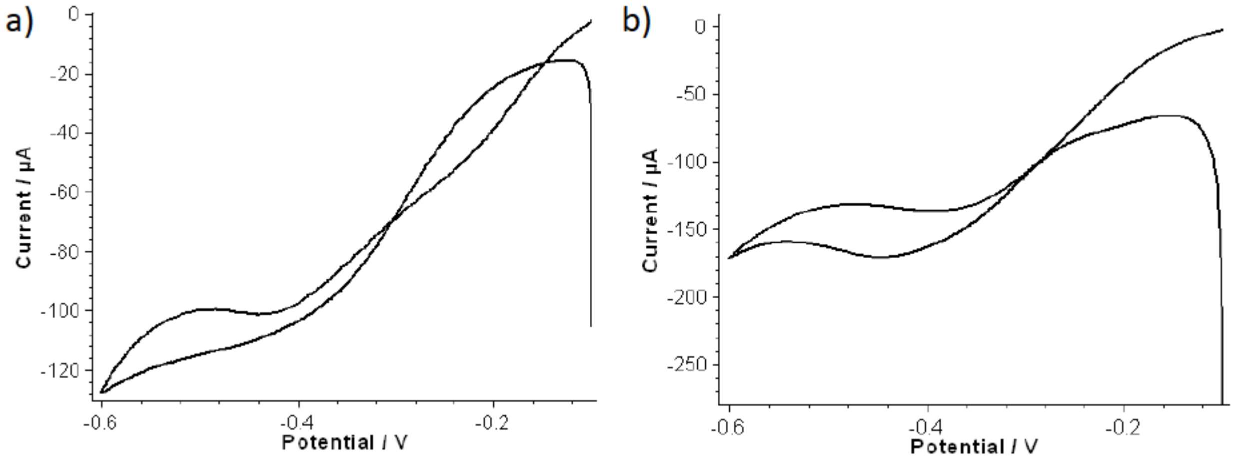

Figure 5.6: Cyclic voltammograms (CVs) for 0.3 M $ZnCl_2$ in ethaline (a) In the absence and (b) presence of 0.05 mole fraction of water, with a scan rate of 50 mV / s.

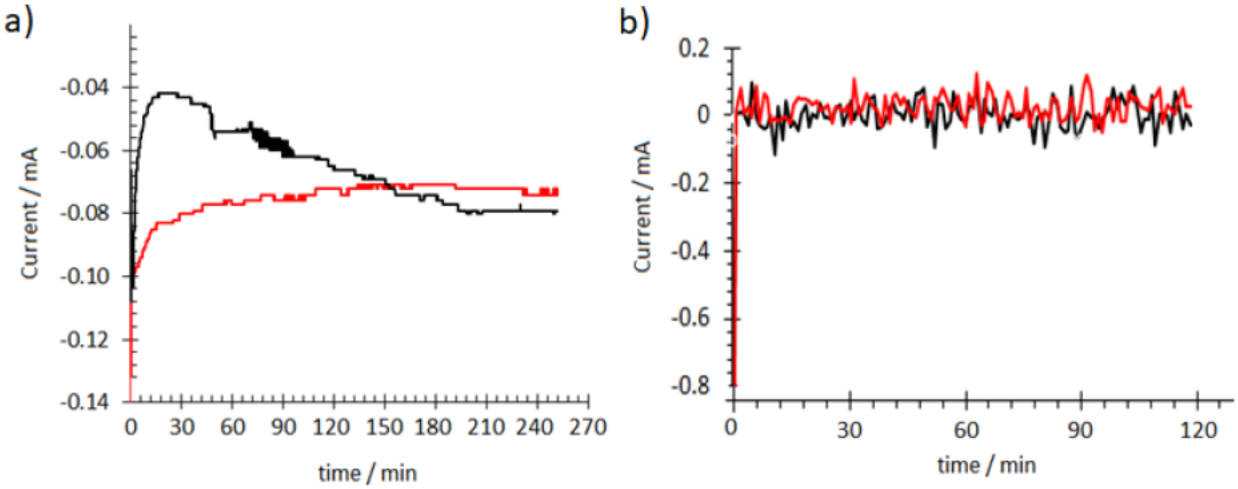

Figure 5.7: A plot of the current as a function of time plot resulting from the chronoamperometry experiment for (a) *in operando*, zinc electroplating from 0.15 M $Zn(TfO)_2$-[$C_2C_1Im(TfO)$] and (b) *in situ*, zinc electroplating from 0.3 M $ZnCl_2$-ethaline, in the absence (black) and presence of 0.05 mole fraction of water (red). For $Zn(TfO)_2$-[$C_2C_1Im(TfO)$] samples zinc was plated by applying a constant potential, − 1.0 V, for four hours, in the presence and absence of water. For $ZnCl_2$-ethaline samples zinc was plated by applying a constant potential, − 0.43 V (for dry sample) and − 0.35 V (for sample containing water), for two hours.

Figure 5.8 and **Figure 5.9** show a time series of ^{19}F MR T_1 relaxation maps during zinc electroplating, *in operando*, from [C_2C_1Im(TfO)] containing 0.15 M Zn(TfO)$_2$, in the absence and presence of water, respectively. The pre-plating map, (**Figure 5.8, b)**, was expected to have a homogeneous T_1 relaxation time for the electrolyte across the electrochemical cell. However, an unexpected increase in the T_1 relaxation time can be observed near the Cu electrode, compared to the value observed in the centre of the electrochemical cell. During electroplating, (**Figure 5.8**, **c - i)**, an increase in the T_1 relaxation time is observed in the vicinity of Cu and Zn electrodes. In the presence of water, **Figure 5.9**, a similar trend of ^{19}F T_1 relaxation time is observed, where T_1 relaxation time increases during the electroplating near Cu and Zn electrodes. In the vicinity of Cu, T_1 relaxation time goes from 1.11 ± 0.03 s to 1.22 ± 0.01 s, whereas in the vicinity of anode it goes from 1.12 ± 0.03 s to 1.22 ± 0.04 s.

By comparing **Figure 5.8** and **Figure 5.9** it can be seen that the T_1 relaxation times, in the presence of 0.05 mole fraction of water, were lower than that observed in the absence of water. This was also observed in the ^{19}F NMR T_1 relaxation times of the [C_2C_1Im(TfO)], which were measured spectroscopically using inversion recovery sequence as a function of Zn and water, shown in **Figure 3.7.**

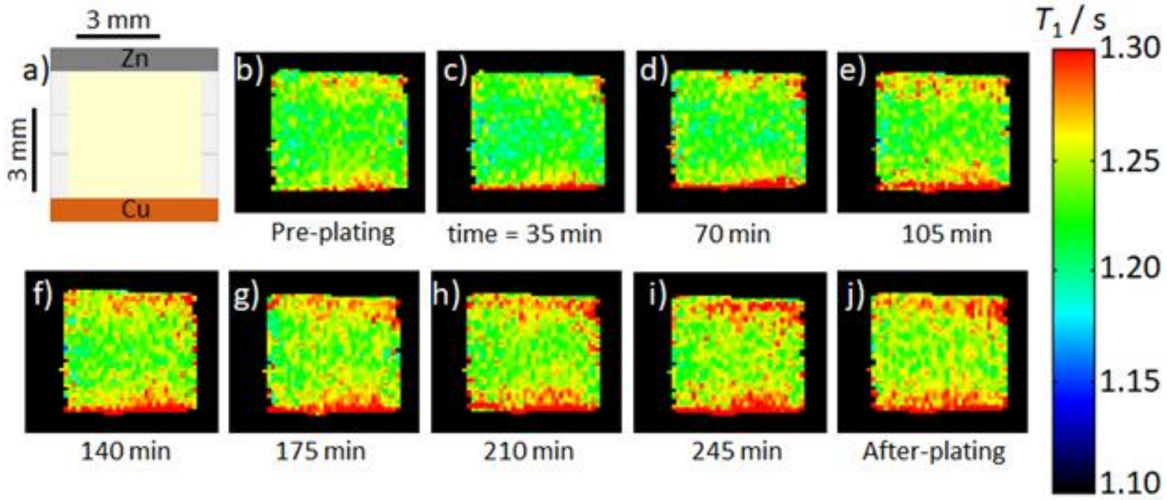

Figure 5.8: a) A schematic diagram of electrochemical cell, Zn electrode as anode and Cu electrode as a cathode. Vertical ^{19}F MR T_1 relaxation maps, b) taken before the electroplating, (c-i) taken *in operando* while zinc is electroplated on Cu substrate, and j) taken after the electroplating. Zinc was plated using a constant potential –1 V, for four hours, form 0.15 M $Zn(TfO)_2$ in [C_2C_1Im(TfO)], in the absence of water. Times were determined at the endpoint of each scan.

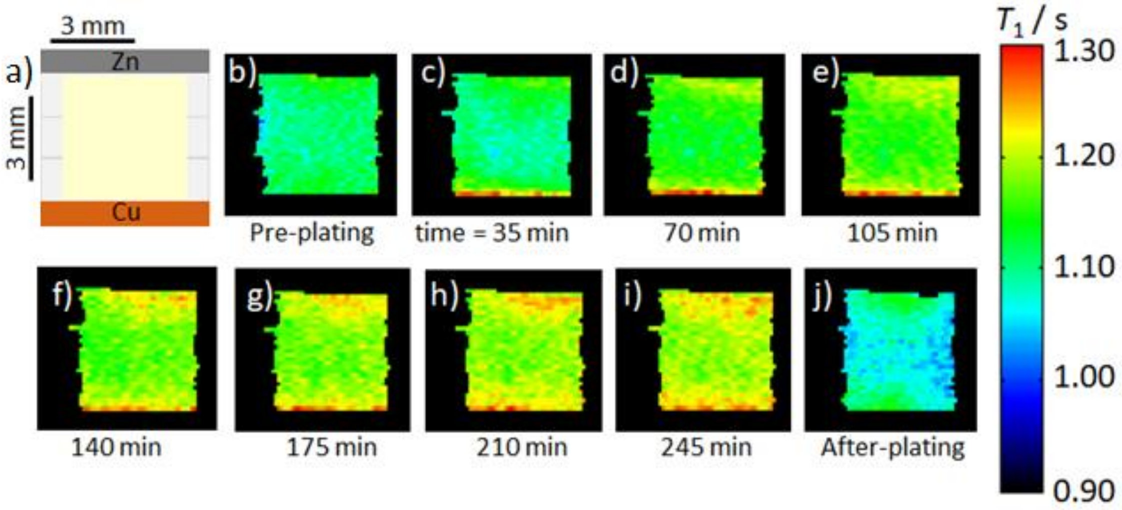

Figure 5.9: a) A schematic diagram of electrochemical cell, Zn electrode as anode and Cu electrode as a cathode. Vertical ^{19}F MR T_1 relaxation maps, b) taken before the electroplating, (c-i) taken *in operando* while zinc is electroplated on Cu substrate, and j) taken after the electroplating. Zinc was plated using a constant potential –1 V, for four hours, form 0.15 M $Zn(TfO)_2$ in [C_2C_1Im(TfO)], in the presence of 0.05 mole fraction of water. Times were determined at the endpoint of each scan.

A time series of ^{19}F MR T_2 relaxation maps during zinc electroplating, *in operando*, from [C_2C_1Im(TfO)] containing 0.15 M Zn(TfO)$_2$, in the absence and presence of water, are shown in **Figure 5.10** and **Figure 5.11**, respectively. It can be seen that the ^{19}F T_2 NMR relaxation time changes universally across the electrochemical cell, it is not located near the electrodes as the T_1 relaxation time changes. It can be seen from **Figure 5.10** that, in the absence of water, during the electroplating of zinc, T_2 relaxation time almost remains constant around 0.62 ± 0.02 s. Whereas in the presence of water, **Figure 5.11**, T_2 relaxation time increases over time, while the zinc is electroplated, from 0.56 ± 0.01 s to 0.61 ± 0.02 s.

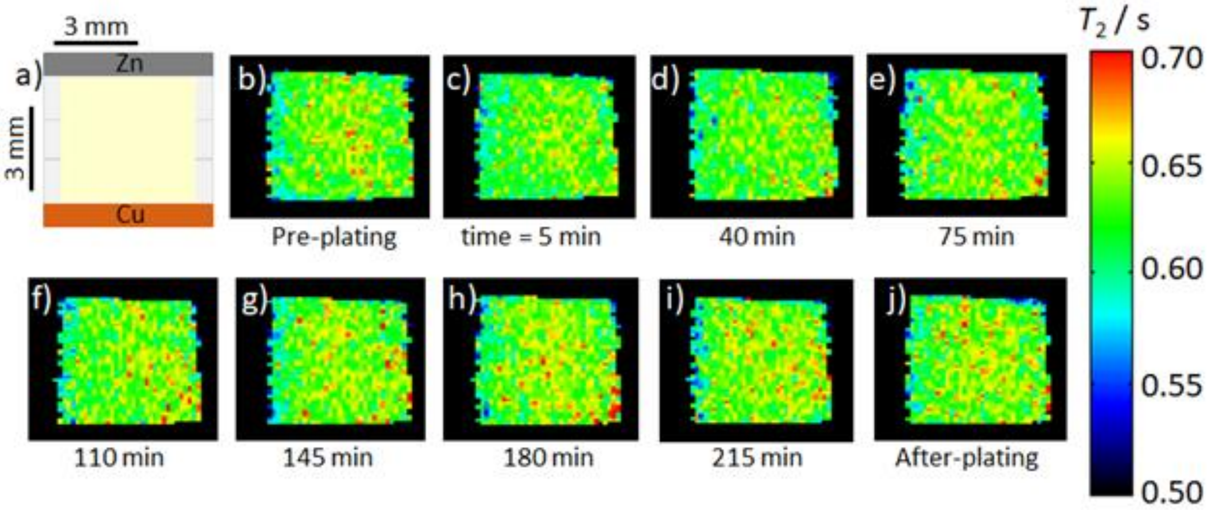

Figure 5.10: a) A schematic diagram of electrochemical cell, Zn electrode as anode and Cu electrode as a cathode. Vertical ^{19}F MR T_2 relaxation maps, b) taken before the electroplating, (c-i) taken *in operando* while zinc is electroplated on Cu substrate, and j) taken after the electroplating. Zinc was plated using a constant potential –1 V, for four hours, form 0.15 M Zn(TfO)$_2$ in [C_2C_1Im(TfO)], in the absence of water. Times were determined at the endpoint of each scan.

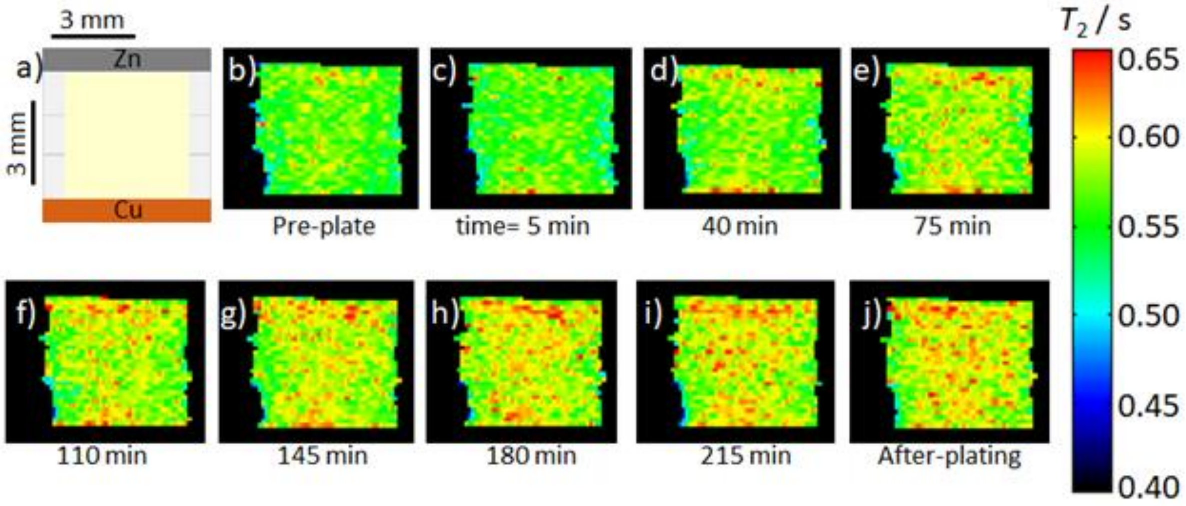

Figure 5.11: a) A schematic diagram of electrochemical cell, Zn electrode as anode and Cu electrode as a cathode. Vertical ^{19}F MR T_2 relaxation maps, b) taken before the electroplating, (c-i) taken *in operando* while zinc is electroplated on Cu substrate, and j) taken after the electroplating. Zinc was plated using a constant potential –1 V, for four hours, form 0.15 M $Zn(TfO)_2$ in $[C_2C_1Im(TfO)]$, in the presence of 0.05 mole fraction of water. Times were determined at the endpoint of each scan.

Unfortunately, it was not possible to image the electroplating of zinc from $ZnCl_2$-ethaline, *in operando*, because of COVID-19 lockdown and the shortcut of experimental time. Therefore, the electroplating of zinc from $ZnCl_2$-ethaline was imaged *in situ*, before and after the electroplating, where the electroplating process was performed outside the magnet. ^{1}H MR T_2 relaxation maps of an electrochemical cell before and after the electroplating of zinc from 0.3 M $ZnCl_2$-ethaline, in the presence and absence of 0.05-mole fraction of water, are shown in **Figure 5.12**. As was observed in the ^{19}F MR T_2 relaxation maps of $Zn(TfO)_2$-$[C_2C_1Im(TfO)]$, T_2 relaxation time changes across the electrochemical cell, it is not located near the electrodes. It can be seen that in the absence of water, the ^{1}H T_2 relaxation time remained around 0.20 s, even after the electroplating of Zn. Whereas in the presence of water, T_2 relaxation time, after the electroplating, is higher than that observed prior to the electroplating.

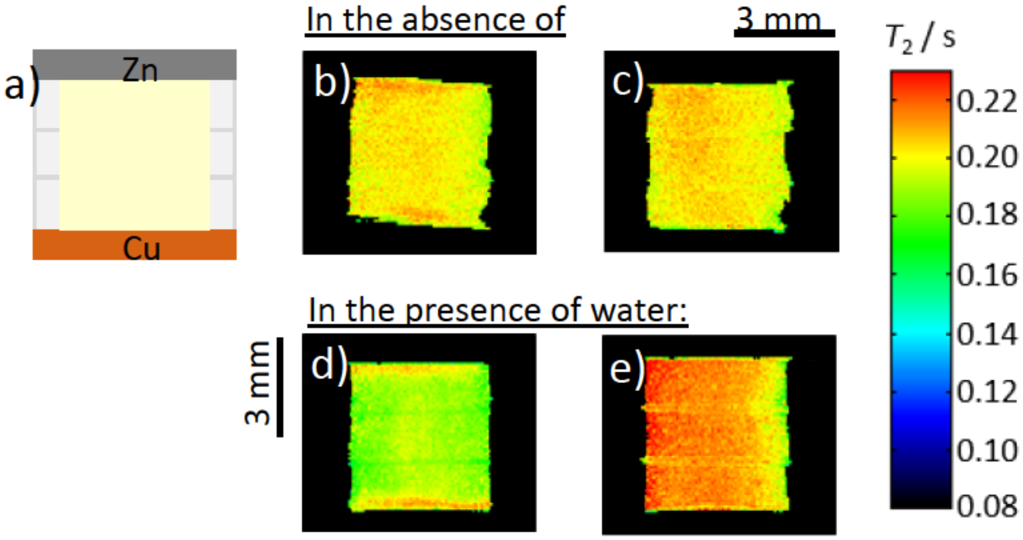

Figure 5.12: a) A schematic diagram of electrochemical cell, Zn electrode as anode and Cu electrode as a cathode. ^{1}H MR T_2 relaxation maps of an electrochemical cell containing 0.3 M $ZnCl_2$ in ethaline, in the absence and presence of water, (b&d) before and (c&e) after, *in situ*, zinc electroplating.

Figure 5.13 shows pictures of the copper and the zinc electrodes, after zinc electroplating on the Cu surface from $ZnCl_2$-ethaline and $Zn(TfO)_2$-[C_2C_1Im(TfO)] systems. The colour and the morphology of the deposited zinc film have been affected by the addition of water, for both ethaline and [C_2C_1Im(TfO)] systems. Light-grey deposits zinc were obtained from [C_2C_1Im(TfO)] in the presence of 0.05 mole fraction of water. Where in the absence of water, the colour of the deposited zinc tended to be blackish-grey. For ethaline system, a blackish-grey deposit zinc was obtained. Zinc electrodes in both all systems have been oxidized during the electroplating, and that also affects the colour and thickness of the zinc electrode, it looks thinner.

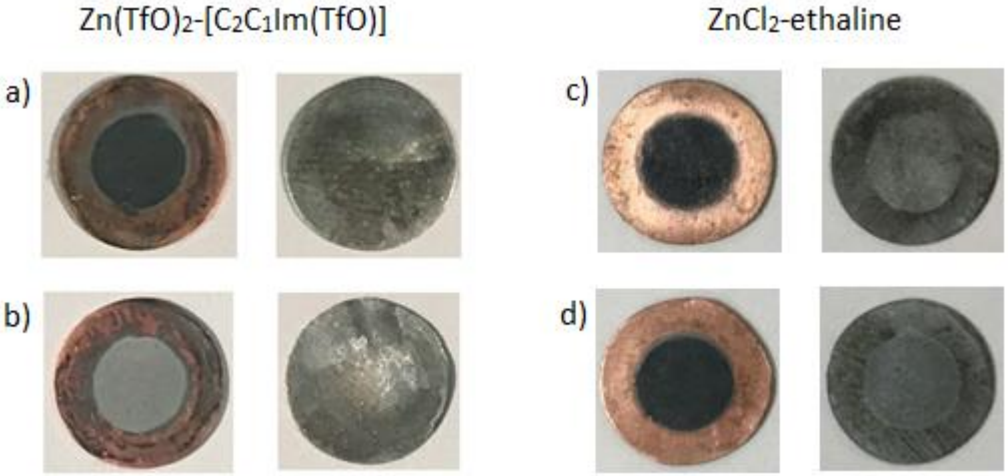

Figure 5.13: A photograph of the zinc and copper electrodes after the electroplating of zinc on the Cu electrode, from 0.15 M $Zn(TfO)_2$ in $[C_2C_1Im(TfO)]$ and 0.3 M $ZnCl_2$-ethaline systems, in the (a&c) absence and (b&d) presence of 0.05 mole fraction of water.

5.4 Discussion

^{19}F MRI of the TfO anion, in the 0.15 M $Zn(TfO)_2$-$[C_2C_1Im(TfO)]$ systems, has revealed changes in both T_1 and T_2 during the electroplating of zinc. To understand the causes of these changes in relaxation times, we need to consider the influence of Zn and water on the relaxation time of the TfO anion. It has been observed that ^{19}F T_1 and T_2 MR relaxation times are affected by the concentrations of zinc and water (**Figure 3.7).** Measurements of a range of $Zn(TfO)_2$-$[C_2C_1Im(TfO)]$ systems show that ^{19}F T_1 relaxation time increases from 1.27 ± 0.01 s to 1.39 ± 0.01 s, as the concentration of Zn^{2+} decreases from 0.15 to 0 M. The effect of water concentration on the T_1 relaxation time (**Figure 3.7)** shows that the addition of 0.05 mole fraction of water lowers the ^{19}F T_1 relaxation time from 1.28 ± 0.01 s to 1.14 ± 0.01 s. When the concentration of added water becomes higher than 0.05 mole fraction, the ^{19}F T_1 relaxation time of the TfO anion increases to 1.28 ± 0.01 s with increasing water content due to a reduction in viscosity of the solution.

The ^{19}F MR T_2 relaxation time for the TfO anion is found to be insensitive to the concentration of Zn, as shown in **Figure 5.3**. The ^{19}F MR T_2 relaxation time is around 0.66 ± 0.04 s over the range 0.02 - 0.15 M of $Zn(TfO)_2$. The effect of water on the ^{19}F T_2 relaxation time has a similar trend as the effect of water on T_1 relaxation time. **Figure 3.8** shows that the addition of 0.05 mole fraction of water lowers the T_2 relaxation time, and then above that water content the T_2 relaxation increases with increasing water content due to viscosity reduction. Moreover, from the NMR fundamental, it is known that the concentration of paramagnetic species, such as dissolved oxygen, affects the T_1 and T_2 relaxation times. When the concentration of dissolved oxygen increases, that gives a lower relaxation time.[16]

During the electroplating of zinc from $Zn(TfO)_2$-$[C_2C_1Im(TfO)]$ systems, in the presence and absence of water, the ^{19}F T_1 relaxation time increases in the vicinity of the copper, as shown from **Figure 5.8** and **Figure 5.9**. This suggests that during the electroplating, the concentration of Zn^{2+} near the Cu electrode lowered from 0.15 M to 0.08 M, where Zn^{2+} is reduced to its metallic state ($Zn^{2+} + 2e^- \rightarrow Zn$). The concentration of Zn^{2+} in the vicinity of the Cu electrode after the electroplating was determined from the ^{19}F T_1 values, using **Figure 3.7**. The change of T_1 relaxation time during the electroplating might be clearer in the 1D average ^{19}F T_1 relaxation time profiles, as shown in **Figure 5.14** and **Figure 5.15**.

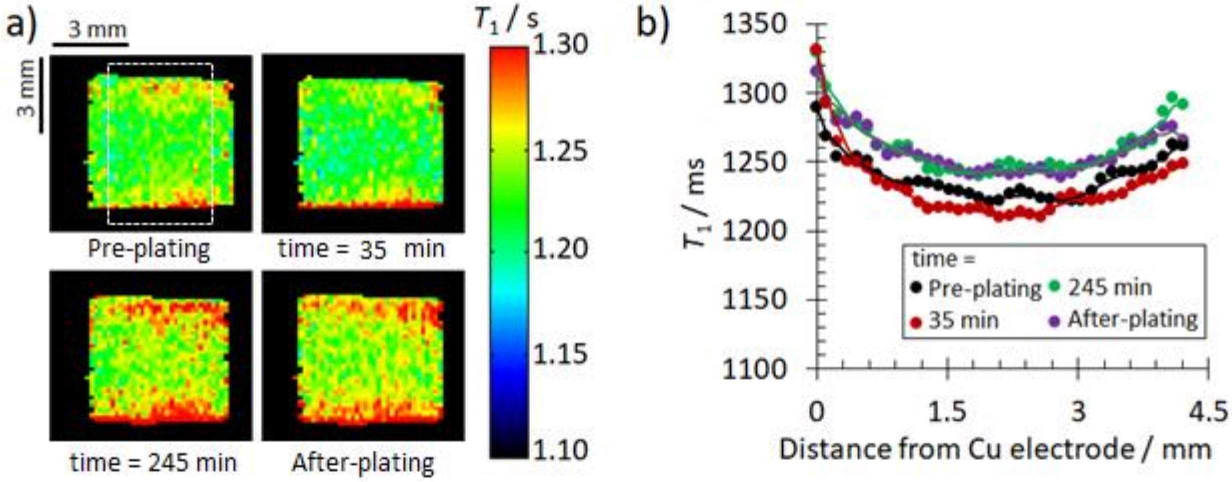

Figure 5.14: a) ^{19}F MR T_1 relaxation maps taken *in operando* while the zinc deposit on Cu electrode over the time, from [C_2C_1Im(TfO)] containing 0.15 M Zn(TfO)$_2$, in the absence of water. b) Plot of averaged 1D profiles of T_1 map images in (a), at different times, the line is averaged of 3 points. The dashed box indicates the region that used to produce the averaged T_1 1D profile in (b).

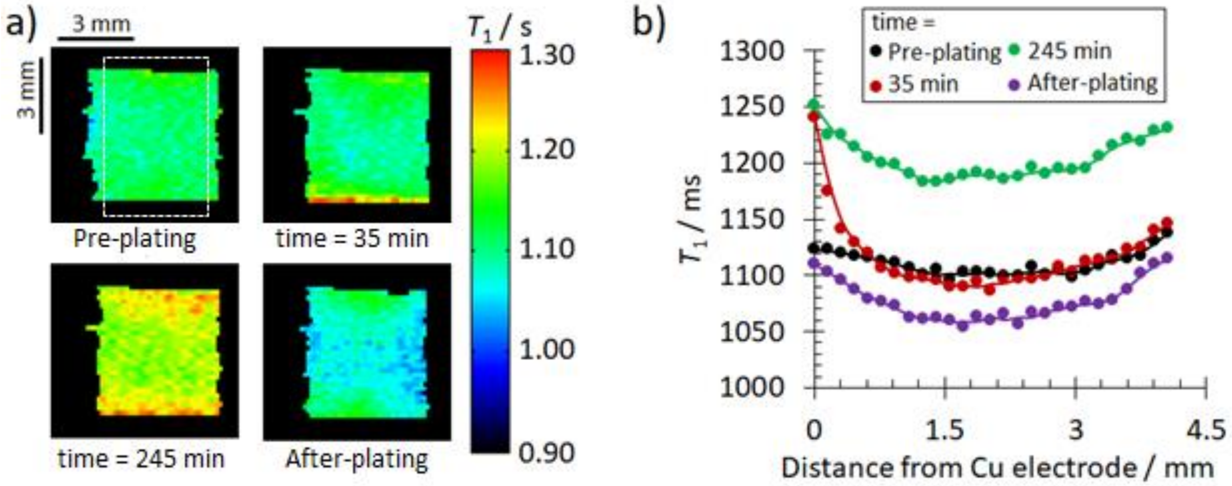

Figure 5.15: a) ^{19}F MR T_1 relaxation maps taken *in operando* while the zinc deposit on Cu electrode over the time, from [C_2C_1Im(TfO)] containing 0.15 M Zn(TfO)$_2$, in the presence of 0.05 mole fraction of water. b) Plot of averaged 1D profiles of T_1 map images in (a), at different times, the line is averaged of 3 points. The dashed box indicates the region that used to produce the averaged T_1 1D profile in (b).

An unexpected increase in the ^{19}F T_1 relaxation time in the vicinity of Zn anode, during the electroplating of zinc from $Zn(TfO)_2$-[$C_2C_1Im(TfO)$] systems, was observed in the images in **Figure 5.14** and **Figure 5.15**. It was expected to see a reduction in the T_1 relaxation time near the anode, due to the electrodisslotion of the Zn anode. When the sacrificial anode is electrodissolved, the concentration of Zn^{2+} increases near the anode, and that gives a lower T_1 relaxation time. This unexpected increase in T_1 relaxation time might be due to the occurrence of side reactions of water or the dissolved O_2. The side reaction of water would be possible only when the zinc is electroplated from $Zn(TfO)_2$-[$C_2C_1Im(TfO)$] containing 0.05 mole fraction of water. The side reaction of water makes the water content lower than 0.05 mole fraction, and that increases the T_1 relaxation time, as shown in **Figure 3.7**. Another suggested explanation of the unexpected T_1 increment near the Zn anode, which is the side reaction of dissolved oxygen. This would be possible for $Zn(TfO)_2$-[$C_2C_1Im(TfO)$], whether in the presence or absence of water. Previous studies[17-18] have shown that dissolved oxygen reacts with Zn^{2+} and formed zinc peroxide, ZnO_2. Therefore, the increase in the T_1 relaxation at the anode might be associated with the removal of dissolved oxygen, leading to an increase in T_1 as it is paramagnetic.

After Zn electroplating, **Figure 5.15** shows that, in $Zn(TfO)_2$-[$C_2C_1Im(TfO)$] system containing water, the T_1 relaxation time of the image taken after the electroplating is lower than that observed at the final experiment of electroplating at 245 min. This might be due to continuous zinc corrosion after electroplating, which might be enhanced by the presence of water. As the zinc anode corroded, the concentration of Zn^{2+} increases in the solution, and that gives a lower T_1 relaxation time.

^{19}F T_2 relaxation maps, **Figure 5.10** and **Figure 5.11** show that T_2 changes happen homogeneously across the cell, and are not located near the electrodes as the T_1 relaxation time changes are. This might suggest that this variation is because T_2 is not sensitive to changes in Zn concentration. From the T_1 relaxation map, **Figure 5.8** it has been predicted that the concentration of Zn near to the cathode changes during the electroplating from 0.15 M to 0.08 M. This has a good agreement with the T_2 relaxation data in phantom sample, **Figure 5.3**, where T_2 relaxation time is not sensitive to zinc concentration over the range (0.02 - 0.15 M). The change of T_2 relaxation time during the electroplating might be clearer in the 1D average ^{19}F T_2 relaxation time profiles, as shown in **Figure 5.16** and **Figure 5.17**. However, in the presence of water, T_2 relaxation time increase over time while Zn is plated on Cu, as shown in **Figure 5.17**. This ^{19}F T_2 increment suggests that there are some side reactions going on with water, and that lowers the water content. **Figure 3.8** shows that when water content becomes lower than 0.05 mole fraction, there will be an increase in ^{19}F T_2 relaxation time. This gives a good agreement with what was observed in the ^{19}F T_2 relaxation maps.

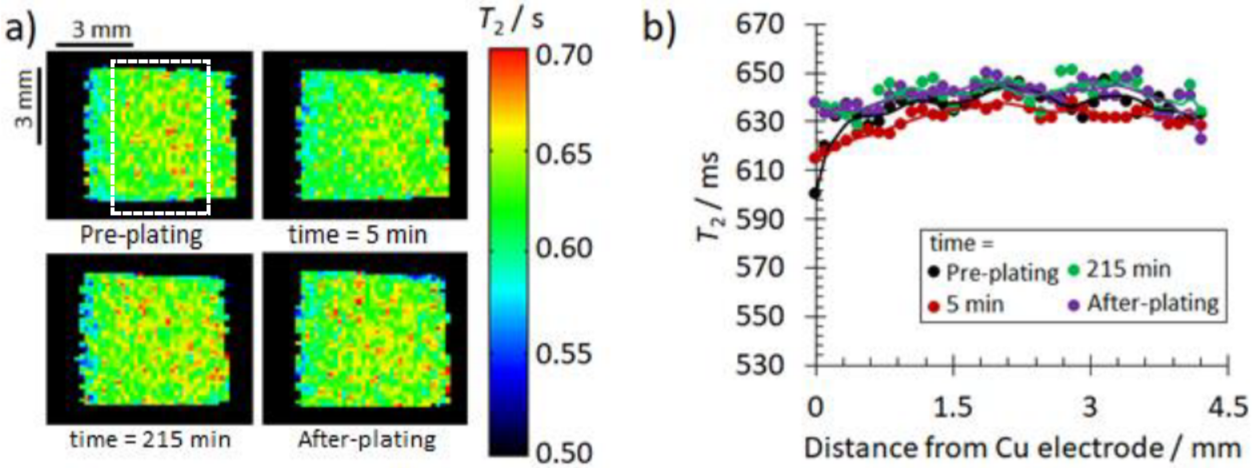

Figure 5.16: a) ^{19}F MR T_2 relaxation maps taken *in operando* while the zinc deposit on Cu electrode over the time, from [$C_2C_1Im(TfO)$] containing 0.15 M $Zn(TfO)_2$, in the absence of water. b) Plot of averaged 1D profiles of T_2 map images in (a), at different times, the line is averaged of 3 points. The dashed box indicates the region that used to produce the averaged T_2 1D profile in (b).

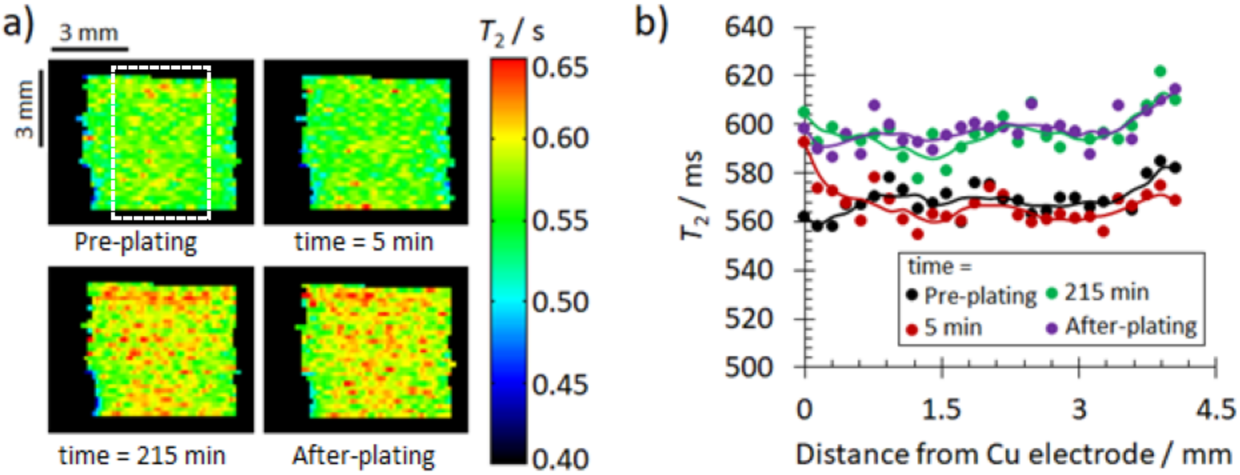

Figure 5.17: a) ^{19}F MR T_2 relaxation maps taken *in operando* while the zinc deposit on Cu electrode over the time, from [$C_2C_1Im(TfO)$] containing 0.15 M $Zn(TfO)_2$, in the presence of 0.05 mole fraction of water. b) Plot of averaged 1D profiles of T_2 map images in (a), at different times, the line is averaged of 3 points. The dashed box indicates the region that used to produce the averaged T_2 1D profile in (b).

The electroplating of zinc from $ZnCl_2$-ethaline systems was imaged using ^1H MR T_2 relaxation time, *in situ*, before and after electroplating, which was performed outside the magnet. Therefore, it is important to understand how zinc and water influence the ^1H T_2 relaxation time. **Figure 4.11** shows that ^1H T_2 relaxation time increases slightly from 0.165 to 0.169 s, when zinc concentration goes from 0.3 M to 0.2 M. ^1H T_2 relaxation time lowers from 0.165 to 0.151 s as water added to the 0.3 M $ZnCl_2$-ethaline system until the water content reach 0.44 mole fraction of water (5.5 wt.%). Then, above 5.5 wt.% of water, the ^1H T_2 relaxation time increase with water, due to viscosity reduction. Therefore, the addition of 0.05 mole fraction of water will lower the ^1H T_2 relaxation time of $ZnCl_2$-ethaline system.

Figure 5.12 shows that T_2 relaxation time, pre-plating, is lower in the presence of water, which is agreed with ^1H T_2 relaxation data in **Figure 4.11**. After the electroplating, in the absence of water, it can be seen that T_2 does not increase in the vicinity of the Cu electrode. This might suggest that ^1H T_2 relaxation time is not sensitive to zinc. Moreover, it can be seen that in the presence of water, T_2 relaxation time increase and this might be due to the occurrence of water side reaction. Where the T_2 relaxation increases when the water content becomes lower than 0.05 mole fraction of water. Overall, it can be seen that the ^1H MR T_2 relaxation maps of the electroplating of zinc from $ZnCl_2$-ethaline systems, have shown a similar trend of ^{19}F MR T_2 relaxation time of $Zn(TfO)_2$-$[C_2C_1Im(TfO)]$ systems.

The morphology and the colour of the deposited zinc depends on the zinc speciation, the size/shape of zinc particles. Zinc was deposited from different systems, $ZnCl_2$-ethaline and $Zn(TfO)_2$-$[C_2C_1Im(TfO)]$, in the presence and absence of water. Therefore, it is expected to have different zinc species. This has been explained in more detail in chapter 3 (for [C_2C_1Im(TfO)]) system) and chapter 4 (for ethaline system). Moreover, the mass transport of each system will vary depending on its viscosity. This might affect the nucleation mechanism which plays a big role in the size and the shape of zinc particles.

5.5 Conclusion

Magnetic resonance T_1 and T_2 relaxation maps are used to visualize ion transport and chemical reactions during the electroplating of Zn. Two different systems were used, $Zn(TfO)_2$-[C_2C_1Im(TfO)] and $ZnCl_2$-ethaline systems, in the absence and presence of water. Relaxation MR studies indicate that during the electroplating of Zn, from $Zn(TfO)_2$-[C_2C_1Im(TfO)] and $ZnCl_2$-ethaline systems, side reactions have occurred, possibly with dissolved oxygen or water. ^{19}F MR T_1 relaxation maps show that, in the presence of water, the zinc anode undergoes a continuous electrodissolotion, even after the electroplating. ^{19}F NMR T_1 relaxation maps spatially quantify the concentration of zinc ions in the vicinity of the copper electrode. During the electroplating of Zn from $Zn(TfO)_2$-[C_2C_1Im(TfO)], the concentration of Zn^{2+} near the copper electrode goes from 0.15 M to 0.08 M. In the $ZnCl_2$-ethaline system, ^{1}H T_1 relaxation was not sensitive to zinc concentration, while ^{1}H T_2 is sensitive to the large zinc concentration difference. Therefore, when 0.3 M $ZnCl_2$ was used to deposit zinc, zinc concentration in the vicinity of Cu, was not low enough to be detected by T_2 relaxation time. Overall, these MRI techniques are able to give new insight in future studies, which focus on developing new materials for electrochemical applications.

5.6 References

1. Whitehead, A. H.; Pölzler, M.; Gollas, B., Zinc Electrodeposition from a Deep Eutectic System Containing Choline Chloride and Ethylene Glycol. J. Electrochem. Soc. **2010,** 157, D328-D334.
2. Abbott, A. P.; Barron, J. C.; Ryder, K. S., Electrolytic deposition of Zn coatings from ionic liquids based on choline chloride. Trans. Inst. Met. Finish. **2009,** 87, 201-207.
3. Abbott, A. P.; Capper, G.; McKenzie, K. J.; Ryder, K. S., Electrodeposition of zinc–tin alloys from deep eutectic solvents based on choline chloride. J. Electroanal. Chem **2007,** 599, 288-294.
4. Liu, Z.; Abedin, S. Z. E.; Endres, F., Electrodeposition of zinc films from ionic liquids and ionic liquid/water mixtures. Electrochim. Acta **2013,** 89, 635-643.
5. Liu, Z.; El Abedin, S. Z.; Endres, F., Electrochemical and spectroscopic study of Zn(ii) coordination and Zn electrodeposition in three ionic liquids with the trifluoromethylsulfonate anion, different imidazolium ions and their mixtures with water. Phys. Chem. Chem. Phys. **2015,** 17, 15945-15952.
6. Britton, M. M., Magnetic Resonance Imaging of Electrochemical Cells Containing Bulk Metal. Chem. Phys. Chem. **2014,** 15, 1731-1736.
7. Britton, M. M., Magnetic resonance imaging of chemistry. Chem. Soc. Rev. **2010,** 39, 4036-4043.
8. Chandrashekar, S.; Trease, N. M.; Chang, H. J.; Du, L.-S.; Grey, C. P.; Jerschow, A., 7Li MRI of Li batteries reveals location of microstructural lithium. Nat. Mater. **2011,** 11, 311–315
9. Chandrashekar, S.; Oparaji, O.; Yang, G.; Hallinan, D., Communication—7Li MRI Unveils Concentration Dependent Diffusion in Polymer Electrolyte Batteries. J. Electrochem. Soc. **2016,** 163, A2988-A2990.
10. Chang, H. J.; Ilott, A. J.; Trease, N. M.; Mohammadi, M.; Jerschow, A.; Grey, C. P., Correlating Microstructural Lithium Metal Growth with Electrolyte Salt Depletion in Lithium Batteries Using 7Li MRI. J. Am. Chem. Soc. **2015,** 137, 15209-15216.
11. Bray, J. M.; Doswell, C. L.; Pavlovskaya, G. E.; Chen, L.; Kishore, B.; Au, H.; Alptekin, H.; Kendrick, E.; Titirici, M.-M.; Meersmann, T.; Britton, M. M., Operando visualisation of battery chemistry in a sodium-ion battery by 23Na magnetic resonance imaging. Nat. Commun. **2020,** 11, 2083.
12. Ilott, A. J.; Mohammadi, M.; Chang, H. J.; Grey, C. P.; Jerschow, A., Real-time 3D imaging of microstructure growth in battery cells using indirect MRI. Proc. Natl. Acad. Sci. U.S.A. **2016,** 113, 10779-10784.
13. Britton, M. M.; Bayley, P. M.; Howlett, P. C.; Davenport, A. J.; Forsyth, M., In Situ, Real-Time Visualization of Electrochemistry Using Magnetic Resonance Imaging. J. Phys. Chem. Lett. **2013,** 4, 3019-3023.
14. Davenport, A. J.; Forsyth, M.; Britton, M. M., Visualisation of chemical processes during corrosion of zinc using magnetic resonance imaging. Electrochem. Commun. **2010,** 12, 44-47.
15. Hennig J, N. A., Friedburg H. , RARE imaging: a fast imaging method for clinical MR. Magn. Reson. Med. **1986,** 3, 823-833.

16. Bray, J. M.; Davenport, A. J.; Ryder, K. S.; Britton, M. M., Quantitative, In Situ Visualization of Metal-Ion Dissolution and Transport Using H-1 Magnetic Resonance Imaging. Angew. Chem. Int. Ed. **2016,** 55, 9394-9397.

17. Sun, W.; Wang, F.; Zhang, B.; Zhang, M.; Küpers, V.; Ji, X.; Theile, C.; Bieker, P.; Xu, K.; Wang, C.; Winter, M., A rechargeable zinc-air battery based on zinc peroxide chemistry. Science **2021,** 371, 46.

18. Alwast, D.; Schnaidt, J.; Jusys, Z.; Behm, R. J., Ionic Liquid Electrolytes for Metal-Air Batteries: Interactions between O2, Zn2+ and H2O Impurities. J. Electrochem. Soc **2019,** 167, 070505.

Chapter 6 The Summary and Future Works

The research carried out in this thesis has focused on investigating novel electrolytes for zinc electrochemical technologies using NMR and MRI. Three systems have been investigated, two ChCl-based deep eutectic solvents, ethaline and reline, and [C_2C_1Im(TfO)] ionic liquid. Previously, these three electrolytes have been investigated as alternative electrolytes for zinc electroplating.[1-3] They have also shown promise as electrolytes for different Zn electrochemical technologies such as zinc-based batteries.[4-6] However, the high viscosity, and hence, low conductivity of these liquids limit their electrochemical applications. Previous studies have investigated, such as the addition of water, can improve their viscosity and, overcome other poor physical properties. Therefore, it is important to understand how water affects the physical and chemical properties of these liquids, in the presence of Zn, to develop their practical applications. In this thesis, a range of ethaline and reline DESs and [C_2C_1Im(TfO)] IL have been investigated, in the presence and absence of Zn and water.

6.1 Summary

^{19}F NMR T_1 relaxation measurements of TfO anion in [C_2C_1Im(TfO)] revealed that when water is added, Zn ions prefer to associate with water molecules, rather than the TfO anions. ^{19}F T_1 NMR relaxation data suggests that this speciation change occurs gradually until all four coordinated TfO^- ions replaced with water. Two competing effects are observed by the addition of water, increasing the availability of H-bonds and lowering the viscosity of the system. This has been indicated from the T_1 relaxation time measurements of TfO anion and C_2C_1Im cation.

Diffusion measurements of TfO anion and C_2C_1Im cation in $[C_2C_1Im(TfO)]$ were performed as a function of water and for the first time in the presence of Zn. Normalized diffusion co-efficient (D_{ion}/D_{neat}) is used to analyze the excess ionic diffusivity, to understand how zinc and water affect the diffusional properties on a molecular level. At all water concentrations, diffusion co-efficient of TfO anion (D^{-}) exceeds the diffusion co-efficient of C_2C_1Im cation (D^{+}), indicating that TfO anions interact more with water than the C_2C_1Im cation. In the presence of Zn, and small amount of water ($\chi_{water} < 0.1$), D^{-} is almost constant and lower than D^{+}. This indicates that, at this hydration level, water molecules interact more with Zn rather than TfO anion. As water content increases ($\chi_{water} > 0.1$), D^{-} start to increase and exceeds D^{+}, indicating that TfO anion has interacted with water. This means that TfO anions would not associate with water until all zinc ions are solvated by water molecules. To the best of our knowledge, the effect of such a small amount of water, (χ_{water} = 0.015 - 0.25), on the properties of $[C_2C_1Im(TfO)]$ ionic liquid, in presence of Zn, have not been studied before. These ^{19}F NMR studies were used as a foundation to visualize the electroplating of zinc from $Zn(TfO)_2$-$[C_2C_1Im(TfO)]$ systems, *in operando*, using ^{19}F MR relaxation maps. Where ^{19}F NMR relaxation time of TfO anion is affected by the concentration of Zn and water.

Molecular interactions and dynamics in ethaline and reline systems have been investigated using 1D ^{1}H NMR and two-dimensional 2D ^{1}H-^{1}H nuclear Overhauser exchange (NOESY). This research has provided the first quantification of proton exchange in the ethaline and reline systems in the presence and absence of Zn, as a function of water, using ^{1}H-^{1}H exchange spectroscopy (EXSY). In this study, we suggested that the zinc species in ethaline and reline systems are not $[ZnCl_4]^{2-}$ as proposed in previous studies.[7] It has been suggested from 1D ^1H NMR spectra and the calculated exchange rate that the addition of zinc facilitates the proton exchange between protons of the hydroxyl group in choline cation (Ch^+) and ethylene glycol (EG), in the ethaline system. This indicates that co-ordination around Zn brings these protons in close proximity with each other, where EG and Ch^+ are coordinated around the zinc by the oxygen atom in their hydroxyl groups. Whereas, in the reline system, the orientation of Ch^+ and U when they coordinated around the zinc ion, reduces the opportunity for proton exchange between the NH_2 proton in urea and the hydroxyl proton of (Ch^+). Nevertheless, we found the addition of water has changed the zinc speciation in the ethaline system. Where the exchange rate increase in the presence of water, suggests that water, EG, and Ch^+ are all coordinated with the zinc. The addition of water to the Zn-reline system does not change the speciation of zinc. This was indicated from ^1H NMR spectra, where the presence of zinc narrows the line width of hydroxyl and water peaks, which suggests that the presence of Zn slows down their protons exchange. To our knowledge, this is the first study that investigates the effect of zinc or both (water and zinc) on the ^1H NMR spectra of ethaline and reline systems. The influence of water and zinc on relaxation times has been used as a key for interpreting MRI results.

In this thesis, MRI techniques have been used to visualize electrochemistry, *in operando*, such as ions transport and chemical reactions non-invasively while the Zn is being plated from $Zn(TfO)_2$-$[C_2C_1Im(TfO)]$ and $ZnCl_2$-ethaline systems. Relaxation MR studies revealed that during the electroplating of Zn, from $Zn(TfO)_2$-$[C_2C_1Im(TfO)]$ and $ZnCl_2$-ethaline systems, side reactions have occurred, possibly with dissolved oxygen or water. ^{19}F MR T_1 relaxation maps show that, in the presence of water, the zinc anode undergoes a continuous electrodissolotion, even after the electroplating. ^{19}F NMR T_1 relaxation maps specialty quantify the concentration of zinc ions in the vicinity of the copper electrode. During the electroplating of Zn from $Zn(TfO)_2$-[C_2C_1Im(TfO)], the concentration of Zn^{2+} near the copper electrode goes from 0.15 M to 0.08 M. In the $ZnCl_2$-ethaline system, ^{1}H T_1 relaxation was not sensitive to zinc concentration, while ^{1}H T_2 is sensitive to the large zinc concentration difference. Therefore, when 0.3 M $ZnCl_2$ was used to deposit zinc, zinc concentration in the vicinity of Cu, was not low enough to be detected by T_2 relaxation time.

6.2 Future Works

Consequences of COVID and the lockdown in 2020 prevented me completely the final 4 weeks of laboratory work, which would have enabled me to visualize the electroplating of Zn from $ZnCl_2$-ethaline systems, *in operando*. Moreover, it would be interesting to study the surface morphologies of electrodes (anode, cathode), to understand the morphology differences that affect the apparent color of the deposited Zn film. In the last chapter, an unexpected increase in the T_1 relaxation in the vicinity of Zn anode was observed during the electroplating of zinc. As suggested this was attributed to the occurrence of side reactions with water or dissolved oxygen. In order to be more accurate, the dissolved oxygen needs to be removed, this can be done by bubbling argon through the solution or using the freeze/thaw method. Then, it would be possible to repeat the experiment and see if we would observe the same observation or not. In addition, molecular modeling techniques can be used to examine our proposed molecular interactions and zinc speciation in each system, in the presence and absence of water.

In conclusion, by using the MRI techniques, it would be possible to combine the chemical and physical information obtained from NMR spectroscopy with spatial information. This would be very useful to probe what is going on in the electrolyte, and give an insight on the distribution of species in the electrolytes, and possible side reactions while the electrochemical cell is in operation. Overall, these MRI techniques are able to give new insight in future studies, which focus on developing new materials for electrochemical applications. It would be interesting to visualize the electrochemical process inside a zinc-air battery using ethaline, reline, or [C_2C_1Im(TfO)] electrolyte.

6.3 Reference

1. Whitehead, A. H.; Pölzler, M.; Gollas, B., Zinc Electrodeposition from a Deep Eutectic System Containing Choline Chloride and Ethylene Glycol. J. Electrochem. Soc. **2010,** 157, D328-D334.
2. Abbott, A. P.; Barron, J. C.; Ryder, K. S., Electrolytic deposition of Zn coatings from ionic liquids based on choline chloride. Trans. Inst. Met. Finish. **2009,** 87, 201-207.
3. Liu, Z.; Abedin, S. Z. E.; Endres, F., Electrodeposition of zinc films from ionic liquids and ionic liquid/water mixtures. Electrochim. Acta **2013,** 89, 635-643.
4. Kao-ian, W.; Pornprasertsuk, R.; Thamyongkit, P.; Maiyalagan, T.; Kheawhom, S., Rechargeable Zinc-Ion Battery Based on Choline Chloride-Urea Deep Eutectic Solvent. J. Electrochem. Soc. **2019,** 166, A1063-A1069.
5. Kao-ian, W.; Pornprasertsuk, R.; Thamyongkit, P.; Maiyalagan, T.; Kheawhom, S., Rechargeable Zinc-Ion Battery Based on Choline Chloride-Urea Deep Eutectic Solvent. J. Electrochem. Soc. **2019,** 166, A1063-A1069.
6. Fan, J.; Xiao, Q.; Fang, Y.; Li, L.; Yuan, W., A rechargeable Zn/graphite dual-ion battery with an ionic liquid-based electrolyte. Ionics **2019,** 25, 1303-1313.
7. Abbott, A. P.; Barron, J. C.; Frisch, G.; Gurman, S.; Ryder, K. S.; Fernando Silva, A., Double layer effects on metal nucleation in deep eutectic solvents. Phys. Chem. Chem. Phys. **2011,** 13, 10224-31.

Chapter 7 Appendix 1

Table A. 1: Chemical shift values of all protons in the dry $[C_2C_1Im]$ cation, as a function of $Zn(TfO)_2$ concentration. ^1H peaks were calibrated to TMS, and it used as external reference.

$Zn(TfO)_2$ concentration / M	Peak H_a	Peak H_b	Peak H_c	Peak H_d	Peak H_e	Peak H_f
0	8.7498	7.575	7.493	4.145	3.829	1.370
0.02	8.747	7.574	7.491	4.145	3.829	1.370
0.08	8.743	7.569	7.486	4.143	3.829	1.370
0.15	8.738	7.564	7.481	4.144	3.829	1.372

Table A. 2: Chemical shift values of all protons in the $[C_2C_1Im]$ cation, as a function of water mole fraction, in the absence of Zn. ^1H peaks were calibrated to TMS, and it used as external reference.

Pure $[C_2C_1(TfO)]$ as a function of water							
Water mole fraction	Chemical shift / ppm						
	Peak H_a	Peak H_b	Peak H_c	Peak H_d	Peak H_e	Peak H_f	Water Peak
0	8.7498	7.575	7.493	4.145	3.829	1.370	
0.015					3.829	1.370	
0.05	8.7488	7.571	7.489	4.145	3.829	1.370	3.52
0.1	8.7457	7.568	7.486	4.145	3.829	1.370	3.44
0.15	8.7437	7.564	7.482	4.145	3.829	1.370	3.39
0.2	8.7406	7.560	7.478	4.145	3.829	1.370	3.4
0.25	8.7371	7.555	7.473	4.145	3.829	1.370	3.41

Table A. 3: Chemical shift values of all protons in the $[C_2C_1Im]$ cation, as a function of water mole fraction, in the presence of 0.02 M of $Zn(TfO)_2$. ^1H peaks were calibrated to TMS, and it used as external reference.

Water mole fraction	Chemical shift / ppm						
	Peak H_a	Peak H_b	Peak H_c	Peak H_d	Peak H_e	Peak H_f	Water Peak
0	8.747	7.574	7.491	4.145	3.829	1.370	
0.015	8.747	7.574	7.491	4.145	3.829	1.370	
0.05	8.745	7.571	7.487	4.145	3.829	1.370	3.52
0.1	8.742	7.566	7.484	4.145	3.829	1.370	3.42
0.15	8.740	7.563	7.480	4.145	3.829	1.370	3.39
0.2	8.737	7.558	7.476	4.145	3.829	1.370	3.4
0.25	8.735	7.555	7.472	4.145	3.829	1.370	3.38

Table A. 4: Chemical shift values of all protons in the [C_2C_1Im] cation, as a function of water mole fraction, in the presence of 0.08 M of Zn(TfO)$_2$. ^{1}H peaks were calibrated to TMS, and it used as external reference.

Water mole fraction	Chemical shift / ppm						
	Peak H_a	Peak H_b	Peak H_c	Peak H_d	Peak H_e	Peak H_f	Water Peak
0	8.743	7.569	7.486	4.143	3.829	1.370	
0.015	8.743	7.569	7.486	4.143	3.829	1.370	5.53
0.05	8.742	7.568	7.485	4.143	3.829	1.370	5.14
0.1	8.738	7.564	7.481	4.143	3.829	1.370	4.53
0.15	8.736	7.561	7.478	4.143	3.829	1.370	4.2
0.2	8.733	7.557	7.475	4.143	3.829	1.370	4.02
0.25	8.731	7.554	7.471	4.143	3.829	1.370	3.91

Table A. 5: Chemical shift values of all protons in the [C_2C_1Im] cation, as a function of water mole fraction, in the presence of 0.15 M of Zn(TfO)$_2$. ^{1}H peaks were calibrated to TMS, and it used as external reference.

Water mole fraction	Chemical shift / ppm						
	Peak H_a	Peak H_b	Peak H_c	Peak H_d	Peak H_e	Peak H_f	Water Peak
0	8.738	7.564	7.481	4.144	3.829	1.372	
0.015	8.738	7.564	7.481	4.144	3.829	1.372	6.04
0.05	8.738	7.564	7.481	4.144	3.829	1.372	5.77
0.1	8.736	7.562	7.480	4.144	3.829	1.372	5.43
0.15	8.733	7.559	7.477	4.144	3.829	1.372	5.03
0.2	8.730	7.555	7.473	4.144	3.829	1.372	4.69
0.25	8.727	7.550	7.469	4.144	3.829	1.372	4.44

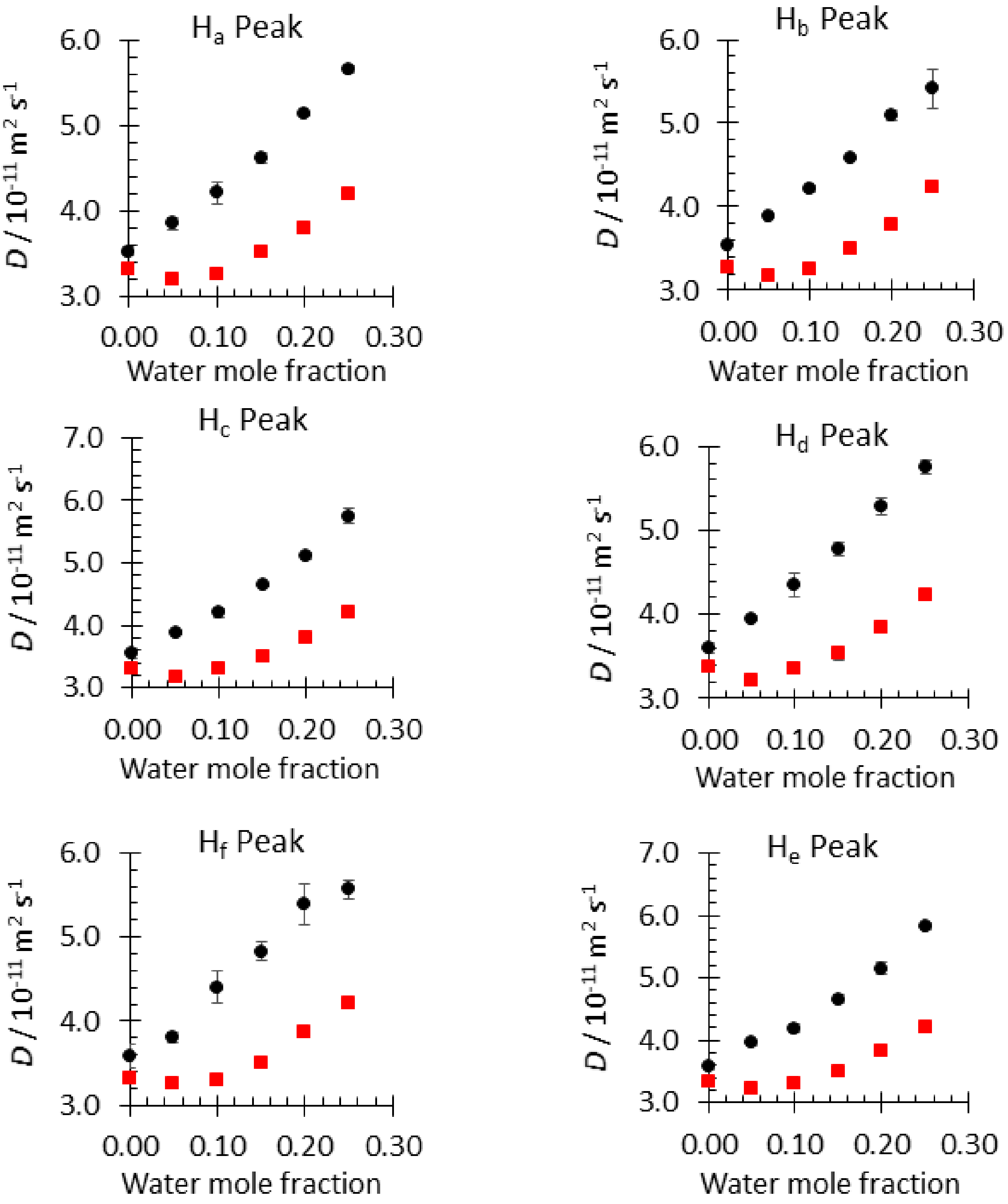

Figure A. 1: ^{1}H NMR diffusion co-efficients of each protons in the $C_2C_1Im^+$ cation, as a function of water mole fraction, in the presence (🟥) and absence (●) of 0.15 M $Zn(TfO)_2$. ^{1}H diffusion measurements were collected using a maximum gradient ($\boldsymbol{G}_{max}$) of 300 G cm^{-1}, pulse duration (δ) of 2 ms and observation time (Δ) of 60 ms.

PCCP

ROYAL SOCIETY OF CHEMISTRY

PAPER

View Article Online
View Journal | View Issue

Cite this: *Phys. Chem. Chem. Phys.*, 2021, 23, 21913

Probing the influence of Zn and water on solvation and dynamics in ethaline and reline deep eutectic solvents by ^{1}H nuclear magnetic resonance†

Yasmeen M. AlZahrani and Melanie M. Britton *

A range of ethaline and reline deep eutectic solvents (DESs) have been investigated in the absence and presence of Zn (0 0.3 M) and water (0 29 wt%) by one-dimensional ^{1}H NMR spectroscopy, two-dimensional ^{1}H ^{1}H nuclear Overhauser effect and exchange spectroscopy, ^{1}H T_1 NMR relaxation times and ^{1}H NMR diffusion. The role of zinc and water in controlling solvation and microstructure in reline and ethaline were investigated. We show that in ethaline there is proton exchange between hydroxyl groups in ethaline glycol and choline chloride. The rate of exchange between these protons is found to significantly increase in the presence of Zn, but decreases with increasing water content. In the case of reline, no proton exchange is observed between the amide protons in urea and hydroxyl protons in choline chloride. However, the addition of water decreases the viscosity of the system, as well as changes the distance between amide and hydroxyl protons in urea and choline chloride, respectively. The addition of Zn does not appear to change the interactions between urea and choline chloride species, but does reduce the rate of exchange between water and hydroxyl protons in reline formulations containing water.

Received 14th July 2021,
Accepted 15th September 2021

DOI: 10.1039/d1cp03204f

rsc.li/pccp

Introduction

In recent years, there has been increasing interest in the use of deep eutectic solvents (DESs) as a replacement for aqueous and organic electrolytes in many electrochemical applications, including metal electrodeposition,[1–3] metal electropolishing[4,5] and batteries.[6] This increasing interest largely arises from their high chemical stability, wide potential window, low flammability and volatility. Another important benefit of DESs is that they can be formed by mixing, typically, inexpensive, low-toxicity, biodegradable components, and, hence, also offer economic and environmental benefits.[7–9]

A widely investigated class of DES is based on the quaternary ammonium salt choline chloride (ChCl).[6,10,11] This class includes ethaline, which is a mixture of 1 : 2 molar ratio of ChCl and ethylene glycol (EG), and reline, a 1 : 2 molar ratio mixture of ChCl and urea (U).[12] While multiple interactions contribute to the intermolecular network within DESs, including van der Waals interactions, hydrogen bonding and/or ionic bonding,[13] it is hydrogen bonding that is considered to be the primary cause of their melting point depression and physicochemical properties, such as viscosity and conductivity.[8] Ethaline and reline have been investigated as more sustainable electrolytes in the electrodeposition of Zn, as an anti-corrosion layer.[3,11,14,15] However, zinc deposits have been found to have different morphologies, depending on the DES used, which has been attributed to differences in the hydrogen bond network between ethaline and reline systems[15] and zinc ion species, which play an important role in the mechanisms of deposition.[3] Abbott *et al.*[15] proposed that the predominant zinc species in both ethaline and reline systems is $[ZnCl_4]^{2-}$. Reline has also been investigated as a novel electrolyte for rechargeable zinc-batteries.[6] Reversible plating/stripping of zinc species has been observed, without hydrogen evolution or the formation of a passivation layer on the zinc electrode.[6] However, despite this initial interest in these DES systems for Zn-electrochemical applications, there are several challenges currently preventing their commercialisation. Primarily, these are associated with poor physical properties, such as their typically high viscosity, and, hence, lower conductivity.[12] Also, a lack of understanding of the species formed has limited the optimisation of DES formulations.[16]

In order to overcome poor physical properties in DESs, the addition of water has been investigated.[12,17–20] Computer simulations have revealed that the addition of water, to

---

School of Chemistry, University of Birmingham, Edgbaston, B15 2TT, UK.
E mail: [redacted]

† Electronic supplementary information (ESI) available. See DOI: 10.1039/d1cp03204f

ethaline or reline DESs, decreases the number of hydrogen bonds formed and consequently lowers the viscosity of both DES systems.[20] However, as more water is added, it has been observed[12] that ChCl-based DESs start to lose their DES structure, and form aqueous solutions, above a 1 : 1 equivalent of water:chloride. This transition is also reported to change the electrochemical properties of ChCl-based DESs, in particular, by narrowing their potential window.[21,22] Cyclic voltammetry (CV) experiments have shown that reline retains a wide potential window until the amount of added water reaches 9 wt%.[21] The effects of adding water to reline[21] and ethaline,[22] for electroplating Cu[22] and Ni[21] have been investigated. It has been observed that the addition of 15 wt% water in ethaline, for Cu electroplating, results in a reduction in the ethaline viscosity without reducing the wide potential of the electolyte.[22] Adding 6 wt% of water to reline, for nickel electroplating, lowers the reline viscosity, and suppresses nickel dendritic growth, resulting in a smooth, dense nickel deposit.[21]

The study of speciation and solvation, and the effect of additives such as water, on the chemical and physical properties of DES have been investigated computationally, using quantum mechanics (QM) simulations,[18,23] and experimentally, using nuclear magnetic resonance (NMR),[24] Fourier-transform infra-red (FTIR) and Raman spectroscopies.[25] In these studies, it has been proposed that the addition of water affects the hydrogen bond network of DESs, by forming new hydrogen bonds between water and DESs components, which subsequently affect the properties of the DES, such as viscosity.[18,23] Moreover, it has been observed that the number of hydrogen bonds formed between water and EG, in ethaline, are comparatively higher than those formed between water and U in the reline system.[25] In the case of reline, while water can hydrogen bond with ChCl and U,[19,23] it has been found that water molecules also occupy the interstices within the hydrogen bond network, reducing the number of hydrogen bonds between water and ChCl or U.[25] Following investigation by diffusion NMR, D'Agostino *et al.*[12] proposed that, in the presence of 20 wt% of water, ethaline forms a homogenous ethaline–water mixture, while reline forms a non-homogeneous reline–water mixture with a rich-water region. Zinc speciation in ethaline and reline has been studied using mass spectrometry.[26] However, as this is typically an *ex situ* technique, it is not able to provide information on speciation during electrochemical processes. Non-invasive, *in situ* techniques have been explored, which are able to provide information on speciation and dynamics of metal ions in DES electrolytes.[26] Furthermore, there is growing interest in developing operando techniques for observing speciation and dynamics, *in situ* and in real time, under working conditions. Such techniques have been demonstrated using ^{1}H NMR T_1 relaxation times to determine Zn speciation in aqueous electrolytes during Zn corrosion and discharging of a Zn-battery.[27,28]

In this paper, a range of ethaline and reline DESs have been investigated, in the absence and presence of Zn (0–0.3 M) and water (0–29 wt%). Molecular interactions and dynamics have been investigated using one-dimensional (1D) ^{1}H NMR and two-dimensional (2D) ^{1}H–^{1}H nuclear Overhauser exchange (NOESY) and exchange (EXSY) NMR spectroscopy. The influence of zinc and water, on the mobility and microstructure with each DES system, has been investigated using ^{1}H NMR T_1 relaxation time and diffusion measurements. We demonstrate that the zinc species are different in ethaline and reline, and the interaction between zinc and water is also different in ethaline and reline.

Experimental details

Materials and samples preparation

Choline chloride (ChCl, 99%), ethylene glycol (EG, 99.8%), urea (U, 99.9%) and zinc chloride ($ZnCl_2$, 99.99%) were supplied by Sigma-Aldrich. All components were used without further purification, but dried in a vacuum oven under reduced pressure (100 mbar), at 80 °C (ChCl, EG and U) or at 120 °C ($ZnCl_2$), for a minimum of 24 hours and were stored in a glove-box under argon atmosphere. In a glove-box, ethaline was prepared by mixing ChCl and EG in a 1 : 2 molar ratio and reline was prepared by mixing ChCl and U in a 1 : 2 molar ratio before sonication and heating to 60 °C until homogenous clear colourless liquids were formed. Solutions of zinc in ethaline or reline were prepared in a glove-box by dissolving dry $ZnCl_2$ in either ethaline or reline, over a range of $ZnCl_2$ concentrations (0.1, 0.2 and 0.3 M in ethaline and 0.3 M in reline) at 25 °C. A range of concentrations of water were prepared by adding water (Nanopure filtered, resistivity 18 MΩ cm), to ethaline and reline, in the presence and absence of 0.3 M $ZnCl_2$. Solutions of water in ethaline, at concentrations of 2.7, 5.5, 8.3, 16 and 29.2 wt%, were prepared by adding 26, 52, 79, 151 and 277 μl, respectively, of water to 850 μl of ethaline. Solutions of water in reline, at concentrations of 5.5, 8.3 and 26.2 wt%, were prepared by adding by adding 58.5, 88 and 279 μl of water, respectively, to 850 μl of reline. Samples were put, immediately after preparation, into 5 mm Wilmad® NMR tubes fitted with J Young valves, to prevent the absorption of additional water. NMR measurements were performed <12 h after sample preparation. The amount of water in each sample was confirmed using ^{1}H NMR spectroscopy.

NMR measurements

NMR data were collected on a Bruker AVANCE III HD 300 spectrometer equipped with a 7 T vertical wide-bore superconducting magnet, operating at a proton resonance frequency of 300.13 MHz, with a 10 mm ^{1}H diff30 radiofrequency (RF) coil. NMR experiments were performed at 293 ± 0.3 K, controlled by the temperature of the water-cooled gradient coils. The 90° RF pulse was calibrated for each sample and found to be 20 ± 1 μs.

^{1}H NMR spectra were acquired using a pulse-acquire sequence, with a repetition time of 6 s. The chemical shift of peaks were calibrated to an external reference of TMS in deuterated chloroform, which was put in a 10 mm NMR tube, with the sample in a 5 mm NMR tube inside. 2D ^{1}H–^{1}H NOESY experiments were acquired using the sequence, [90° τ_1 90° τ_{mix} 90° acq], with 256 point in the F1 direction and 2048 in the F2 direction, with a repetition time of 2 s, 16 signal averages and 16 dummy scans. The mixing time, τ_{mix}, was increased from 0 to 300 ms, over a series of six experiments. Proton exchange rates (k_{ex}) were calculated,[29] by fitting, in Kaleidagraph,[30] the signal intensity of exchange peaks (I_{AB} and I_{BA}), as a function of mixing time (τ_{mix}), to eqn (1):

$$I_{\text{AB}} = I_{\text{BA}} = P_{\text{A}}P_{\text{B}}(1 \quad \exp(\quad k_{\text{ex}}\tau_{\text{mix}}))\exp(\quad R_1\tau_{\text{mix}}) \tag{1}$$

where $P_{\text{A}} = \dfrac{I_{\text{A}}}{I_{\text{A}} + I_{\text{B}}}$, $P_{\text{B}} = \dfrac{I_{\text{B}}}{I_{\text{A}} + I_{\text{B}}}$ and $R_1 = (R_{1\text{A}} + R_{1\text{B}})$, I_{A} and I_{B} are the intensities at $\tau_{\text{mix}} = 0$ ms, and $R_{1\text{A}}$, $R_{1\text{B}}$ are the relaxation rates of species A and B. In the fitting, an average value of I_{AB} and I_{BA} was used. Exchange peaks were identified as having the same phase as the diagonal peaks, which, in this study, are plotted positively. Cross-peaks arising from the nOe have a phase depending on the molecular size of species and viscosity of the solvent.[31] In the case of small molecules in low viscosity DES, where tumbling rates are faster, the nOe cross-peaks are expected to have the opposite sign to diagonal peaks and are negative where diagonal peaks are positive. For molecules in high viscosity solvents, where molecular tumbling is slow, the nOe cross-peaks are expected to be positive, where diagonal peaks are also positive.

Spin–lattice (T_1) NMR relaxation times were measured using an inversion recovery experiment,[31] $[180^\circ \quad \tau \quad 90^\circ \quad \text{acq}]_n$, with a repetition time of 6 s and 8 signal averages. A series of spectra ($n = 12$) were collected with logarithmically spaced time delays, τ, ranging from 5×10^{-6} s to 6 s. T_1 relaxation times were determined by fitting the normalised signal intensity ($I_{(\tau)}/I_{(0)}$), as a function of time, to eqn (3).

$$\frac{I(\tau)}{I(0)} = 1 \quad 2\exp^{\frac{-\tau}{T_1}} \tag{3}$$

Self-diffusion co-efficients (D) were measured using a pulsed gradient stimulated echo (PGSTE) sequence[31] with 16 gradient steps. Diffusion measurements of dry ethaline samples were collected with a maximum gradient ($G_{\max}$) of 300 G cm^{-1}, pulse duration (δ) of 2 ms, observation time ($\varDelta$) of 60 ms, and repetition time of 2 s. Diffusion measurements of dry reline samples were collected using $G_{\max} = 600$ G cm^{-1}, $\delta = 2$ ms, $\varDelta = 100$ ms, with a repetition time of 2 s. Diffusion measurements for ethaline and reline systems containing water were collected using $G_{\max} = 300$ G cm^{-1}, $\delta = 2$ ms, $\varDelta = 30$ ms, and a repetition time of 4 s. The average self-diffusion co-efficients (D) were determined by fitting the normalised signal intensity as a function of gradient strength, ($I_{(G)}/I_{(0)}$), to the Stejskal–Tanner[32] eqn (4). Where a single diffusion co-efficient was not sufficient to fit the data, fitting to a bi-exponential function was performed.

$$\frac{I(G)}{I(0)} = \exp\left[\quad \gamma^2\delta^2G^2D\left(\varDelta \quad \frac{\delta}{3}\right)\right] \tag{4}$$

Results

Fig. 1 shows the ^{1}H NMR spectra for dry ethaline and reline DESs, along with the molecular structures and proton labelling scheme of constituent species in each DES. The broad line widths observed for peaks in the ^{1}H NMR spectrum of reline are indicative of the higher viscosity for reline compared to ethaline.

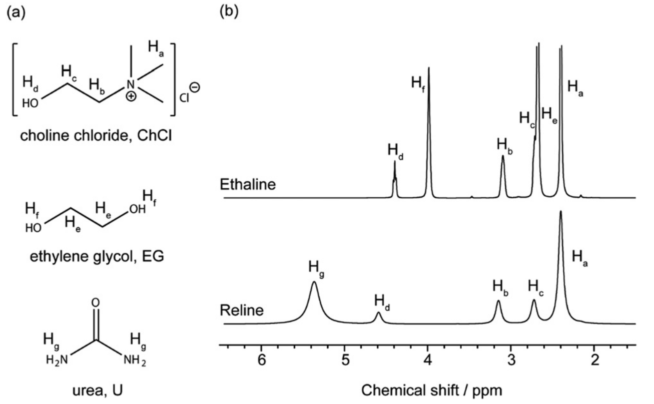

Fig. 1 (a) Molecular structures for the constituent species of ethaline (1ChCl:2EG) and reline (1ChCl:2U) with proton numbering scheme, and (b) ^{1}H NMR spectra for pure dry ethaline and reline systems, at 293 K.

^{1}H NMR spectra for dry ethaline and reline, with increasing ZnCl$_2$ concentration, are shown in Fig. 2. For both reline and ethaline, no visible change in viscosity was observed upon the addition of zinc. This observation is consistent with the ^{1}H NMR spectra in Fig. 2, which do not show a change in line width for the peaks of the non-exchanging protons (H$_a$, H$_b$, H$_c$ and H$_e$; Table S1 in the ESI†). In the ethaline system, the line widths for hydroxyl protons in choline cation (Ch$^+$) and EG (H$_d$ and H$_f$ respectively) are observed to increase gradually, as the concentration of Zn increases. This is matched by a slight upfield shift of the peak for the hydroxyl proton in Ch$^+$ (H$_d$). However, in the reline system, the line width and chemical shift for the H$_d$ peak do not appear to be affected by the addition of zinc.

Fig. 3 shows ^{1}H NMR spectra for ethaline, in the presence and absence of Zn and water. There is a gradual shift for all hydroxyl proton peaks (H$_d$, H$_f$ and H$_w$) downfield, as the water content increases. Also, the addition of water narrows the line width for (H$_a$, H$_b$, H$_c$ and H$_e$) peaks, irrespective of whether Zn is present or not. However, the presence of zinc broadens the H$_d$, H$_f$ and H$_w$ peaks.

Fig. 4 shows ^{1}H NMR spectra for reline, in the presence and absence of Zn and water. The presence of Zn does not appear to have a significant effect on the ^{1}H NMR spectra. However, the presence of water leads to a significant reduction in line width of the urea peak (H$_g$), which also shifts upfield as the water content increases. The water peak (H$_w$) shifts gradually to higher chemical shift, as water content increases. As the water content increases, both in the presence and absence of Zn, there is a slight reduction in the line width of the H$_a$, H$_b$, H$_c$ and H$_g$ peaks. The addition of water broadens, and slightly shifts down field, the peak for the hydroxyl protons in Ch$^+$ (H$_d$). At the highest water content, the H$_d$ peak overlaps completely with H$_w$ peak, in the absence of Zn (Fig. 4a), whereas in the presence of Zn (Fig. 4b), the H$_d$ peak remains at 4.6 ppm. However, the presence of zinc affects the line width of H$_d$ and H$_w$ peaks, which become narrower in the presence of Zn.

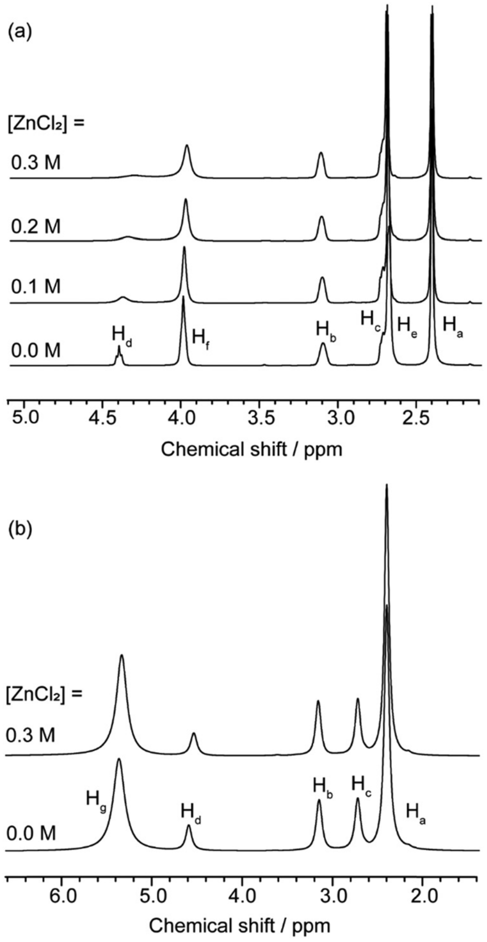

Fig. 2 A series of ^{1}H NMR spectra for dry (a) ethaline and (b) reline as a function of $ZnCl_2$ concentration, at 293 K. Molecular structures and numbering scheme of peak assignments were presented in Fig. 1. Associated line widths can be found in Table S1 in the ESI.†

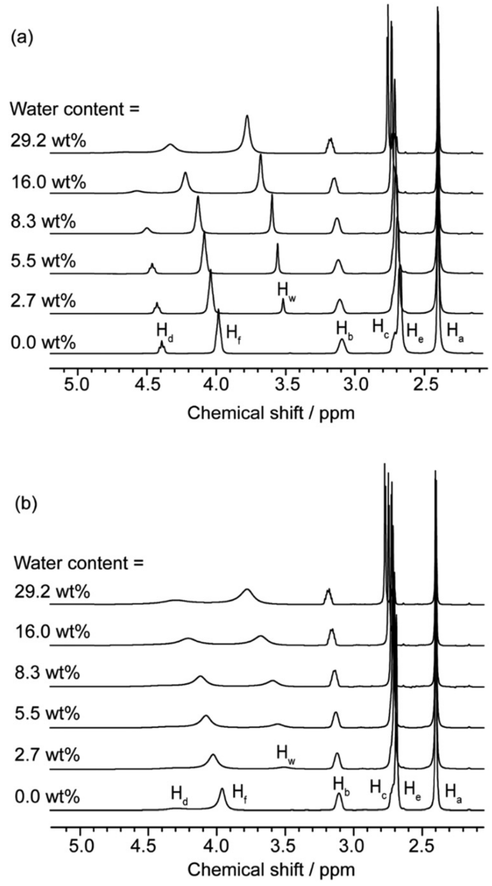

Fig. 3 A series of ^{1}H NMR spectra for ethaline system in the absence (a) and presence (b) of 0.3 M $ZnCl_2$ as a function of water content (H_w), at 293 K. Molecular structures and numbering scheme of peak assignments were presented in Fig. 1. Associated line widths can be found in Table S2 in the ESI.†

Fig. 5 shows 2D NOESY spectra for dry ethaline, in the presence and absence of $ZnCl_2$. In the absence of Zn, intense exchange (positive) peaks are observed between the hydroxyl protons (H_d and H_f) of Ch^+ and EG (Fig. 5a). The hydroxyl proton peaks, and exchange peaks, broaden in the presence of Zn (Fig. 5b), indicating increased exchange. 2D NOESY spectra for ethaline with 8.3 wt% water, in the presence and absence Zn, are shown in Fig. 6. Exchange peaks are observed between water (H_w) and the hydroxyl protons in Ch^+ and EG (H_d and H_f). In the presence of Zn, however, these exchange peaks are broader. In addition to the exchange peaks, nOe (negative) cross-peaks are also observed between the other protons in EG and Ch^+, which appear to become less intense in the presence of Zn.

Fig. 7–9 show 2D NOESY spectra for reline with 0, 8.3 and 26 wt% water, respectively, in the presence and absence of $ZnCl_2$. The higher viscosity of reline at 0 and 8.3 wt% water has led to all cross-peaks being positive.[33] In the dry reline system (Fig. 7), cross-peaks peaks are observed between the hydroxyl protons in Ch^+ (H_d) and the amide protons in U (H_g). However, as the viscosity of this system is high, it is not possible to identify whether these cross-peaks arise from exchange or nOe interactions. In the presence of water (Fig. 8), no cross-peaks are observed between these protons, indicating no exchange nor spatial proximity. The spectra in Fig. 8 show cross-peaks between H_g protons and the aliphatic protons in Ch^+ (H_a, H_b and H_c). These are negative and hence arise from the nOe, indicating their close spatial-proximity. Table 1 shows the proton exchange rates (k_{ex}), for both reline and ethaline, determined from the 2D ^1H–^1H NOESY spectra. Proton exchange is observed between the hydroxyl protons in Ch^+ (H_d) and water protons (H_w) in Fig. 8 and 9, as has been observed previously.[24] This exchange appears to increase with increasing water concentration (Fig. 4), resulting in a coalesced peak in the NOESY spectrum (Fig. 9) and a cross peak between $H_{d,w}$ and the amide protons H_g.

Diffusion co-efficients for Ch^+, in dry ethaline and reline, are shown in Table 2. It can be seen that, Ch^+ has a lower mobility in reline than ethaline, as expected because of the higher viscosity in reline. The diffusion coefficient for Ch^+ is largely unaffected by the presence of zinc. However, in ethaline, the diffusion co-efficient for the hydroxyl (H_d) and methyl protons (H_a), in Ch^+, are the same in the absence of Zn, but are different in the presence of Zn.

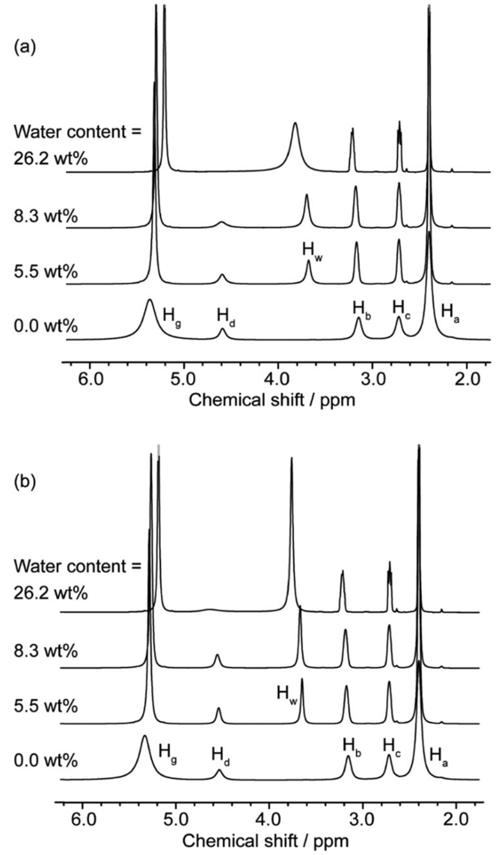

Fig. 4 A series of ^{1}H NMR spectra for reline system in the absence (a) and presence (b) of 0.3 M $ZnCl_2$ as a function of water content (H_w), at 293 K. Molecular structures and numbering scheme of peak assignments were presented in Fig. 1. Associated line widths can be found in Table S3 in the ESI.†

Diffusion co-efficients for ethaline species, with increasing water content, in the absence and presence of $ZnCl_2$, are presented in Tables 3 and 4, respectively. These data show that diffusion co-efficients, for all species, increase with increasing water content. At lower concentrations of water (≤8.3 wt%), two diffusion co-efficients are observed for water. However, at high concentrations of water (29 wt%), only a single diffusion co-efficient is observed.

Diffusion co-efficients for Ch^+, U and water in reline, with increasing water content and in the absence and presence of $ZnCl_2$, are presented in Tables 5 and 6, respectively. It can be seen that the diffusion co-efficients of both Ch^+ and U increase with the addition of water, as expected. Two diffusion co-efficients are observed for water for all water concentrations. The diffusion co-efficients reported in our study are comparable with those reported by D'Agostino *et al.*[12] However, only a single diffusion coefficient was observed for water in their study.

Fig. 9 shows the T_1 relaxation times for Ch^+, in ethaline and reline, in the presence and absence of zinc and water. It can be seen that for ethaline, the T_1 NMR relaxation time for the H_a protons in Ch^+ increases, monotonically, with water content, but with a slight discontinuity around 8 wt% of water. However, for reline, the T_1 relaxation time for the H_a protons in Ch^+ decreases on addition of water, but then increases with increasing water content.

Discussion

The viscosity of ethaline is lower than the viscosity of reline, because U is a much stronger HBD than EG, therefore, reline is ten times more viscose than ethaline.[15] The effect of zinc on the viscosity of reline and ethaline has been studied previously.[15] It has been shown that the viscosity of ethaline is largely unaffected by the addition of Zn, but for reline, a significant decrease in viscosity was observed with increasing Zn.[15] The effect is expected to be minimised for ethaline because it already has a low viscosity (∼22 cP for [$ZnCl_2$] = 0 to 0.3 mol dm^{-3}), compared to reline (∼800 cP to 280 cP for [$ZnCl_2$] = 0 to 0.3 mol dm^{-3}).[15] However, the significant change in viscosity for reline, when Zn was added, was not observed in our study. This could be explained by our use of dried $ZnCl_2$,

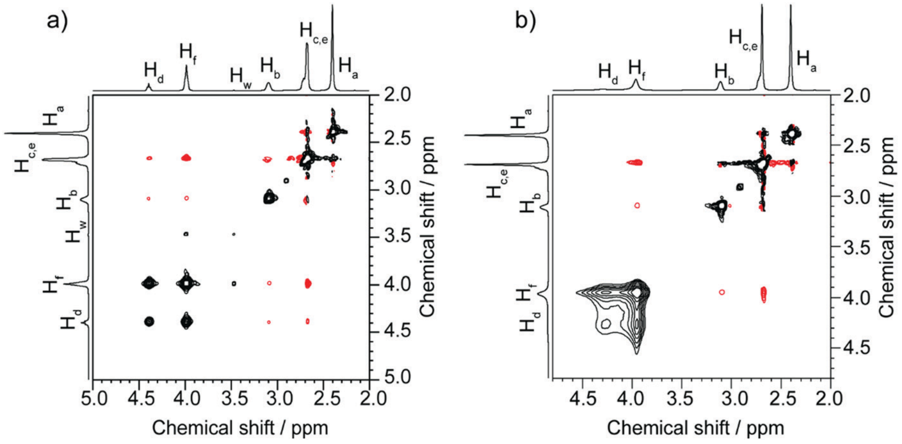

Fig. 5 ^{1}H ^{1}H NOESY NMR spectra for dry ethaline samples in the absence (a) and presence (b) of 0.3 M $ZnCl_2$, for a mixing time τ_m 300 ms. Positive peaks are black, negative peaks are red.

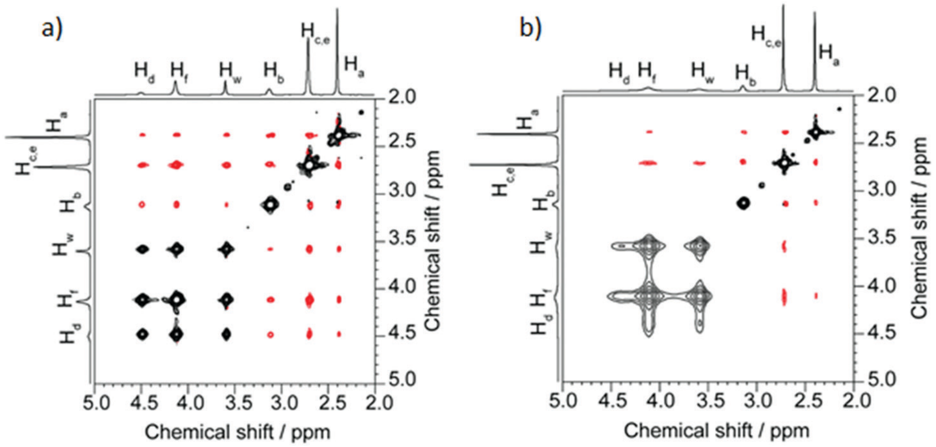

Fig. 6 ^1H ^1H NOESY NMR spectra for ethaline samples with addition of 8.3 wt% water in the absence (a) and presence (b) of 0.3 M $ZnCl_2$, for a mixing time τ_m 300 ms. Positive peaks are black, negative peaks are red.

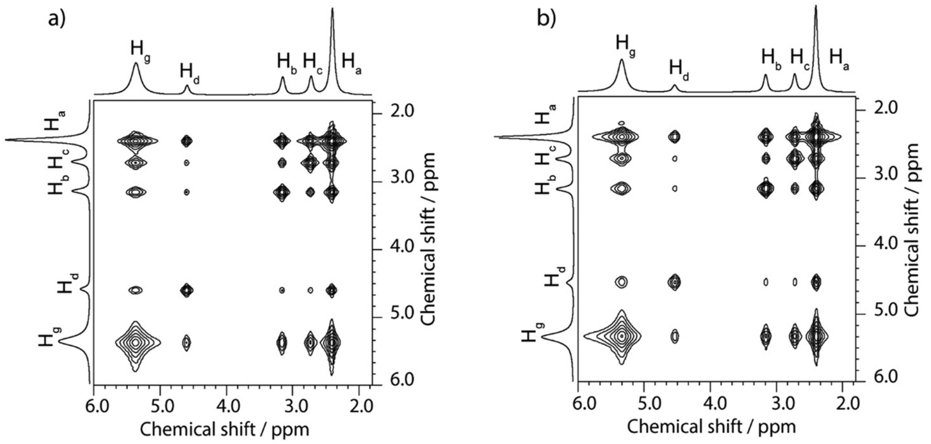

Fig. 7 ^1H ^1H NOESY NMR spectra for dry reline samples in the absence (a) and presence (b) of 0.3 M $ZnCl_2$, for a mixing time τ_m 100 ms. All peaks are positive (black) and no negative peaks (red) are observed.

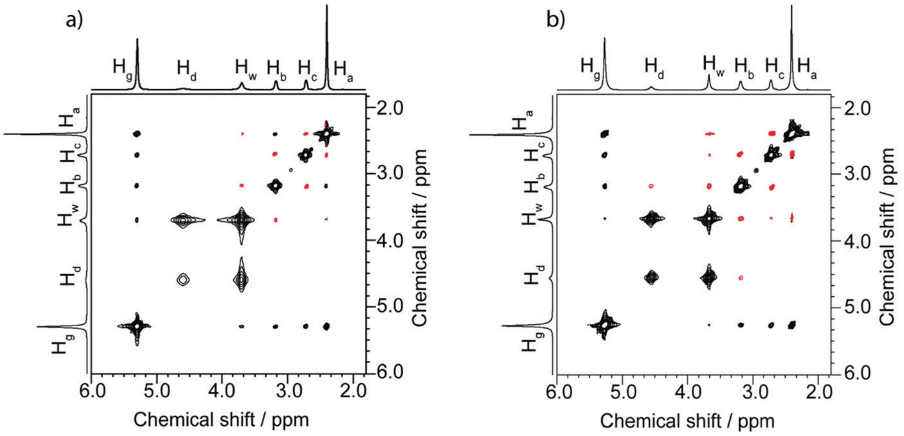

Fig. 8 ^1H ^1H NOESY NMR spectra for reline samples with addition of 8.3 wt% water in the absence (a) and presence (b) of 0.3 M $ZnCl_2$, for a mixing time τ_m 300 ms. Positive peaks are black, negative peaks are red.

Table 1 Proton exchange rates (k_{ex}) for ethaline and reline systems, at [Zn^{2+}] = 0 and 0.3 M, at different water concentrations. Note, some exchange rates could not determine due to overlap of peaks, such as H_f–H_d for dry ethaline in presence of Zn. Also, an exchange rate between H_g–H_w protons could not be determined from the mixing times used in these experiments, where longer mixing times required

Water wt%	[Zn^{2+}] = 0 M	[Zn^{2+}] = 0.3 M
Ethaline		
0	k_{ex} (H_f–H_d) 11.36 s^{-1}	
8.3	k_{ex} (H_f–H_d) 8.66 s^{-1} k_{ex} (H_w–H_f) 5.71 s^{-1} k_{ex} (H_w–H_d) 1.03 s^{-1}	k_{ex} ($H_{d,f}$–H_w) 77.8 s^{-1}
29	k_{ex} (H_f–H_d) 7.96 s^{-1} k_{ex} (H_w–H_f) 29.3 s^{-1} k_{ex} (H_w–H_d) 10.8 s^{-1}	k_{ex} ($H_{d,f}$–H_w) 124.8 s^{-1}
Reline		
8.3	k_{ex} (H_d–H_w) 77 s^{-1}	k_{ex} (H_d–H_w) 24 s^{-1}

Table 2 Diffusion co-efficients of Ch$^+$ alkyl protons (H_a) and Ch$^+$ hydroxyl protons (H_d) in dry ethaline and reline species in the absence and presence of $ZnCl_2$

	Diffusion co-efficient/10^{-11} m^2 s^{-1}	
System	H_a	H_d
Ethaline	1.92 ± 0.06	1.90 ± 0.07
Ethaline + 0.3 M $ZnCl_2$	1.76 ± 0.01	2.23 ± 0.07
Reline	0.05 ± 0.01	0.06 ± 0.01
Reline + 0.3 M $ZnCl_2$	0.06 ± 0.01	0.06 ± 0.01

Table 3 Diffusion co-efficients of ethaline species, Ch$^+$ (H_a) and EG (H_e), as a function of water (H_w) in the absence of zinc

	Diffusion co-efficient/10^{-11} m^2 s^{-1}, (contribution %)		
Water (wt%)	H_a	H_e	H_w
5.5	3.12 ± 0.01	5.46 ± 0.03	3.40 ± 0.08 (5.1 ± 0.1%) 15.47 ± 0.04 (94.9 ± 0.1%)
8.3	3.66 ± 0.01	6.33 ± 0.14	4.23 ± 0.01 (14.1 ± 1.1%) 16.25 ± 0.49 (85.9 ± 1.1%)
29.2	8.91 ± 0.07	14.61 ± 1.00	30.75 ± 0.46

Table 4 Diffusion co-efficients of ethaline species, Ch$^+$ (H_a) and EG (H_e), as a function of water (H_w) in the presence of 0.3 M $ZnCl_2$

	Diffusion co-efficient/10^{-11} m^2 s^{-1}, (contribution %)		
Water wt%	H_a	H_e	H_w
5.5	2.91 ± 0.03	5.19 ± 0.01	1.72 ± 0.23 (13.1 ± 3.4%) 14.22 ± 0.25 (86.9 ± 3.4%)
8.3	3.54 ± 0.06	6.34 ± 0.20	3.28 ± 0.49 (57.0 ± 23.7%) 12.75 ± 4.94 (43.0 ± 23.7%)
29.2	8.90 ± 0.45	16.24 ± 2.00	9.60 ± 0.71 (10.8 ± 2.6%) 31.75 ± 0.78 (89.2 ± 2.6%)

compared to the previous study,[15] which used $ZnCl_2$ as obtained. As $ZnCl_2$ is hygroscopic, it is possible the previously observed change in viscosity could be due to the introduction of water. The possible effects of added water to the viscosity of ethaline are not observed, because of its significantly lower viscosity.

From previous studies of ethaline,[34] it is known that the hydroxyl groups of Ch$^+$ and EG coordinate around the Cl$^-$, bringing the H_d and H_f protons into close proximity. It is expected that this close proximity will facilitate proton exchange, which is observed in this study, by the presence of positive cross-peaks between H_d and H_f protons in the NOESY spectrum of pure ethaline (Fig. 5a). When water is added, it is known[17] that water also coordinates with the Cl$^-$, Ch$^+$ and EG. Again, this proximity is expected to facilitate exchange between H_d, H_f and H_w protons. This has been observed previously by diffusion NMR[12] and is also observed, in this study, by the positive cross-peaks between H_d, H_f and H_w protons in the NOESY spectrum (Fig. 6a). However, this study has shown, for the first time, that the addition of zinc, to both pure ethaline and ethaline-water systems, increases the rate of exchange between these protons (Table 1). This increase in proton exchange explains the increase in diffusion co-efficient for the H_d proton in the presence of Zn (Table 2). These observations indicate that EG, Ch$^+$ and water are predominantly co-ordinated around Zn^{2+}, rather than Cl$^-$.

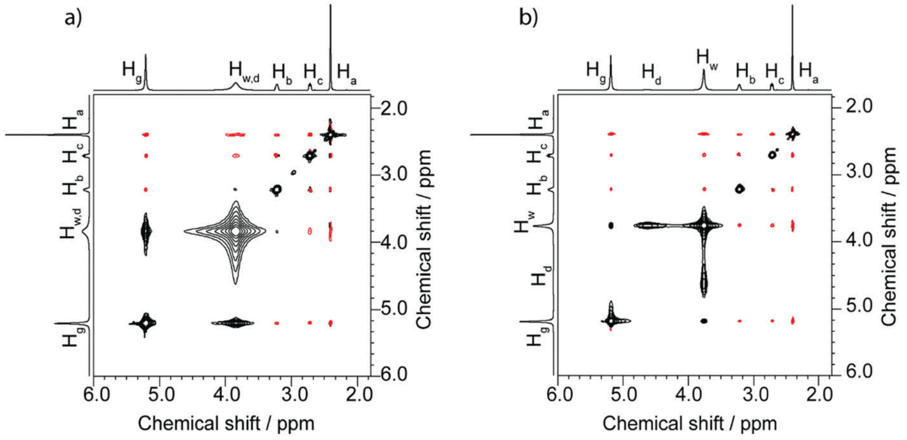

Fig. 9 ^{1}H–^{1}H NOESY NMR spectra for reline samples with addition of 26 wt% water in the absence (a) and presence (b) of 0.3 M $ZnCl_2$, for a mixing time τ_m = 100 ms. Positive peaks are black, negative (nOe) peaks are red.

Table 5 Diffusion coefficients of reline species, Ch^+ (H_a) and U (H_g) as a function of water (H_w) in the absence of zinc

	Diffusion coefficient/10^{-11} m^2 s^{-1}, (contribution %)		
Water (wt%)	H_a	H_g	H_w
5.5	0.60 ± 0.04	1.02 ± 0.07	0.93 ± 0.06 (20.0 ± 1.2%) 4.57 ± 0.21 (80.0 ± 1.2%)
8.3	1.18 ± 0.15	1.98 ± 0.23	1.77 ± 0.13 (13.0 ± 1.1%) 7.83 ± 0.49 (87.0 ± 1.1%)
26.2	9.26 ± 0.45	14.33 ± 0.61	12.93 ± 0.04 (3.2 ± 0.5%) 38.06 ± 0.93 (96.8 ± 0.5%)

Table 6 Diffusion coefficients of reline species, Ch^+ (H_a) and U (H_g) as a function of water (H_w) in the presence of 0.3 M $ZnCl_2$

	Diffusion coefficient/10^{-11} m^2 s^{-1}, (contribution %)		
Water (wt%)	H_a	H_g	H_w
5.5	0.64 ± 0.03	1.12 ± 0.05	1.08 ± 0.12 (17.0 ± 0.4%) 5.99 ± 0.16 (83.0 ± 0.4%)
8.3	1.28 ± 0.09	2.19 ± 0.15	2.22 ± 0.10 (11.7 ± 0.4%) 9.64 ± 0.42 (88.3 ± 0.4%)
26.2	10.01 ± 0.25	15.67 ± 0.7	10.11 ± 0.06 (23.8 ± 1.6%) 32.85 ± 0.29 (76.2 ± 1.6%)

From previous studies of reline,[35] it has been suggested that the hydroxyl group in Ch^+ and carbonyl group in U co-ordinate around the Cl^- ion. It is expected that such an orientation reduces the opportunity for proton exchange between H_d (U) and H_g (Ch^+) protons. This is supported by the diffusion data (Table 2), which show that alkyl and hydroxyl protons in Ch^+ diffuse at the same rate. However, the 2D ^1H–^1H NOESY spectrum shows a cross peak between H_d and H_g protons (Fig. 7a). If proton exchange is not the origin of this cross peak, it can arise from the nOe, indicating these protons are in close ($\lesssim 3$ Å) proximity. The addition of Zn does not appear to change the interactions between U and Ch^+ species, where 1D ^1H (Fig. 4) and 2D ^1H–^1H NOESY (Fig. 7) spectra and ^1H diffusion data (Table 2) are observed to remain largely unchanged.

When water is added to reline, it has been previously observed[23] that water coordinates with Cl^- and Ch^+. This co-ordination brings the H_w and H_d protons into close proximity, facilitating proton exchange between these protons. This is observed in this study in the 2D ^1H–^1H NOESY spectra (Fig. 8 and 9). In the NOESY spectrum with 8.3% wt water (Fig. 8a), not only is a cross peak observed between H_d and H_w protons, but there is now an absence of an nOe interaction between H_g and H_d protons, indicating a change in co-ordination between U and Ch^+ species. The addition of water to reline, in the presence of Zn, does not appear to change the interactions between U or Ch^+ species (Fig. 4 and 8) However, the presence of zinc appears to slow the exchange rate between H_d and H_w protons (Table 1). This is also supported by the 1D ^1H NMR spectra (Fig. 4b), where, in the presence of Zn, there is a narrowing of the line width of H_d and H_w peaks, which suggests that the presence of Zn slows down proton exchange. It is not clear why this is, but it could be because Zn^{2+} may compete with Cl^- to co-ordinate with either the water or Ch^+, or both, and thus reduces the number H_d and H_w protons able to exchange.

For both ethaline and reline, the addition of water reduces the viscosity.[12] This can be seen in the narrowing of peaks for non-exchangeable protons (Fig. 3 and 4) and increase in T_1 relaxation times (Fig. 10) and diffusion co-efficients, with increasing water (Tables 3–6). However, the T_1 relaxation time and diffusion co-efficient data also indicate a phase transition for both reline and ethaline with increasing water concentration. This can be seen in (Fig. 11), where these data are combined into a single plot for each DES. In ethaline, a discontinuity is observed in T_1 data around 8.3 wt% water. A more marked discontinuity in the T_1 relaxation time is observed for reline, where there is an initial decrease then increase. It should be noted, that a similar discontinuity can also be observed in the diffusion co-efficient data reported by D'Agostino *et al.*,[12] where a wider range of water concentrations were investigated. The origins of this behaviour in reline are most likely to come from a change in the distribution of water within the system. At low

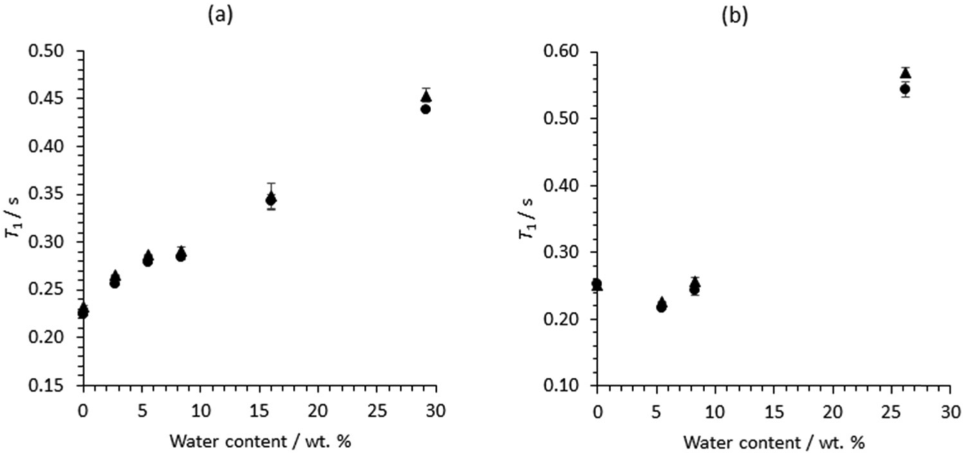

Fig. 10 T_1 relaxation times for Ch^+ protons (H_a), in (a) ethaline and (b) reline, as a function of water content, (●) in the absence and (▲) presence of 0.3 M $ZnCl_2$.

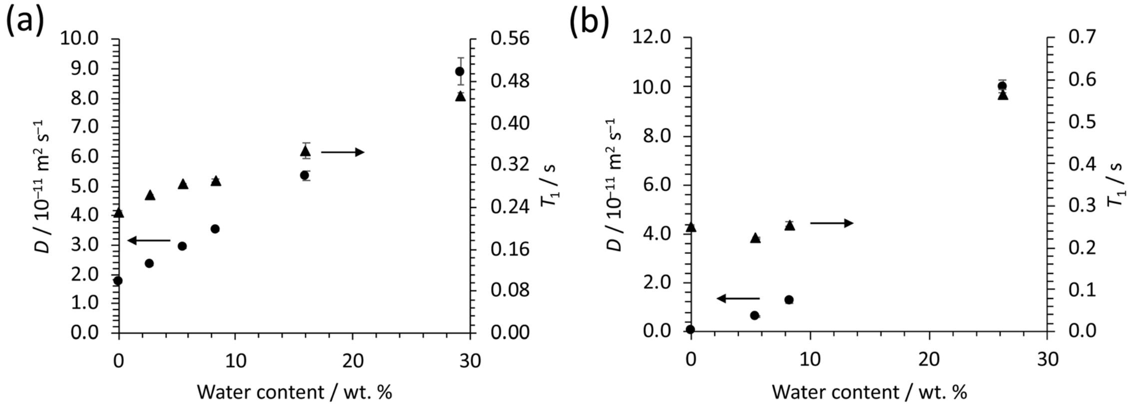

Fig. 11 Plot of T_1 relaxation times (▲) and diffusion coefficient (●) for ChCl protons (H_a) in (a) ethaline and (b) reline, as a function of water content.

concentrations, water molecules embed in the reline network, forming a supermolecular complex. In such structures, there is an associated increase in size, leading to a higher rotational correlation time, for ChCl, and, hence, lower T_1 relaxation time.[36] However, when the water content increases (>6 wt%), there is an increase in the T_1 relaxation time for ChCl, which suggests a reduction in the tumbling rate for ChCl, indicating a change in the structures (solvation) formed within reline. This observation could be indicative of a transition to the heterogeneous distribution of water from discrete microscopic 'pockets' of water, within the reline network, proposed by Posada *et al.*[24] and D'Agostino *et al.*[12] at high water concentrations. Ethaline shows more of a monotonic increase in T_1 relaxation time, with increasing water content. However, a slight discontinuity can also be observed around 8 wt% of water, which is at a concentration equivalent to 1 : 1 (water : ChCl) mole ratio, a concentration that has previously[12] been observed to correspond to a transition in behaviour of other deep eutectic solvents.

Lastly, diffusion measurements for both reline and ethaline have shown that water has two diffusion co-efficients, over all water concentrations, in the presence and absence of Zn. This suggests that water exists in two different environments, with no, or slow, exchange between these environments. As we see this bi-exponential diffusion co-efficient for water, over all water concentrations, it is unlikely that these environments are associated with the water within the DES network and interstitial water, which has been observed at >6 wt% water (reline) and >8 wt% (ethaline). It is unclear what the origins are for the bi-exponential diffusion co-efficient of water, and further studies are required.

Conclusions

This paper has investigated the role of Zn and water on solvation, and dynamics, in reline and ethaline DES systems, using ^{1}H NMR spectroscopy, T_1 NMR relaxation times, NMR diffusion and 2D NOESY/EXSY spectroscopy. In ethaline, it is found that Zn promotes proton exchange between hydroxyl protons (H_d and H_f) in ChCl and EG, in the presence and absence of water. However, in reline, the presence of Zn was found to have little effect on the interactions between ChCl and U species, but did reduce the proton exchange between hydroxyl (H_d) and water (H_w) protons, in systems containing water. The presence of water was also found to change the interaction between ChCl and U species, removing the nOe cross-peak between amide and hydroxyl protons. These findings reveal key changes in solvation and dynamics, in both reline and ethaline, as a function of water and Zn concentration, proving insight into the role of solvation and dynamics in these electrolytes for a range of Zn electrochemical applications. These data support previous observations of changes in microstructure for both reline and ethaline, with increasing water content. Moreover, the variation in T_1 NMR relaxation times, for certain proton environments, in both DES, also demonstrates the potential for Zn electrochemical processes to be visualised by operando magnetic resonance imaging.[27,28]

Data availability

The data generated in this study are available at https://doi.org/10.25500/edata.bham.00000719.

Conflicts of interest

There are no conflicts to declare.

Acknowledgements

The authors thank the University of Birmingham and EPSRC (grant EP/K039245/1) for financial support. YAZ thanks the Saudi Arabian Ministry of Higher Education and the chemistry department in Imam Abdulrahman Bin Faisal University for their financial support.

References

1 F. I. Danilov, V. S. Protsenko, A. A. Kityk, D. A. Shaiderov, E. A. Vasil'eva, U. P. Kumar and C. J. Kennady, *Prot. Met. Phys. Chem.*, 2017, **53**, 1131–1138.

2 V. S. Protsenko, L. S. Bobrova, D. E. Golubtsov, S. A. Korniy and F. I. Danilov, *Russ. J. Appl. Chem.*, 2018, **91**, 1106–1111.

3 A. P. Abbott, J. C. Barron and K. S. Ryder, *Trans. Inst. Met. Finish.*, 2009, **87**, 201–207.

4 A. P. Abbott, K. J. McKenzie and K. S. Ryder, *Ionic Liquids IV*, American Chemical Society, 2007, vol. 975, ch. 13, pp. 186–197.

5 A. P. Abbott, G. Capper, K. J. McKenzie, A. Glidle and K. S. Ryder, *Phys. Chem. Chem. Phys.*, 2006, **8**, 4214–4221.

6 W. Kao-ian, R. Pornprasertsuk, P. Thamyongkit, T. Maiyalagan and S. Kheawhom, *J. Electrochem. Soc.*, 2019, **166**, A1063–A1069.

7 E. L. Smith, A. P. Abbott and K. S. Ryder, *Chem. Rev.*, 2014, **114**, 11060–11082.

8 Q. Zhang, K. De Oliveira Vigier, S. Royer and F. Jerome, *Chem. Soc. Rev.*, 2012, **41**, 7108–7146.

9 E. L. Smith, *Trans. Inst. Met. Finish.*, 2014, **91**, 241–248.

10 A. P. Abbott, K. El Ttaib, G. Frisch, K. J. McKenzie and K. S. Ryder, *Phys. Chem. Chem. Phys.*, 2009, **11**, 4269–4277.

11 A. H. Whitehead, M. Pölzler and B. Gollas, *J. Electrochem. Soc.*, 2010, **157**, D328–D334.

12 C. D'Agostino, L. F. Gladden, M. D. Mantle, A. P. Abbott, E. I. Ahmed, A. Y. M. Al-Murshedi and R. C. Harris, *Phys. Chem. Chem. Phys.*, 2015, **17**, 15297–15304.

13 B. B. Hansen, S. Spittle, B. Chen, D. Poe, Y. Zhang, J. M. Klein, A. Horton, L. Adhikari, T. Zelovich, B. W. Doherty, B. Gurkan, E. J. Maginn, A. Ragauskas, M. Dadmun, T. A. Zawodzinski, G. A. Baker, M. E. Tuckerman, R. F. Savinell and J. R. Sangoro, *Chem. Rev.*, 2021, **121**, 1232–1285.

14 A. P. Abbott, J. C. Barron, G. Frisch, K. S. Ryder and A. F. Silva, *Electrochim. Acta*, 2011, **56**, 5272–5279.

15 A. P. Abbott, J. C. Barron, G. Frisch, S. Gurman, K. S. Ryder and A. Fernando Silva, *Phys. Chem. Chem. Phys.*, 2011, **13**, 10224–10231.

16 X. Ge, C. Gu, X. Wang and J. Tu, *J. Mater. Chem. A*, 2017, **5**, 8209–8229.

17 A. T. Celebi, T. J. H. Vlugt and O. A. Moultos, *J. Phys. Chem. B*, 2019, **123**, 11014–11025.

18 T. Zhekenov, N. Toksanbayev, Z. Kazakbayeva, D. Shah and F. S. Mjalli, *Fluid Phase Equilib.*, 2017, **441**, 43–48.

19 C. Ma, A. Laaksonen, C. Liu, X. Lu and X. Ji, *Chem. Soc. Rev.*, 2018, **47**, 8685–8720.

20 J. R. Bezerra-Neto, N. G. Sousa, L. P. M. dos Santos, A. N. Correia and P. de Lima-Neto, *Phys. Chem. Chem. Phys.*, 2018, **20**, 9321–9327.

21 C. Du, B. Zhao, X.-B. Chen, N. Birbilis and H. Yang, *Sci. Rep.*, 2016, **6**, 1–14.

22 P. E. Valverde, T. A. Green and S. Roy, *J. Appl. Electrochem.*, 2020, **50**, 699–712.

23 O. S. Hammond, D. T. Bowron and K. J. Edler, *Angew. Chem., Int. Ed.*, 2017, **56**, 9782–9785.

24 E. Posada, N. López-Salas, R. J. Jiménez Riobóo, M. L. Ferrer, M. C. Gutiérrez and F. del Monte, *Phys. Chem. Chem. Phys.*, 2017, **19**, 17103–17110.

25 A. Pandey and S. Pandey, *J. Phys. Chem. B*, 2014, **118**, 14652–14661.

26 J. C. Barron, Doctor of Philosophy, University of Leicester, 2009.

27 A. J. Davenport, M. Forsyth and M. M. Britton, *Electrochem. Commun.*, 2010, **12**, 44–47.

28 M. M. Britton, P. M. Bayley, P. C. Howlett, A. J. Davenport and M. Forsyth, *J. Phys. Chem. Lett.*, 2013, **4**, 3019–3023.

29 I. R. Kleckner and M. P. Foster, *Biochim. Biophys. Acta*, 2011, **1814**, 942–968.

30 KaleidaGraph (Synergy, USA).

31 T. D. W. Claridge, *High-Resolution NMR Techniques in Organic Chemistry*, 2nd edn, Elsevier, Oxford, UK, 2009.

32 E. O. Stejskal and J. E. Tanner, *J. Chem. Phys.*, 1965, **42**, 288.

33 R. R. Gil and A. Navarro-Vázquez, *Modern NMR Approaches to the Structure Elucidation of Natural Products: Volume 2: Data Acquisition and Applications to Compound Classes*, The Royal Society of Chemistry, 2017, vol. 2, pp. 1–38.

34 R. Stefanovic, M. Ludwig, G. B. Webber, R. Atkin and A. J. Page, *Phys. Chem. Chem. Phys.*, 2017, **19**, 3297–3306.

35 C. R. Ashworth, R. P. Matthews, T. Welton and P. A. Hunt, *Phys. Chem. Chem. Phys.*, 2016, **18**, 18145–18160.

36 N. Bloembergen, E. M. Purcell and R. V. Pound, *Phys. Rev.*, 1948, **73**, 679–712.